SMIP15

SMIP15 SEMINAR ON
UTILIZATION OF STRONG-MOTION DATA

Davis, California
October 22, 2015

PROCEEDINGS

Sponsored by

California Strong Motion Instrumentation Program
California Geological Survey
California Department of Conservation

Co-Sponsors

California Seismic Safety Commission
California Governor's Office of Emergency Services
California Department of Transportation
Office of Statewide Health Planning and Development

The California Strong Motion Instrumentation Program (CSMIP), a program within the California Geological Survey (CGS) of the California Department of Conservation, records the strong shaking of the ground and structures during earthquakes for analysis and utilization by the engineering and seismology communities through a statewide network of strong motion instruments (www.conservation.ca.gov/CGS/smip). CSMIP is advised by the Strong Motion Instrumentation Advisory Committee (SMIAC), a committee of the California Seismic Safety Commission. Major program funding is provided by an assessment on construction costs for building permits issued by cities and counties in California, with additional funding from the California Governor's Office of Emergency Services (Cal OES), the California Department of Transportation (Caltrans) and the Office of Statewide Health Planning and Development (OSHPD).

In July 2001, the California Governor's Office of Emergency Services (Cal OES) began funding for the California Integrated Seismic Network (CISN), a newly formed consortium of institutions engaged in statewide earthquake monitoring that grew out of TriNet, funded by FEMA, and includes CGS, USGS, Caltech and UC Berkeley. The goals are to record and rapidly communicate ground shaking information in California, and to analyze the data for the improvement of seismic codes and standards (www.cisn.org). CISN produces ShakeMaps of ground shaking, based on shaking recorded by stations in the network, within minutes following an earthquake. The ShakeMap identifies areas of greatest ground shaking for use by OES and other emergency response agencies in the event of a damaging earthquake.

The Center for Engineering Strong Motion Data (CESMD) is operated by the CSMIP Program of the CGS in cooperation with the National Strong-Motion Project (NSMP) and the Advanced National Seismic System (ANSS) of the U.S. Geological Survey (USGS). The CESMD builds on and incorporates the CISN Engineering Data Center and will continue to serve the California region while expanding to serve other ANSS regions. The Data Center provides strong-motion data rapidly after a significant earthquake in the United States. Users also have direct access to data from previous earthquakes and detailed information about the instrumented structures and sites. The Data Center is co-hosted by CGS and USGS at www.strongmotioncenter.org

DISCLAIMER

SMIP15

SMIP15 SEMINAR ON
UTILIZATION OF STRONG-MOTION DATA

Davis, California
October 22, 2015

PROCEEDINGS

Edited by

Moh Huang

Sponsored by

California Strong Motion Instrumentation Program
California Geological Survey
California Department of Conservation

Co-Sponsors

California Seismic Safety Commission
California Governor's Emergency Services
California Department of Transportation
Office of Statewide Health Planning and Development

PREFACE

The California Strong Motion Instrumentation Program (CSMIP) in the California Geological Survey of the California Department of Conservation established a Data Interpretation Project in 1989. Each year CSMIP Program funds several data interpretation contracts for the analysis and utilization of strong-motion data. The primary objectives of the Data Interpretation Project are to further the understanding of strong ground shaking and the response of structures, and to increase the utilization of strong-motion data in improving post-earthquake response, seismic code provisions and design practices.

As part of the Data Interpretation Project, CSMIP holds annual seminars to transfer recent research findings on strong-motion data to practicing seismic design professionals, earth scientists and post-earthquake response personnel. The purpose of the annual seminar is to provide information that will be useful immediately in seismic design practice and post-earthquake response, and in the longer term, useful in the improvement of seismic design codes and practices. Proceedings and individual papers for each of the previous annual seminars are available at http://www.conservation.ca.gov/cgs/smip/Pages/proceedings.aspx in PDF format. Due to the State budget restraints, CSMIP did not fund as many projects as in other years and did not hold an annual seminar in 2010 or 2011. The SMIP15 Seminar is the twenty-fourth in this series of annual seminars.

The SMIP15 Seminar is divided into two sessions in the morning and two sessions in the afternoon. The sessions in the morning include three presentations. Dr. David Boore of USGS is invited to present the 2014 William Joyner Lecture on the past, present, and future for ground motion prediction equations in the first session. The second session will focus on ground motions and will include presentations of the results from two CSMIP-funded projects on effectiveness of 1D site response analysis by Professor Stewart of UCLA and on topographic effects on strong ground motion by Professor Rodriguez-Marek of Virginia Tech.

The afternoon session will start with presentations of the final results from two CSMIP-funded projects on ASCE/SEI 7 direction of loading provisions by Mr. Lizundia of Rutherford + Chekene and on building response to bi-directional excitation by Professor Bernal of Northeastern University. The third presentation by Dr. Imbsen of SC Solutions will include preliminary results from a CSMIP-funded project on rapid post-earthquake safety evaluation of a suspension bridge. The last session will include presentations of some preliminary results from two CSMIP-funded projects on identifications of building periods and modal damping ratios for buildings by Professor Zareian of UC Irvine and on identification of soil-foundation impedance functions from building response records by Professor Taciroglu of UCLA. Individual papers and the proceedings are available to the SMIP15 participants in an USB flash drive, and will be available at the CSMIP website.

Moh Huang
CSMIP Data Interpretation Project Manager

Appreciation to Members of the Strong Motion Instrumentation Advisory Committee

Main Committee

Farzad Naeim, Chair, Farzad Naeim, Inc.
Norman Abrahamson, Pacific Gas & Electric Company
Bruce Clark, Leighton & Associates
Martin Eskijian, California State Lands Commission (retired)
Wilfred Iwan, California Institute of Technology
Tom Ostrom, Caltrans
Marshall Lew, Amec Foster Wheeler
Bret Lizundia, Rutherford + Chekene
Chris Tokas, Office of Statewide Health Planning and Development
Robert Anderson (ex-officio), Seismic Safety Commission

Ground Response Subcommittee

Marshall Lew, Chair, Amec Foster Wheeler
Abbas Abghari, Caltrans
Brian Chiou, Caltrans
Geoffrey Martin, Univ. of Southern California
Ben Tsai, Pacific Gas & Electric Company (retired)

Buildings Subcommittee

Bret Lizundia, Chair, Rutherford + Chekene
Lucie Fougner, Degenkolb Engineers
Donald Jephcott, Structural Engineer
Ifa Kashefi, City of Los Angeles
David Leung, City of San Francisco
Eduardo Miranda, Stanford University
John Robb, Structural Engineer
Roy Lobo, Office of Statewide Health Planning and Development
Chia-Ming Uang, UC San Diego

Lifelines Subcommittee

Martin Eskijian, Chair, California State Lands Commission (retired)
Craig Davis, Los Angeles Dept. of Water and Power
David Gutierrez, DWR Division of Safety of Dams
Marsha McLaren, Pacific Gas & Electric Company
Tom Ostrom, Caltrans

Data Utilization Subcommittee

Wilfred Iwan, Chair, California Institute of Technology
Representatives from each Subcommittee

TABLE OF CONTENTS

SMIP15 SEMINAR ON UTILIZATION OF STRONG-MOTION DATA

October 22, 2015

Putah Creek Facility
University of California, Davis, California

PROGRAM

8:15 am **REGISTRATION**

9:15 am **WELCOMING REMARKS**
Farzad Naeim, Strong Motion Instrumentation Advisory Committee (SMIAC)
John Parrish, State Geologist, California Geological Survey
David Bunn, Director, Department of Conservation

INTRODUCTION
Anthony Shakal, Manager, California Strong Motion Instrumentation Program
Moh Huang, California Strong Motion Instrumentation Program

Session I

Moderator: *Wilfred Iwan*, Caltech and SMIAC

9:30 am **Ground Motion Prediction Equations: Past, Present, and Future**
The 2014 William Joyner Lecture
David Boore, US Geological Survey (invited speaker)

10:30 am Break

Session II

Moderator: *Marshall Lew*, AMEC Foster Wheeler and SMIAC

11:00 am **Effectiveness of 1D Ground Response Analyses at Predicting Site Response at California Vertical Array Sites**
Kioumars Afshari and *Jonathan Stewart*, UC Los Angeles.

11:30 pm **Parametrization of Topography for Ground Motion Prediction: Summary and Findings**
Manisha Rai and *Adrian Rodriguez-Marek*, Virginia Polytechnic Institute and State University.

12:00 pm **Lunch**
Lunch will be provided

Session III

Moderator: *Martin Eskijian*, California State Lands Commission and SMIAC

12:50 pm **Evaluation of ASCE/SEI 7 Direction of Loading Provisions Using CSMIP Records**
Reid Zimmerman, *Bret Lizundia* and *Saeed Fathali*, Rutherford + Chekene

1:20 pm **Elastic Force Demands from Bi-Directional Excitation**
Dionisio Bernal, Northeastern University

1:50 pm **Rapid Post-Earthquake Safety Evaluation of Bridges**
Roy Imbsen, *Shahriar Vahdani* and *Jinquan Zhong*, SC Solutions

2:20 pm Break

Session IV

Moderator: *Bret Lizundia*, Rutherford + Chekene and SMIAC

2:40 pm **Identification and Validation of Natural Periods and Modal Damping Ratios for Steel and Reinforced Concrete Buildings in California**
Angie Harris, Yijun Xiang, Farzad Naeim and *Farzin Zareian*, UC Irvine

3:10 pm **Identification of Soil-Foundation Impedance Functions from Seismic Response Signals of Instrumented Buildings**
S. Farid Ghahari, *Fariba Abazarsa* and *Ertugrul Taciroglu*, UC Los Angeles

3:40 pm **Adjourn**

GROUND-MOTION PREDICTION EQUATIONS: PAST, PRESENT, AND FUTURE
(The 2014 William Joyner Lecture)

David M. Boore

U.S. Geological Survey, Menlo Park, CA, United States (boore@usgs.gov)

Abstract

Ground-motion prediction equations (GMPEs) typically give amplitudes of ground motion as a function of distance from earthquakes of a particular magnitude. They are the foundations on which the seismic hazard maps used in building codes are built, they provide motions for the design of critical structures, and they and the databases used in their derivation conveniently summarize a large amount of information about the seismic waves radiated from earthquakes. The development of GMPEs requires knowledge of many aspects of seismology, including data acquisition, data processing, source physics, the determination of crustal structure, the effects of that structure on the propagation of seismic waves, the measurement and characterization of the geotechnical properties near the Earth's surface, and the nonlinear response of soils to strong shaking. Generally, GMPEs are developed for three regions: active crustal regions (ACR), stable continental regions (SCR), and subduction zones (SZ). Most GMPEs in ACRs and SZs are based on empirical analysis of observed ground motion, while those in data-poor areas such as SCRs rely primarily on simulations of ground shaking. As data sets increase and theoretical simulations improve, previous GMPEs are revised and new ones are proposed. As a result, many hundreds of GMPEs have been published, and more are on their way. As an example of the current state-of-practice for GMPEs in ACRs, I will discuss a recent multi-year project undertaken by the Pacific Earthquake Engineering Research Center (PEER). The future is bound to bring more data, but most of these data will be for magnitudes and distances where present GMPEs are well constrained by existing data, at least in ACRs. Significant gaps will continue to exist in our knowledge of ground shaking in certain distance and magnitude ranges for ACRs and for SCRs in general. For this reason, combinations of simulated and observed motions will be used to create future GMPEs.

Introduction

Ground-motion prediction equations (GMPEs) provide ground motions for various ground-motion intensity measures (GMIMs) as a function of various predictor variables, such as a measure of earthquake magnitude, distance from the earthquake to the site, and a characterization of the geology near the site. The predicted motions include a complete statistical distribution, not just a mean value. GMPEs are widely used in earthquake engineering to provide design motions for critical structures as well as being the foundation on which the design maps in modern building codes are built. This talk concentrates in GMPEs developed as part of the Pacific Earthquake Engineering Research Center's NGA-West2 project (Bozorgnia et al., 2014). GMPEs were developed both for horizontal component and for vertical component

ground motions. A critical part of that project was the construction of a well-vetted global database of GMIMs and associated metadata (Ancheta et al., 2014). In addition to their engineering uses, the GMPEs developed from the database are a convenient summary of the overall magnitude and distance behavior of a very large number of ground-motion recordings, and as such, they are useful in assessing the magnitude scaling of ground motion, which is intimately related to the source processes of earthquakes.

These notes accompany the Joyner Lecture presented at the SMIP15 meeting in Davis, California, on 22 October 2015.

The PEER NGA-West2 Database

The Pacific Earthquake Engineering Center (PEER) NGA-West2 database, developed by Ancheta et al. (2014), contains 21,336 three-component recordings from 599 shallow crustal earthquakes in active tectonic regions around the world. Great care was taken in developing the database: the recordings were processed in a uniform and consistent manner to provide high-quality seismic intensity measures and metadata, such as source and site properties. The metadata were evaluated by several teams of researchers to ensure consistency in view of the different regions and methods used to obtain the metadata by various researchers.

The ground-motion intensity measures used for the NGA-West2 database are 5%-damped pseudo-absolute response spectral acceleration (*PSA*), peak ground acceleration (*PGA*), and peak ground velocity (*PGV*). The horizontal components were combined to produce a measure that is independent of the orientation of the instruments as installed at a site. The GMPEs for the NGA-West2 project use the measure *rotd50* (Boore, 2010), which represents the median value of PSA over all possible instrument orientations (*rotd100* represents the maximum PSA for a pair of records overall all possible orientations; there is a relatively robust, period-dependent relation between rotd50 and rotd100).

The most common metadata used in developing GMPEs are measures of distance, magnitude, and site geology. In the NGA-West2 database, the magnitude measure is moment magnitude **M** (Hanks and Kanamori, 1979). The two main distance measures used in the NGA-West2 project are R_{RUP} and R_{JB}, defined in Figure 1 (along with a number of other possible measures of distance from a site to a fault rupture surface).

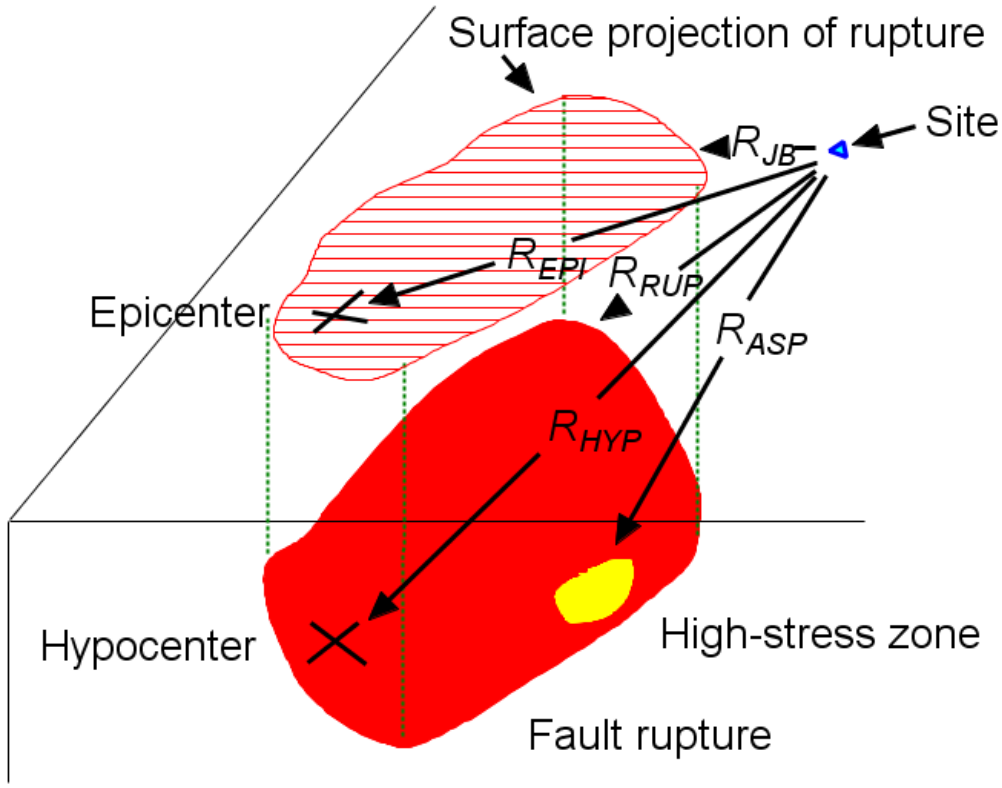

Figure 1. Some distance measures. The most commonly used measures in modern GMPEs are R_{RUP}, the closest distance to the rupture surface, and R_{JB}, the closest horizontal distance to the surface projection of the rupture surface ("*JB*" for Joyner and Boore, who introduced this measure in Joyner and Boore, 1981). $R_{JB} = 0.0$ for sites over the fault.

The site geology is characterized in the NGA-West2 project by the time-weighted average of the shear-wave velocity from the surface to 30 m (V_{S30}). While it has been argued that such a velocity may not be representative of the shear-wave velocities at deeper depths, which can affect longer period motions, Boore et al. (2011) show that there is a good correlation of V_{S30} and the shear-wave velocity averaged to depths significantly greater than 30 m (Figure 2).

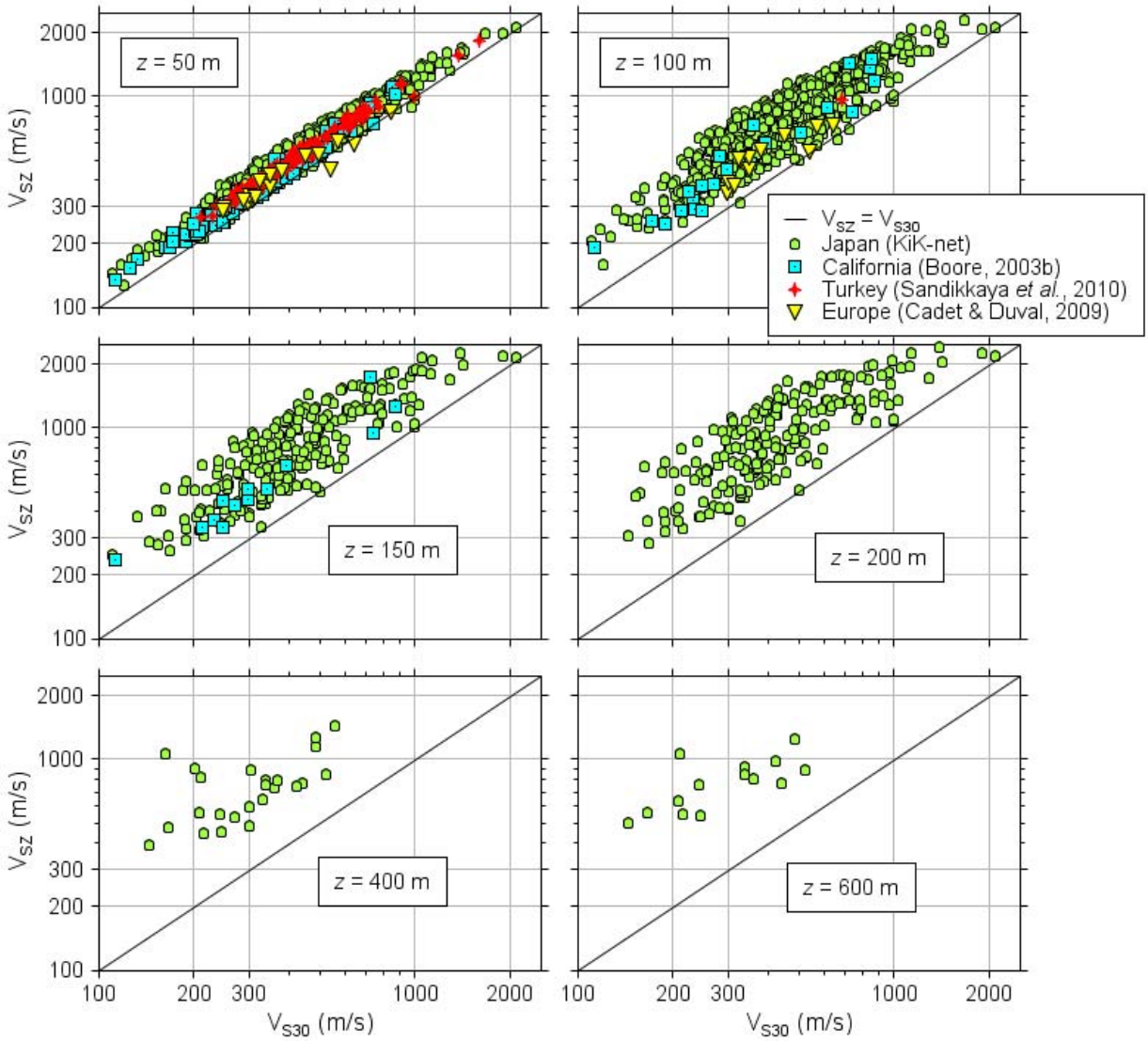

Figure 2. Scatterplot of V_{S30} and V_{SZ} from shear-wave velocity profiles for six averaging depths z (only the profiles for KiK-net stations had profiles to the three greatest values of z). (Modified from Figure 10 in Boore et al., 2011, which contains formal correlation coefficients for each graph; these range from 0.98 for $z = 50$ m to 0.79 for $z = 600$ m .)

The NGA-West2 database contains *PSA* for periods from 0.01 s to 20 s. The magnitude-distance distribution of the *PSA* are shown in Figure 3 for T_{OSC} of 1.0 s and 10.0 s, with the data differentiated by earthquake source mechanism. It is clear from Figure 3 that there are many fewer data for the long-period oscillator (and in fact, the fall-off in available data begins at a period of about 1.0 s, as shown in Boore et al., 2014); this is an inevitable consequence of the signal-to-noise characteristics of ground motions recorded on accelerographs (which provide the bulk of the data for the larger earthquakes).

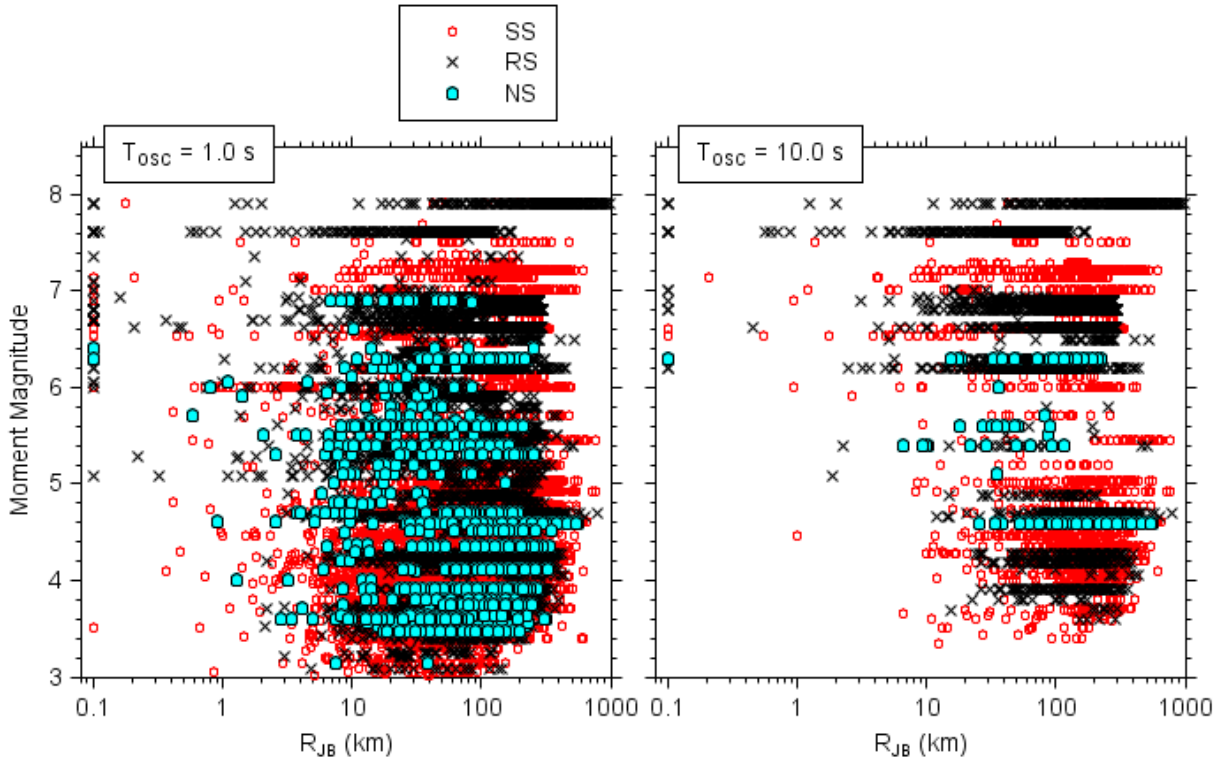

Figure 3. Magnitude-distance distribution of data from the PEER NGA-West2 database, differentiated by fault type (SS=StrikeSlip; NS=NormalSlip; RS=ReverseSlip). The distributions are shown for two oscillator periods, 1.0 s and 10.0 s.

What the Data Tell Us about Choosing the Functions for Ground-Motion Prediction Equations

The functions used in GMPEs are guided by what is expected from physical grounds and also by what the data show. In this section I show various aspects of the NGA-W2 data used by BSSA14 that must be captured by the functions. To provide an overview of the magnitude and distance dependence of the global data, Figure 4 shows *PSA* values for four periods plotted against distance, with magnitude bins indicated by symbols of different color. The data are from strikeslip earthquakes, adjusted to a common V_{S30} value of 760 m/s using the site response equations of Seyhan and Stewart (2014). This figure shows a number of robust features related to magnitude and distance scaling of ground motions for a wide range of magnitudes and distances, without assuming any functional forms for this dependence (aside from the V_{S30} adjustment). The motions are shown for two oscillator periods: 0.2 s and 6.0 s.

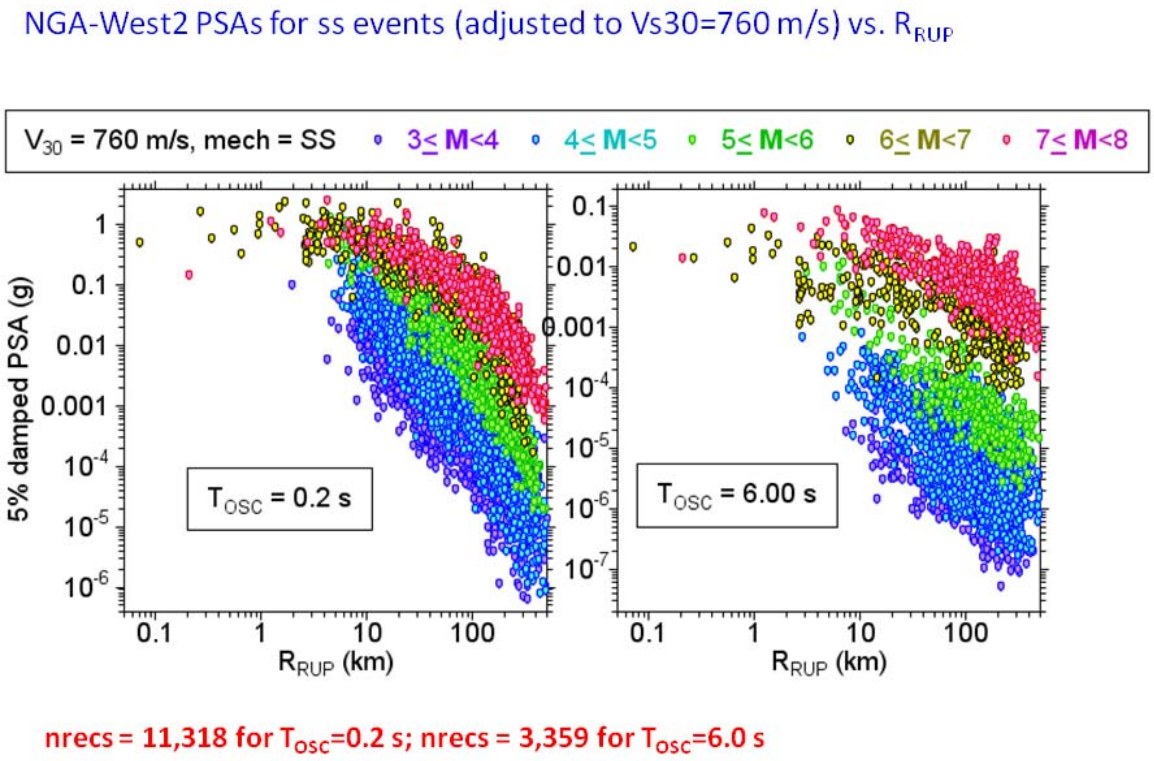

Figure 4. NGA-West2 PSAs for strike-slip events (adjusted to Vs30=760 m/s) vs. R_{RUP} for 2 oscillator periods (0.2 s and 6.0 s).

These figures contain useful information about the magnitude and distance dependence of the data. Before showing this dependence, I first discuss the scatter in the data, as indicated in Figure 5.

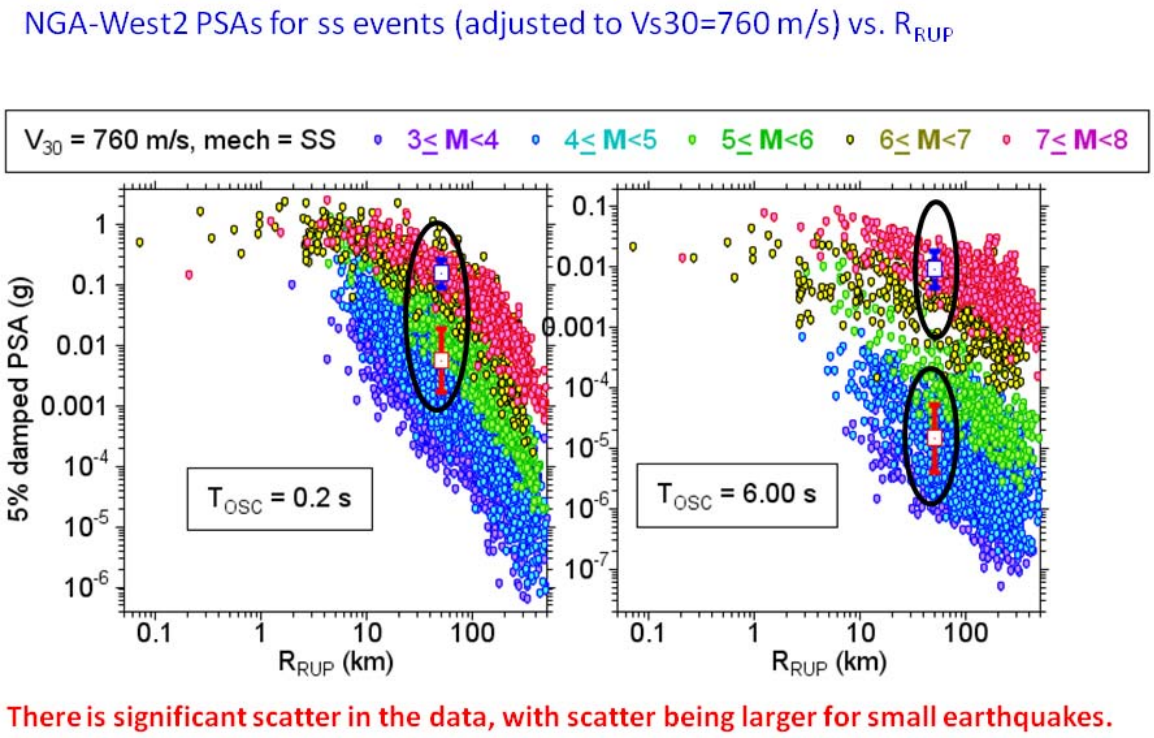

Figure 5. The same as Figure 4, but indicating standard deviations of the data for two magnitude bins and a small distance range centered on 50 km.

There is clearly significant scatter in the data, and representing this scatter accurately in the GMPEs is essential for deriving hazard curves, particularly for small yearly frequencies of exceedance. Figure 5 shows that the scatter is larger for small earthquakes and generally increases with distance (at least to distances of about 200 km). In spite of the scatter, however, there are systematic distance and magnitude trends in the data, as discussed in the next figures.

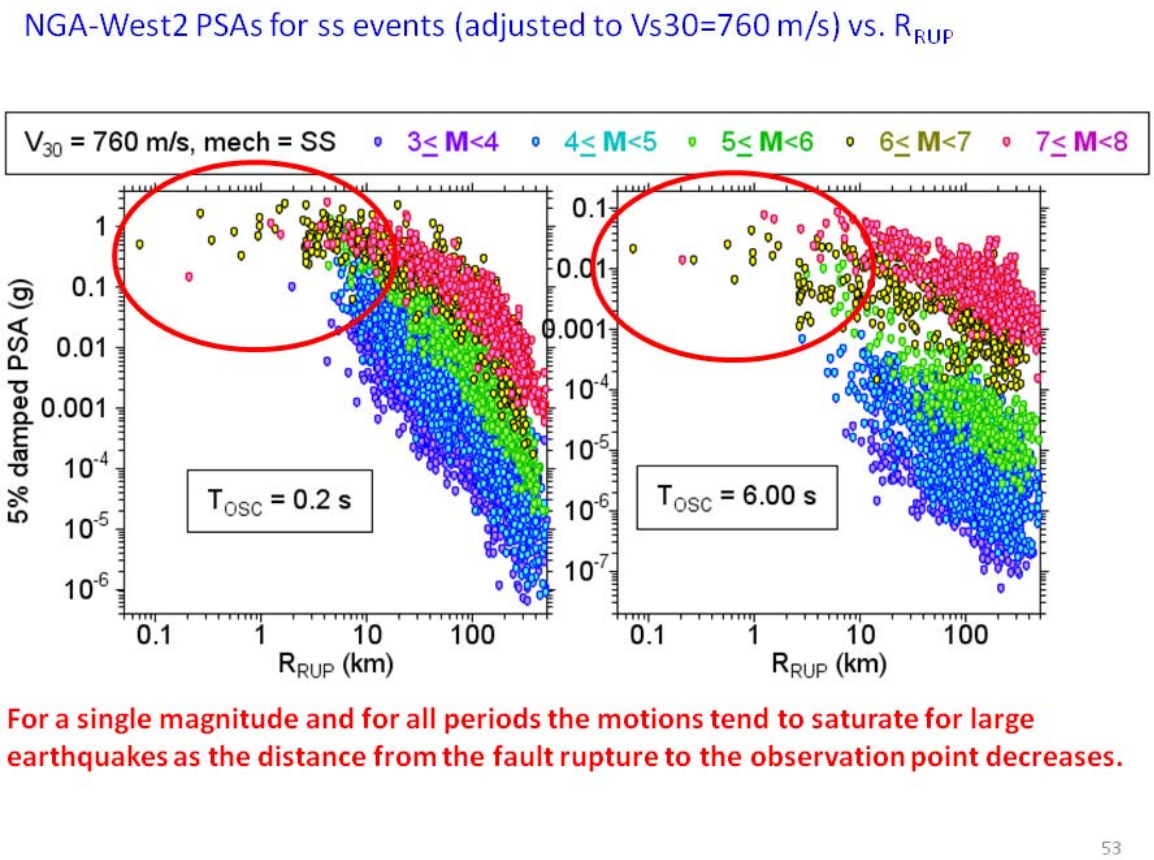

Figure 6. The same as Figure 4, but highlighting the saturation at close distances for a single magnitude and all periods.

For a single magnitude and for all periods the motions tend to saturate for large earthquakes, that is, they approach a constant value, as the distance from the fault rupture to the observation point decreases. This can only be concluded definitively for large magnitudes, for which the rupture approaches the ground surface and therefore the distance measure used in Figure 6 can approach 0.0. Smaller earthquakes do not reach the surface, and therefore surface observations cannot be used to infer whether or not the motions near the rupture surfaces of small earthquakes saturate.

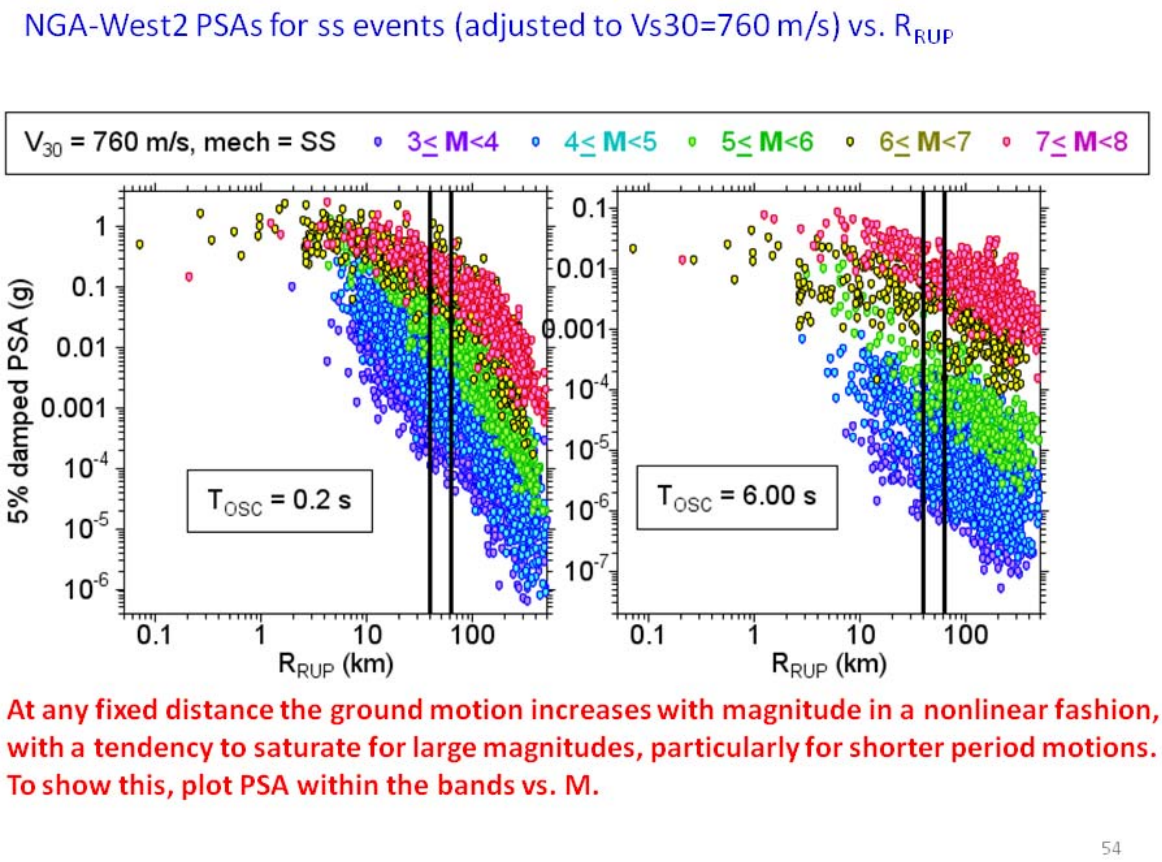

Figure 7. The same as Figure 4, but showing the distance bands to be used to illustrate the scaling of motions at a fixed distance (next figure).

At any fixed distance the ground motion increases with magnitude in a nonlinear fashion, with a tendency to saturate for large magnitudes, particularly for shorter period motions. The overall magnitude scaling increases with increasing period, but it is smaller at short distances than at longer distances. For short periods and close distances there appears to be almost complete saturation for the motions from large earthquakes.

To emphasize the magnitude scaling for a fixed distance, Figure 8 shows that scaling for data in a small distance range centered on 50 km.

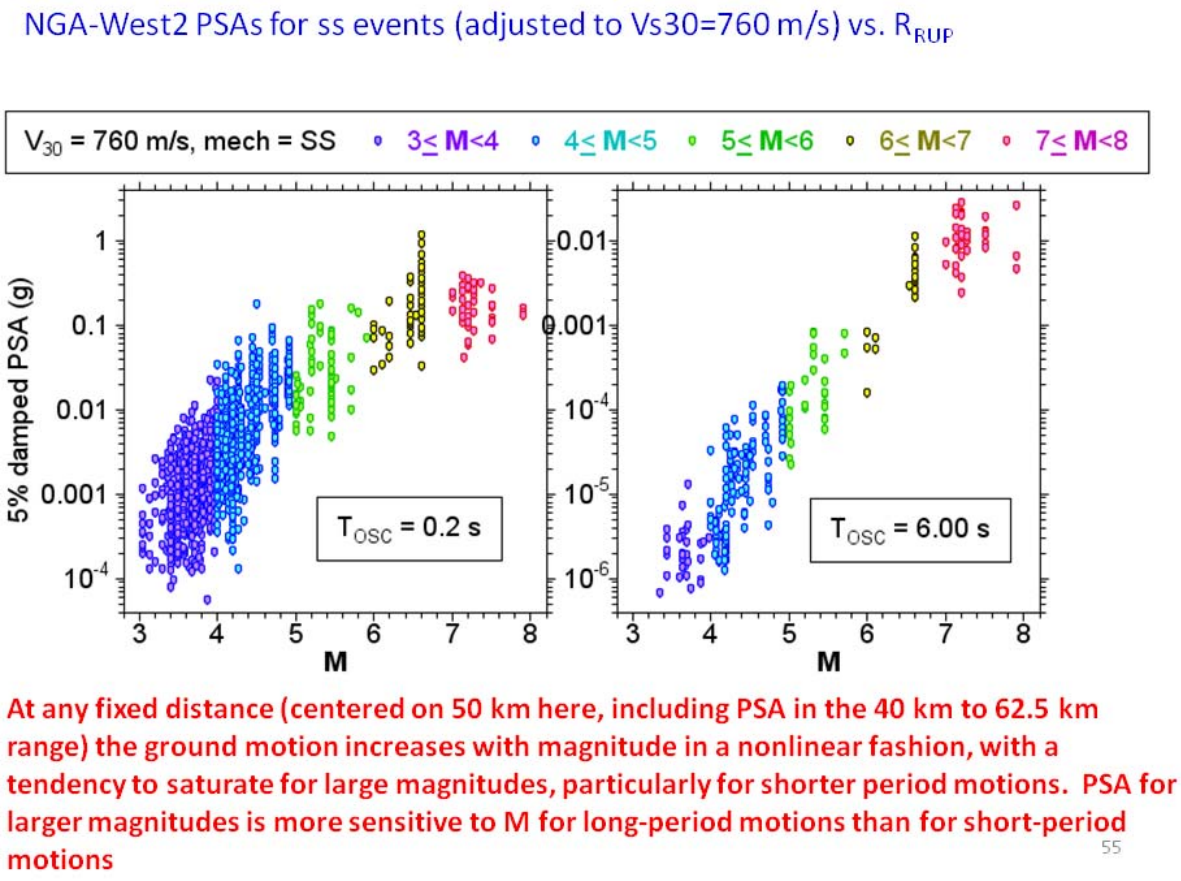

Figure 8. The scaling of motions at two periods as a function of magnitude. Note that the shorter period motions exhibit more saturation of the scaling at large magnitudes than do the longer period motions.

Note shown here is that theoretical predictions for a standard seismological model of the ground motion are in good agreement with this magnitude scaling (Figures 17, 18, and 18 in Boore, 2013).

For a given period and magnitude the median ground motions decay with distance; this decay shows curvature at greater distances on the log-log plot used in Figure 9. This decay can be parameterized as $\exp(-\alpha R_{RUP})/R_{RUP}^{\beta}$, where the terms in the numerator and denominator are similar to the decay from a point source due to anelastic attenuation and geometrical spreading, respectively. In log-log plots the anelastic attenuation produces the curvature at greater distances, and the geometrical spreading produces the linear decay at closer distances. Careful inspection of Figure 9 shows that the apparent geometrical spreading decreases as magnitude increases.
In addition to the dependencies shown in the preceding figures, the equations need to capture site dependence of the motion (including basin depth dependence and nonlinear response), earthquake type, hanging wall, depth to top of rupture, etc. This results in what seems to be complicated equations.

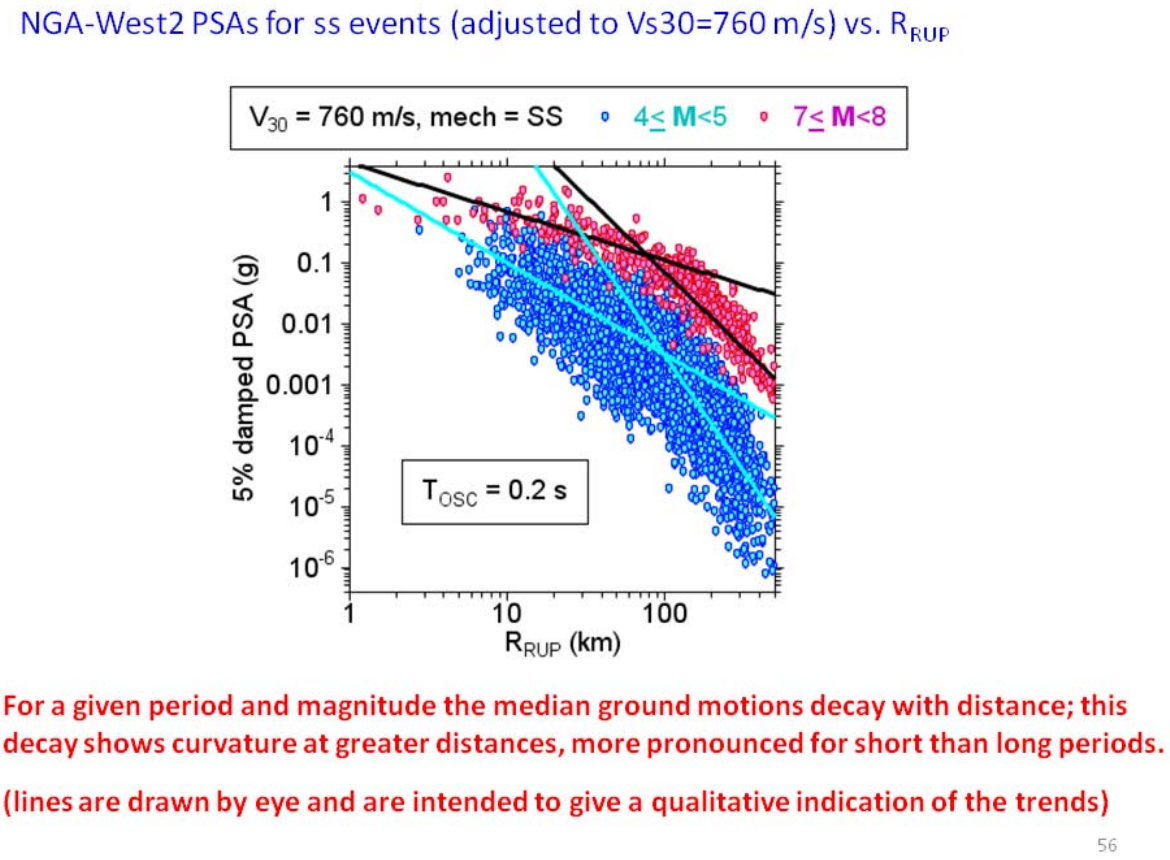

Figure 9. This shows both the steepening of attenuation as distance increases and the magnitude dependence of the attenuation with distances.

Horizontal-Component GMPES from the NGA-West 2 Project

- Need complicated equations to capture effects of:
  - **M**: 3 to 8.5 (strike-slip)
  - Distance: 0 to 300km
  - Hanging wall and footwall sites
  - Soil V_{S30}: 150-1500 m/sec
  - Soil nonlinearity
  - Deep basins
  - Strike-slip, Reverse, Normal faulting mechanisms
  - Period: 0-10 seconds
- The BSSA14 GMPEs are probably the simplest, but there may be situations where they should be used with caution.

Courtesy of Yousef Bozorgnia)

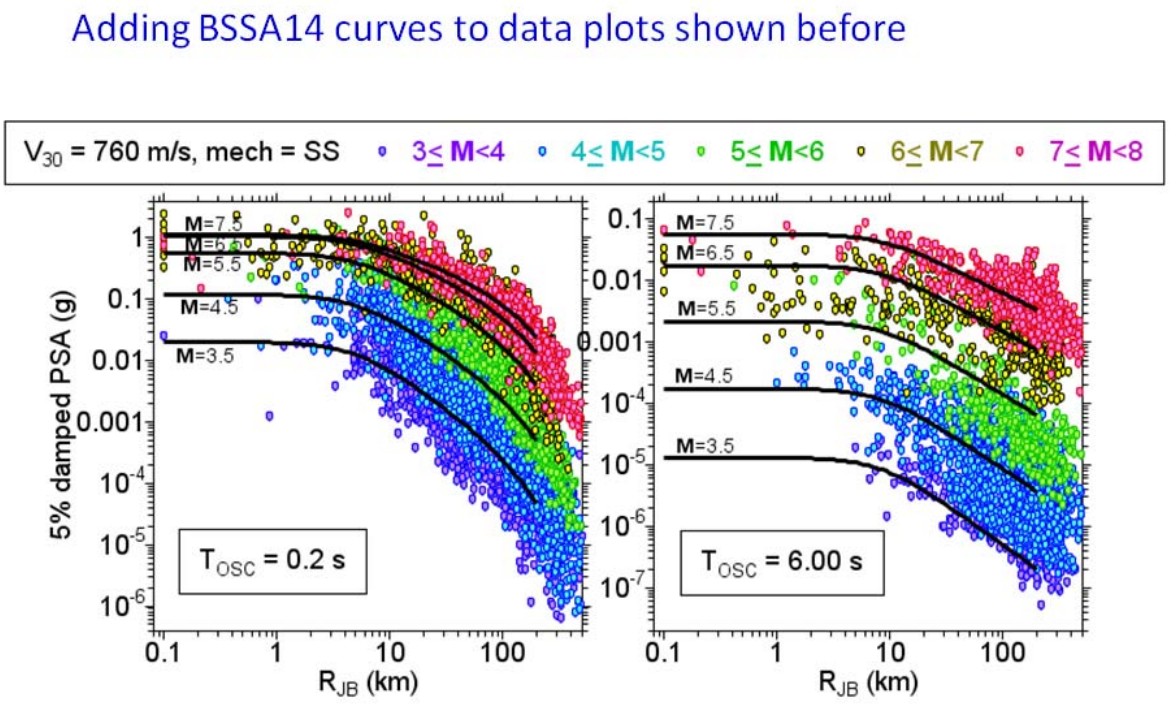

Figure 10. This compares the data initially shown in Figure 4 (but plotted vs R_{JB} rather than R_{RUP}) with the motions from the Boore et al. (2014) (BSSA14) GMPEs.

A few comparisons of the GMPEs resulting from the NGA-West2 project are given in Figures 11 and 12.

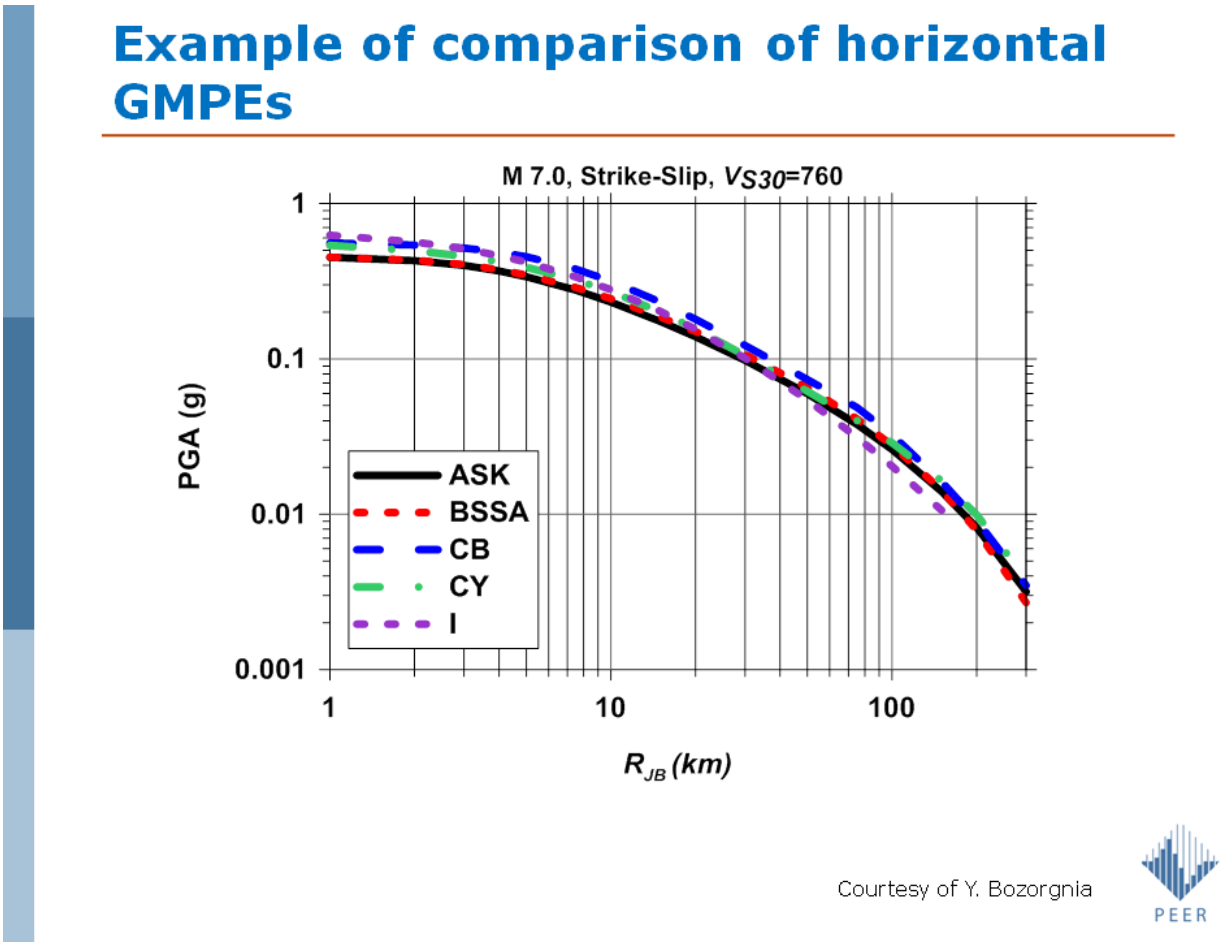

Figure 11. Comparing predictions from the five NGA-West2 GMPEs.

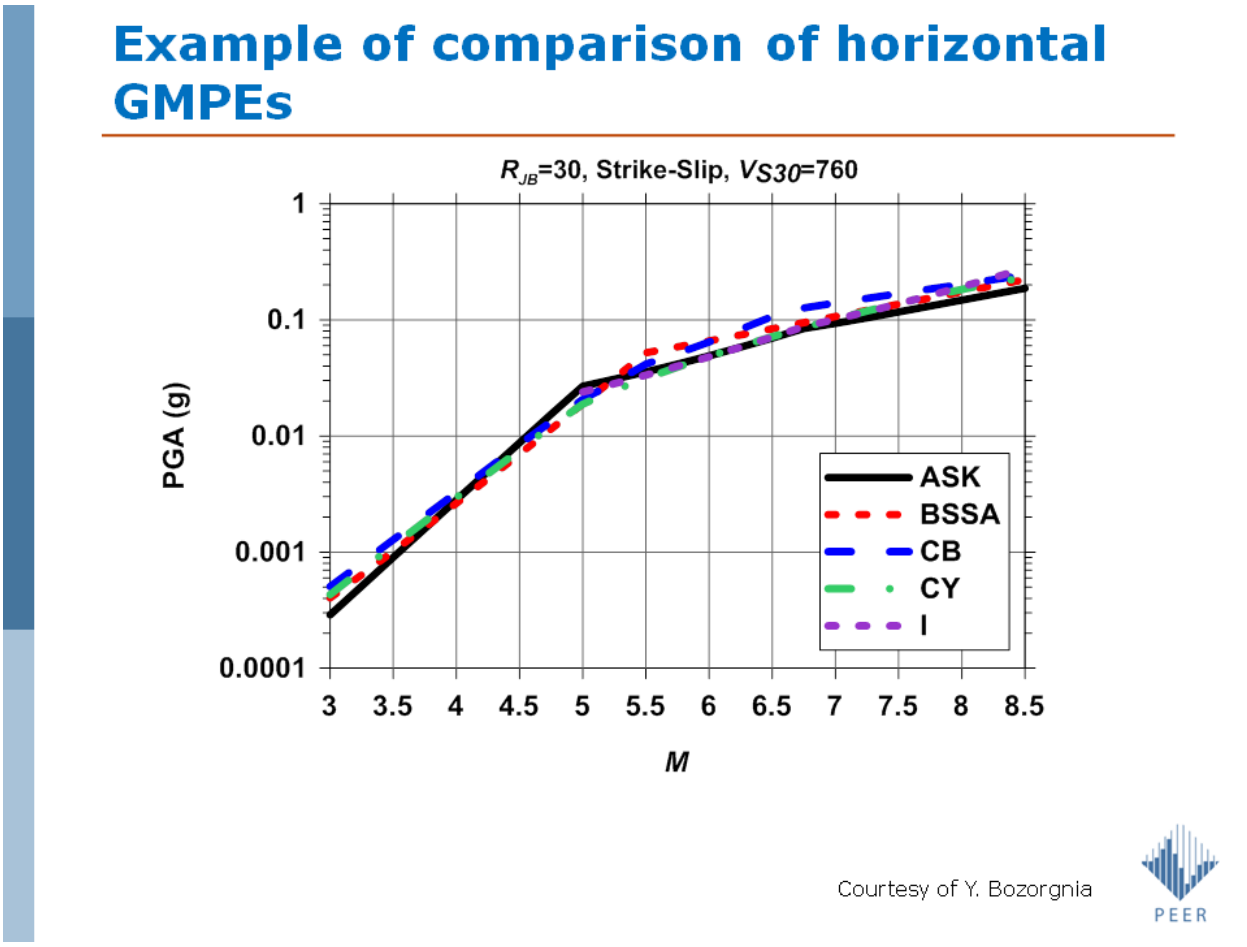

Figure 12. Comparing magnitude scaling from the five NGA-West2 GMPEs for a fixed distance (30 km).

Use of GMPEs in Building Codes

The following figures illustrate the probabilistic seismic hazard results from the U.S.G.S. National Seismic Hazard Mapping (NSHM) program. Underlying the results are the GMPEs from the previous NGA-West project, published in 2008 (the latest NSHM results are for 2014 and use the NGA-West2 GMPEs; the NSHM web site, however, does not allow for generation of the deaggregation figures, so I used the 2008 NSHM results; the essential points to be made would not change if the more recent results were used.

Make a map of the ground-motion values for a given FOE; this is the hazard map that is the basis for the design maps included in building codes

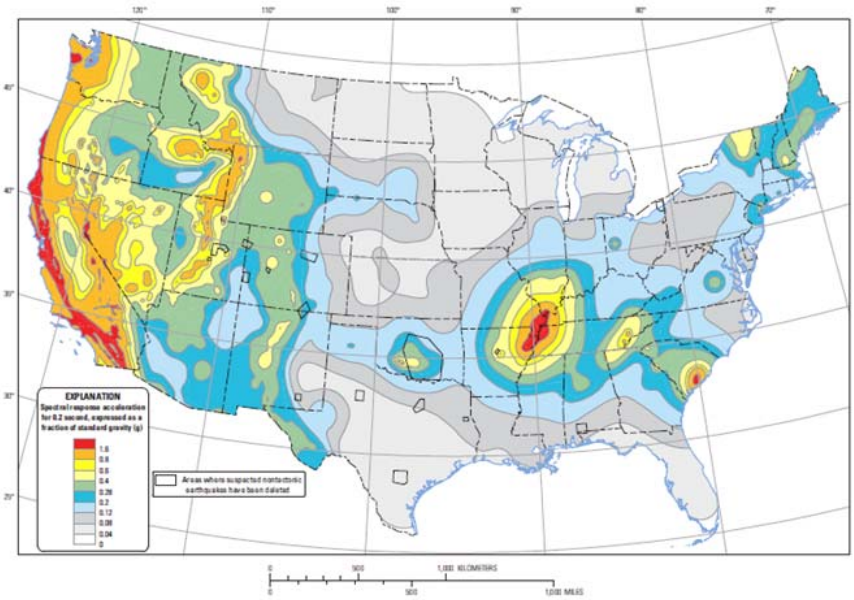

Figure 13. A hazard map for the US, from the National Seismic Hazard Mapping program of the USGS.

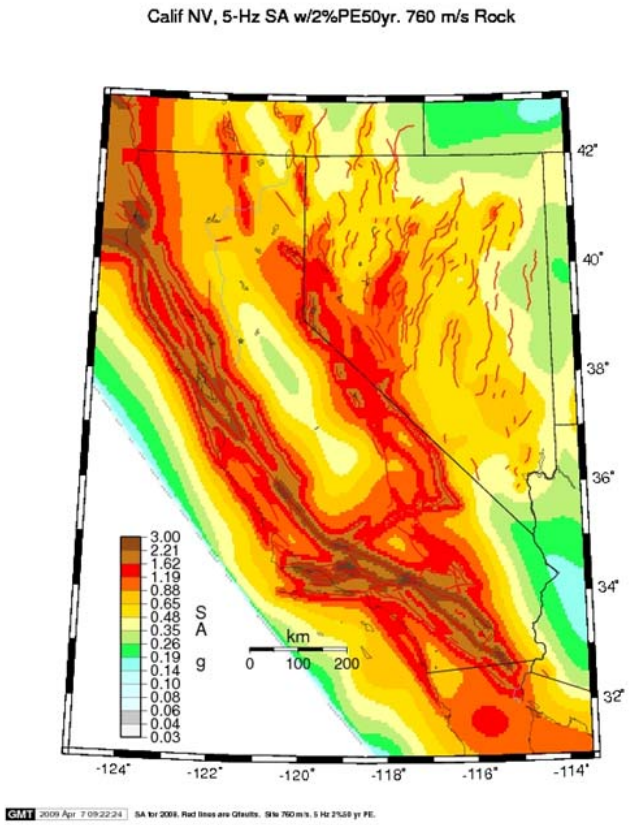

Figure 14. A hazard map for California, from the 2008 version of the National Seismic Hazard Maps of the USGS.

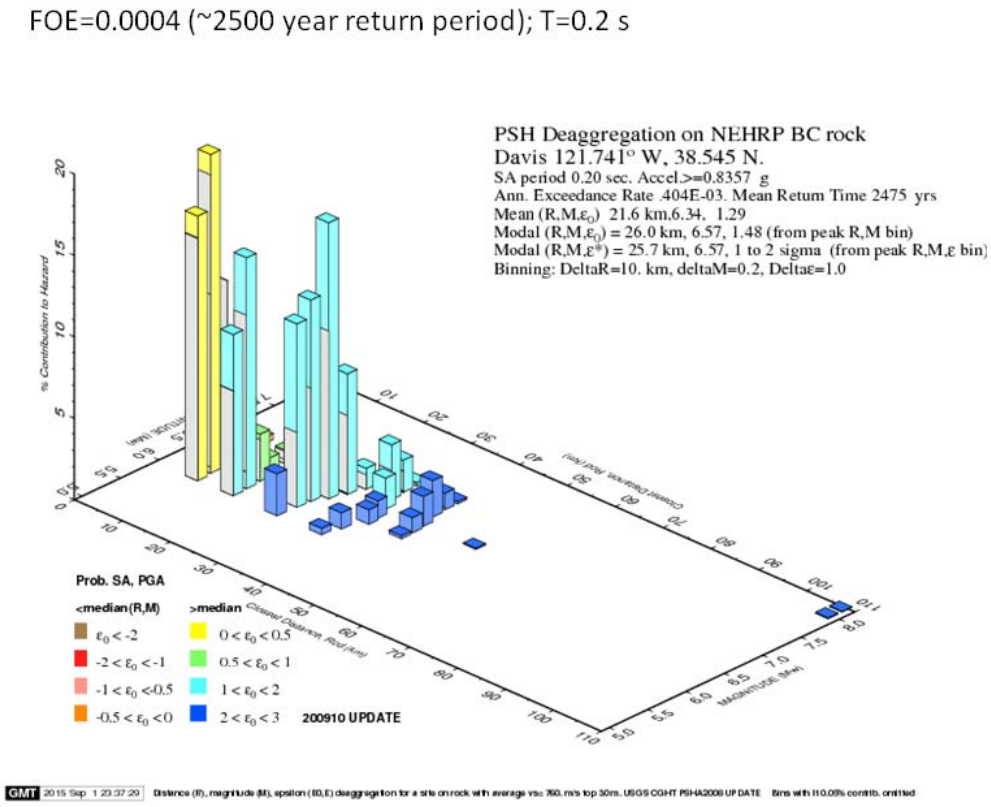

Figure 15. The deaggregation for Davis, California, from the 2008 USGS National Seismic Hazard Mapping web site. The period is 0.2 s. with a frequency of exceedance of 2% in 50 years. The colors refer to the number of standard deviation about the median ground motion that contribute to the hazard at the chosen frequency of exceedance.

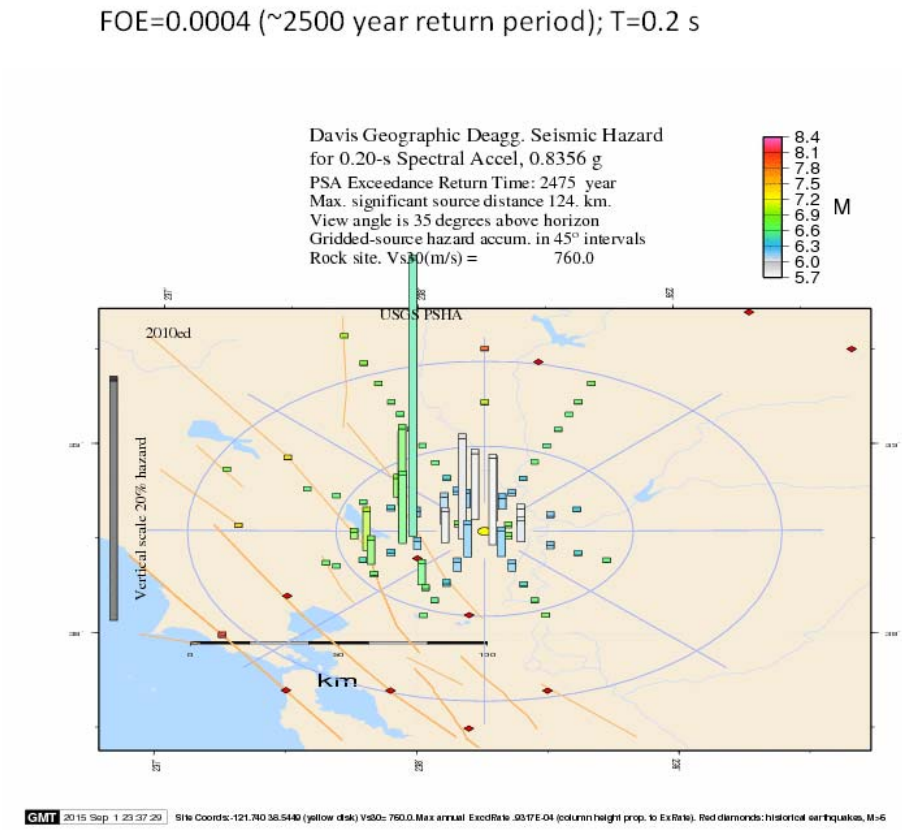

Figure 16. The geographic deaggregation for Davis, California, from the 2008 USGS National Seismic Hazard Mapping web site. The period is 0.2 s. with a frequency of exceedance of 2% in 50 years. The colors refer to the magnitudes contributing to the hazard at the chosen frequency of exceedance.

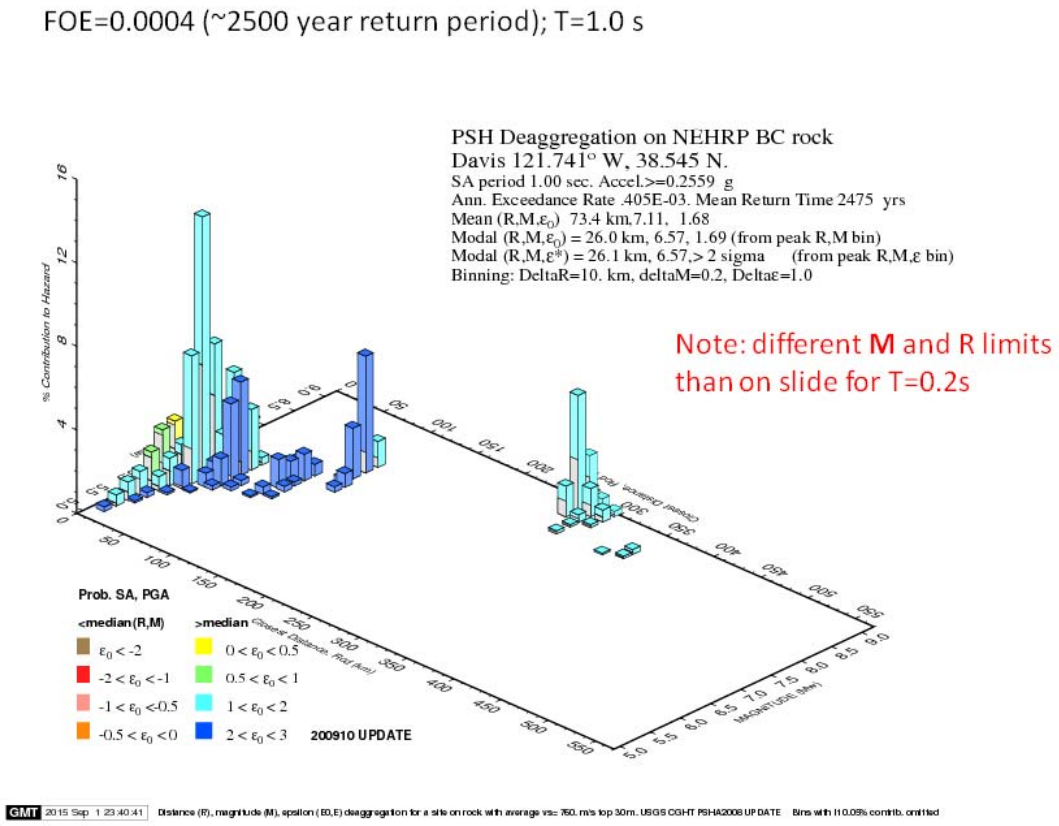

Figure 17. As in Figure 15, but for a period of 1.0 s. Note that the axis ranges are different than in Figure 15.

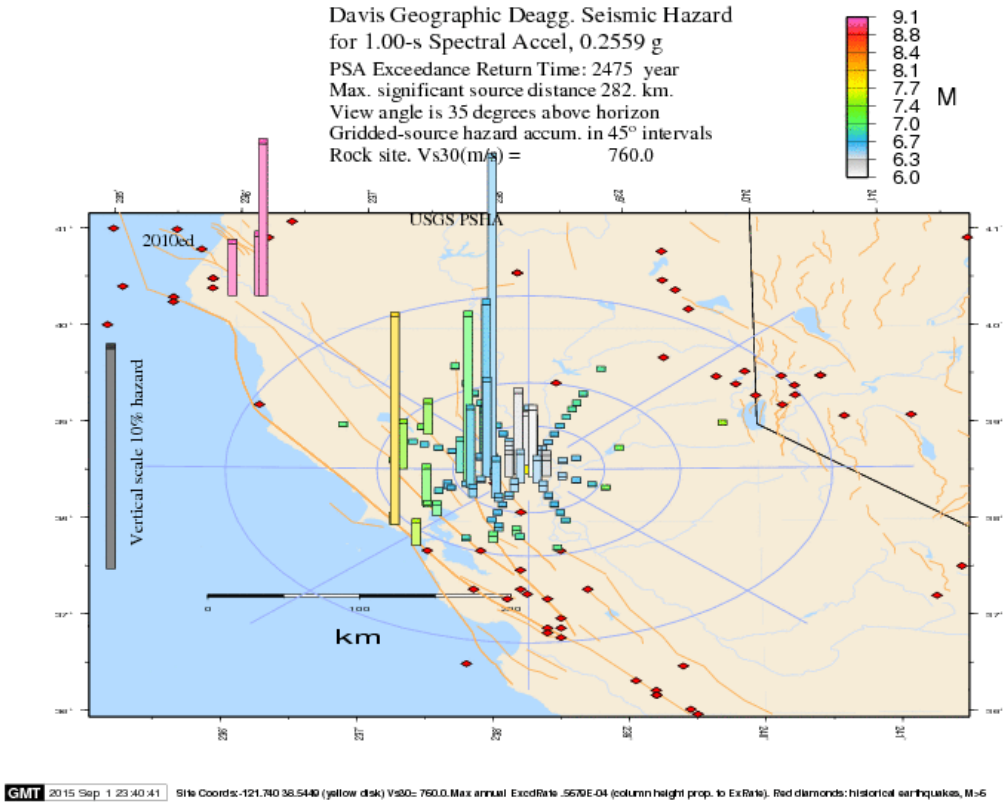

Figure 18. As in Figure 16, but for a period of 1.0 s.

References

Ancheta, T.D., R.B. Darragh, J.P. Stewart, E. Seyhan, W.J. Silva, B.S.J. Chiou, K.E. Wooddell, R.W. Graves, A.R. Kottke, D.M. Boore, T. Kishida, and J.L. Donahue (2014). NGA-West2 database, *Earthquake Spectra* **30**, 989–1005.

Baltay, A. S. and T. C. Hanks (2014). Understanding the magnitude dependence of PGA and PGV in NGA-West2 data, *Bull. Seismol. Soc. Am.* **104**, 2851–2865.

Boore, D.M. (2010). Orientation-independent, non geometric-mean measures of seismic intensity from two horizontal components of motion, *Bull. Seismol. Soc. Am.* **100**, 1830–1835.

Boore, D.M. (2014). What do data used to develop ground-motion prediction equations tell us about motions near faults?, *Pure and Applied Geophysics* **171**, 3023–3043.

Boore, D.M., E.M. Thompson, and H. Cadet (2011). Regional correlations of V_{S30} and velocities averaged over depths less than and greater than 30 m, *Bull. Seismol. Soc. Am.* **101**, 3046–3059.

Boore, D.M., J.P. Stewart, E. Seyhan, and G.M. Atkinson (2014). NGA-West 2 equations for predicting PGA, PGV, and 5%-Damped PSA for shallow crustal earthquakes, *Earthquake Spectra* **30**, 1057–1085.

Bozorgnia, Y., N.A. Abrahamson, L. Al Atik, T.D. Ancheta, G.M. Atkinson, J.W. Baker, A. Baltay, D.M. Boore, K.W. Campbell, B.S.-J. Chiou, R. Darragh, S. Day, J. Donahue, R. W. Graves, N. Gregor, T. Hanks, I.M. Idriss, R. Kamai, T. Kishida, A. Kottke, S.A. Mahin, S. Rezaeian, B. Rowshandel, E. Seyhan, S. Shahi, T. Shantz, W. Silva, P. Spudich, J.P. Stewart, J. Watson-Lamprey, K. Wooddell, and R. Youngs (2014). NGA-West2 Research Project, *Earthquake Spectra* **30**, 973–987.

Hanks, T.C. and H. Kanamori (1979). A moment magnitude scale, *J. Geophys. Res.* **84**, 2348–2350.

Joyner, W.B. and D.M. Boore (1981). Peak horizontal acceleration and velocity from strong-motion records including records from the 1979 Imperial Valley, California, earthquake, *Bull. Seismol. Soc. Am.* **71**, 2011—2038.

Seyhan, E. and J.P. Stewart (2014). Semi-empirical nonlinear site amplification from NGA-West 2 data and simulations, Earthquake Spectra **30**, 1241–1256.

EFFECTIVENESS OF 1D GROUND RESPONSE ANALYSES AT PREDICTING SITE RESPONSE AT CALIFORNIA VERTICAL ARRAY SITES

Kioumars Afshari and Jonathan P. Stewart

Department of Civil & Environmental Engineering
University of California, Los Angeles

Abstract

We investigate the ability of 1-D ground response simulations to match observed levels of site amplification from California vertical arrays. Using 10 vertical arrays, we find simulations to best match data using a V_S-based damping model from the literature. We find a higher percentage of California sites, as compared to KiK-net sites from Japan, to have a reasonable match of empirical and theoretical transfer function shapes. The empirical transfer functions also have a greater degree of event-to-event consistency than has been found previously in Japan. Cases with poor matches highlight that 1-D simulations can fail to accurately model site response.

Introduction

Evaluating the role of local site conditions on ground shaking is an essential part of earthquake ground motion prediction, which can be done using ergodic models or site-specific analyses. One-dimensional (1D) simulation of shear waves propagating vertically through shallow soil layers, also known as ground response analysis (GRA), is a common approach for capturing the effects of site response on ground shaking. In GRA, different approaches have been used for modeling soil behavior, namely linear, equivalent-linear (EL), and various nonlinear (NL) methods. Much attention has been directed in recent research to which of these approaches is best suited to a particular problem, with the intention of guiding the selection of an appropriate method of analysis (e.g., choosing when NL is preferred to EL) (e.g., Kim et al., 2015; Kaklamanos et al, 2013, 2015; Zalachoris and Rathje, 2015). However, a crucial issue that has received much less attention is the degree to which 1D simulations (the essential assumption behind all GRA methods) are effective.

While site response can include important contributions from the wave propagation mechanics simulated in GRA, site response as a whole is considerably more complex. True site response represents the difference between ground motions for a given site condition and what would have occurred had the site had a reference condition (typically rock with a particular V_{S30}). Processes that can control site response in this context include surface waves, basin effects (including focusing and basin edge-generated surface waves), and topographic effects. Because GRA only simulates a portion of the physics controlling site response, there should be no surprise that it is not always effective at accurately predicting site effects.

Validation and testing of 1D GRA is possible by studying recordings from vertical array sites. The KiK-net array in Japan (Aoi et al., 2000) provides a large inventory of vertical arrays that has been extensively used for validation purposes (Thompson et al., 2012; Kaklamanos et al, 2013, 2015; Zalachoris and Rathje, 2015). As described in the next section, when viewed as a whole, these KiK-net data challenge the notion that 1D GRA provides a reliable estimate of site response. Were this result found to be widely applicable, it would upend a good deal of current practice that relies on GRA to estimate first-order site response. Our objective in this study, for which this paper provides preliminary results, is to utilize the growing body of vertical array data from California to investigate applicability of 1D GRA to predict observed site response. In short, we seek to answer the question – are the poor matches of 1D GRA from the KiK-net array a product of particular geological conditions at the sites in that array, and hence not generally applicable in California?

Prior Work Utilizing KiK-net Array Sites

Thompson et al. (2012) studied 100 KiK-net sites in Japan in order to assess the variability in site amplification and the performance of linear 1D GRA. These sites have recorded a large number of surface and downhole (in rock) recordings. The presence of multi-depth records enables the calculation of empirical transfer functions (ETFs) directly from surface $G(f,x_1)$ and downhole $G(f,x_2)$ amplitude spectra:

$$H(f) = \frac{G(f,x_1)}{G(f,x_2)} \tag{1}$$

where $H(f)$ is the ETF. For GRA, they used the program NRATTLE, which is a part of the ground motion simulation program SMSIM (Boore, 2005). NRATTLE performs linear GRA using quarter-wavelength theory. In order to minimize the potential for nonlinear effects, only records having a ground surface PGA < 0.1 g were selected.

ETFs were computed with Eq. (1) using available data meeting certain selection requirements. In total, 3714 records from 1573 earthquakes were considered for the 100 KiK-net sites. The mean and 95% confidence intervals were computed across all selected recordings at a given site, with the example results (for two sites) given in Figure 1. Transfer functions from the quarter-wavelength GRA are also shown in Figure 1 (these are referred to as theoretical transfer functions, TTFs). The input parameters for NRATTLE include shear wave velocity (V_S), soil density, and the intrinsic attenuation of shear-waves (Q_S^{-1}) which represents damping. Profiles of V_S are available from the KiK-net web site (http://www.kyoshin.bosai.go.jp). Soil density was estimated from P-wave velocity using the procedures suggested by Boore (2008), and Q_S^{-1} was estimated using a grid-search algorithm to optimize the fit to $H(f)$.

Figure 1(a) provides an example of poor fit between the ETF and TTF whereas Figure 1(b) shows a good fit. Goodness-of-fit was quantified using Pearson's sample correlation coefficient (r); a value of r=0.6 was taken by Thompson et al. as the threshold for good fit. The corresponding r values for the two sites in Figure 1 are 0.10 for the poor fit site and 0.79 for the good fit site. Dispersion curves (phase velocity vs. frequency) for the two example sites are shown in Figure 1. The results show that there is a large degree of variability in the dispersion curves for the poor-fit site and consistency in the dispersion curves for the good-fit site. These

and other similar results for additional sites indicate that geologic complexity, as reflected by spatial variability in the Rayleigh wave velocity structure, may correlate to the accuracy of GRA prediction. More complex geologic structure would be expected to produce 3D site effects that are not captured by GRA.

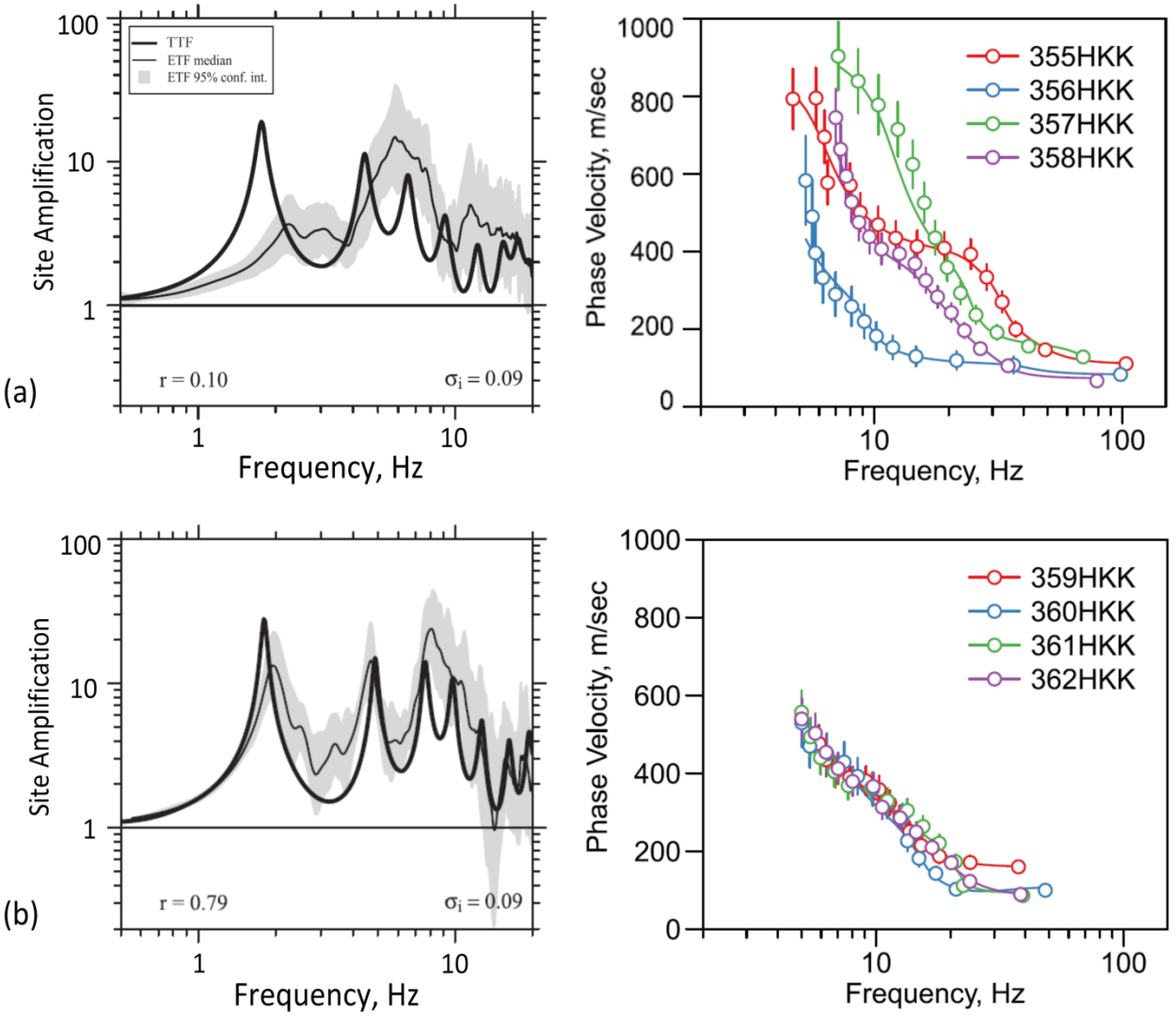

Figure 1. Examples of a poor fit (a) and good fit (b) between ETF and TTF at two KiK-net sites along with the dispersion curves from multiple SASW tests for both sites (adapted from Thompson et al., 2012)

Results for the 100 considered sites show that only 18% have a good fit between ETFs and TTFs, indicating 1D GRA fails to provide an accurate estimation of site response for a larger majority of KiK-net sites. Subsequent to Thompson et al. (2012), Kaklamanos et al. (2013) use subsets of KiK-net sites where a good ETF-TTF fit was obtained to study the issue identified in the introduction (i.e., when increased levels of sophistication in nonlinear modeling is needed in GRA). In this study, we do not screen sites to identify those for which the ETF matches the

shape of a TTF; instead we seek to understand how frequently such a match is achieved in relatively weak motion data from California vertical array sites.

Inventory of Vertical Arrays and Their Recordings in CA

We have collected site data for 39 vertical arrays in California as listed in Table 1. Our main source of site properties and ground motion data is the Center for Engineering Strong Motion Data (CESMD) website (*http://www.strongmotioncenter.org/*). Velocity profile data is available for some of the sites, and ground motion time series can be downloaded through a search engine. In addition, CESMD maintains an FTP folder containing a database of weaker motions for all vertical array and surface-only sites. We have also considered four sites owned and maintained by the University of California at Santa Barbara (UCSB). The site information and recorded motions for these sites are available at *http://nees.ucsb.edu/*.

Interestingly, a major factor limiting the inventory of usable vertical array sites in California is the availability of V_S profile data; of the 39 vertical arrays, we have been able to collect usable V_S profile data for 30 sites (26 CESMD, 4 UCSB), and boring logs are available for 24 sites (22 CESMD and 2 UCSB). Given the relative cost of array installation (high) vs V_S profile development (low), a priority in future work should be to fill this data gap.

For our study, we utilize vertical array sites with measured V_S profile and having at least five pairs of surface/downhole recordings to increase the statistical significance of ETFs. The location of the vertical array sites are shown in Figure 2. The sites shown in blue were considered in the present work. .

Figure 2. The location of vertical array sites in California (The sites used in this study are shown in blue)

Table 1. Summary of site characteristics for California vertical arrays. Sites considered in present work are bolded.

Station NO	Station Name	Owner	Low-amp. recs?[1]	# Rec	Latitude	Longitude	V_{S30} (m/s)	V_S profile Depth (m)[2]	Geotech log?[2]
58137	Alameda - Posey & Webster Geotech Array	CGS - CSMIP	NA	7	37.790	-122.277	208 (inferred)	N	Y
67265	Antioch – San Joaquin River N Geo. Array	CGS	NA	1	38.038	-121.752	Problematic	60*	N
67266	Antioch – San Joaquin River S Geo. Array	CGS	N	1	38.018	-121.752	272	105	Y
47750	Aptos - Seacliff Bluff Array	CGS - CSMIP	NA	4	36.972	-121.910	463	N**	N
68321	Benicia – Martinez Br N Geotech Array	CGS - CSMIP	N	3	38.051	-122.128	582	31	Y
68323	Benicia – Martinez Br S Geotech Array	CGS - CSMIP	N	4	38.033	-122.117	546	31	Y
13186	Corona – I15/Hwy 91 Geotech Array	CGS - CSMIP	N	2	33.882	-117.549	349	37	Y
68206	Crockett – Carquinez Br Geotech Array #1	CGS - CSMIP	N	4	38.054	-122.225	345	43	Y
68259	Crockett – Carquinez Br Geotech Array #2	CGS - CSMIP	N	4	38.055	-122.226	--	N	Y
1794	**El Centro – Meloland Geotechnical Array**	**CGS - CSMIP**	**Y**	**32**	32.774	-115.449	**182**	**240**	**Y**
89734	**Eureka - Geotechnical Array**	**CGS - CSMIP**	**Y**	**23**	40.819	-124.166	**194**	**225**	**Y**
58968	Foster City – San Mateo Br Geotech Array	CGS - CSMIP	N	1	37.573	-122.264	195	31	N
58964	Half Moon Bay - Tunitas Geotech Array	CGS - CSMIP	N	2	37.358	-122.398	309	39	Y
58487	Hayward - I580/238 West Geotech Array	CGS	N	1	37.689	-122.107	223	88	Y
58798	Hayward – San Mateo Br Geotech Array	CGS	N	1	37.617	-122.154	185	93	Y

Station NO	Station Name	Owner	Low-amp. recs?[1]	# Rec	Latitude	Longitude	V_{S30} (m/s)	V_S profile Depth (m)[2]	Geotech log?[2]
24703	**Los Angeles – La Cienega Geotech Array**	**CGS - CSMIP**	**Y**	**19**	34.036	-118.378	**241**	**280**	**Y**
24400	**Los Angeles - Obregon Park**	**CGS - CSMIP**	**Y**	**23**	34.037	-118.178	**449**	**64**	**Y**
14783	Los Angeles – Vincent Thm Geo Array W1	CGS - CSMIP	N	3	33.750	-118.275	149	192	N
14784	Los Angeles – Vincent Thm Geo Array W2	CGS - CSMIP	N	3	33.750	-118.278	149	195	N
14786	Los Angeles – Vincent Thos W Geo Array	CGS - CSMIP	N	1	33.750	-118.280	149	192	Y
24185	Moorpark - Hwy118/Arroyo Simi Geo. Array	CGS - CSMIP	NA	1	34.288	-118.865	--	N	Y
58204	Oakland – Bay Bridge Geotech Array	CGS - CSMIP	NA	3	37.821	-122.327	Problematic	155*	N
58526	Palo Alto – Dumbarton Br W Geotech Array	CGS	NA	1	37.499	-122.129	123	N**	Y
36529	Parkfield – Turkey Flat #1	CGS - CSMIP	N	3	35.878	-120.359	907	N**	N
36520	Parkfield – Turkey Flat #2	CGS - CSMIP	N	1	35.882	-120.351	467	N**	N
89289	Petrolia - Downhole [abandoned]	CGS - CSMIP	NA	1	40.317	-124.292	--	N	N
68797	Rohnert Park - Hwy 101 Geotech Array	CGS - CSMIP	N	2	38.347	-122.713	223	47.5	N
23792	**San Bernardino - I10/215 W Geotech Array**	**CGS - CSMIP**	**N**	**5**	34.064	-117.298	**271**	**92**	**Y**
3192	San Diego – Coronado East Geotech Array	CGS - CSMIP	N	2	32.698	-117.145	315	89	Y
3193	San Diego – Coronado West Geotech Array	CGS - CSMIP	N	2	32.688	-117.164	209	102	Y
58961	San Francisco – Bay Bridge Geotech Array	CGS - CSMIP	N	3	37.787	-122.389	387	36	Y

Station NO	Station Name	Owner	Low-amp. recs?[1]	# Rec	Latitude	Longitude	V_{S30} (m/s)	V_S profile Depth (m) [2]	Geotech log? [2]
58267	San Rafael – Richmond Brdg Geotech Array	CGS	N	1	37.943	-122.481	921	42	N
24764	Tarzana – Cedar Hill B	CGS - CSMIP	N	4	34.161	-118.535	302	N	N
58642	Treasure Island - Geotechnical Array	CGS - CSMIP	N	3	37.825	-122.374	159	120	N
68310	**Vallejo - Hwy 37/Napa River E Geo. Array**	**CGS - CSMIP**	**Y**	**17**	38.122	-122.275	**509**	**42**	**Y**
UCSB Arrays	**Garner Valley Downhole Array**	**UCSB**	**--**	**20**	33.401	-116.403	**240**	**210**	**Y**
UCSB Arrays	**Wildlife Liquefaction Array**	**UCSB**	**--**	**45**	33.058	-115.318	**203**	**98**	**Y**
UCSB Arrays	**Borrego Valley Field Site**	**UCSB**	**--**	**21**	33.259	-116.321	**350**	**230**	**N**
UCSB Arrays	**Hollister Digital Array**	**UCSB**	**--**	**23**	36.453	-121.365	**359**	**185**	**N**

[1]NA: Not applicable; we have not sought low-amplitude recordings because site not useful due to lack of V_S profile.
N: Data may be available but not yet obtained.
[2]Y: Data available; N: Data not available.
* Top 20m is missing in the V_S measurements.
** There is V_S measurements, but not available at CESMD website.

Data Selection and Processing

Unprocessed records for the sites identified in the previous section were downloaded from CESMD and the nees.ucsb websites. Acceleration time series were visually inspected to identify and exclude low-quality, noise-dominated records. The data were processed using procedures developed in the NGA-West2 research project (Ancheta et al., 2014) and coded into an R routine (T. Kishida, *personal communication*, 2015). Low-cut and high-cut corner frequencies have been identified for each record by visual inspection, and low- and high-pass acausal Butterworth filters are used for filtering high and low frequency noise in the frequency domain. Baseline correction is also applied as needed.

Figure 3 shows an example of a record processed using these procedures, including time series (acceleration, velocity, displacement for processed record) and Fourier amplitude spectra and pseudo-acceleration response spectra at 5% damping for the unprocessed and processed versions of the record. Based on the records we have been able to access and process thus far, the usable database currently includes 10 sites and 225 record pairs. Figure 4 shows the number of usable recor

ds as a function of period; the decrease as period increases is due to application of low-cut corner frequencies in the record processing. The longest usable period is taken as ($0.877/f_c$), where f_c is the low-cut corner frequency selected in record processing.

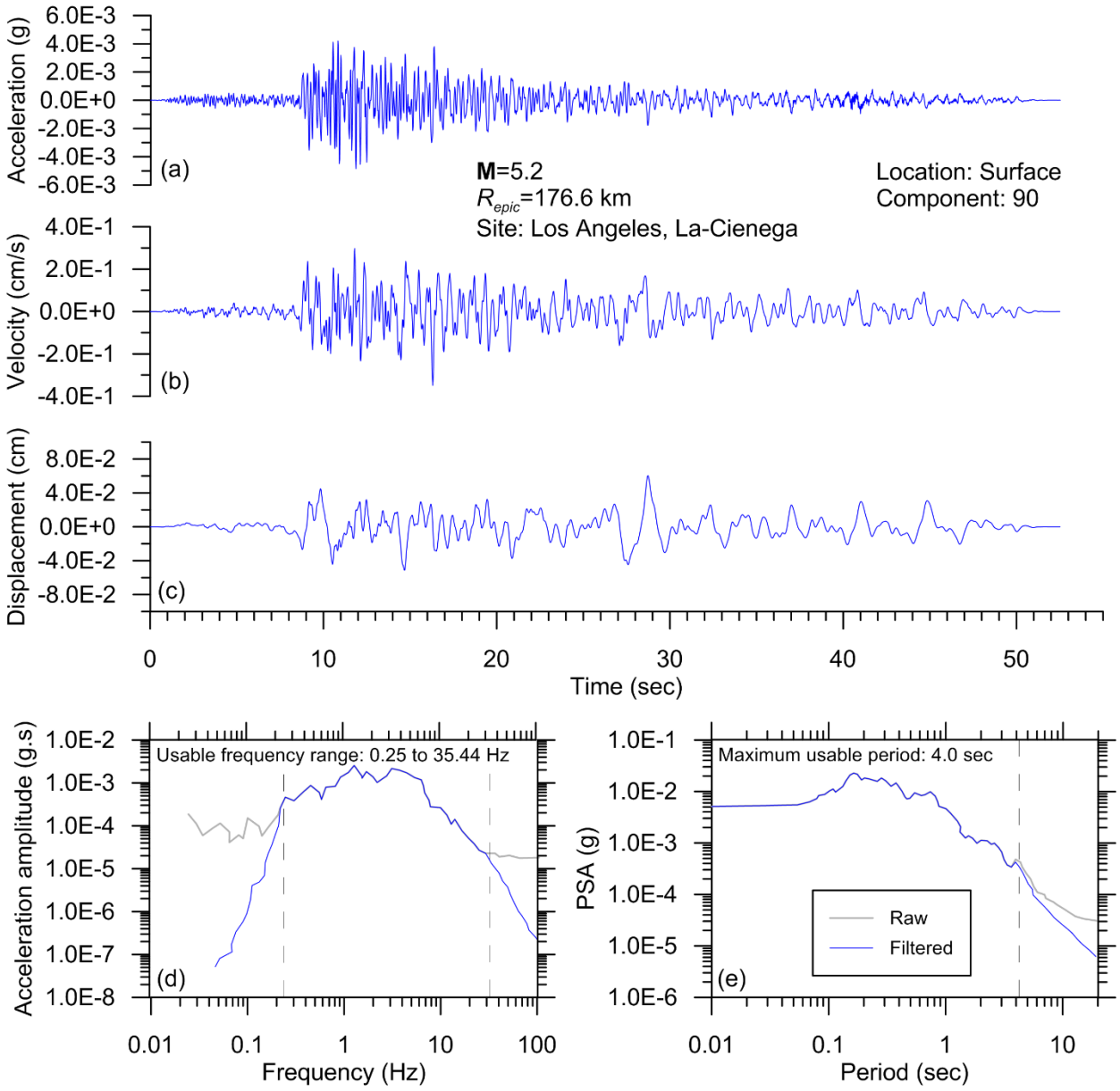

Figure 3. Example of record processed using PEER protocols developed in NGA-West2 project (Ancheta et al., 2014), including (a) acceleration time series, (b) velocity time series, (c) displacement time series, as well as (d) Fourier amplitude spectra and (e) pseudo-acceleration response spectra (PSA) at 5% damping for raw and filtered records.

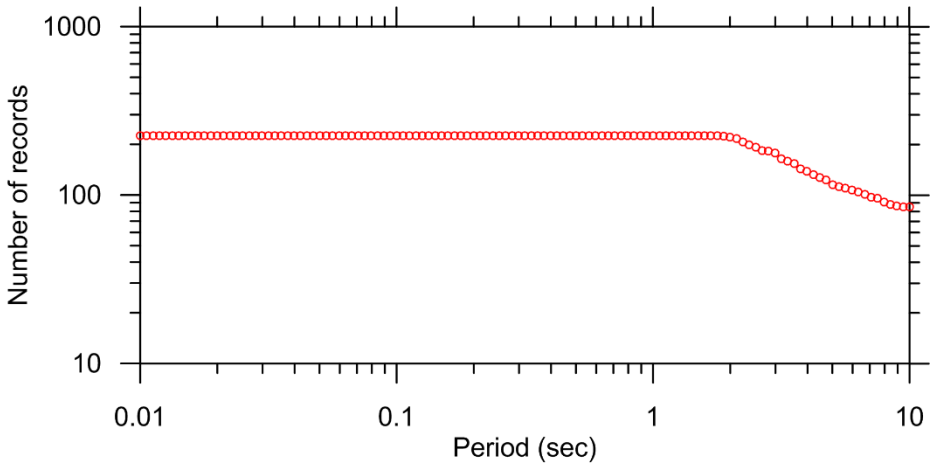

Figure 4. Number of available record pairs in the database according to their longest usable periods.

Analysis of Empirical Transfer Functions

Empirical transfer functions (ETFs) representing site response between the downhole and surface accelerometers are computed from ratios of Fourier amplitudes as given in Eq. (1). ETFs are only used over the usable frequency range based on record processing. The ETF is taken as the geometric-mean of ETFs for the two horizontal components of the recordings (at their as-recorded azimuths) for each site. The results shown subsequently are smoothed through the use of a Tukey (moving cosine) window with a width of 33 frequency steps (window width of approximately 0.5 Hz) in the frequency domain. This window size was selected for approximate compatibility with the prior work of Thompson et al. (2012).

We assume a log-normal distribution for ETF ordinates and compute for each site the median ($\mu_{\ln}$) (equivalent to the exponent of the natural log mean) and the natural log standard deviation of ETF ($\sigma_{\ln}$) at each frequency using all available record pairs. Figure 5 shows example ETFs for all record pairs at the San Bernardino and Obregon Park sites along with the median and 95% confidence intervals of ETF. For plotting purposes, we show results over a frequency range between 0.5 and 10 Hz, which encompasses the usable frequency range for all records and focuses attention on frequencies that significantly contribute to PSA ordinates.

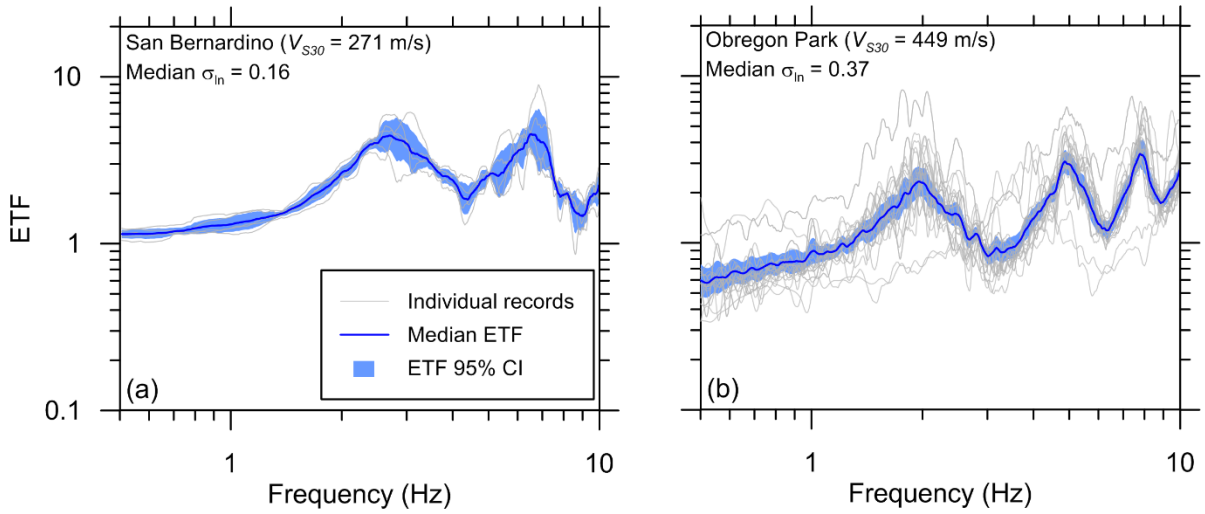

Figure 5. Empirical transfer functions plots for (a) San Bernardino site with low ETF variability, and (b) Obregon park with high ETF variability.

The two sites in Figure 5 have relatively low and high site response variability, as represented by frequency-dependent standard deviation term σ_{ln}. In order to represent this variability with a single metric that can be compiled for each site, we take the median σ_{ln} across the 0.5-10 Hz frequency range. These values are provided in Figure 5, being 0.11 for the low-variability site and 0.32 for the high-variability site.

Analysis of Theoretical Transfer Functions

Theoretical transfer functions (TTF) are computed by visco-elastic 1D GRA in DEEPSOIL. We exclude recordings with strong ground shaking (PGA at surface instrument > 0.1 g) so as to minimize nonlinear effects. Figure 6 shows histograms of PGA and PGV for the downhole instrument records used in the present work. We acknowledge that there are some records for which improved results could be obtained with EL procedures but have not undertaken such analyses to date with this data set.

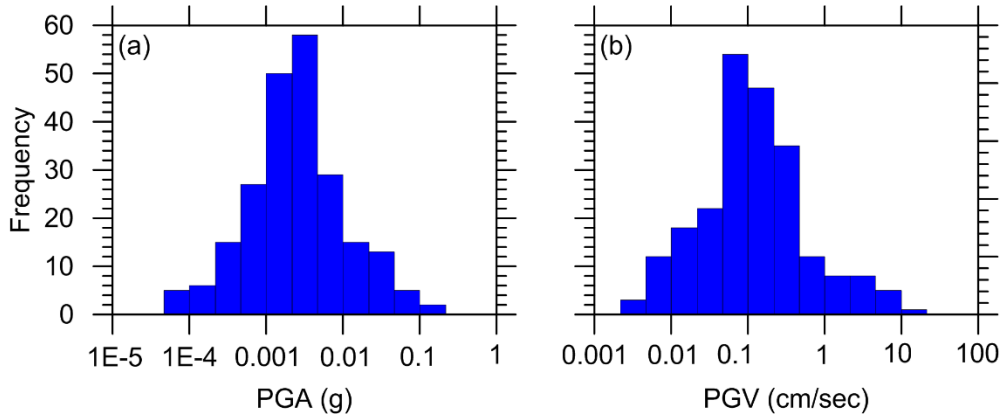

Figure 6. Histograms of PGA (a) and PGV (b) for downhole recordings used in this study.

Input soil properties for the visco-elastic analysis include the V_S profile, layer mass densities (assumed based on soil types and material descriptions), and material damping. Unlike Thompson et al. (2012), we utilize alternate approaches for estimating small-strain soil damping instead of back-calculating this parameter to optimize the ETF-TTF fit. These steps of considering alternate damping models are undertaken because best practices for selection of small-strain damping (D_{min}) are not well established (Stewart et al., 2014). Alternate approaches for modeling small-strain soil damping are described in the next section, which is followed by example results.

Damping Models

Laboratory-Based Models. We apply the traditional approach of taking damping from geotechnical laboratory cyclic testing, whereby the damping at small strains is taken as $D_{\min}^{L}$. We estimate laboratory-based $D_{\min}^{L}$ using Darendeli (2001) relations for clays and silts, and Menq (2003) relations for granular soils. The input parameters for the $D_{\min}^{L}$ models are plasticity index (PI), overconsolidation ratio (OCR), and effective stress for Darendeli (2001), and mean grain size (D_{50}), coefficient of uniformity (C_u), and effective stress for Menq (2003). The $D_{\min}^{L}$ relations can only be used when geotechnical log and/or description of soil conditions are available for the site.

Depth-Dependent Q Factors. The effective material quality factor (Q_{ef}) can be estimated based on shear wave velocity using an empirical model developed by Campbell (2009) as follows:

$$Q_{\text{ef}} = 7.17 + 0.0276 V_S \tag{2}$$

Eq. (2) was derived by Campbell (2009) so as to match target site attenuation parameter (κ_0) for a sediment column in Memphis Tennessee. The value of Q_{ef} from Eq. (2) can be readily converted to soil damping as follows:

$$D_{\min}(\%) = \frac{100}{2Q_{\text{ef}}} \tag{3}$$

This approach for modeling D_{min} does not require a geotechnical log.

Damping Estimated from κ_0 Model. Anderson and Hough (1984) showed that the shape of the Fourier amplitude spectrum for ground acceleration at high frequencies can be described as:

$$A(f) = A_0 \exp(-\pi \kappa f) \tag{4}$$

where κ is the controlling spectral decay parameter. Adopting the Hough and Anderson (1988) relationships and using notation from Campbell (2009), site attenuation parameter (κ_0) can be computed as:

$$\kappa_0 = \kappa_0^{rock} + \int_0^z Q_{ef}(z)^{-1} V_S(z)^{-1} dz \tag{5}$$

where κ_0^{rock} is the attenuation parameter for the bedrock, which sometimes matches the site condition at the downhole sensor. Using Eq. (3) to convert Q_{ef} to D, we re-write Eq. (5) as:

$$\kappa_0 = \kappa_0^{rock} + \int_0^z \frac{2D_{\min}(z)}{100} V_S(z)^{-1} dz \tag{6}$$

We take κ_0^{rock} = 0.007 sec as the mean estimate for western North America (Campbell, 2009), which then allows iterative adjustment of the D_{min} profile to match a target κ_0 value. The target κ_0 value is taken from an empirical global model conditional on V_{S30} (Van Houtte et al., 2011):

$$\ln(\kappa_0) = 3.490 - 1.062 \ln(V_{S30}) \tag{7}$$

for which the standard error is 0.505 for the intercept and 0.076 for the slope.

We begin with the laboratory-based estimate of the D_{min} profile ($D_{\min}^L$) and add a value (ΔD_i) at layer i. Modifying Eq. (6), we have:

$$\kappa_0 = \kappa_0^{rock} + \int_0^z \frac{2\left(D_{\min}^L(z) + \Delta D_i\right)}{100} V_S(z)^{-1} dz \tag{8}$$

We use three approaches for considering the depth-variation of ΔD_i: depth-invariant, depth-dependent per a prescribed relation, and V_S-dependent ΔD:

1- Depth-invariant $\Delta D_i = \Delta D_0$:

$$\Delta D_i = \Delta D_0 \tag{9}$$

2- Visual inspection of $D_{\min}^L$ profiles at the subject sites, suggest that the following relation approximately captures typical trends for the soil conditions present at the sites:

$$D_{\min}^L\left(z\right) = D_{\min}^L\left(z=0\right)(z_i)^{-0.04} \tag{10}$$

where z is the depth of the center of the layer in meters. This relation gives more weight to shallower layers. We propose a model for ΔD_i that follows this same trend:

$$\Delta D_i = \Delta D_0 (z_i)^{-0.04} \tag{11}$$

3- The V_S-dependent model is motivated by the negative correlation that exists between $D_{\min}^L$ and V_S at most sites. Based on visual inspection and some trial and error, we apply the following relation:

$$\Delta D_i = \Delta D_0 \left(\frac{V_S}{200}\right)^{-0.3} \tag{12}$$

where V_S is the shear wave velocity for the layer in meters per second.

Eqs (9), (11), and (12) allow for single parameters (ΔD_0) to produce ΔD_i profiles, which can be used with Eq. (8) to compute κ_0. In our case, we take κ_0 from Van Houtte et al. (2011) and use Eq. (8) to compute three values of ΔD_0 for each site. For sites without a geotechnical log we do not have the $D_{\min}^L$ profile – in these cases we assume $D_{\min}^L$ = 0 for use with the above procedures.

Example Application

We apply the procedures described in the previous subsection for the El Centro-Meloland vertical array site. Figure 7 shows the geotechnical log, V_S profile, and damping profiles derived from the three approaches presented in the previous section. A considerable difference between damping profiles from the three approaches is evident, with the lab-based damping being smallest, the damping derived from κ_0 being largest, and the Campbell (2009) relation providing intermediate values. The alternate methods for capturing the depth-dependence of ΔD_i are seen to be of second-order importance as compared to the variations from the three modeling approaches for damping.

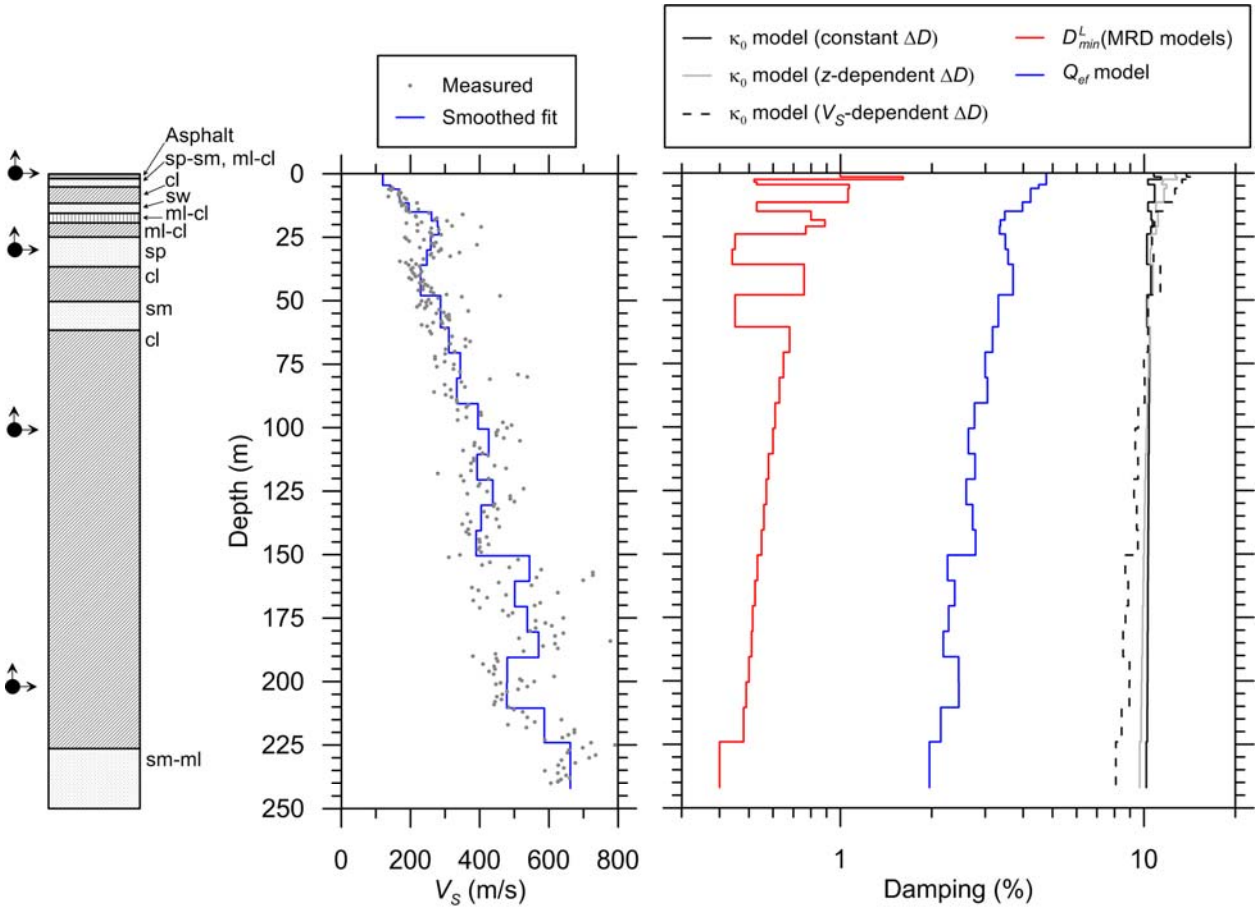

Figure 7. Site characteristics for El Centro-Meloland site including simplified geotechnical log, V_S profile, and soil damping profile estimated using empirical lab-based damping models by Darendeli (2001) and Menq (2003), damping derived from Q_{ef} model by Campbell (2009), and damping derived from κ_0 model by Van Houtte et al. (2011) (three alternate depth relations for ΔD).

Using the V_S profile, damping profiles (five alternatives), and estimated soil densities, we perform visco-elastic GRA in DEEPSOIL, and compute surface-downhole theoretical transfer functions (TTFs). As the downhole sensor is recording both up-going and down-going waves, we

take the boundary condition at the base of the model as rigid (Kwok et al., 2007). The visco-elastic analysis is performed in the frequency domain, and the site amplification predicted by the model is independent of the input motion. The resulting TTF is shown in Figure 8 for the El Centro-Meloland site. No smoothing was applied to these TTFs.

The overall shape and the position of the peaks in TTF plots (corresponding to modal frequencies of the site) are controlled by the V_S profile, and hence do not vary across damping models. However, the level of amplification at high frequencies is sensitive to damping levels, being much higher for low-damping approaches (lab-based) as opposed to high-damping approaches (κ_0-based).

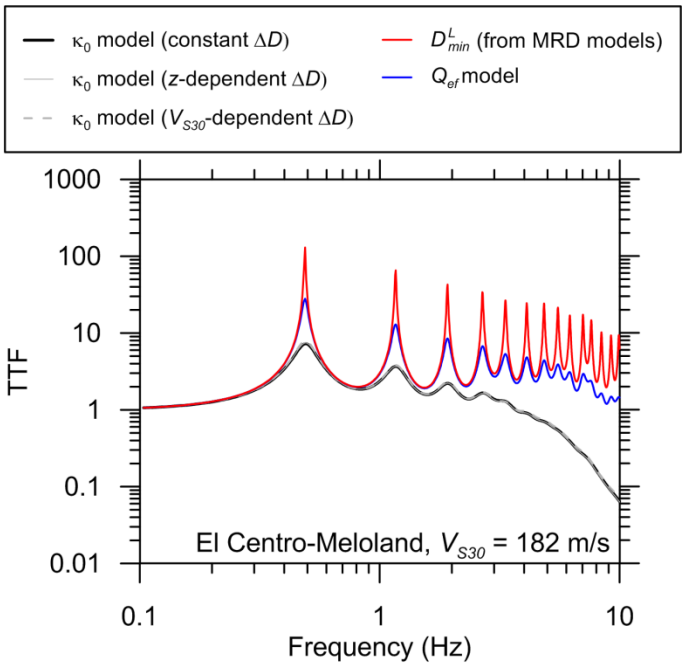

Figure 8. Plots of TTF vs. frequency using different approaches for estimating damping. El Centro-Meloland site

Model-Data Comparisons and Interpretation

Model-data comparisons can be visual by plotting together TTFs and ETFs. However, it is also useful to evaluate the goodness of fit, which we quantify with Pearson's sample correlation coefficient r (also used by Thompson et al., 2012) and the mean residual of the transfer function ($\bar{R}$). We define both metrics here and show example results.

Pearson's sample correlation coefficient (r)

We use this parameter as a measure of how well the model predictions and the data are correlated. Parameter r quantifies how well the shapes of the transfer functions align, including the locations and shapes of peaks. Parameter r is insensitive to relative overall levels of amplification, which is quantified in the next subsection. We calculate the Pearson's sample

correlation coefficient for i^{th} earthquake and j_{th} analysis (based on damping estimation approach) as follows for a given site:

$$r_{ij} = \frac{\sum\left(\mathrm{ETF}_i(f) - \overline{\mathrm{ETF}_i}\right)\left(\mathrm{TTF}_j(f) - \overline{\mathrm{TTF}_j}\right)}{\sqrt{\sum\left(\mathrm{ETF}_i(f) - \overline{\mathrm{ETF}_i}\right)^2}\sqrt{\sum\left(\mathrm{TTF}_j(f) - \overline{\mathrm{TTF}_j}\right)^2}} \tag{14}$$

where we take the summations between f_{min} = 0.1 and f_{max} = 10 Hz. The summation is performed over all frequency points between f_{min} and f_{max}. The average value of r across all events (r_j) for a given site is denoted $\bar{r}$.

Mean Transfer Function residual ($\bar{R}$)

We quantify bias in the prediction of site response transfer functions by computing the mean residual of predictions over all frequency points between f_{min} and f_{max}. The residuals are calculated for the i^{th} earthquake and j^{th} damping estimation approach as follows:

$$R_{ij}(f) = \ln\left(\mathrm{ETF}_i(f)\right) - \ln\left(\mathrm{TTF}_j(f)\right) \tag{15}$$

where R_{ij} is the prediction residual. We average R_{ij} over all events and frequency points to calculate the overall bias for a site, which is denoted by $\overline{R}_j$. For sites with reasonably high values of $\bar{r}$, bias $\overline{R}_j$ provides an indication of how well alternate damping models fit the data.

Results and Interpretation

Figure 9 shows model-data comparisons for two example sites in which the fit is reasonably good (El Centro-Meloland) and relatively poor (San Bernardino). Figure 9 plots median for ETFs as well as TTFs based on the three principle soil damping models (we only show results for the second of the three κ_0-based approaches, given a lack of sensitivity). The TTFs in Figure 9 are smoothed in an equivalent manner to the ETFs.

For the El Centro-Meloland site (Fig 9a), the higher value of $\bar{r}$ = 0.30 indicates relatively good alignment between the shapes of the ETF and TTF (the summary statistics shown in Fig. 9 apply for the Campbell 2009 damping formulation). In contrast, the San Bernardino site has a shape misfit between ETF and TTF and $\bar{r}$ =0.06. The general level of site amplification at high frequencies is better matched using the Campbell (2009) damping model than the other two models considered (the D^{L}_{min} model under-damps, the κ_0-based model over-damps). This result most often holds for other sites as well.

Based on preliminary results obtained thus far, California $\bar{r}$ values are higher, and median σ_{ln} values are lower, than their counterparts for the KiK-net arrays in Japan. This suggests that the ability of GRAs to match observation is better for the California vertical arrays than for KiK-net sites. This likely results from California sites mostly being located within large sedimentary basins, whereas KiK-net sites are often on firmer ground conditions (often weathered rock or thin soil over rock). The California sites with poor matches of data to model,

including the San Bernardino array, tend to be located near basin edges, where heterogeneous velocity structure is relatively likely to be present.

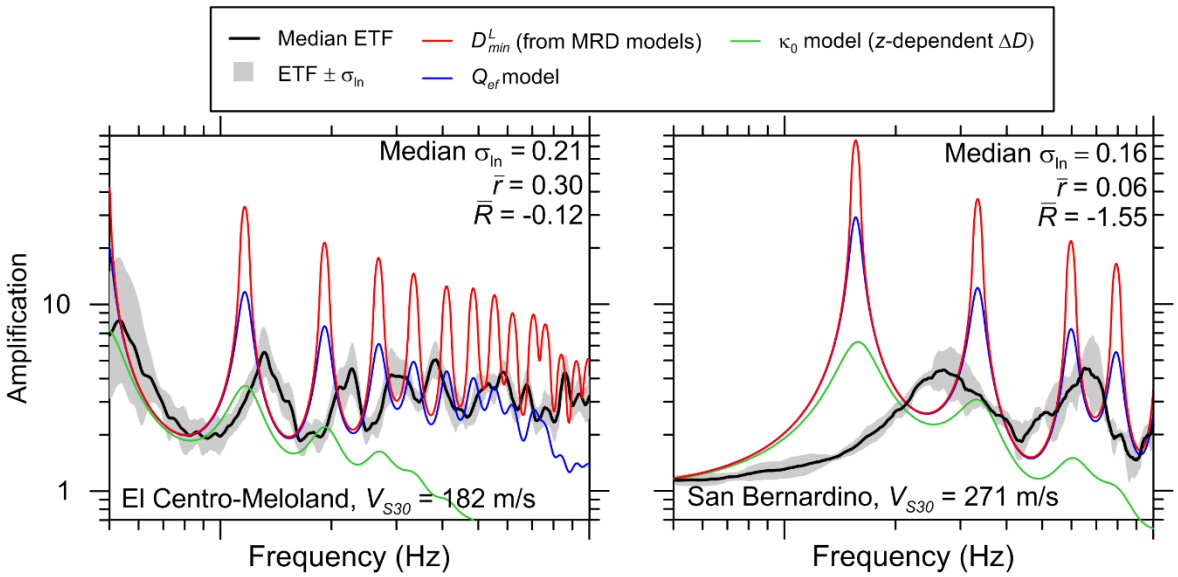

Figure 9. Comparison of ETF and TTFs for sites with good (El Centro-Meloland) and poor (San Bernardino) matches. Indicated values of $\bar{r}$ and $\bar{R}$ are based on Campbell (2009) damping model.

Conclusions

The motivation for this work is to examine whether the very low rate of match between 1-D ground response analysis (1D GRA) results and vertical array data observed in prior research in Japan (KiK-net array) is also found in vertical array data from California. We have compiled basic information for 39 vertical array sites in California; however, to date we have been able to use only 10 of these sites. In some cases, sites are not usable because of lack of measured V_S profiles. We compute theoretical transfer functions by performing 1D GRA using a visco-elastic procedure with three different damping models. We compute empirical transfer functions from the recordings that are generally of sufficiently low amplitude that the site response can be considered to be approximately linear. Pearson's sample correlation coefficients ($\bar{r}$) are used to quantify the alignment of transfer function shapes and mean residuals ($\bar{R}$) are used to quantify average data-model bias.

Our results show that a V_S-based damping model derived for sites in the eastern US (Campbell 2009) provides a better match of GRA results to data than damping evaluated from laboratory tests or damping derived to be compatible with relationships with spectral attenuation parameter κ_0. We find that a higher percentage of California sites, as compared to KiK-net sites, have a reasonably good match of empirical and theoretical transfer functions, as demonstrated by higher (on average) $\bar{r}$ values. The empirical transfer functions also have a greater degree of event-to-event consistency, as reflected by lower (on average) standard deviations of empirical transfer function ordinates. While these results are encouraging, it is notable that cases with a poor match also occur at some of the California sites investigated here, suggesting that 1D GRA

does not provide a suitable means by which to estimate site response for those sites. Understanding on an *a priori* basis, when GRA is unlikely to be effective remains an unsolved problem and an important priority for future research.

Acknowledgments

Funding for this study is provided by California Strong Motion Instrumentation Program, California Geological Survey, Agreement No. 1014-961. This support is gratefully acknowledged. We also thank Tadahiro Kishida for providing access to data processing codes, and Hamid Haddadi for providing geotechnical logs and weak motion records from the Center for Engineering Strong Motion Data FTP folders. We gratefully acknowledge former nees@ucsb staff (namely, Jamison Steidl) for maintaining the ground motion database for UCSB vertical array sites.

References

Anderson, J.G., and Hough, S.E. (1984). A model for the shape of the Fourier amplitude spectrum of acceleration at high frequencies, *Bull. Seismol. Soc. Am*. 74, 1969-1993.

Aoi, S. ,Obara, K., Hori, S., Kasahara, K., Okada, Y. (2000). New Japanese uphole–downhole strong-motion observation network: KiK-Net, Seismological Research Letters *Seism. Res. Lett.* 72:239.

Ancheta, T.D., Darragh, R.B., Stewart, J.P., Seyhan, E., Silva, W.J., Chiou, B.S.-J., Wooddell, K.E., Kottke, A.R., Boore, D.M., Kishida, T., and Donahue, J.L. (2014). NGA-West2 database, *Earthquake Spectra* 30, 989–1005.

Boore, D.M. (2005). SMSIM-Fortran programs for simulating ground motions from earthquakes: version 2.3. A revision of U.S. Geological Survey Open-File Report 96-80-A:55.

Boore, D.M. (2008). Some thoughts on relating density to velocity <http://quake.wr.usgs.gov/boore/daves_notes/daves_notes_on_relating_density_to_velocity_v1.2.pdf>

Campbell, K.W. (2009). Estimates of shear-wave Q and κ_0 for unconsolidated and semiconsolidated sediments in Eastern North America, *Bull. Seismol. Soc. Am*. 99, 2365-2392.

Darendeli M.B. (2001). Development of a New Family of Normalized modulus reduction and material damping curves, PhD Thesis, Department of Civil Engineering, University of Texas, Austin, TX.

Hashash, Y.M.A (2015). DEEPSOIL Version 6.0 User Manual and Tutorial, University of Illinois at Urbana-Champaign, Urbana, IL.

Hough, S.E., and Anderson, J.G. (1988). High-frequency spectra observed at Anza, California: Implications of Q structure, *Bull. Seismol. Soc. Am*. 78, 692-707.

Kaklamanos, J., Baise, L.G., Thompson, E.M., Dorfmann, L. (2015). Comparison of 1D linear, equivalent-linear, and nonlinear site response models at six KiK-net validation sites, *Soil Dyn. Earthq. Eng.* 69, 207-215.

Kaklamanos, J., Bradley, B.A., Thompson, E.M., and Baise, L.G. (2013). Critical parameters affecting bias and variability in site-response analyses using KiK-net downhole array data, *Bull. Seismol. Soc. Am*. 103, 1733–1749.

Kim, B., and Hashash, Y.M.A. (2013). Site response analysis using downhole array recordings during the March 2011 Tohoku-Oki Earthquake and the effect of long-duration ground motions." *Earthquake Spectra* 29, S37–S54.

Kim, B., Hashash, Y.M.A., Stewart, J.P., Rathje, E.M., Harmon, J.A., Musgrove, M.I., Campbell, K.W, and Silva, W.J. (2015). Relative differences between nonlinear and equivalent-linear 1D site response analyses, submitted to *Earthquake Spectra*. In review.

Kwok, A.O.L., Stewart J.P., Hashash, Y.M.A., Matasovic, N., Pyke, R.M., Wang, Z.L., and Yang, Z. (2007). Use of exact solutions of wave propagation problems to guide implementation of nonlinear seismic ground response analysis procedures, *J. Geotech. Geoenvir. Eng*. 133, 1385-1398.

Menq F.Y. (2003). Dynamic Properties of Sandy and Gravelly Soils, PhD Thesis, Department of Civil Engineering, University of Texas, Austin, TX.

Mikami, M., Stewart, J.P., Kamiyama, M. (2008). Effects of time series analysis protocols on transfer functions calculated from earthquake accelerograms, *Soil Dyn. Earthquake Eng*. 28, 695-706.

Stewart, J.P., Afshari, K., and Hashash, Y.M.A. (2014). Guidelines for performing hazard-consistent one-dimensional ground response analysis for ground motion prediction, *PEER Report No. 2014/16*, Pacific Earthquake Engineering Research Center, UC Berkeley, CA.

Thompson, E.M., Baise, L.G., Tanaka, Y., and Kayen, R.E. (2012). A taxonomy of site response complexity, *Soil Dyn. Earthquake Eng*. 41, 32-43.

Van Houtte, C., Drouet, S., Cotton, F. (2011). Analysis of the origins of κ (kappa) to compute hard rock to rock adjustment factors for GMPEs, *Bull. Seismol. Soc. Am.* 101, 2926-2941.

Zalachoris, G., and Rathje E.M. (2015). Evaluation of one-dimensional site response techniques using borehole arrays, *J. Geotech. Geoenviron. Eng.*, 10.1061/(ASCE)GT.1943-5606.0001366, 04015053.

PARAMETRIZATION OF TOPOGRAPHY FOR GROUND MOTION PREDICTION: SUMMARY AND FINDINGS

Manisha Rai and Adrian Rodriguez-Marek

Department of Civil and Environmental Engineering
Virginia Tech, Blacksburg, Virginia

Abstract

This paper summarizes our findings from a previous study on the effects of topography on ground motions. We analyzed the NGA-West2 dataset and proposed a model to predict topographic effects at a site. The model proposes modification factors for the expected amplifications or de-amplifications at a site, as a function of the relative elevation value at the site. As a part of this study, we also computed 2D topographic amplification at ground motion stations from simplistic numerical analyses and found that the logarithm of amplifications at stations, averaged over multiple orientations, were highly correlated with relative elevation value at the stations.

Introduction

Topography can significantly affect ground motions at sites located close to them (Bouchon, 1973; Boore et al., 1981; Bard, 1982). Typically, hills and ridges cause ground motion amplifications, whereas valleys and depressions cause de-amplification of ground motions compared to ground motions on a flat terrain (Davis and West, 1973; Rogers et al., 1974; Griffiths and Bollinger, 1979; Geli et al., 1988; Bouchon and Barker, 1996; Assimaki and Gazetas, 2004; Meunier et al., 2008; Rai et al. 2012; Maufroy et al., 2014; Rai et al. 2015). Topographically correlated damage patterns have been reported in a number of past earthquakes (Trifunac and Hudson, 1971; Celebi, 1987; Geli et al., 1988; Kawase and Aki, 1990; Hatzfeld et al., 1995; Bouchon and Barker, 1996). These effects however are not included in existing ground motion prediction equations. Consequently, there are no engineering tools to correctly estimate these effects at a site. In a previous study (Rai, 2015), we addressed this problem by proposing an empirical model to predict the effects of topography at a site. This paper presents a summary and important findings from that work.

Since topographic effects are systematically observed in the ground motions, they should also be predictable. Prediction of topographic effects can only be achieved by studying the dependence of the effects at a site on a family of topographic proxies or parameters. These proxies can then be used to predict the expected amplification/de-amplification at a given site. To develop topographic proxies for a given site, we employed two methods. In the first method, we used the elevation data around the site to compute geomorphometric parameters such as slopes, curvatures, and relative elevations and used them as topographic proxies for the sites. In the second method, we computed 2D topographic amplification at a given site from simple numerical analyses, and used the amplifications to develop a family of topographic parameters

for the sites. We used the NGA-West2 ground motion dataset, and computed topographic proxies from the two methods for each of the ground motion stations. We used the ground motion model residuals at those stations and tested if the residuals showed any trends with respect to one or more of the computed parameters. Statistical tests were performed to determine if the trends in the residuals with respect to the computed parameters were statistically significant. When the trends were found to be significant for a given parameter, we fit regression models to predict topographic effects as a function of that parameter. In the end, we compared different models to determine which model fitted the residuals most effectively. In the ensuing, we briefly cover the details of the analysis, and summarize our findings from that study. For a complete discussion, the readers are referred to Rai (2015).

Ground motion data

A subset of the NGA-West2 database used by Chiou and Youngs (2014) was used for the study. The subset consisted of ground motion recordings from 300 earthquakes of magnitude 3 and higher, at 3208 stations located in the regions of California, Alaska, Japan, Taiwan, China, Turkey, Italy, Iran, and New Zealand. As topographic effects are site effects, the residual component of interest for this study was the site residual, which represents the average error in

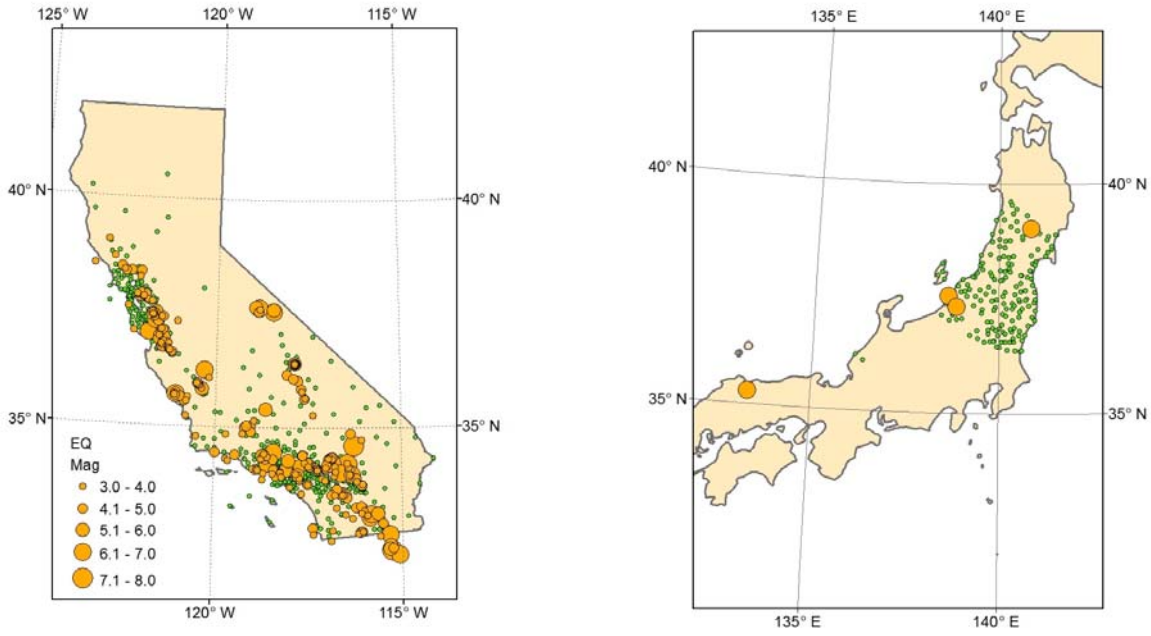

Figure 1. Locations of earthquake hypocenters (orange circles) and ground motion recording stations (green dots) for the data used in this study. Only stations with three or more recordings are considered. This filtering of data results in stations only within California and Japan.

prediction at a site, after removing the effects of earthquake. To obtain site residuals, the intra-event residuals (δW_{es}) from the Chiou and Youngs (2014) model were partitioned as follows:

$$\delta W_{es} = \delta S2S_s + \delta WS_{es} \quad (1)$$

where $\delta S2S_s$ are the site residuals, δWS_{es} are the site-and-event corrected residuals, and the subscripts *e* and *s* represent event and site, respectively. Each of the components of Equation 1 are assumed to be zero mean random variables with standard deviations ϕ, ϕ_{s2s}, and ϕ_{ss} for δW_{es}, $\delta S2S_s$ and δWS_{es}, respectively. To get stable estimates of site residuals at each station, we included those stations that had three or more earthquake recording on them. This constraint resulted in a total of 9,195 ground motions at 798 stations, located in California and Japan (Figure 1). The dataset consisted of ground motion residuals at 105 spectral periods from 0.01 s to 10 s.

Topographic parameters

We used two methods to compute topographic parameters. In the first method, we used the elevation data around the ground motion stations, and the resulting parameters are referred to here as the "geometry-based" parameters. In the second method, we performed a series of numerical analyses, and used the results from the analysis to obtain topographic parameters at the ground motion stations. These parameters are referred to here as the "numerical-analyses-based" parameter. In the following, we present a brief overview of the two types of parameters.

Geometry-based parameters

These parameters were computed in ArcGIS (ESRI, 2011) using the elevation data at the ground motion stations. We computed three parameters for each station: smoothed slopes (S_d), smoothed curvature (C_d) and relative elevation (H_d), where d is the scale-parameter that defines the size of the neighborhood used to compute the parameters. *Slope* is defined as the first spatial derivative of elevation and quantifies the steepness of the earth's surface. *Curvature* is the second spatial derivative of a surface and quantifies the convexity/concavity of the surface. Curvature values are positive for convex feature such as a hill or a ridge, and are negative for concave feature such as a valley or a canyon. *Relative elevation* is the difference between the elevation at a point on the surface and the mean elevation in the neighborhood of the point. Relative elevations have been used in the past to delineate ridges, slopes, and valleys in watershed study (Guisan et al., 1999; Jones et al., 2000). We used several different values of d in the analysis to study the effect of scale on the parameter values (see Rai, 2015). Figure 2 and 3 show the variation in the values of these geometry-based parameters with scale d.

Numerical-analysis-based parameter

These parameters were based on the results of a series of simplistic 2D numerical analyses. The idea behind this parameterization was to compute estimates of 2D amplifications due to surface topography at the stations, and then use these amplifications as an input in a regression analysis to predict actual amplifications at the stations. To compute these parameters, we performed simplistic numerical analyses on FLAC (Itasca Consulting Group, 2005) for each

station in the dataset. For each of these analyses we used by used planar 2D meshes with simplified V_s profiles, elastic soil properties, transmitting boundary conditions, and sinusoidal input motions. The top surface of the mesh was fit to the shape of the cross-sectional profile of the surface at the station in a given orientation. As an example, Figure 4 shows the cross-

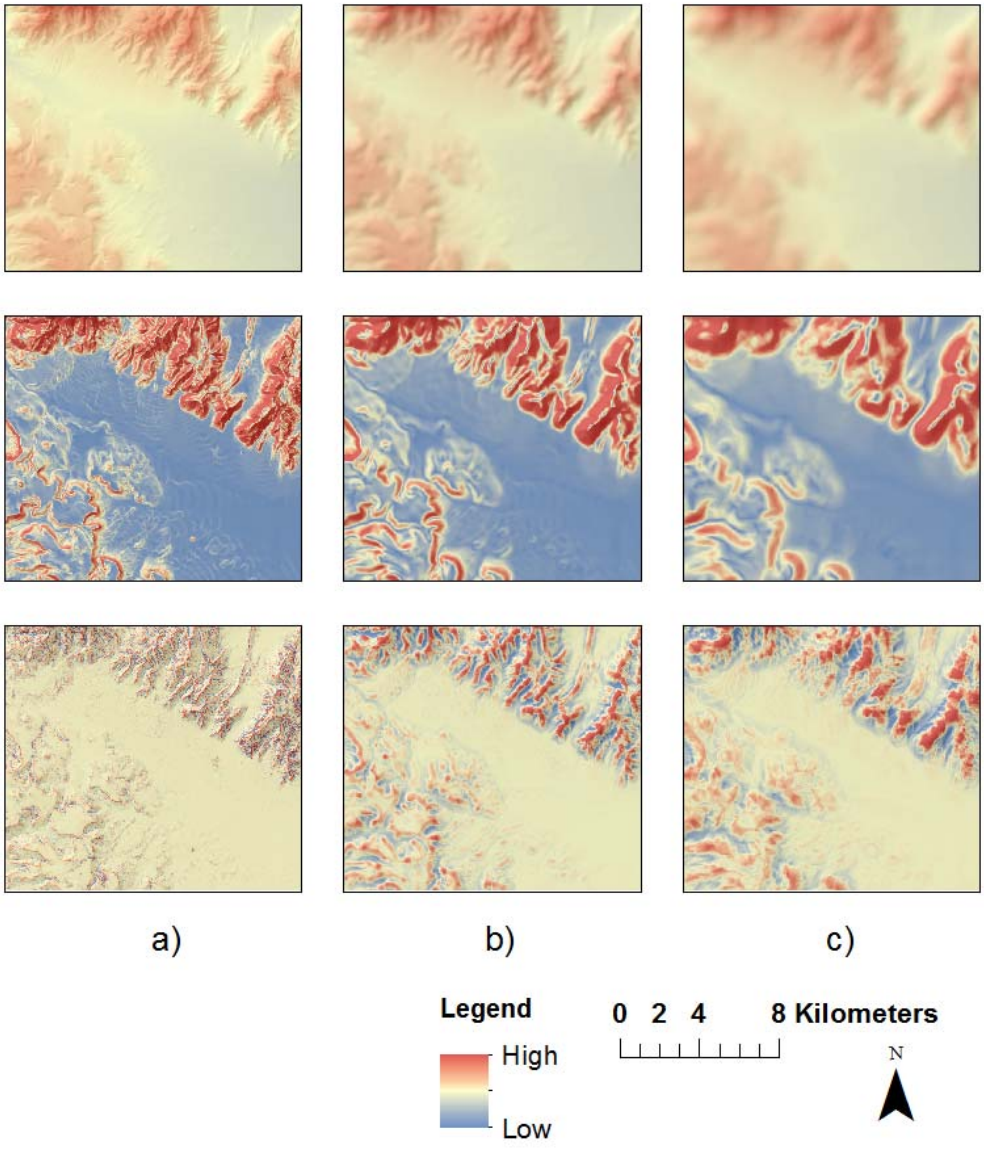

Figure 2. The top row consists of smoothed elevation raster, with a) no smoothing, b) smoothing using a scale (d) of 360 m, and c) smoothing using a scale of 720 m. The middle row shows corresponding smoothed slopes and the bottom row shows corresponding smoothed curvatures. Both smoothed slopes and curvatures are computed using corresponding smoothed elevations.

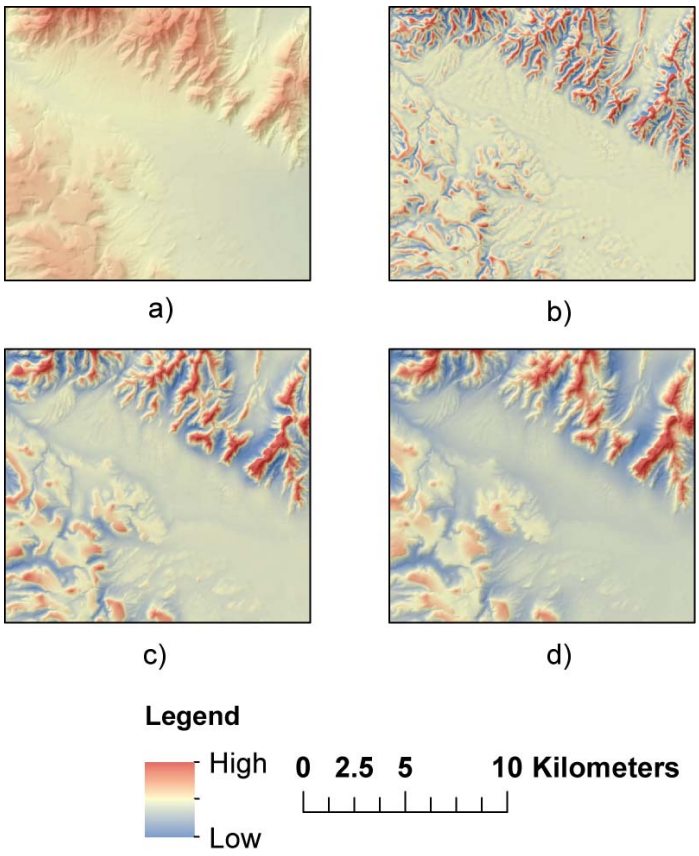

Figure 3. The variation of relative elevation with scale is shown. Shown are the a) elevation raster, b) H_{500}, c) H_{1500}, and d) H_{3000}. Note that at smaller scales, finer features are visible. As the scale is increased, the broader features become more prominent and finer details are lost.

sectional profiles that were computed for the Tamalpais peak station in California using the elevation data around the station in six orientations. This step was repeated for all the other stations in the dataset. A cosine tapered sinusoidal velocity was used as an input at the base of the mesh, and the resultant time history was recorded at the top surface of every mesh. Using the recorded motions at every station, and for every orientation, we computed the peak ground acceleration (PGA) at the station in six orientations. For each 2D analysis, we also performed a 1D analysis with no topography. The ratio of PGAs from the 2D and 1D analyses was computed. This ratio represents the value of amplification due to topography from the 2D analysis. A schematic illustration of the mesh and the applied boundary conditions are shown in Figure 5 for the Tamalpais peak stations for one of the orientations shown in Figure 4.

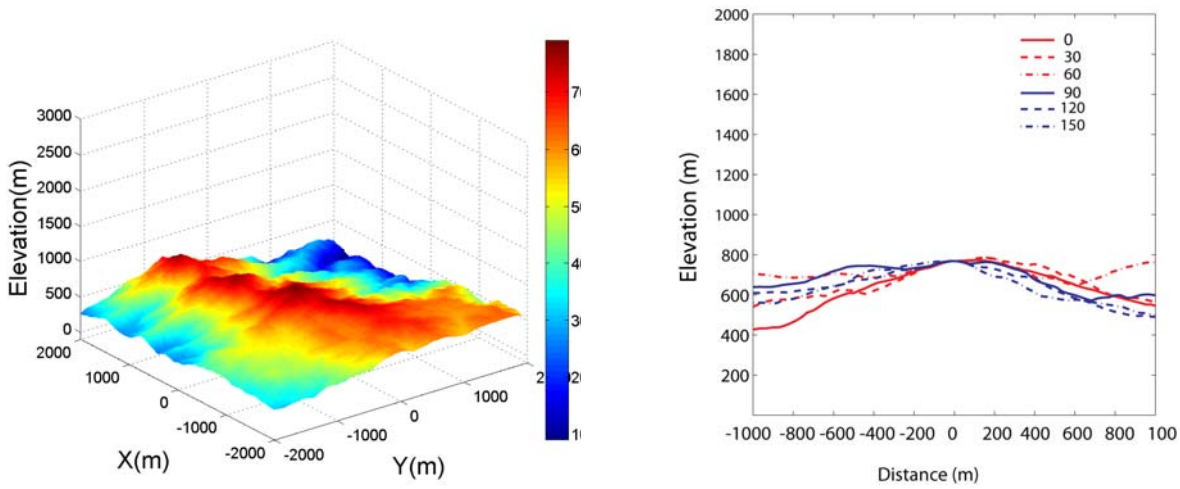

a) b)

Figure 4. 3D terrain around a site (left) and cross-sectional profiles across the station in 6 different directions (right) are shown for the Tamalpais peak B station (37.9231, -122.5983). The recording station is located at [0, 0] m.

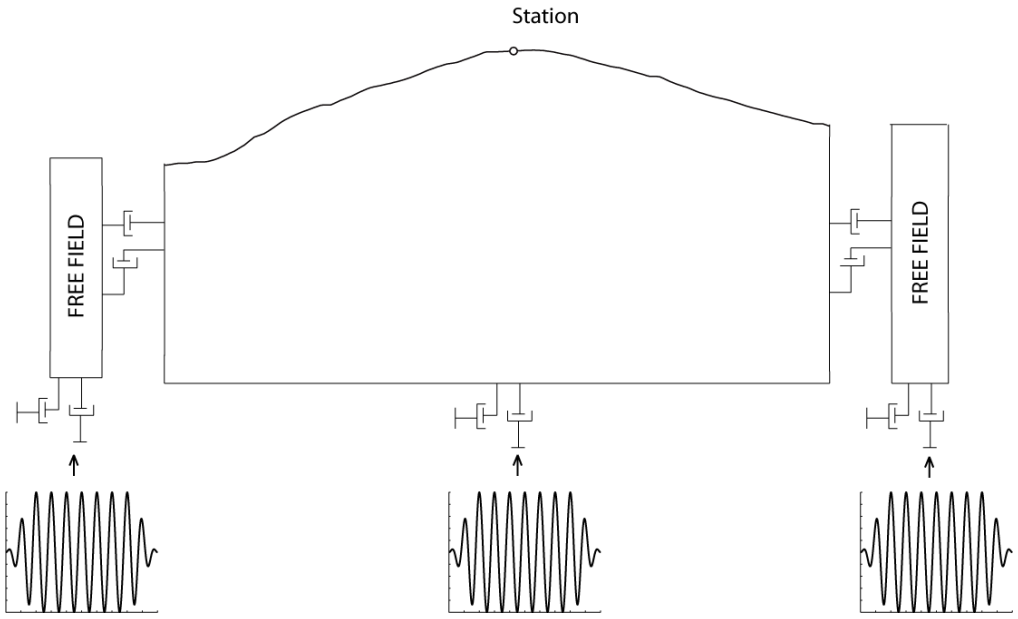

Figure 5. Schematic illustration of the finite difference model used for the analysis at one of the recording stations. The model uses a realistic topographic cross-section profile at the top. The station is located at the surface, equidistant from both the lateral edges. The height of the station from the base is the same for all stations. Free-field boundary conditions are applied to the lateral boundaries and quiet boundary conditions are applied at the base.

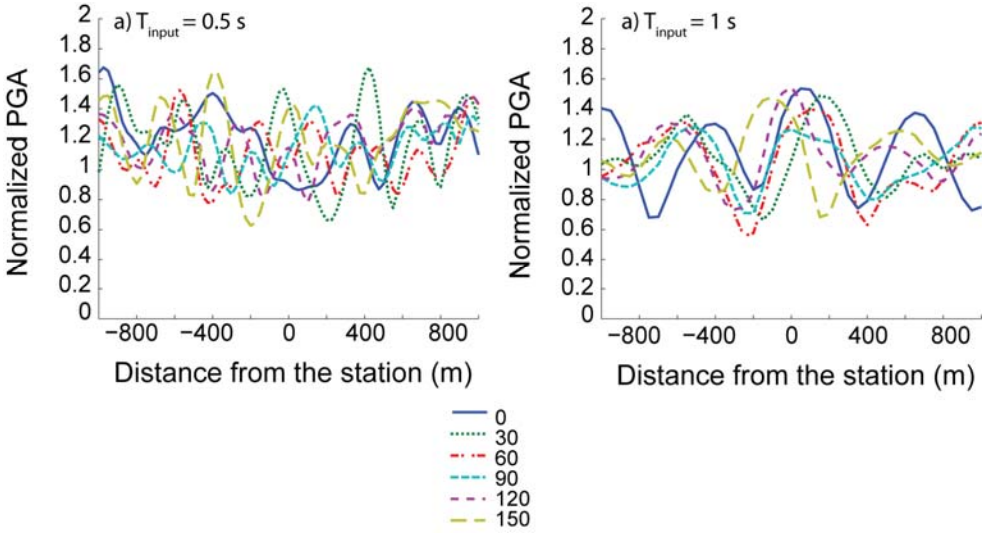

Figure 6. *Normalized PGA* values for the six cross-sections of the Tamalpais peak B station are shown for an input wave of period 0.5 s, and 1 s. The amplification and deamplification patterns seem to emerge at distances proportional to the wavelength of input motion. Also note that the normalized PGA values are greater than one for most of the azimuths, indicating an average amplification at the station.

Each of the six analysis for a given station resulted in a steady-state *Normalized PGAs* for that direction. The *Normalized PGAs* is referred to here as the ratio of the PGA from the 2D analysis to the PGA from the corresponding 1D analysis. Figure 6 shows the variation of *normalized PGA* at the surface of Tamalpais peak station for six orientations. A pattern of amplification and de-amplification emerges along the surface, and the distances over which these variations occurred were proportional to the wavelength of input motion. Using these *Normalized PGA* values, we computed the sets of parameters listed in Table 1.

Table 1. List of parameters computed from the numerical analyses.

Parameter	**Description**
$\ln Amp_{avg}$	Mean of the six *lnAmp* values
$\ln Amp_{min}$	Minimum of the six *lnAmp* values
$lnAmp_{max}$	Maximum of the six *lnAmp* values
$\ln Amp_{par}$	*lnAmp* value parallel to line joining recording station and hypocenter
$\ln Amp_{perp}$	*lnAmp* value perpendicular to line joining station and hypocenter

The term ln*Amp* in the table is used to define the natural logarithm of the *Normalized PGAs*. We used the natural logarithm of amplification as a parameter because the ground motion residuals are also in the units of natural logarithm of spectral accelerations, and we were using these parameters to model the trends in these residuals. To compute lnAmp_{par} and lnAmp_{perp}, we computed the angle of the line joining the station to the earthquake hypocenter. Using this angle, we selected one of the six azimuths where we obtained the cross-sections and selected the one that is closest to the computed angle, and assigned the corresponding *lnAmp* value in that direction to $lnAmp_{par}$. We repeated this process to obtain the $lnAmp_{perp}$, this time selecting the azimuth closest to the angle perpendicular to the computed angle. This process resulted in a total of 15 ln*Amp* parameters for each ground motion station. Using these parameters, and the previous geometry-based parameter, we studied the trends in the intra-event residuals from the Chiou and Youngs (2014) ground motion model to determine if one or more of these parameters can predict biases in the residuals.

Residual analysis and parameter selection

Figure 7 shows a scatterplot of the site residuals ($\delta S2S_s$) and the H_{1500} values at the station. The figure shows a positive trend in the site residuals with respect to H_{1500} for periods greater than 0.3 s. Similar trends were seen for other values of scale *d* used to compute H_d. A similar analysis of the scatterplot of site residuals and corresponding slopes showed no systematic trends. We therefore removed slope values from our analysis.

We tested the statistical significance of the trends in the site residuals with respect to the relative elevation parameter H_d by first dividing the stations into three classes based on the value of the topographic parameter H_d and then testing if the mean site residuals in each of the three classes are statistically different from each other. To do this, we denoted the group of stations with $H_d > t\sigma_{H_d}$ as '*High*', the group with $H_d < -t\sigma_{H_d}$ as '*Low*', and the group with $-t\sigma_{H_d} < H_d < t\sigma_{H_d}$ as '*Intermediate*'. Here, *t* is a constant threshold and was used to set the class boundaries and σ_{H_d} is the standard deviation of H_d values at the stations in the dataset used in the study. We used t values of 0.5 and 1 to determine the effect of changing threshold on the classification and on the mean site residuals within each class. Note that this classification depended on the value of *d* (used to compute mean elevation), and t (used to set the class boundaries). As we had selected 3 values of *d* and 2 values of *t*, there were a total of 6 *d*-*t* combinations. Each of these *d*-*t* combinations resulted in a different classification.

After determining the topographic class for each ground-motion station for a particular combination of d and t, we used mixed-effects regression using Equation 1 on stations from a single class to compute class-specific ϕ_{s2s} and ϕ_{ss}, as well as the mean site residual ($\overline{\delta S2S_s}$), which is the average of the site residuals in that class. Regressions were conducted using the R package *lme4* (Bates et al. 2014). We repeated this process for stations in the other two classes and also for other combinations of d and t. The resultant $\overline{\delta S2S_s}$ values for the three classes are shown as a function of the spectral period for different combination of *d* and *t* (Figure 8). We can see that there is an intermediate period range (T = 0.2 s to T = 1.0 s) for which the $\overline{\delta S2S_s}$ value for the *high* class became greater than the $\overline{\delta S2S_s}$ value for the other two classes. Higher $\overline{\delta S2S_s}$ value implies that the recorded ground motions on the stations in that class were on average higher than predicted by the GMPE. The $\overline{\delta S2S_s}$ value for the *low* class typically reduces as

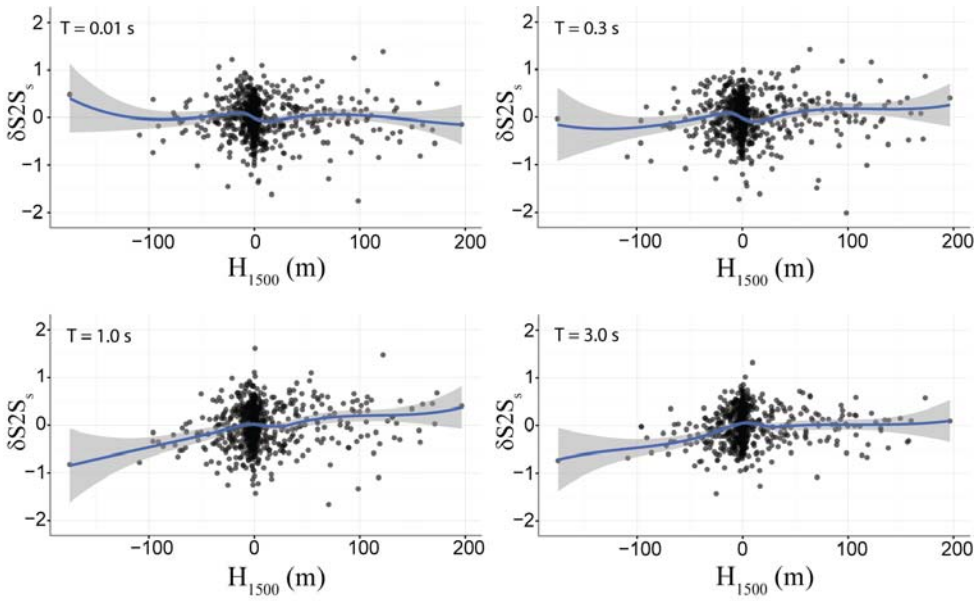

Figure 7. Site residuals ($\delta S2S_s$) from Equation 1 with relative elevation at a scale of 1500 m (H_{1500}). A moving average of the $\delta S2S_s$ terms computed using local regression (loess) is also shown.

period increases and becomes the lowest of the three classes for periods longer than 0.5 s. This means that at longer periods, the recorded motions in the *low* class were on average lower than the median predictions. As a majority of the stations in the dataset were classified as *intermediate* (e.g., 557 classified as *intermediate*, 103 as *low*, and 138 as *high,* for a scale of 1500 m, and t = 0.5), the $\overline{\delta S2S_s}$ value for the *intermediate* class can be expected to approximate the total $\overline{\delta S2S_s}$for the data. Thus, the $\overline{\delta S2S_s}$ value for the stations in the *intermediate* class was closer to zero compared to the other two classes. As the ground motions are presented in the log scale, the average amplification and de-amplification for each class were computed by taking the exponent of the observed $\overline{\delta S2S_s}$ for that class. After performing some statistical tests we selected a scale of 1500 m, and a threshold t of 0.5 for topographic classification.

We also compared the predictive abilities of the different numerical-analysis-based parameter. To do this comparison we fitted smoothed models to the intra-event residuals from the Chiou and Youngs (2014) GMPE by performing loess regression (Cleveland et al., 1992) as a function of each of the *lnAmp* parameters. For this regression, we used an α value of 1. α controls the degree of smoothing in the loess regression, with a value of 1 resulting in maximum smoothed function. We used this setting to avoid over-fitting the data. The coefficient of determination, or the R^2 values from these regressions are shown in Figure 9. Note that these R^2 values are of the order of 0.01, which seem to be rather small. These models are only accounting for a site-specific effect, thus we are only reducing a part of the total variance i.e. the site-specific variance. Other components of variability are still present in the residuals, even after removing the site-specific biases. Therefore the overall reduction in the variability of the intra-

event residual after the regression is small. Even though these R^2 values are small, they still provide information about the relative predictive abilities of individual *lnAmp* parameters. We can see in Figure 9 that out of the 5 *lnAmp* models, the $lnAmp_{avg}$ model has a relatively higher R^2 value on average. We therefore selected the $lnAmp_{avg}$ parameter from all the other *lnAmp* parameters for further analysis.

We compared the two types of shortlisted parameters, namely relative elevation and the $lnAmp_{avg}$ parameter and found that the two were very highly correlated linearly (Figure 10). The correlations between H_d and $lnAmp_{avg}$ reached a maximum when the value of d was equal to the wavelength of the input motion used to compute $lnAmp_{avg}$ (Figure 11). This is an important result as it shows that H_d was in essence modeling the average elastic 2D amplification of a wave with wavelength *d*. A similar observation was also made by Maufroy et al. (2014) who noted that the

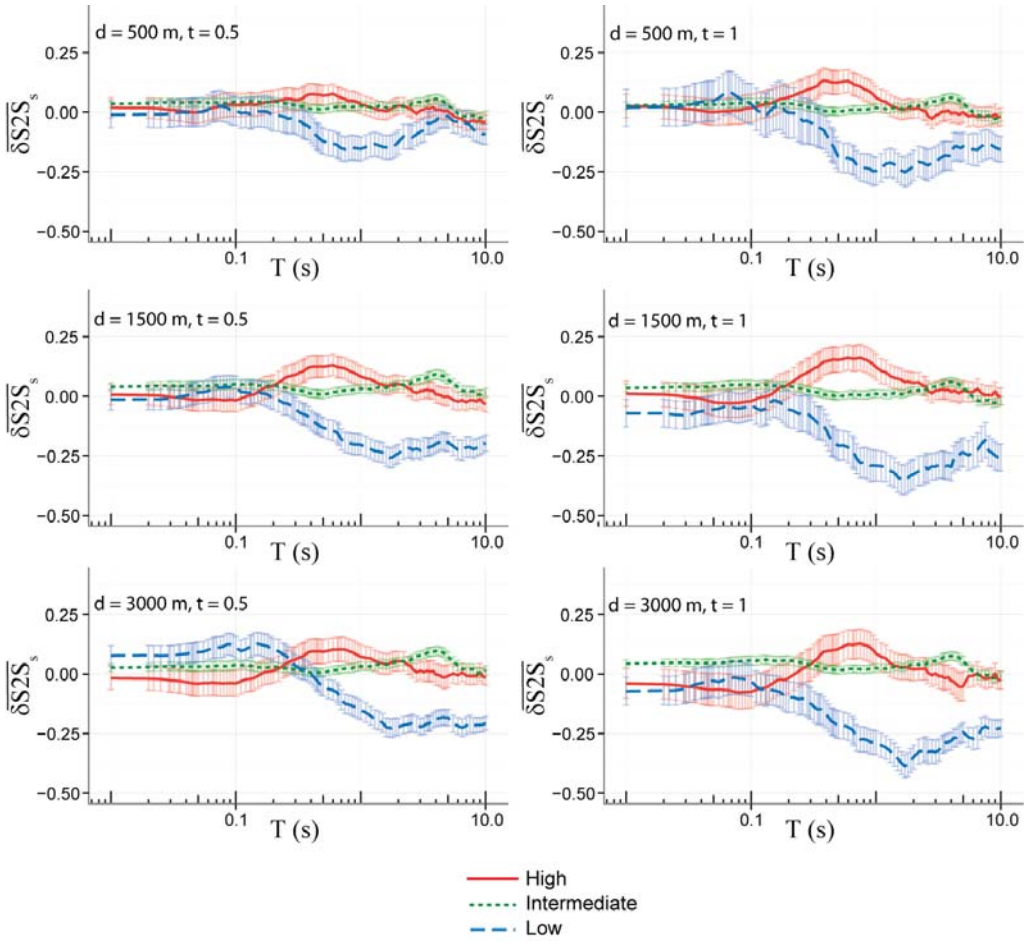

Figure 8. Mean site residuals ($\overline{\delta S2S_s}$) for the high, intermediate and low classes along with the +/- 1 standard deviation error bars.

amplifications at sites were highly correlated with the smoothed curvatures. However, this result also contrasts the findings from Burjánek et al (2014) who found that the amplifications at sites with pronounced topography are mostly controlled by the sub-surface shear wave velocities and not so much by the shape of the topographic feature.

The high correlation between H_d parameters, and the $lnAmp_{avg}$ parameters showed that the two parameters have similar information and they both captured topographic information. Thus they should have very similar predictive power, and we found that this was the case. Since computing the $lnAmp_{avg}$ parameters are expensive, and we are not gaining any additional reduction in the standard deviation in the fitted model, we used H_{1500} parameter for our final model.

Regression and model development

To account for the trends in ground motion residuals with respect to H_{1500} , we added a term containing the parameter to the right side of Equation 1, as follows:

$$\delta W_{es} = f(H_{1500}) + \delta S2S_s + \delta WS_{es} \qquad 2)$$

where δW_{es} is the intra-event residual from the Chiou and Youngs (2014) ground motion model, f is a function of the topographic parameter H_{1500}, $\delta S2S_s$ is the site residual after accounting for topographic effects, and δWS_{es} is the site-and-event corrected residual. We selected a multi-linear functional form for function f that has constant levels of spectral acceleration value for each topographic class with a linear transition from one class to the next class. The choice of this functional form was based on the fact that we observed distinct behavior within each class, as demonstrated by the different levels of mean site residuals. A multi-linear form proposes average levels of amplifications expected at sites within each class (e.g., high, low, or intermediate), and therefore it is much more robust in predictions than fitting say a linear model, that would predict increasing values of amplification for higher values of the topographic parameter, even though we did not have physical evidence to support such a model. The functional form we selected for accounting topographic effect is given by:

$$f = \begin{cases} c_{low} & H_{1500} < -20 \\ c_{int} & -17 < H_{1500} < 17 \\ c_{high} & H_{1500} > 20 \end{cases} \qquad 3)$$

with linear transition zones for intermediate values of H_{1500} (e.g., -20 to -17 or 17 to 20 m). In the model, we kept the transition zone from low/high class to intermediate class very steep such that the coefficient values can be more realistically constrained. The value of the coefficient c_{int} obtained from regression was fairly close to zero at all periods, and there was no reason to assume that they were different than zero. Because, we wanted to preserve the difference between different levels, we subtracted c_{int} from c_{high}, and c_{low} and smoothed out these values, ensuring that the c_{high}, c_{low} values gradually reached zero for periods where they were not significantly different than c_{int}. The updated values of coefficients c_{low}, c_{high}, ϕ_{ss}, and ϕ_{s2s} obtained through the mixed-effects regression on the full data set, and the epistemic uncertainties

(σ) associated with each coefficient, obtained from bootstrapping are reported in Table 2. These values can be added directly to the GMPE to estimate topographic effects at a site.

Table 2. Smoothed period dependent factors for f in Equation 3

Spectral Period (s)	c_{low}	$\sigma_{c_{low}}$	c_{high}	$\sigma_{c_{high}}$	ϕ_{s2s}	ϕ_{ss}
0.01	0	-	0	-	-	-
0.05	0	-	0	-	-	-
0.10	0	-	0	-	-	-
0.15	0	-	0	-	-	-
0.2	-0.0323	0.0263	0	-	0.4894	0.5518
0.25	-0.0573	0.0248	0.0293	0.0167	0.4704	0.5497
0.3	-0.0778	0.0255	0.0532	0.0175	0.4580	0.5428
0.4	-0.1100	0.0254	0.0910	0.0162	0.4396	0.5165
0.5	-0.1351	0.0226	0.1202	0.0158	0.4346	0.5060
0.75	-0.1805	0.0220	0.0851	0.0155	0.4335	0.4680
1	-0.2128	0.0219	0.0601	0.0142	0.4450	0.4460
1.5	-0.2583	0.0195	0.0250	0.0134	0.4309	0.4192
2	-0.2906	0.0192	0	-	0.4110	0.4054
3	-0.2906	0.0207	0	-	0.3854	0.3948
4	-0.2906	0.0213	0	-	0.3776	0.3830
5	-0.2764	0.0199	0	-	0.3772	0.3602
7.5	-0.2506	0.0236	0	-	0.3406	0.3483
10	-0.2323	0.0263	0	-	0.2802	0.3268

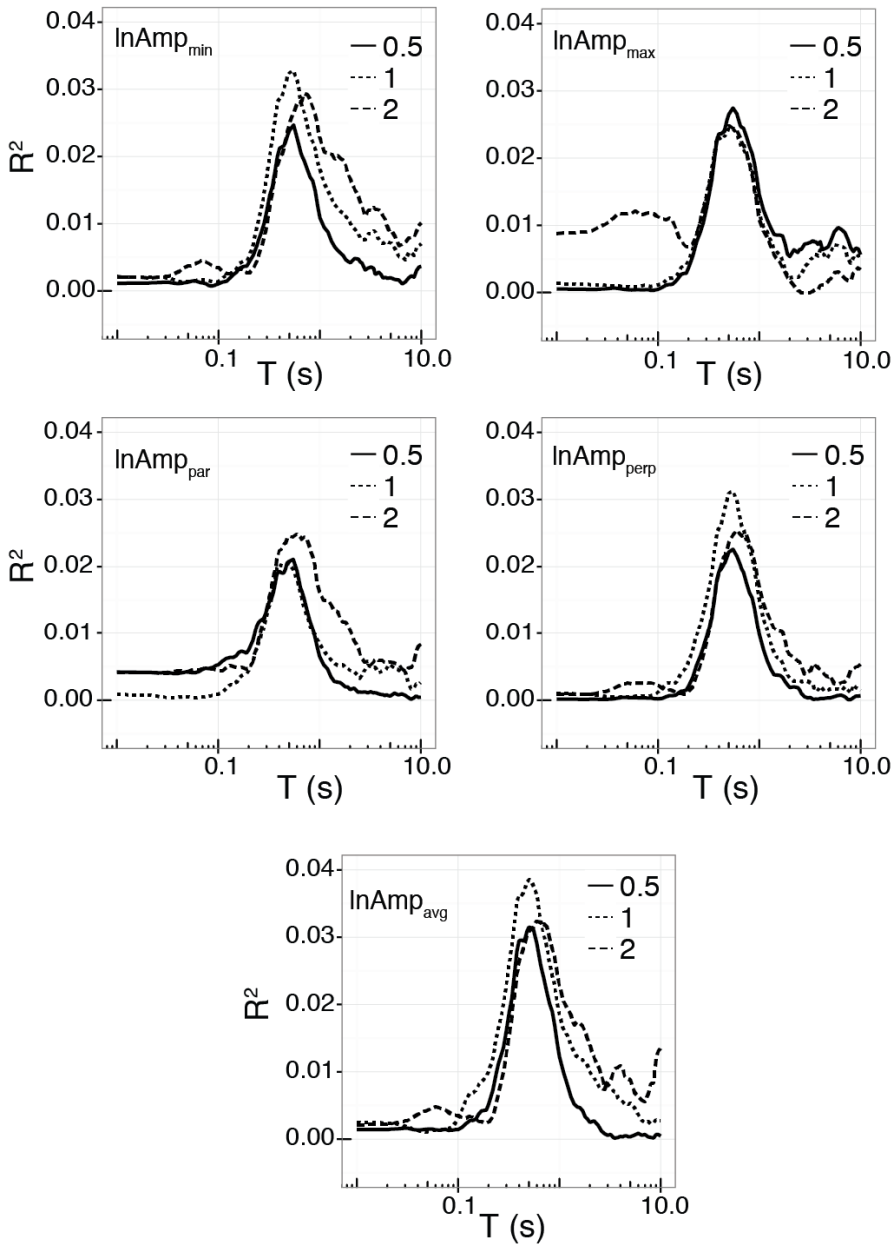

Figure 9. Coefficient of determination (R^2) value from the loess regressions on the intra-event residuals from the Chiou and Youngs (2014) model using the five *lnAmp*.

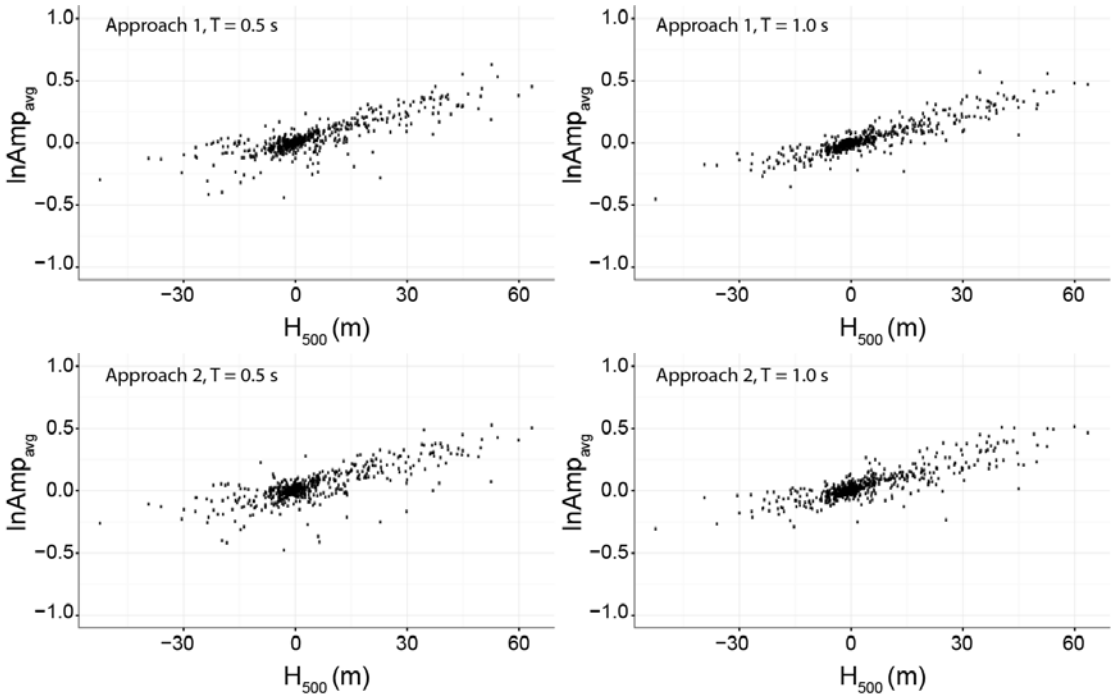

Figure 10. Scatterplot of the *lnAmp*$_{avg}$ obtained from the analysis using Approach 1 (constant V_s of 500 m/s for every station), and Approach 2 ($V_s = V_{s30}$), and the relative elevation parameter H_d for d values of 250 m - 3000 m. The values are shown for an input wave of period 0.5 s and 1 s.

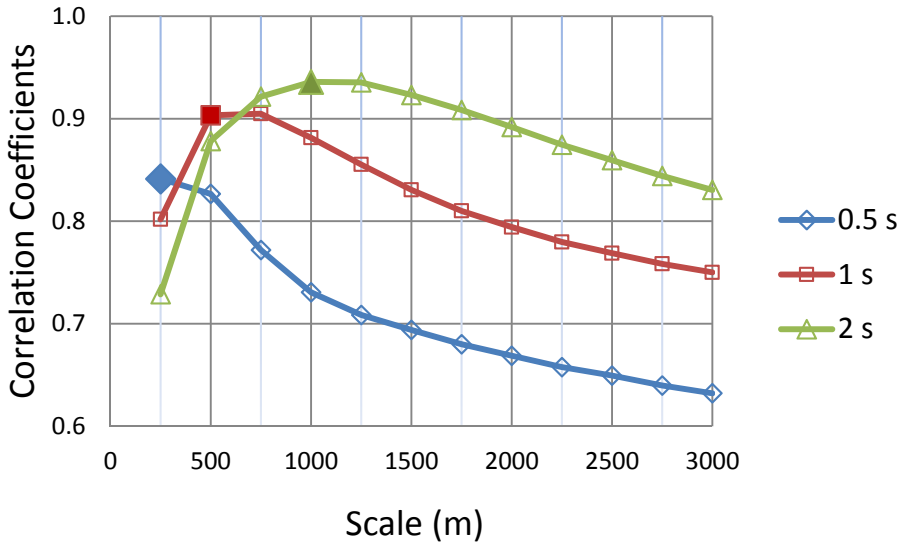

Figure 11. Correlation coefficient values between *lnAmp*$_{avg}$, and H_d for d values of 250 m - 3000. The three lines correspond to input wave of period 0.5 s, 1 s and 2s. The peaks are shown with solid symbols. Note that the respective peaks occur at a scale equal to the wavelength of the input motion.

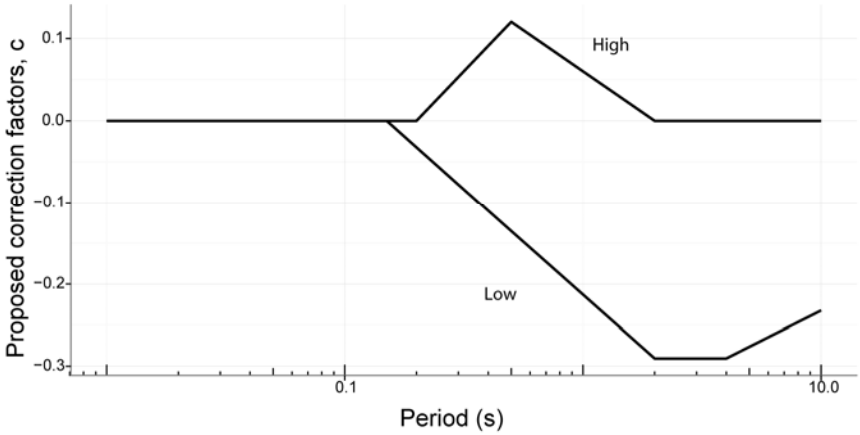

Figure 12. Proposed correction factors, c_{low} ($H_{1500} < -20$ m) and c_{high} ($H_{1500} > 20$ m) for topography. Linear interpolation should be used to estimate the correction factors for absolute H_{1500} values of 17 m – 20 m.

The *high* sites in the model showed a maximum amplification at a period of 0.5 s, and the *low* sites showed maximum deamplification between periods of 2 - 4 s. We could not establish the exact reason for this behavior; however we think that the majority of sites classified as *high* and *low* might be experiencing some sort of topographic resonance at these periods. Figure 12 shows the variation of the proposed correction factors for *high* and *low* class with period.

Conclusions

We used the NGA-West2 database to empirically study the effects of topography on earthquake ground motions. Topography was quantified using two types of parameters; the geometry-based parameters, and the numerical-analyses-based parameters. The three geometry-based topographic parameters that we studied were smoothed slope, smoothed curvature, and relative elevation. Two of these parameters, smoothed curvature and relative elevation, were highly correlated linearly. Of these two parameters, we only used relative elevation parameter for the regression analysis, as it a relatively simpler parameter to compute. The numerical-analysis-based parameters were computed using simplistic 2D numerical analyses. We computed approximate estimates of topographic amplifications at ground motion stations in multiple orientations, and used the natural logarithm of these amplifications to develop five other parameters at each station. We compared the predictive powers of these numerical-analyses-based parameters to determine the most efficient predictor of topographic effects. We finally selected $lnAmp_{avg}$ parameter, as it resulted in the highest R^2 value when a loess model was fit to the intra-event residuals with respect to each of the l*nAmp* parameters.

We compared the $lnAmp_{avg}$ values at the stations with the H_d values at the same stations and found that the two are highly correlated for several values of scale d. We found that for a given wavelength of input motion, the correlations between resulting $lnAmp_{avg}$ values and the H_d parameter reaches a maximum at a d value equal to the wavelength of input motion. This result

shows that the relative elevation parameter is modeling the elastic 2D amplification at the sites. Due to the high correlations between the $lnAmp_{avg}$ parameter and the H_d parameter, the two parameters carry very similar information, and also have similar predictive power. Using the ground motion residuals and the H_{1500} parameter, we fitted a model that predicts expected amplification or deamplification at a site as a function of H_{1500} at the site. The model proposes modification factors that can be used with an existing ground motion model. The proposed approach for computing topographic effects that is of using simplified numerical models to obtain parameters that can be used in regression analyses can also be used for capturing other effects of site amplification.

References

Assimaki, D., and Gazetas, G. (2004). "Soil and topographic amplification on canyon banks and the 1999 Athens earthquake." *Journal of earthquake engineering*, 8(01), 1–43.

Bard, P.-Y. (1982). "Diffracted waves and displacement field over two-dimensional elevated topographies." Geophysical Journal International, 71(3), 731–760.

Bates, D., Maechler, M., Bolker, B., and Walker, S., 2014. *lme4: Linear mixed-effects models using Eigen and S4*. R package version 1.1-7, http://CRAN.R-project.org/package=lme4.

Boore, D. M., Harmsen, S. C., and Harding, S. T. (1981). "Wave scattering from a step change in surface topography." *Bulletin of the Seismological Society of America*, 71(1), 117–125.

Bouchon, M. (1973). "Effect of topography on surface motion." *Bulletin of the Seismological Society of America*, 63(2), 615–632.

Bouchon, M., and Barker, J. S. (1996). "Seismic response of a hill: the example of Tarzana, California." Bulletin of the Seismological Society of America, 86(1A), 66–72.

Burjánek, J., Edwards, B., & Fäh, D. (2014). "Empirical evidence of local seismic effects at sites with pronounced topography: A systematic approach." Geophysical Journal International, ggu014.

Celebi, M. (1987). "Topographical and geological amplifications determined from strong-motion and aftershock records of the 3 March 1985 Chile earthquake." Bulletin of the Seismological Society of America, 77(4), 1147–1167.

Chiou, B. S. -J., and Youngs, R. R., 2014. Update of the Chiou and Youngs NGA Model for the Average Horizontal Component of Peak Ground Motion and Response Spectra, Earthquake Spectra, 30(3), 1117-1153.

Cleveland, W. S., E. Grosse, and W. M. Shyu (1992). Local regression models. Statistical models in S, 309–376.

Davis, L. L., and West, L. R. (1973). "Observed effects of topography on ground motion." *Bulletin of the Seismological Society of America*, 63(1), 283–298.

ESRI (2011). "ArcGIS Desktop: Release 10." Redlands, CA.

Geli, L., Bard, P.-Y., and Jullien, B. (1988). "The effect of topography on earthquake ground motion: a review and new results." *Bulletin of the Seismological Society of America*, 78(1), 42–63.

Griffiths, D. W., and Bollinger, G. A. (1979). "The effect of Appalachian Mountain topography on seismic waves." *Bulletin of the Seismological Society of* America, 69(4), 1081–1105.

Guisan, A., Weiss, S. B., & Weiss, A. D. (1999). "GLM versus CCA spatial modeling of plant species distribution." *Plant Ecology*, 143(1), 107-122.

Jones, K. B., Heggem, D. T., Wade, T. G., Neale, A. C., Ebert, D. W., Nash, M. S., Mehaffey, M. H., Goodman, I. A., Hermann, K. A., Selle, A. R., Bolgrien, D., Augustine, S., Pedersen, J., Lin, C. J., Viger, J. M., Chiang, D., Zhong, Y., Baker, J., and Remortel, R. D. V., 2000. Assessing Landscape Condition Relative to Water Resources in the Western United States: A Strategic Approach." Monitoring Ecological Condition in the Western United States, S. S. Sandhu, B. D. Melzian, E. R. Long, W. G. Whitford, and B. T. Walton, eds., Springer Netherlands, 227–245.

Hatzfeld, D., Nord, J., Paul, A., Guiguet, R., Briole, P., Ruegg, J.-C., Cattin, R., Armijo, R., Meyer, B., Hubert, A., Bernard, P., Makropoulos, K., Karakostas, V., Papaioannou, C., Papanastassiou, D., and Veis, G. (1995). "The Kozani-Grevena (Greece) Earthquake of May 13, 1995, Ms = 6.6. Preliminary Results of a Field Multidisciplinary Survey." *Seismological Research Letters*, 66(6), 61–70.

Itasca Consulting Group, Inc. (2005). "FLAC: fast lagrangian analysis of continua. User's manual"

Maufroy, E., Cruz-Atienza, V., Cotton, F., and Gaffet, S. (2014). "Frequency-scaled curvature as a proxy for topographic site-effect amplification and ground motion variability." *Bulletin of Seismological Society of America.*

Meunier, P., Hovius, N., and Haines, J. A. (2008). "Topographic site effects and the location of earthquake induced landslides." *Earth and Planetary Science Letters*, 275(3-4), 221–232.

Rai, M., Rodriguez-Marek, A., and Yong, A. (2012). "Topographic effects in strong ground motion." *Proceedings of the 15th World Conference on Earthquake Engineering, Lisbon, Portugal*, paper number 3843

Rai, M., Rodriguez-Marek, A., and Yong, A. (2015). "An empirical model to predict topographic effects in strong ground motion: Study using California small to medium magnitude earthquake database." *Earthquake spectra, In press*

Rai, M (2015). "Topographic effects in strong ground motion." Ph.D. dissertation, Virginia tech.

Rogers, A. M., Katz, L. J., and Bennett, T. J. (1974). "Topographic effects on ground motion for incident P waves: A model study." *Bulletin of the Seismological Society of America*, 64(2), 437–456.

Trifunac, M. D., and Hudson, D. E. (1971). "Analysis of the Pacoima dam accelerogram—San Fernando, California, earthquake of 1971." *Bulletin of the Seismological Society of America*, 61(5), 1393–1411.

EVALUATION OF ASCE/SEI 7 DIRECTION OF LOADING PROVISIONS USING CSMIP RECORDS

Reid B. Zimmerman, P.E.
Bret Lizundia, S.E.
Saeed Fathali, Ph.D., P.E.

Rutherford + Chekene
Structural and Geotechnical Engineers
San Francisco, CA

Abstract

The data recorded from seismically instrumented buildings over the past approximately 40 years is used to indirectly evaluate the ASCE/SEI 7 direction of loading provisions. Direction of loading provisions require combining the maximum response in one direction, with a percentage of the maximum response in the orthogonal direction. In ASCE/SEI 7, a value of 30% is used for response in the orthogonal direction. This research shows that, for a wide range of conditions and assumptions, building response exceeds combinations with maximum response in one direction and only 30% of the maximum in the other direction. Alternative combination values are provided that better bound the recorded data.

Research Motivation and Limitations

The foundation of the direction of loading provisions in ASCE/SEI 7-10 (ASCE, 2010) date back to Newmark (1975) and Rosenblueth and Contreras (1977) and have remained relatively unchanged as codes have evolved in other ways. Direction of loading provisions often use the shorthand of 100%+XX% where XX% is the percentage of the maximum in the orthogonal direction. Past research on orthogonal combination criteria has almost universally concluded that a 100%+30% criterion is unconservative, although the literature differs on the degree of unconservatism. For a complete literature review and extensive background, refer to Zimmerman et al. (2014). Most of the research on direction of loading provisions since Rosenblueth and Contreras (1977) proposed the 100%+30% criterion has focused on analytical studies based on computer simulations of building or bridge response (e.g., MacRae and Mattheis, 2000; Zaghlool et al., 2001; MacRae and Tagawa, 2001; Sherman and Okazaki, 2010; Bisadi and Head, 2011; Cimellaro et al., 2014) or on theoretical studies based on generalized parameters (e.g., Menun and Der Kiureghian, 1998; Hernandez and Lopez, 2002; Lopez et al., 2001).

No studies, however, have attempted to use actual earthquake data from instrumented buildings as pursued in this research. The Center for Engineering Strong Motion Data (CESMD, 2015) provides an extensive set of instrumented building records that are used in this research. Using actual building response records, though, has limitations which include the following:

1. The component responses (e.g., moments, shears, etc.) are not available. For example, axial load in a column shared by two intersecting lateral force-resisting systems is not recorded as part of building instrumentation.
2. As compared to analytical studies, it is not possible to design a building to a specific provision and then assess its adequacy. Instead, only the response from an earthquake (which is not necessarily equivalent to a design-basis earthquake) is available while information about building capacity is missing. For example, with only the building response available, a building cannot be designed per the ASCE/SEI 7 (ASCE, 2010) direction of loading provisions and then assessed against the permissible probability of collapse (i.e., the FEMA P695 procedure) (FEMA, 2009).

The first limitation is less restrictive than the second since even an evaluation of a limited set of response types is valuable. The second limitation is more restrictive because assessment of an ASCE/SEI 7 (ASCE, 2010) provision is inherently a comparison of demand (i.e., response) versus capacity. While the demand, available through the recorded building response, is more directly obtained in this research than in analytical studies, the capacity is essentially unavailable. However, it should be noted that the building capacity is not used in the ASCE/SEI 7 direction of loading provisions. Instead, 100% and 30% of the respective demands are. It is, therefore, possible to make an assessment of the *application* of the provisions (i.e., combining 100% and 30% of the demand) even if an assessment of the *effect* of the provisions (i.e., the collapse probability of the resulting design) cannot be made. In other words, this research cannot answer the question: "Does a building designed to the ASCE/SEI 7-10 direction of loading provisions including a 100%+30% criterion have a sufficiently low probability of collapse to meet the intent of provisions?" But this research can answer: "Does an approximation of the actual response, using a 100%+30% criterion, adequately bound the actual response of a building during a real earthquake?"

Presumed Intent of the Direction of Loading Provisions

Before asking how to evaluate a 100%+30% criterion using instrumented building data, it is important to ask what the intent of the 100%+30% criterion is in ASCE/SEI 7-10 (ASCE, 2010). The commentary of ASCE/SEI 7-10 for the direction of loading provisions lacks specificity. While it does directly reference Rosenblueth and Contreras (1977), it does not describe the type of earthquake phenomenon the provisions intend to bound. Instead, engineers and researchers are left to infer the intention of the provisions when facing the following questions:

- Is the intent to account for correlation between the two directions of ground motion? In other words, is the intent to account for the fact that earthquake demand at 45 degrees with respect to the building axes could be as large as the earthquake demand along the x- or y-directions?
- Is the intent to account for the fact that a design-basis earthquake may not produce equal earthquake demand (i.e., spectral acceleration) in both the x- and y-directions of a building?
- Is the intent to account for both of the above phenomenon?

It is the opinion of the authors that a 100%+30% criterion, as implemented in ASCE/SEI 7-10 (ASCE, 2010) was explicitly intended to account for correlation between the two directions of ground motion. This is supported by "triggers" in the ASCE/SEI 7-10 direction of loading provisions which necessitate the use of a 100%+30% criterion. For example, a column which forms part of two or more intersecting frames will see axial load from both x- and y-direction ground motions. If the ground motions were perfectly uncorrelated (e.g., for every point in time, the x-direction ground motion was zero whenever the y-direction ground motion existed and vice versa), the axial demand on such a column could be predicted by the larger of the x-direction and y-direction demand taken independently. On the other hand, if the ground motions were even somewhat correlated, the axial demand at each point in time would be a combination of the full x-direction and full y-direction demand.

The direction of loading commentary in ASCE/SEI 7-10 (ASCE, 2010) does not associate a 100%+30% criterion to the fact that design-basis earthquakes may not produce equal earthquake demand in both directions. However, this is not to say that when the code developers introduced the 100%+30% provision they did not intend for it to cover such cases. They may have. But the ASCE/SEI 7-10 direction of loading provisions and corresponding commentary do not seem to support that interpretation.

Research Objectives

The first objective of this research is to evaluate the ability of a 100%+30% criterion to conservatively bound the actual response of instrumented buildings. This is approached in two different ways by asking the following questions:

1. Does 30% of the maximum y-direction response adequately bound the y-direction response at the point in time when the maximum x-direction response occurs (and vice versa)?
2. Does an approximation of the actual response, using a 100%+30% criterion, adequately bound the actual response for every point in time?

The second objective of this research is to determine a more appropriate 100%+XX% criterion, where XX can take on values from 0 to 100, assuming that a 100%+30% criterion is not conservative. This is also approached in two different ways by asking the following sets of questions:

1. For 50% of the data, what XX% of the maximum y-direction response bounds the y-direction response at the point in time when the maximum x-direction response occurs (and vice versa)? What about for 84% of the data?
2. For 50% of the data, what XX% must be used such that an approximation of the actual response, using a 100%+XX% criterion, bounds the actual response for every point in time? What about for 84% of the data?

The third objective of this research is to assess the dependence of these evaluation methods on different building, earthquake and sensor characteristics (e.g., ground motion intensity, ratio of fundamental period in each direction, etc.). Since the results of these studies do

not demonstrate any significant dependence, they have not been included in this paper. The fourth objective is to assess the dependency on using a set of axes rotated to align with the maximum response rather than aligned with the building's axes. The fifth objective is to assess the dependency on the way in which the approximation of the actual response using a 100%+XX% criterion is constructed (see Figure 5).

Methodology

Response Types and Sensor Combinations

The CESMD (2015) records, whether recorded directly by individual sensors (i.e., absolute acceleration) or calculated based on the recorded data (i.e., relative displacement), were used to define three response types.

1. Sensor-to-sensor drift ratio is computed by taking the displacement of a sensor at a chosen floor and subtracting the displacement of a corresponding sensor at the next instrumented floor below at each instant of time. The resulting displacement difference, also known as drift, is then divided by the difference in height between the sensors to produce a dimensionless drift ratio. Figure 1a shows how sensor-to-sensor drift ratio is computed for an example station with the slope of the red line indicating Sensor 11 to Sensor 10 drift ratio.
2. Sensor-to-ground drift ratio is computed by taking the displacement of a sensor at a chosen floor and subtracting the displacement of a corresponding sensor at the base of the building at each instant of time. The resulting displacement difference, also known as drift, is then divided by the difference in height between the sensors to produce a drift ratio. See Figure 1b for an example.
3. Absolute acceleration (the response recorded by the accelerometers) is taken as the acceleration of a sensor at a chosen floor at each instant of time. See Figure 1c for an example.

The evaluation of a 100%+XX% criterion necessarily requires consideration of response in two orthogonal directions. As such, some relation must be established between sensors which measure response in one direction and those which measure response in the perpendicular direction. In the stations from the CESMD (2015), a station north is established based on the axis of the building that most closely aligns with true north. From that, sensors are typically oriented station north-south and station east-west. The task is therefore to define relationships between north-south sensors and corresponding east-west sensors. This creates a pair of sensors at an individual floor which must also be, depending on the response type used, related to a corresponding pair of sensors at another floor. Figure 1 illustrates this process where red and blue sensors measure east-west and north-south response, respectively. A sensor combination for a given station and earthquake is referred to as a station-earthquake-sensor combination in this research. Note that the different response types (i.e., sensor-to-sensor drift ratio, sensor-to-ground drift ratio, and absolute acceleration) require different combinations of sensors. The same sensor combinations for sensor-to-ground drift ratio and absolute acceleration are used in this research so that a displacement-based and acceleration-based response parameter can be

compared for the same station-earthquake-sensor combinations. For further information about sensor combinations, refer to the full report on this research (Zimmerman et al., in preparation).

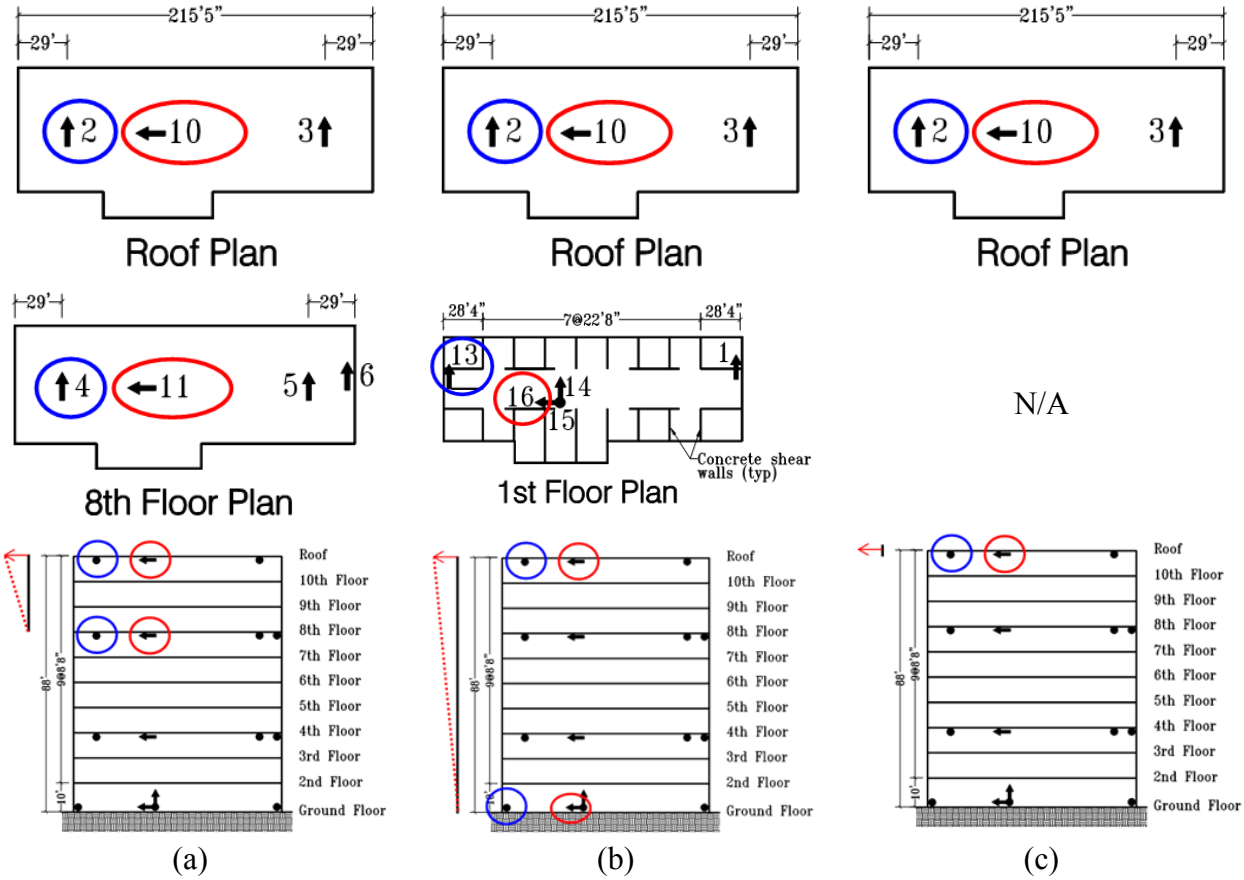

Figure 1. Illustration of (a) sensor-to-sensor drift ratio, (b) sensor-to-ground drift ratio, and (c) absolute acceleration for CSMIP Station No. 24385. Red and blue indicate sensors measuring east-west and north-south, respectively.

CESMD Database

As mentioned previously, this is the first study to use actual building response to assess the direction of loading provisions in ASCE/SEI 7 (ASCE, 2010). The following summarizes the data from CESMD (2015) that was available for this study:

- 182 stations (i.e., buildings) located throughout the State of California
- 144 earthquakes ranging from the Santa Barbara Earthquake in 1978 to the Fontana Earthquake on January 15, 2014
- 860 station-earthquakes, where one station-earthquake represents one earthquake affecting one station. Since each earthquake can affect multiple stations and some stations have records from multiple earthquakes, the number of station-earthquakes exceeds both the number of earthquakes and the number of stations.
- 2,061 station-earthquake-sensor combinations for sensor-to-sensor drift ratio

- 1,787 station-earthquake-sensor combinations for sensor-to-ground drift ratio and absolute acceleration.

In order to arrive at the number of stations, station-earthquakes and station-earthquake-sensor combinations provided above, a comprehensive filtering process was conducted. This process accomplished eliminating unsuitable data, combining the parameters of interest for redundant sensors, and balancing the quality and quantity of the data used. For a complete description, see the full report on this research (Zimmerman et al., in preparation).

Orbital Plots

Orbital plots, such as the one shown in Figure 2, show the response along one direction versus the response along the perpendicular direction.

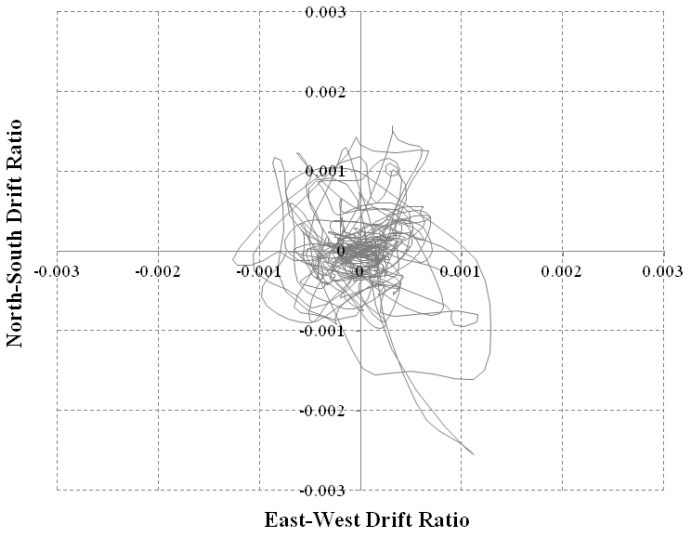

Figure 2. Orbital plot of sensor-to-sensor drift ratio for Station 24385, 1994 Northridge Earthquake, Sensor Combination [11, 4] and [10, 2].

Orthogonal Ratio Study

For the orthogonal ratio study, two points are identified on the orbital plot. The first point corresponds to the maximum east-west response which has coordinates: (EW_{max}, $NS_{atmaxEW}$). The second corresponds to the maximum north-south response which has coordinates: ($EW_{atNSmax}$, NS_{max}). When determining these points, the maximum response is taken as the absolute maximum of both positive and negative values. Therefore, EW_{max} and/or NS_{max} could be a negative number.

Once these two points have been identified, the 100% component or, more specifically, the 100% East-West and the 100% North-South components of a 100%+XX% criterion are known. To determine the percentage contribution in the orthogonal direction, Equations 1 and 2 are used.

$$\alpha_{EW} = \frac{|EW_{atmaxNS}|}{|EW_{max}|} \qquad \text{Equation 1}$$

$$\alpha_{NS} = \frac{|NS_{atmaxEW}|}{|NS_{max}|} \qquad \text{Equation 2}$$

$$\alpha = max(\alpha_{EW}, \alpha_{NS}) \qquad \text{Equation 3}$$

Equations 1 through 3 are applied for each station-earthquake-sensor combination. Figure 3 shows an example calculation of α_{EW}. Figure 4 shows an example calculation for α_{NS}.

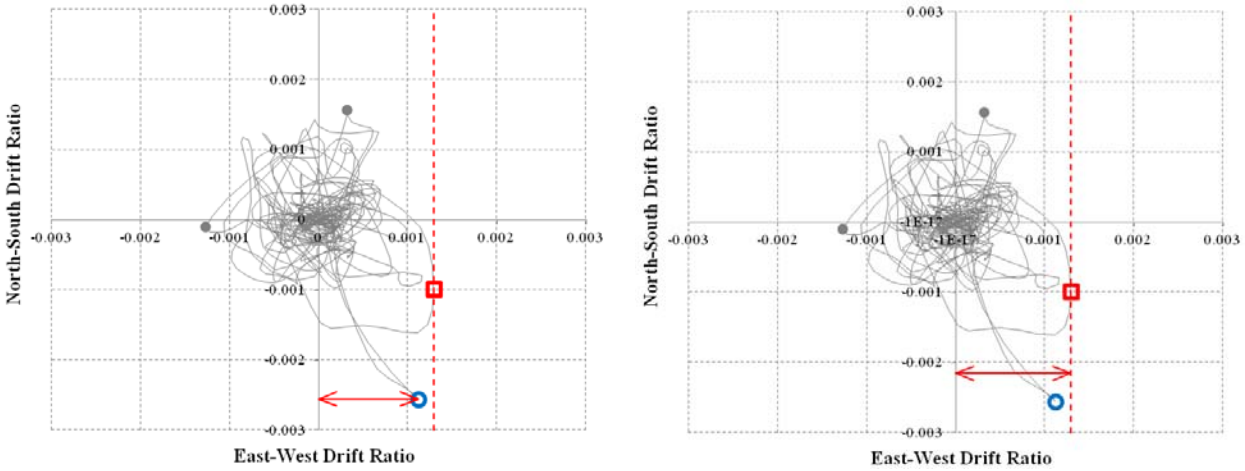

(a) (b)

Figure 3. Calculation of α_{EW} = 87% as the ratio of (a) $|EW_{atmaxNS}|$ = 0.0011 to (b) $|EW_{max}|$ = 0.0013 for sensor-to-sensor drift ratio for Station 24385, 1994 Northridge Earthquake, Sensor Combination [11, 4] and [10, 2].

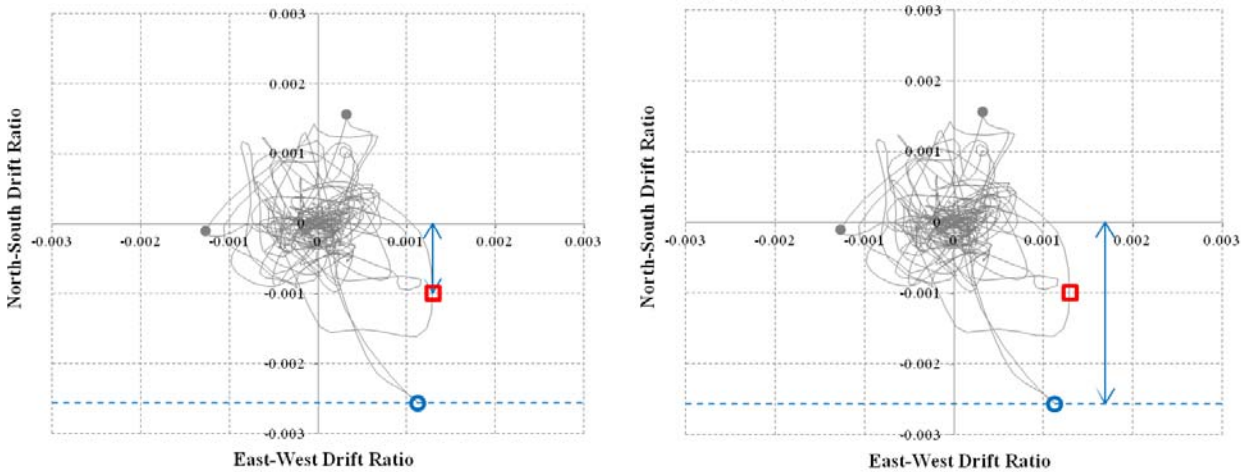

(a) (b)

Figure 4. Calculation of α_{NS} = 39% as the ratio of (a) $|NS_{atmaxEW}|$ = 0.00098 to (b) $|NS_{max}|$ = 0.0026 for sensor-to-sensor drift ratio for Station 24385, 1994 Northridge Earthquake, Sensor Combination [11, 4] and [10, 2].

Octagon and Truncated Ellipse Interaction Studies

The octagon and truncated ellipse interaction studies approach the evaluation of the 100%+XX% criterion in a slightly different manner than the orthogonal ratio study. They similarly begin by finding EW_{max} and NS_{max} as described for the orthogonal ratio study. However, instead of extracting the orthogonal component of response at these two points, they construct eight control points connected by an interaction interpolation. The eight control points have coordinates in the orbital space as presented in generalized form in Figure 5. For generality, each axis in Figure 5 has been normalized by the maximum response along that axis (i.e., $|EW_{max}|$ or $|NS_{max}|$). Figure 5 also shows three potential interpolations between the control points. Figure 5b and Figure 5c are called octagon interaction and truncated ellipse interaction, respectively, in this research. The justification for the various possible interaction interpolations shown in Figure 5 along with discussion on the relationship between the ASCE/SEI 7-10 requirements and the control nodes can be found in Zimmerman et al. (2014).

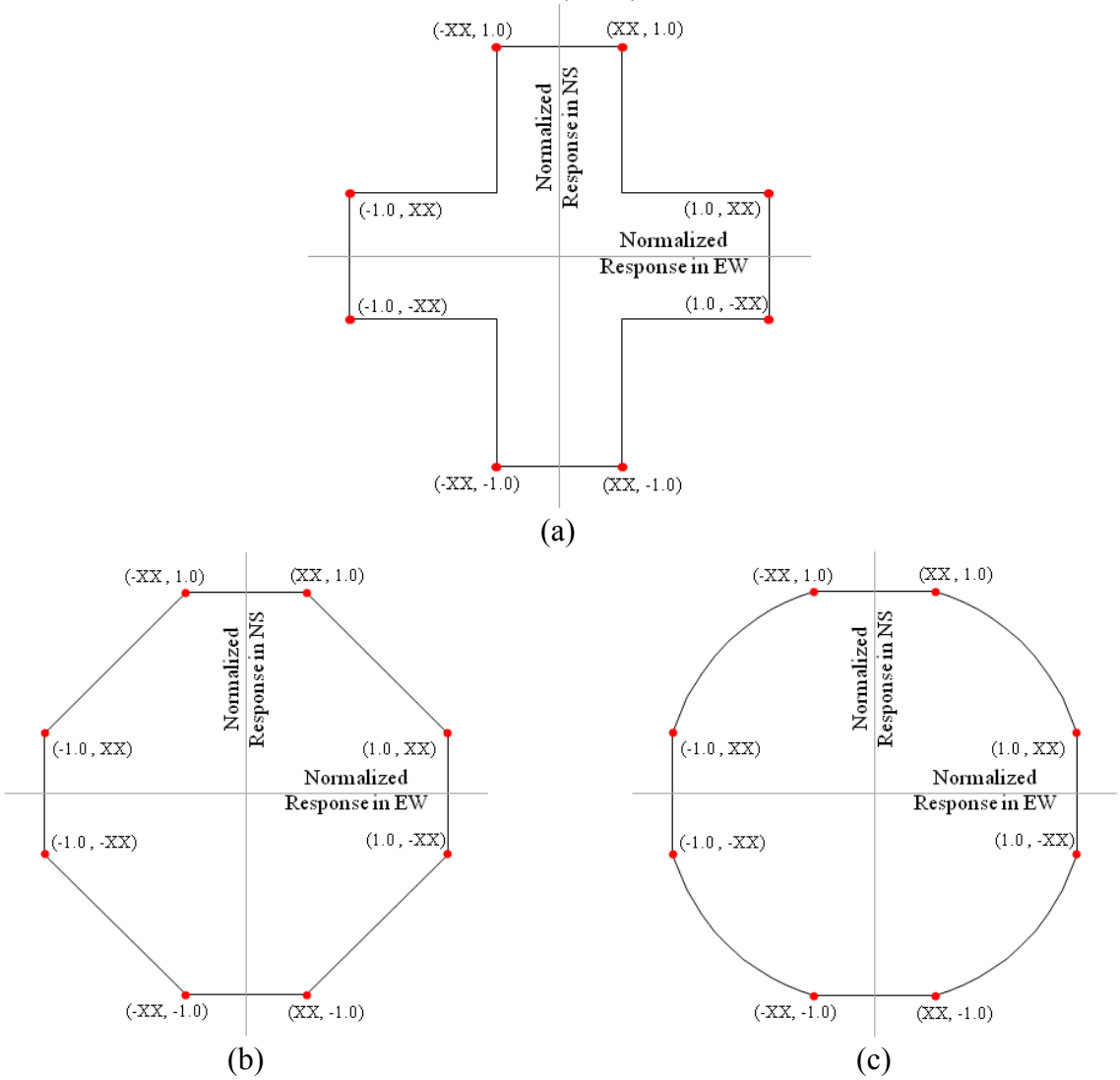

Figure 5. Generalized coordinates of control points for a 100%+XX% criterion and (a) no interpolation on the diagonal, (b) linear interpolation on the diagonal, and (c) elliptical interpolation on the diagonal.

The parameter of interest for the octagon interaction and truncated ellipse interaction studies is termed the response-limit ratio. The response-limit ratio is analogous to the demand-capacity ratio used in structural engineering practice. As the name implies, it is a measure of the ratio of the response to a defined limit. That limit is taken as the octagon interaction or truncated ellipse interaction interpolation. To define the response-limit ratio, two vectors are created for every point in the response history.

The first vector connects the origin of the orbital plot with any point on the response orbital. It represents the radial component of the response. The second vector connects the origin of the orbital plot to a point at the intersection of the interaction interpolation and a line having the same orientation as the first vector (i.e. parallel and in the same quadrant). It is intended to be a quantitative measure of the limit. The response-limit ratio, *RLR*, is then calculated as the ratio of the length of the response vector to the length of the limit vector. An example of these two vectors can be seen in Figures 6 and 7 for the octagon interaction and truncated ellipse interaction studies, respectively. Note that the *RLR* can take on values greater than, less than, or equal to 1.0.

The search for the maximum *RLR*, RLR_{max}, is restricted to the regions of the orbital plot shown on normalized axes in Figure 8. This permits RLR_{max} to take on values greater than, less than, or equal to 1.0.

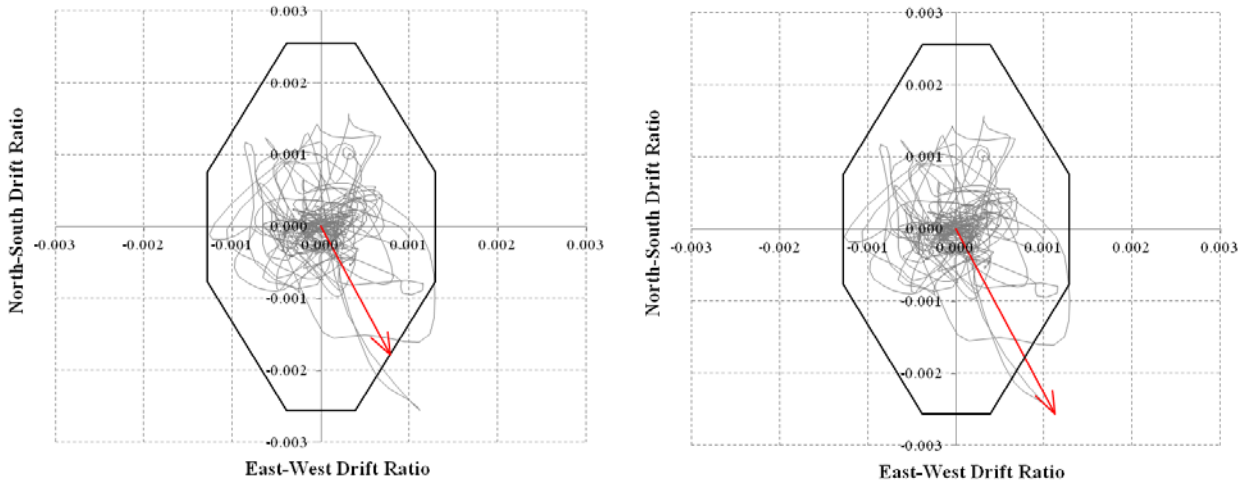

(a) (b)

Figure 6. Vectors used to calculate *RLR* for octagon interaction study where (a) is vector representing response = 0.0019 and (b) is vector representing limit = 0.0028. Vectors shown for point at which RLR_{max} = 1.44 occurs in the response history of sensor-to-sensor drift ratio for Station 24385, 1994 Northridge Earthquake, Sensor Combination [11, 4] and [10, 2], and XX = 0.3.

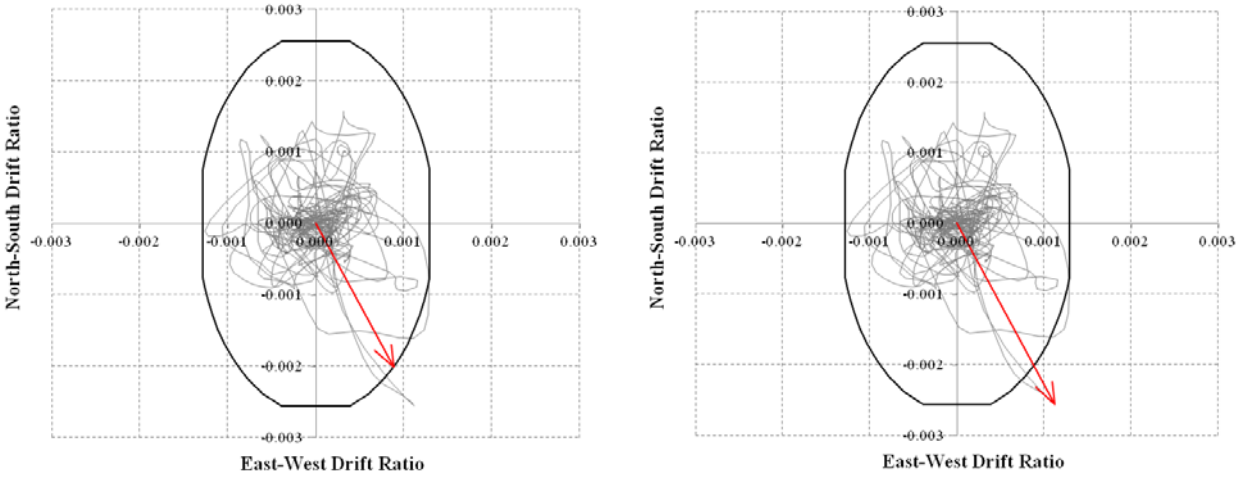

(a) (b)

Figure 7. Vectors used to calculate *RLR* for truncated ellipse interaction study where (a) is vector representing response = 0.0022 and (b) is vector representing limit = 0.0028. Vectors are shown for point at which RLR_{max} = 1.27 occurs in the response history of sensor-to-sensor drift ratio for Station 24385, 1994 Northridge Earthquake, Sensor Combination [11, 4] and [10, 2], and XX = 0.3.

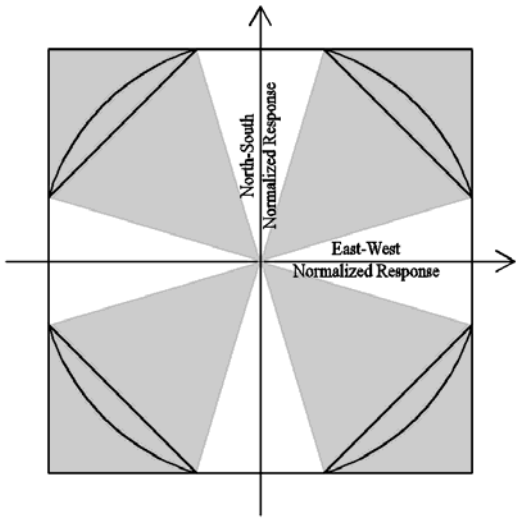

Figure 8. Areas of orbital space in which search for RLR_{max} is restricted shown in grey.

Zone Study

The zone study classifies the response of a specified station-earthquake-sensor combination into one of four "zones" in the orbital space as shown in Figure 9.

Zone 1 corresponds to the region of the orbital space depicted in Figure 5a and represents response which has been directly accounted for by a 100%+XX% criterion. It appears as a cross sign in the orbital space. Station-earthquake-sensor combinations for which all response is within Zone 1 for a given 100%+XX% criterion would be considered to satisfy that criteria explicitly.

Zone 2 corresponds to the region within the octagon interaction interpolation but excluding that already classified as Zone 1. It appears as four triangles, one in each quadrant of the orbital space. Station-earthquake-sensor combinations for which all response is within Zone 1 or Zone 2 for a given 100%+XX% criterion would be considered to satisfy that rule implicitly (under the assumption that linear interpolation between the control points of Figure 5b is appropriate).

Zone 3 corresponds to the region within the truncated ellipse interaction interpolation but excluding that already classified as Zone 1 or Zone 2. It appears as four segments of an ellipse, one in each quadrant of the orbital space. Station-earthquake-sensor combinations for which all response is within Zone 1, 2 or 3 for a given 100%+XX% criterion would be considered to satisfy that rule implicitly (under the assumption that elliptical interpolation between the control points of Figure 5c is appropriate).

Finally, Zone 4 is the region outside of the elliptical interaction interpolation. Station-earthquake-sensor combinations for which any point in the response history is within Zone 4 would be considered to violate that criterion regardless of whether octagon interaction or truncated ellipse interaction is assumed. In this research, the parameter of interest, Z_{crit}, for a given station-earthquake-sensor combination is assigned the value of the highest zone of any point on the response orbital.

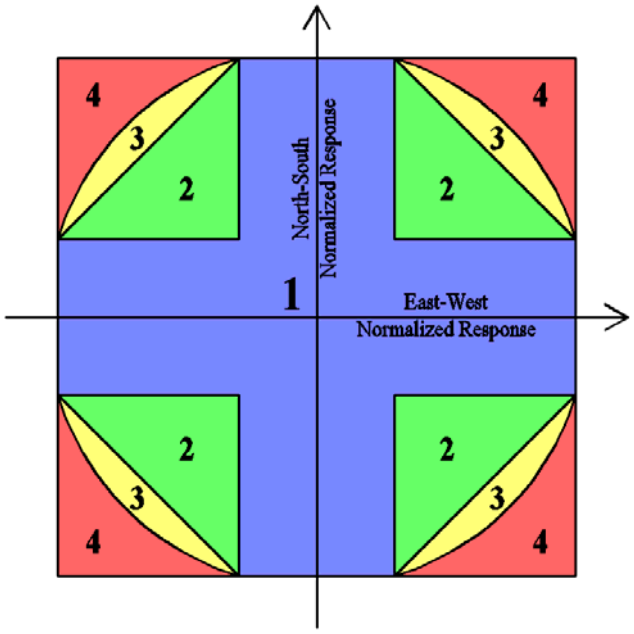

Figure 9. Zones of the orbital space. Zone 1, 2, 3 and 4 shown in blue, green, yellow and red, respectively.

Maximum Direction Study

ASCE/SEI 7-10 (ASCE, 2010), in contrast with its predecessor (ASCE/SEI 7-05), uses the maximum component of ground motion as the basis of design. In this research, the recorded response of the building is used directly to determine the maximum response and the maximum

response direction. The maximum response direction is taken as the orientation of the largest vector from the origin to any point on the response orbital. For example, see Figure 10b where the orientation of maximum response is controlled by the blue circle. After rotating to the maximum direction, all response quantities of interest are recomputed for the maximum direction study. Therefore, the maximum direction study is similar to the methodologies explained previously, only performed in a rotated coordinate system.

The original, unrotated interaction studies recognize that most buildings have a set of axes defined based on their geometry. Even though these axes neglect any influence of ground motion, they are used in the unrotated interaction studies for consistency with the state of engineering practice in regards to the direction of loading provisions in ASCE/SEI 7-10 (ASCE, 2010). The maximum direction study instead recognizes that the building response is the product of both the ground motion and the building characteristics. It therefore attempts to capture the intent of ASCE/SEI 7-10 that the 100% component of the 100%+XX% criteria be based on the maximum response direction, although it only achieves this for one of the two directions.

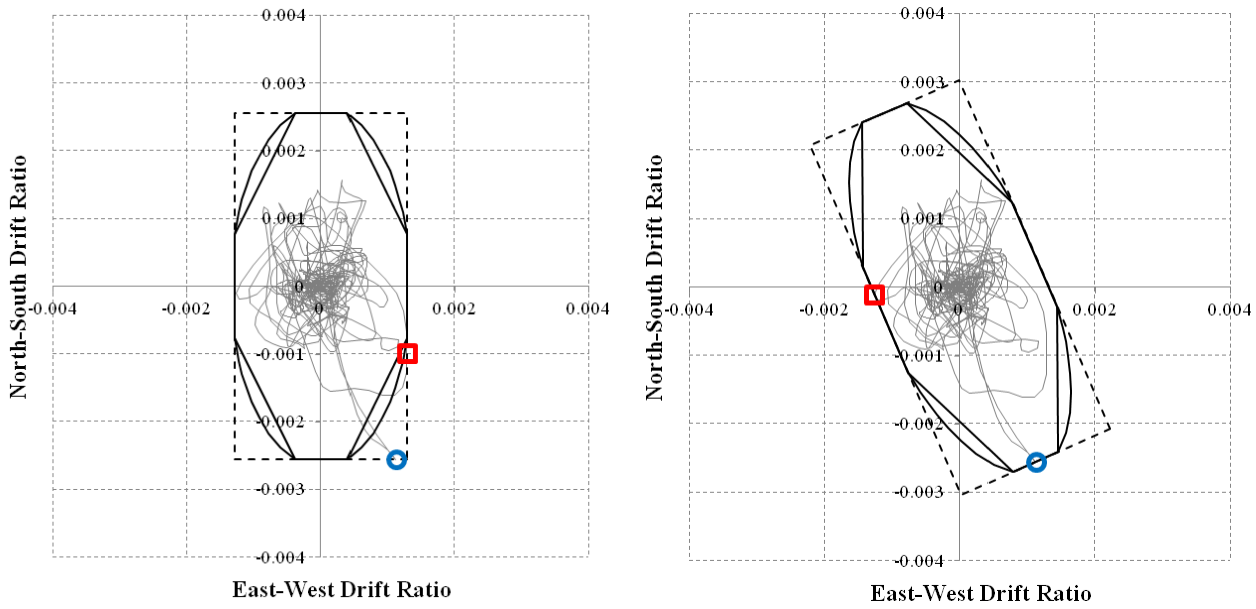

Figure 10. Comparison of (a) unrotated versus (b) rotated-to-maximum direction study. Example shown is for sensor-to-sensor drift ratio for Station 24385, 1994 Northridge Earthquake, Sensor Combination [11, 4] and [10, 2], and XX = 0.3.

Equal Interaction Study

The equal interaction study recalculates the response quantities of interest for the original, unrotated octagon interaction and truncated ellipse interaction studies but uses an equal interaction interpolation that has the same dimension in both the East-West and North-South directions. This dimension is taken as the largest of $|EW_{max}|$ and $|NS_{max}|$. For comparison, the octagon interaction and truncated ellipse interaction studies explained earlier used unequal interaction with an East-West dimension based on $|EW_{max}|$ and a North-South dimension based on $|NS_{max}|$. Once the new, equal interaction is constructed, the response quantities of interest are

computed similarly to that described previously. See Figure 11 for a comparison of equal versus unequal interaction.

The equal interaction study is pursued in addition to the unequal interaction study because both ASCE/SEI 7-10 (ASCE, 2010) and the derivation in Rosenblueth and Contreras (1977) assume equal earthquake response spectra in both directions. As noted previously, the recorded building response does not necessarily result from equal earthquake demand in both directions for every station-earthquake-sensor combination. Therefore, the construction of an equal interaction interpolation may not be suitable when considering response from unequal earthquake demand. Additionally, it may not be suitable to construct an equal interaction interpolation when a building is composed of different lateral force-resisting systems in each direction (e.g., moment frame in the x-direction and braced frame in the y-direction) because the response in each direction will be different even if the earthquake demands were equal.

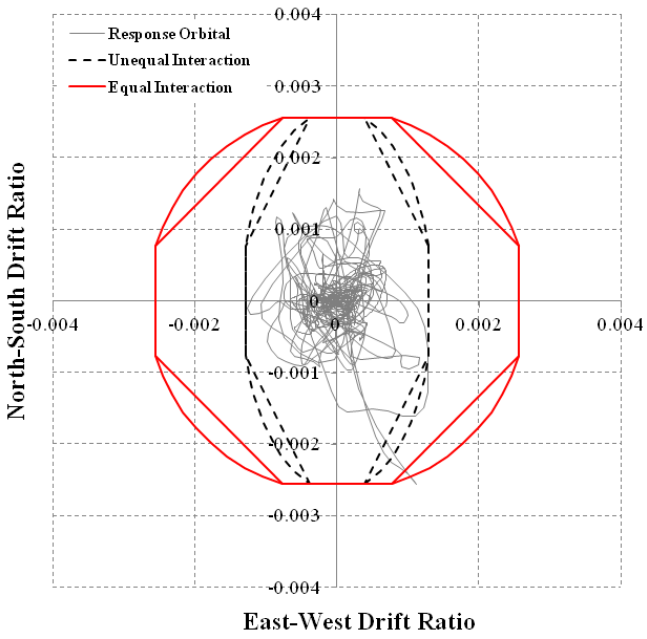

Figure 11. Comparison of unequal versus equal interaction for sensor-to-sensor drift ratio for Station 24385, 1994 Northridge Earthquake, Sensor Combination [11, 4] and [10, 2], and XX = 0.3.

Evaluation Methods

There are several evaluation methods pursued in this research. The evaluation methods operate on the parameters of interest (i.e., α, RLR_{max} and Z_{crit}) after assembling the parameters of interest for all station-earthquake-sensor combinations.

The evaluation method applicable for the orthogonal ratio study is the probability of non-exceedance, computed in accordance with Equation 4. The parameter α is calculated using Equation 3 for each station-earthquake-sensor combination and XX is the component of the selected 100%+XX% criterion. The probability of non-exceedance is therefore equivalent to the probability that α will be less than a selected XX for any given station-earthquake-sensor

combination. By performing the calculation in Equation 4 for each value of XX ranging from 0 to 1.0, a probability of non-exceedance curve can be constructed. See Figure 12 for an example curve of the entire database for sensor-to-sensor drift ratio.

$$Probability\ of\ Non-Exceedance =$$

$$P(\alpha \leq XX) = \frac{\#\ of\ "station-earthquake-sensor\ combinations"\ for\ which\ \alpha \leq XX}{total\ \#\ of\ "station-earthquake-sensor\ combinations"}$$

Equation 4

The probability of non-exceedance is also an evaluation method used for the octagon interaction and truncated ellipse interaction studies. In this case, however, the probability of non-exceedance is computed via Equation 5. RLR_{max} is the maximum response limit ratio for each station-earthquake-sensor combination with the limit taken in accordance with the octagon interaction or truncated ellipse interaction interpolations for a chosen 100%+XX% criterion. RLR_{max} equals 1.0 when the response and limit are equal. The probability of non-exceedance is therefore equivalent to the probability that RLR_{max} will be less than or equal to 1.0 for any given station-earthquake-sensor combination. By performing the calculation in Equation 5 for each value of XX ranging from 0 to 1.0, a probability of non-exceedance curve can be constructed. See Figure 13 for example curves of the entire database for sensor-to-sensor drift ratio.

$$Probability\ of\ Non-Exceedance =$$

$$P(RLR_{max} \leq 1.0) = \frac{\#\ of\ "station-earthquake-sensor\ combinations"\ for\ which\ RLR_{max} \leq 1.0}{total\ \#\ of\ "station-earthquake-sensor\ combinations"}$$

Equation 5

The probability that Z_{crit} for a given station-earthquake-sensor combination will be less than or equal to each of the four zones defined in Figure 9 is another evaluation method. It is computed via Equation 6. Z_{crit} is the value of the highest zone for any point on the response orbital for a given station-earthquake-sensor combination and 100%+XX% criterion. By performing the calculation in Equation 6 for each value of XX ranging from 0 to 1.0, a probability curve can be constructed. See Figures 14 through 16 for example curves of the entire database for sensor-to-sensor drift ratio. Note that the probability for this evaluation method is expressed as the probability that Z_{crit} is less than or equal to the selected zone (i.e., not that Z_{crit} is equal to the selected zone). To calculate the probability that Z_{crit} is equal to the selected zone, Equation 7 can used. For example, the probability that Z_{crit} is equal to Zone 3 would be the probability that Z_{crit} is less than or equal to Zone 3 minus the probability that Z_{crit} is less than or equal to Zone 2.

$$P(Z_{crit} \leq zone) = \frac{\#\ of\ "station-earthquake-sensor\ combinations"\ for\ which\ Z_{crit} \leq zone}{total\ \#\ of\ "station-earthquake-sensor\ combinations"}$$

Equation 6

$$P(Z_{crit} = zone) = P(Z_{crit} \leq zone) - P(Z_{crit} \leq zone - 1)$$ Equation 7

Results

Orthogonal Ratio, Octagon Interaction and Truncated Ellipse Interaction Studies

Figure 12 presents the probability of non-exceedance curve for the orthogonal ratio study using sensor-to-sensor drift ratios. Similar figures exist for sensor-to-ground drift ratio and absolute acceleration but are excluded here for brevity. Several arrows are drawn that intersect the probability of non-exceedance curve. These identify (1) the probability of non-exceedance given a 100%+30% criterion, (2) the 100%+XX% criterion corresponding to a probability of non-exceedance of 50%, and (3) the 100%+XX% criterion corresponding to a probability of non-exceedance of 84%. Probabilities of non-exceedance of 50% and 84% were selected because they represent the mean and mean plus one standard deviation of a normally distributed random variable. The use of these probabilities does not imply that the underlying data fits a normal distribution, however.

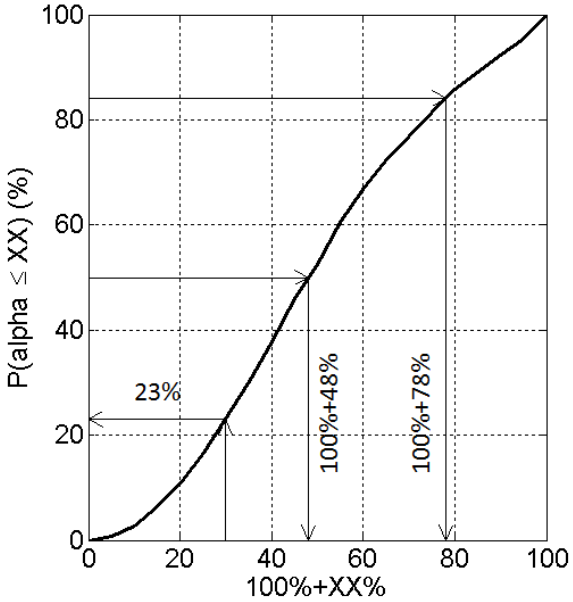

Figure 12. Probability of non-exceedance curve of the orthogonal ratio study using the entire database of sensor-to-sensor drift ratios.

Figure 13a and Figure 13b present the probability of non-exceedance curves for the octagon and truncated ellipse interaction studies, respectively, using sensor-to-sensor drift ratio. Similar figures exist for sensor-to-ground drift ratio and absolute acceleration but are excluded here for brevity. Similar to the results of the orthogonal ratio study, several arrows which intersect the probability of non-exceedance curves at critical points are drawn.

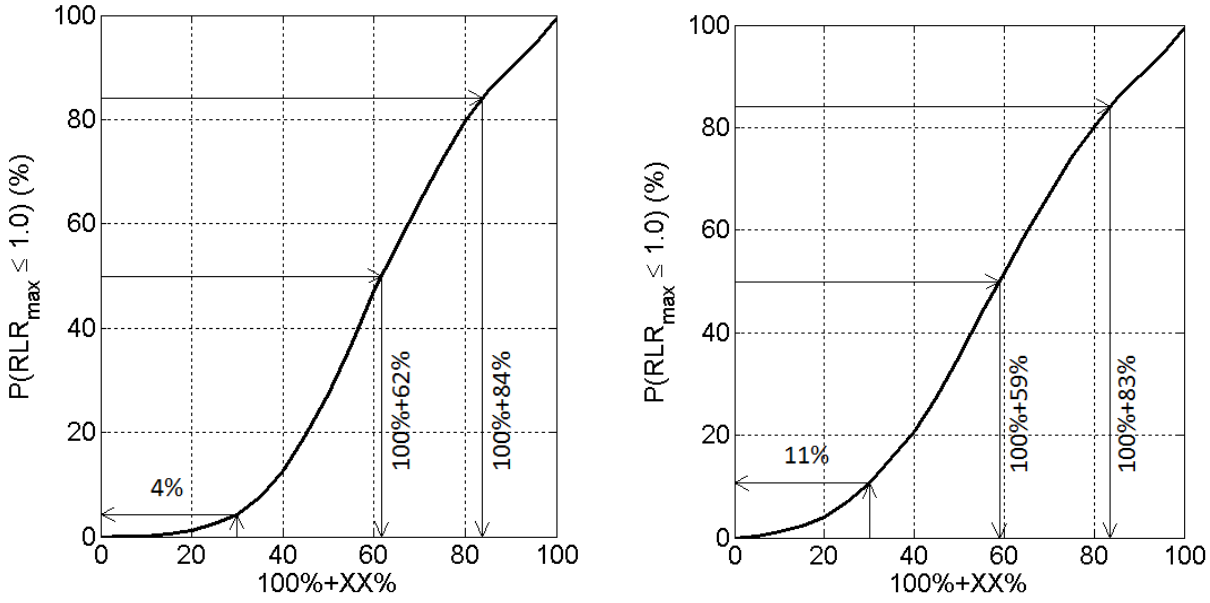

Figure 13. Probability of non-exceedance curves for the (a) octagon and (b) truncated ellipse interaction studies using the entire database of sensor-to-sensor drift ratios.

Tables 1 through 4 present the three critical points described above which intersect the probability of non-exceedance curves and include sensor-to-ground drift ratio and absolute acceleration as well as sensor-to-sensor drift ratio. The results from all response types are fairly consistent both in magnitude (e.g., the 50% probability of non-exceedance corresponds to approximately a 100%+60% criterion for all response types for the octagon interaction study) and in trend (e.g., for all response types, the orthogonal ratio study generally produces the highest probability of non-exceedance followed by the truncated ellipse interaction study and lastly by the octagon interaction study). Furthermore, they all show very low probabilities of non-exceedance (i.e., the data is not adequately bounded) for a 100%+30% criterion.

Table 1. 100%+XX% criterion necessary to satisfy given probabilities of non-exceedance for sensor-to-sensor drift ratio

Probability of Non-Exceedance	Orthogonal Ratio Study	Octagon Study	Truncated Ellipse Study
50%	100%+48%	100%+62%	100%+59%
84%	100%+78%	100%+84%	100%+83%

Table 2. 100%+XX% criterion necessary to satisfy given probabilities of non-exceedance for sensor-to-ground drift ratio

Probability of Non-Exceedance	Orthogonal Ratio Study	Octagon Study	Truncated Ellipse Study
50%	100%+47%	100%+62%	100%+59%
84%	100%+78%	100%+83%	100%+83%

Table 3. 100%+XX% criterion necessary to satisfy given probabilities of non-exceedance for absolute accelerations

Probability of Non-Exceedance	Orthogonal Ratio Study	Octagon Study	Truncated Ellipse Study
50%	100%+44%	100%+58%	100%+55%
84%	100%+71%	100%+78%	100%+78%

Table 4. Probability of non-exceedance given selection of a 100%+30% criterion

Response Parameter	Orthogonal Ratio Study	Octagon Study	Truncated Ellipse Study
Sensor-to-Sensor Drift Ratio	23%	4%	11%
Sensor-to-Ground Drift Ratio	23%	4%	11%
Absolute Acceleration	27%	5%	13%

Zone Study

Figures 14 through 16 present the probability that Z_{crit} will be less than or equal to a selected zone for sensor-to-sensor drift ratio. Similar figures exist for sensor-to-ground drift ratio and absolute acceleration but are excluded here for brevity. Note that Figures 14 through 16 are identical except for the arrows which intersect the probability curves. Similar to the previous studies, these arrows identify (1) the probability given a 100%+30% criterion, (2) the 100%+XX% criterion corresponding to a probability of 50%, and (3) the 100%+XX% criterion corresponding to a probability of 84%.

Probability values shown in Figure 14 are for the probability that Z_{crit} will be less than or equal to a selected zone. Equation 7 must be used if the probability that Z_{crit} is equal to a selected zone is desired. For example, in Figure 14, the probability that Z_{crit} is equal to Zone 4 is 100% - 9% = 91% while the probability that Z_{crit} is equal to Zone 3 is 9% - 4% = 5%. In Figures 15 and 16, a 100%+XX% criterion corresponding to a given probability is shown. For example, a 100%+63% criterion bounds 50% of the data in Zones 1, 2 or 3 while a 100%+77% criterion would be required to bound 50% of the data in Zone 1 only. The probability curve separating Zone 3 from Zone 4 approximately matches the probability of non-exceedance curve for the truncated ellipse interaction study while the curve separating Zone 2 from Zone 3 approximately matches that for the octagon interaction study. Refer to full report on this research for further explanation on the similarity between the probability curves in the zone study as compared to the octagon and interaction studies (Zimmerman et al., in preparation).

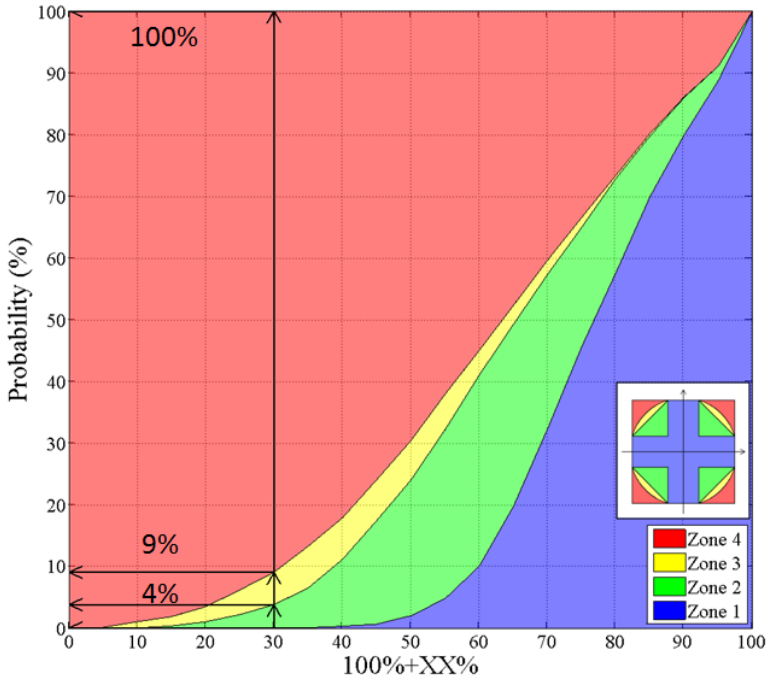

Figure 14. Probability that Z_{crit} for a given station-earthquake-sensor combination will be less than or equal to each of the zones for the entire database of sensor-to-sensor drift ratios. Probabilities specifically indicated are for a 100%+30% criterion. The probability that Z_{crit} is in Zone 1 is too small to show and has therefore been left off the figure.

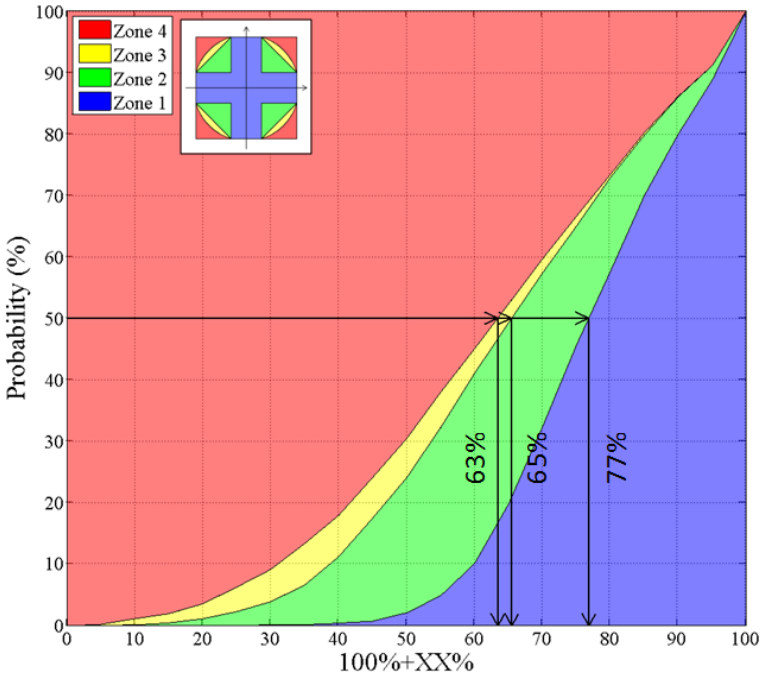

Figure 15. Probability that Z_{crit} for a given station-earthquake-sensor combination will be less than or equal to each of the zones for the entire database of sensor-to-sensor drift ratios. The 100%+XX% criteria necessary to bound 50% of the data is indicated.

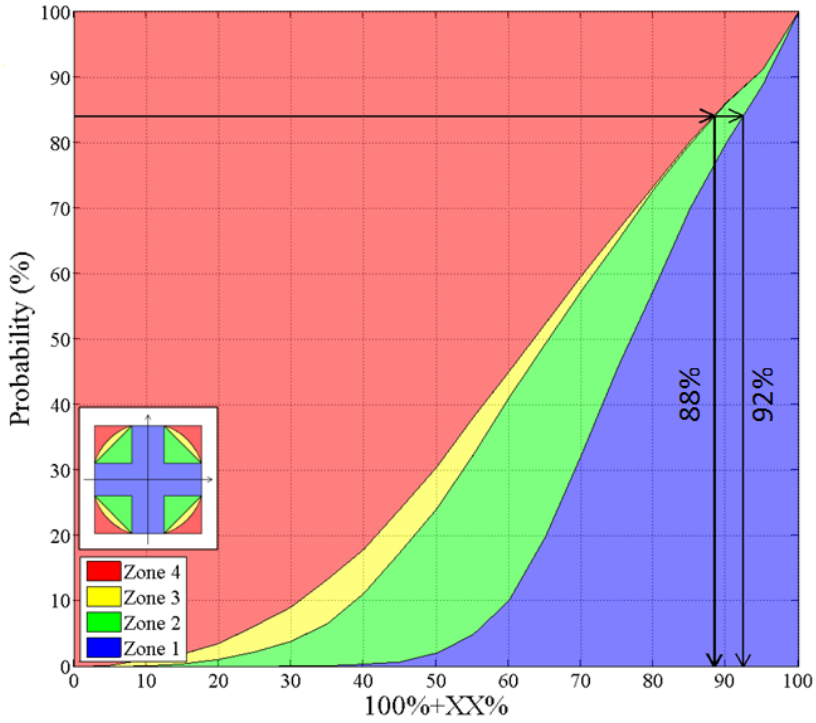

Figure 16. Probability that Z_{crit} for a given station-earthquake-sensor combination will be less than or equal to each of the zones for the entire database of sensor-to-sensor drift ratios. The 100%+XX% criteria necessary to bound 84% of the data is indicated.

Maximum Direction Study

Figure 17 and Figure 18 present the probability of non-exceedance curves for the orthogonal ratio and interaction studies, respectively, considering both unrotated and rotated-to-maximum-direction methodologies using sensor-to-sensor drift ratios. Similar figures exist for sensor-to-ground drift ratio and absolute acceleration but are excluded here for brevity. The unrotated probability of non-exceedance curves are identical to those shown in Figures 12 and 13. The probabilities of non-exceedance for the maximum direction study are significantly greater than those for the unrotated studies. This indicates that when the studies are performed in a coordinate system rotated to align with the maximum direction of response, more of the data are bounded for a given 100%+XX% criterion.

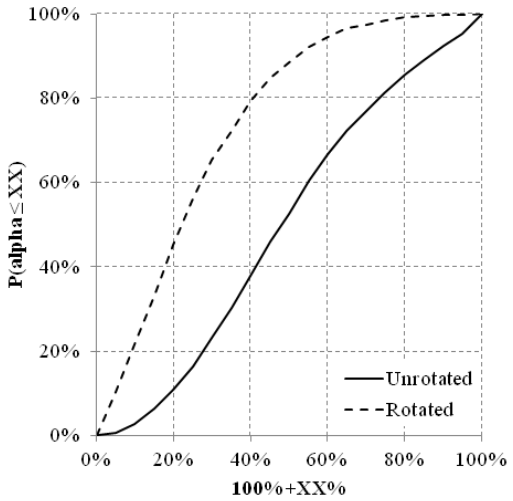

Figure 17. Comparison of unrotated versus rotated-to-maximum-direction probability of non-exceedance curves for the orthogonal ratio study using sensor-to-sensor drift ratio.

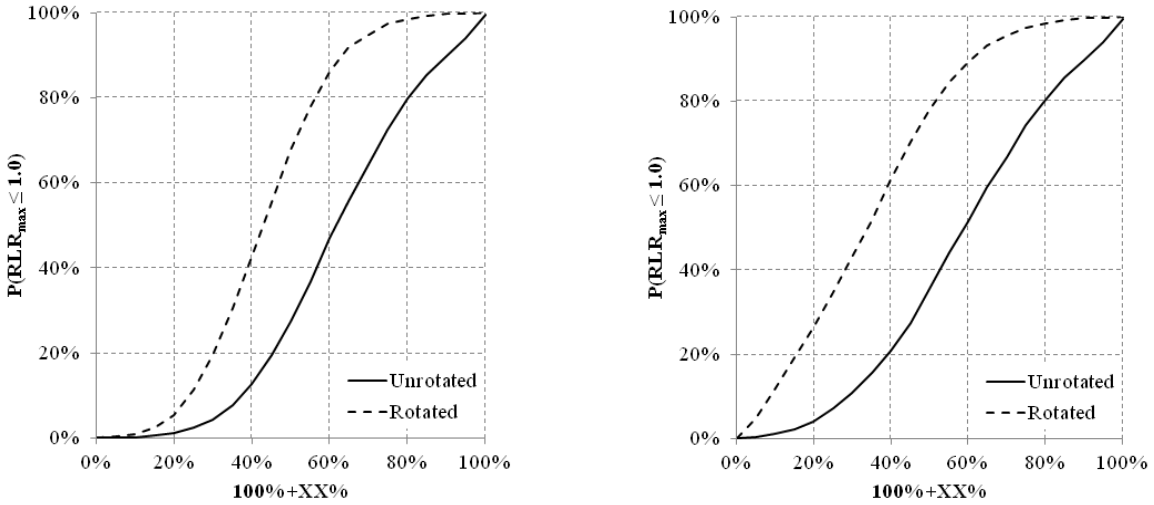

Figure 18. Comparison of un-rotated versus rotated-to-maximum-direction probability of non-exceedance curves for the (a) octagon interaction and (b) truncated ellipse interaction studies using sensor-to-sensor drift ratio.

Equal Interaction Study

Figure 19 presents the probability of non-exceedance curves considering both the original, unequal interaction and equal interaction interpolations. Similar figures exist for sensor-to-ground drift ratio and absolute acceleration but are excluded here for brevity. The probability of non-exceedance curves for unequal interaction are identical to those shown in Figure 13. The probabilities of non-exceedance for equal interaction are significantly greater than the results for unequal interaction. This indicates that when the studies are performed using an equal interaction interpolation, more of the data are bounded for a given 100%+XX% criterion.

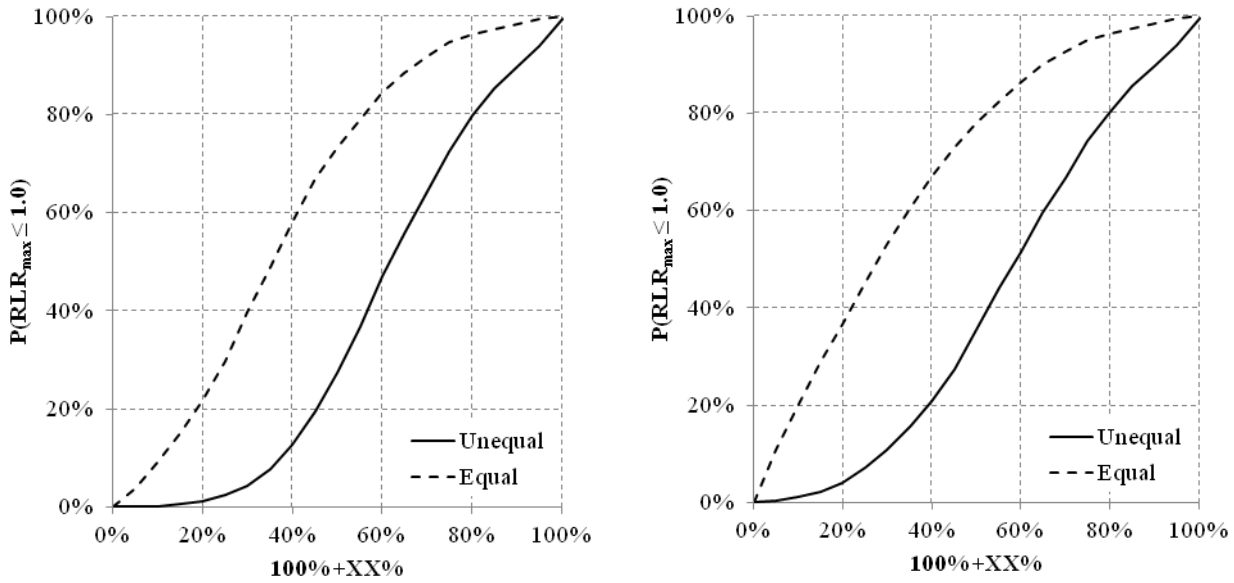

Figure 19. Comparison of probability of non-exceedance curves for equal versus unequal interaction for the (a) octagon interaction and (b) truncated ellipse interaction studies using sensor-to-sensor drift ratio.

Conclusions

Based on results from several evaluation methodologies, response types and a sufficiently populated database obtained from the Center for Engineering Strong Motion Data (CESMD, 2015), the following conclusions are made:

- The 100%+30% criterion, as applied to the response of instrumented buildings during real earthquakes, does not adequately bound the recorded data using all three evaluation methodologies considered in this research (i.e., orthogonal ratio, octagon interaction and truncated ellipse interaction) assuming an unrotated, unequal interaction. To bound 50% and 84% of the data, 100%+60% and 100%+80% criteria, respectively, would be needed.
- The 100%+XX% criterion is fairly insensitive to the three response types used in this research (i.e., sensor-to-sensor drift ratio, sensor-to-ground drift ratio and absolute acceleration).
- Use of the maximum direction of response significantly reduces the estimation of conservatism of the 100%+30% criterion as compared to when the building axes are used. However, it still generally predicts that a 100%+30% criterion does not adequately bound the recorded data. To bound 50% and 84% of the data, 100%+40% and 100%+55% criteria, respectively, would be needed.
- Use of an equal interaction construction significantly reduces the estimation of conservatism of a 100%+30% criterion as compared to the unequal interaction pursued in all other studies. It predicts that the 100%+30% is slightly inadequate in bounding 50% of the recorded data. To bound 50% and 84% of the data, 100%+35% and 100%+60% criteria, respectively, would be needed.

While the conclusions of this research generally find that a 100%+30% criterion does not adequately bound the data, further research is necessary to understand the implications of these findings on the direction of loading provisions in ASCE/SEI 7-10 (ASCE, 2010) and to determine whether revisions are warranted.

Acknowledgements

This paper was developed under research funded by the California Department of Conservation, California Geological Survey, Strong Motion Instrumentation Program, Contract 1012-957. However, the contents do not necessarily represent the policy of that agency nor endorsement by the State Government.

The authors are grateful to Anthony Shakal and Moh Huang of the Strong Motion Instrumentation Program (SMIP) for their assistance and advice during the project, and to the recommendations and comments provided by members of the SMIP Building Subcommittee of the Strong Motion Instrumentation Advisory Committee. Building Subcommittee members included Farzad Naiem, Lucie Fougner, Donald Jephcott, Ifa Kashefi, David Leung, Eduardo Miranda, John Robb, Dan Shapiro, Chris Tokas, and Chia-Ming Uang.

References

ASCE (2010). *Minimum Design Loads for Buildings and Other Structures, ASCE/SEI 7-10*. American Society of Civil Engineers, Reston, Virginia.

Bisadi, V., and Head, M., (2011). "Evaluation of Combination Rules for Orthogonal Seismic Demands in Nonlinear Time History Analysis of Bridges," *Journal of Bridge Engineering, Special Issue: AASHTO-LRFD Bridge Design and Guide Specifications: Recent, Ongoing, and Future Refinements*, p711-717.

"Center for Engineering Strong Motion Data (CESMD)," *strongmotioncenter.org*, Accessed October 14, 2015.

Cimellaro, G., Giovine, T. and Lopez-Garcia, D. (2014). "Bidirectional Pushover Analysis of Irregular Structures," *Journal of Structural Engineering*, Vol. 140, No. 9, 04014059.

FEMA (2009). *Quantification of Building Seismic Performance Factors, FEMA P695*. Federal Emergency Management Agency, Washington, D.C.

Hernandez, J. J. and Lopez, O. A., (2002). "Response to Three-Component Seismic Motion of Arbitrary Direction," *Earthquake Engineering and Structural Dynamics*, Vol. 31, p55-77.

Lopez, O. A., Chopra, A. K. and Hernandez, J. J., (2001). "Evaluation of Combination Rules for Maximum Response Calculation in Multicomponent Seismic Analysis," *Earthquake Engineering and Structural Dynamics*, Vol. 30, p1379-1398.

MacRae, G. and Mattheis, J., (2000). "Three-Dimensional Steel Building Response to Near-Fault Motions," *Journal of Structural Engineering*, Vol. 126, Issue 1, p117-126.

MacRae, G. A. and Tagawa, H., (2001). "Seismic Behavior of 3D Steel Moment Frame with Biaxial Columns," *Journal of Structural Engineering*, Vol. 127, No. 5, p490-497.

Menun, C. and Der Kiureghian, A., (1998). "A Replacement for the 30%, 40% and SRSS Rules for Multicomponent Seismic Analysis," *Earthquake Spectra*, Vol. 14, No. 1, p153-163.

Newmark, N.M., (1975). "Seismic Design Criteria for Structures and Facilities - Trans-Alaska Pipeline System," *Proceedings of the U.S. National Conference on Earthquake Engineering*, Ann Arbor, USA, p94-103.

Rosenblueth, E. and Contreras, H. (1977). "Approximate Design for Multicomponent Earthquakes," *Journal of the Engineering Mechanics Division*, Proceedings of ASCE, Vol. 103, No. EM5, p 881-893.

Sherman, J. and Okazaki, T., (2010). "Bidirectional Loading Behavior of Buckling-Restrained Braced Frames," *Proceedings of ASCE Structures Congress 2010*, Orlando, Florida.

Zaghlool, B. S., Carr, A. J. and Moss, P. J., (2001). "Inelastic Behavior of Three-Dimensional Structures under Concurrent Seismic Excitations," *Proceedings of 12th World Conference on Earthquake Engineering*, EQC, Auckland, New Zealand.

Zimmerman, R. B., Lizundia, B. and Fathali, S., (2014). "Studying Direction of Loading Provisions in Modern Codes: Research Motivation and Literature Review," *Proceedings of the 2014 Strong Motion Instrumentation Program (SMIP14) Seminar*, Berkeley, CA.

Zimmerman, R.B., Lizundia, B. and Fathali, S., (in preparation). *Evaluation of ASCE/SEI 7 Direction of Loading Provisions Using Strong Ground Motion Records*, Report prepared for the California Strong Motion Instrumentation Program, Data Interpretation Project, Agreement 1012-957.

ELASTIC FORCE DEMANDS FROM BI-DIRECTIONAL EXCITATION

Dionisio Bernal

Civil and Environmental Engineering Department, Center for Digital Signal Processing, Northeastern University, Boston, MA

Abstract

When the design response spectra for the two horizontal components of motion are of equal intensity the expectation of the peak seismic demand is given by the SRSS combination of the uni-directional responses. The variance of this response depends, however, on the probability densities of the cross-correlations and thus the upper bounds on the ratios of response to design level in elements that have important contributions from both loading directions are larger than in those dominated by uni-directional motion. This paper operates on the premise that it is desirable to equalize these bounds and attempts to do so by specifying the cross-correlations at a probability of exceedance that attains the objective. Derivation of the *pdf* of the cross correlation is required and is found that for closely spaced frequencies it is well approximated by the *pdf* of the unlagged coherency times the standard correlation coefficient. The *pdf* of the unlagged coherency, in turn, is shown to be well approximated by a shifted and scaled beta distribution with parameters $\alpha = \beta = 2.55$. It is shown that when the results obtained are translated into the 100%+X% combinations rule the consistent value of X is sixty.

Introduction

Combination of modal responses to a uni-directional input is a classical subject in earthquake engineering. The SRSS rule, which applies to stationary uncorrelated responses, appeared first in the Ph.D thesis of E. Rosenblueth (1951) and subsequently in a paper by Goodman, Rosenblueth and Newmark (1953). The pioneering contribution on the rules to combine correlated responses is presented in Rosenblueth and Elorduy (1969) with formulas later developed by Der Kiureghian (1979) now widely adopted under the CQC designation. This paper is concerned with the combination of modal responses to orthogonal input components with attention limited to responses to excitations in the horizontal plane. The pioneering contribution here is from Rosenblueth and Contreras (1977) who proposed, based on analytical considerations and some simplifications, the now popular 30% rule.

The combination of modal responses from multiple inputs involves cross-correlation coefficients that depend on the coherency between components and have symmetric *pdfs* when the motions are specified in so-called principal directions. A proposal that the major principal direction at a site is aligned with a line joining the epicenter with the site was made (based on the analysis of five records) by Penzien and Takizawa (1975) but this contention is not supported by results obtained here using 40 pairs of bi-directional records from the CSMIP database. What examination shows is that the directions for which the correlation between the records is zero

fluctuates notably when computed in a moving window (of 4 to 6 seconds size), suggesting that there is limited usefulness in the principal direction concept. We note that fluctuation in the computed principal directions is a byproduct of the fact that the seismic intensity in any two horizontal directions is not too dissimilar in most records, making the data "quasi-circular" and the principal orientations easily shift as a the computation window moves along. Whether justified on grounds that the spectra are equal, or in any other way, the bottom line is that seismic provisions are based on the premise that any two orthogonal directions in the horizontal plane can be treated as principal directions. From the perspective of elastic force demand computation the implication is that the cross-correlation coefficients that enter in the estimation of the expected value of the peak response are zero.

When one looks at the variance of the peak response, however, the probability density of the cross-correlation enters the picture and the relevant observation, from a design perspective, is that response quantities that are notably affected by bi-directional input may have significantly larger variance than those primarily dependent on one input component. Bounds on the limit by which demands may exceed the design estimate, therefore, are larger in bi-directional sensitive quantities than in unidirectional controlled ones. We note, for clarity, that while any element can be considered as affected by both horizontal components (since axes can be rotated at will) the opposite is not true. Namely, there are elements whose forces are significantly affected by both direction of loading for any orientation of the analysis axes. In this regard note that the typical selection of building axes can be viewed as the one that maximizes the number of response quantities that depend on one input or the other. The purpose of this paper is to determine if the mentioned increase in variance is potentially relevant in design and, if it is, to suggest ways to account for it properly.

Worth noting from the outset is the fact that the *pdf* of correlations and cross correlations are affected differently by the eigenvalue gap. In particular, as two eigenvalues approach each other the correlation between the modal responses approaches unity and, as a consequence, the variance of the realizations approaches zero. The variance of the correlation between closely space modes is, therefore, small. In contrast, in the cross-correlation case the expected value of the distribution is near zero, independent of the frequency ratio, but the variance increases as modal separation decreases. In this paper we pursue consideration of the high variance issue by specifying the cross correlation coefficients at a probability of exceedance smaller than the mean.

An outline of the paper is as follows: it is first shown that for zero eigenvalue gap the *pdf* of the cross correlation is well approximated by the *pdf* of the unlagged coherency and a model for this function is derived using results from a large ensemble of synthetic bi-directional records generated using the Rezaeian Der Kiureghian (2012) ground motion model. Reduction of the cross correlation with frequency separation is shown to be much slower than that of the correlation and it is argued that this results from the difference between the Power Spectral Density (PSD) , which is real and determines correlations, and the coherency, which is complex and determines cross correlations. An explicit formula for reduction of the cross-correlation with frequency gap, however, is not presented. The analytical part of the paper closes with an analysis that translates the results obtained into the 100 +X% rule and a brief concluding section closes the paper.

Principal Ground Motion Directions

The subject of principal directions shows up when bi-directional excitation is considered because these directions specify the orientation for which the coherency between the orthogonal components is zero. Equivalently, the principal directions are also the directions for which the empirical covariance is diagonal. Namely, if $\ddot{\ddot{X}} \in R^{3xN}$ is a matrix that lists the ground motion at a point in any three orthogonal directions and $\ddot{X}_{(n_1,n_2)} = \ddot{\ddot{X}}(:, n_1 : n_2)$ where n1 and n2 are indices selected to clip and internal portion, the empirical covariance for the clipped segment is

$$Q_{(n_1,n_2)} = \frac{1}{n_2 - n_1 + 1} X_{(n_1,n_2)} \cdot X^T_{(n_1,n_2)} \tag{1}$$

where N is the total number of time stations. Analysis shows that one of the principal directions is vertical (or nearly so) so the other two are in the horizontal plane. The first to indicate that principal directions could be defined for seismic records was A. Arias (1970), although reference to the matter is typically misplaced to a publication by Penzien and Watanabe (1975) who apparently were unware of Arias work at the time of writing. Arias did not pursue the principal directions topic but Penzien and Watanabe (1975) made the claim that these directions are reasonably stationary during the strong motion and are approximately aligned with a line connecting the epicenter with the site. Although several writers have used this model (Yeh and Wen 1990; Kubo and Penzien 1979; Heredia-Zavoni and Machicao-Barrionuevo 2004; Menun and Der Kiureghian 1998a, 1998b, 2000; Rezaeian and Der Kiureghian 2010, 2012) confirmation of these claims could not be found in the literature and an examination carried out here using 40 bi-directional records did not support either contention. As noted first in the introduction, the lack of stationarity is easily rationalized by recognizing that principal directions are the axes of an ellipse that essentially contains the data considered and since the dimensions of the ellipse principal axis are not too different, rotations are easily realized. Fig.1 plots data for a 4 sec window during the strong motion at CSMIP station 14311 during the Whittier earthquake and shows the quasi-circular nature of the data while Fig.2 shows the rotation of the axes in two nearby windows.

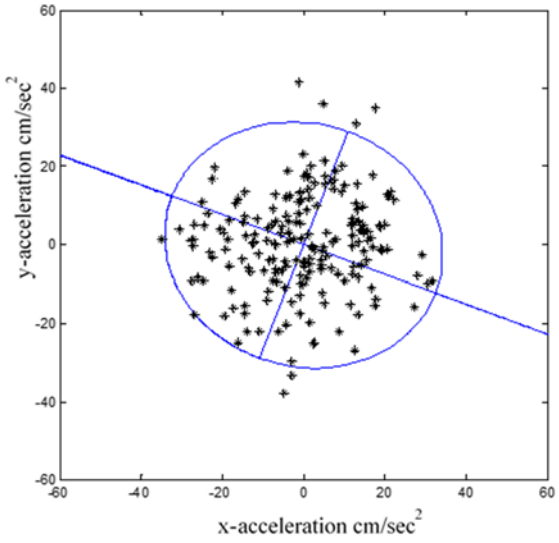

Fig.1. Accelerations, principal directions and inscribing ellipse for the first 4 sec window in the strong motion defined using the $t_{0.9}$ Arias Intensity.

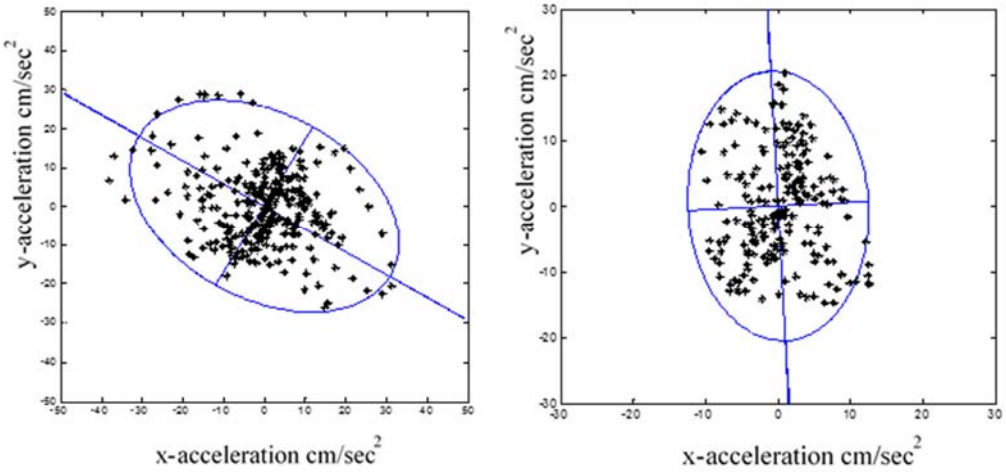

Fig.2. Accelerations, principal directions and inscribing ellipses a) window from 6-10 sec b) window from 12-16 sec (same records as Fig.1)

Directivity

A convenient parameter to characterize the shape of the "best fit" ellipse, which we define here as "directivity", is

$$\gamma = 1 - \sqrt{\frac{s_2}{s_1}} \tag{2}$$

where s_1, and s_2 are the largest and the smallest singular values of the empirical covariance. For a circular shape $\gamma = 0$ and for highly elongated shapes γ approaches 1. The term directivity is also used as a qualitative term to indicate the focusing of wave energy along the fault in the direction of rupture but risk of confusion with the quantitative term in eq.2 does not appear significant. Directivities computed for 40 bidirectional ground motions taken from the CSMIP site proved to have a mean of about 0.3 (Gali, 2015), indicating (again) that the "principal directions" are unlikely to be stationary, some examples of the evolution of the mayor principal direction computed on a 4 second moving window are depicted in Fig.3. We close this section by noting that although the literature is replete with papers that use the concept of ground motion principal directions there is also wide spread recognition that it is reasonable to assume that the motion in any two orthogonal horizontal directions can be treated as uncorrelated, i.e., that any two orthogonal directions in the horizontal plane can be treated as principal.

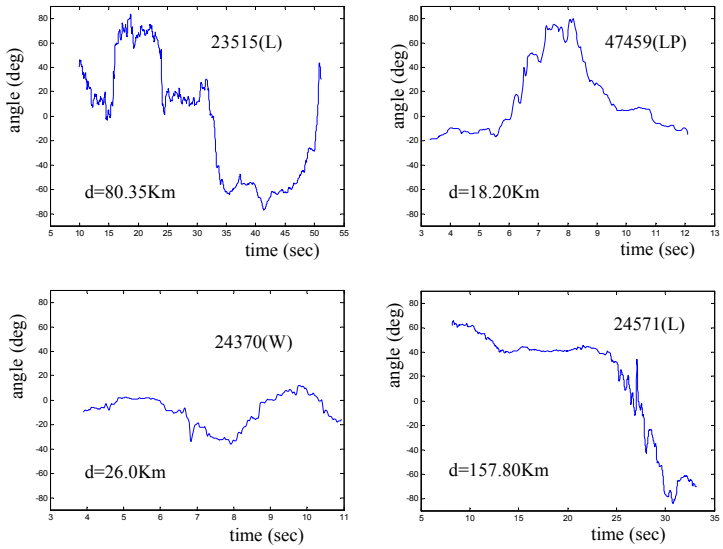

Fig.3. Evolution of major principal direction for four CSMIP stations -distances are from the site to the epicenter and letter in parenthesis designates the earthquake.

Cross-Correlation between Modal Responses

The cross-correlation coefficient between the responses of two modes, *i* and *j* to ground motion components k and ℓ is the expected value of a distribution and writes (Der Kiureghian and Neuhoffer 1991)

$$\rho_{s_{ki},s_{\ell j}} = \frac{1}{\sigma_{ski}\sigma_{s\ell j}} \int_{-\infty}^{\infty} h_i(\omega)\cdot h_j(-\omega)\cdot g_{k,\ell}(\omega)\cdot d\omega \tag{3}$$

with

$$\sigma^2_{s_{a,b}} = \int_{-\infty}^{\infty} h_b(\omega)\cdot h_b(-\omega)\cdot g_{\mathrm{a,a}}(\omega)\cdot d\omega \quad with \quad a=k,\ell \quad b=i,j \tag{4}$$

where $h_b(\omega)$ is the relative displacement transfer function

$$h_b(\omega) = \frac{1}{(\bar{\omega}_b^2 - \omega^2) + 2\bar{\omega}_b\omega\xi_b i} \tag{5}$$

with $\bar{\omega}_b, \xi_b$ as the undamped natural frequency and modal damping ratio and $g_{k,\ell}(\omega)$ is the cross spectral density (CSD) between the *k* and the ℓ excitation components. This last function is the Fourier transform of the cross correlation between the signals and thus

$$g_{k,\ell}(\omega) = \int_{-\infty}^{\infty} g_{k,\ell}(\tau)\cdot e^{-i\omega\tau} d\tau \tag{6}$$

where

$$g_{k,\ell}(\tau) = E\left(\ddot{u}_k(t) \cdot \ddot{u}_\ell(t+\tau)\right) \tag{7}$$

The CSD is typically specified in terms of the coherency function, $\gamma_{k,\ell}(\omega)$ and the PSD functions as

$$g_{k,\ell}(\omega) = \gamma_{k,\ell}(\omega) \cdot \sqrt{g_{k,k}(\omega) \cdot g_{\ell,\ell}(\omega)} \tag{8}$$

Assuming that the PSD functions for both components are equal and vary slowly with frequency one can treat them as a constant without incurring undue error and one can write

$$\rho_{s_{ki}, s_{\ell j}} = \int_{-\infty}^{\infty} \overline{h}_i(\omega) \cdot \overline{h}_j(-\omega) \cdot \gamma_{k,\ell}(\omega) \cdot d\omega \tag{9}$$

where the transfer functions have been normalized such that

$$\int_{-\infty}^{\infty} \left|h_b(\omega)\right|^2 d\omega = 1 \quad for \quad b = i, j \tag{10}$$

Realizations

Let a pair of bi-directional components be referred to by the index q and let the coherency function for a given pair be $z_q(\omega)$. The realized value of the cross correlation is then

$$p_q = \int_{-\infty}^{\infty} \overline{h}_i(\omega) \cdot \overline{h}_j(-\omega) \cdot z_q(\omega) \cdot d\omega \tag{11}$$

and it follows that eq.3 is the mean of the realizations given by eq.11. If one performs a Monte Carlo study that generates values of p_q the distribution of this random variable can be estimated and used to specify the cross correlation at whatever probability of being exceeded one selects.

Zero Eigenvalue Gap

In this case eq.11 reduces to

$$p_q = \int_{-\infty}^{\infty} \left|\overline{h}_i(\omega)\right|^2 \cdot z_q(\omega) \cdot d\omega \tag{12}$$

and if the damping is low, as is typically the case, and the real part of the function $z_q(\omega)$, known as the unlagged coherency, is reasonably flat in the vicinity of the natural frequency, then with good approximation one has

$$p_q \cong \Re\left(z_q(\overline{\omega}_b)\right) \tag{13}$$

Namely, the cross-correlation in this case is well approximated by the unlagged coherency evaluated at the undamped natural frequency of the mode.

Finite Eigenvalue Gap

The finite eigenvalue gap case is more difficult to evaluate because the product of the two transfer functions has real and imaginary parts and the real and the imaginary parts of the coherency enter the formulation. It appears, however, that for small eigenvalue gaps the cross correlation can be approximated as the value for zero gap times the CQC correlation. To illustrate assume the unlagged coherency is sufficiently flat in the region where the transfer function product has important values, one then has

$$p_q = \Re\left(z_q(\bar{\omega})\right) \cdot \int_{-\infty}^{\infty} \bar{h}_i(\omega) \cdot \bar{h}_j(-\omega) \cdot d\omega + \chi \tag{14}$$

where χ is the contribution that comes from the integration of the product of the imaginary part of the coherency times the imaginary part of the product of the transfer functions. Noting that the integral in eq.14 is the CQC correlation coefficient (Der Kiureghian 1979) one has that for values of r near unity

$$p_q \cong \Re\left(z_q(\bar{\omega})\right) \cdot \rho_{CQC} \tag{15}$$

with

$$\rho_{CQC} = \frac{8\xi^2(1+r)\cdot r^{1.5}}{\left(1-r^2\right)^2 + 4\xi^2 r\left(1+r^2\right) + 8\xi^2 r^2} \tag{16}$$

where r is the ratio of the modal frequencies.

Unlagged Coherency

Several models for the expectation of the coherency as a function of distance and frequency have been proposed and a good review can be found in Zerva and Zervas (2002). What is needed for the present application, however, is the probability distribution of the unlagged coherency for orthogonal motions at a point in the horizontal plane. For this distribution no models could be identified so it became necessary to develop one. One possibility was to work with an ensemble of real bi-directional records but we opted for synthetic motions to allow a more convenient examination of the effect of the key motion parameters.

The bi-directional ground motion model selected is the one developed in Rezaeian and Der Kiureghian (2010, 2012). This model generates synthetic earthquake-like signals by filtering white noise through a time dependent impulse response function that is modulated to incorporate the evolution of the ground motion intensity. The model has six parameters *for each direction* of motion, the Arias intensity, I_a, the Arias effective duration taken as the 5-95 interval of the

evolutionary intensity, $D_{5\text{-}95}$, the central value, and rate of change of the evolutionary frequency, ω_{mid} and ω', the critical damping ratio of the filter, ξ, and the time at which the central frequency of the impulse is realized, t_{mid}. These six parameters have probability distributions derived from data that are conditional on four parameters: the type of faulting, F, equal to zero for strike-slip and one for reverse faulting, the magnitude, $M \geq 6$, the epicentral distance R, $10 \leq R \leq 100$ (in Km) and the shear wave velocity in the top 30m V_{S30}, with $V_{s30} \geq 60 \, m/\sec$. The model considers the correlation between the parameters in the two horizontal directions by prescribing a correlation matrix derived from real data.

While derivation of a *pdf* for the unlagged coherency that is a function of all the parameters of the ground motion model is possible the level of complexity would not be useful for the purposes of specifying the cross correlation. The approach we select here is to examine how the unlagged coherency depend on each of the motion parameters individually and then, in light of the results obtained select a set of parameters for which to derive a single *pdf*.

Type of Faulting

The standard deviation of the unlagged coherency vs frequency at 40Km for V_{s30} = 500 m/sec and M = 7.5 based on 50 simulations is depicted for the two types of faulting in Fig.4. As can be seen, there is no clear indication that the unlagged coherency is larger for either type of faulting so we select the strike-slip model for specificity.

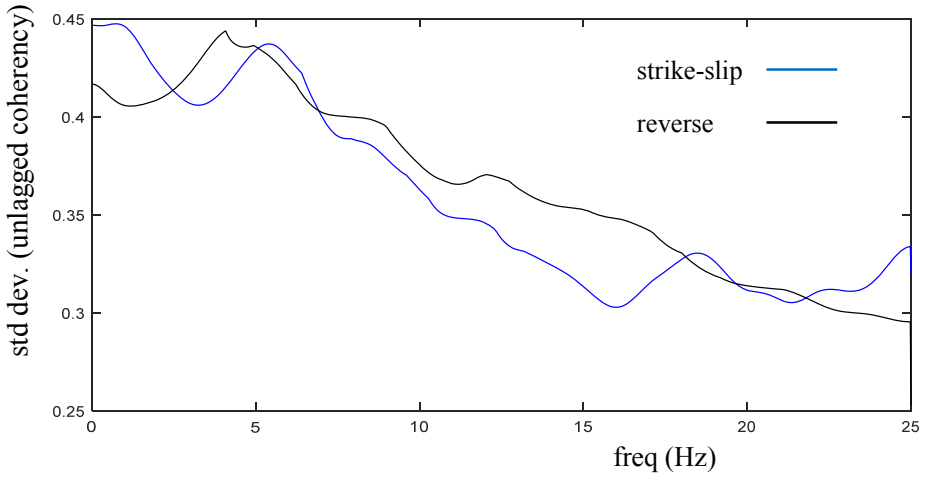

Fig.4. Standard deviation of the unlagged coherency vs frequency, M = 7.5, R = 40Km, V_{S30}=500 m/sec.

Distance to Epicenter

Plots of the standard deviation of the unlagged coherency for three different distances to the epicenter are depicted in Fig.5. The results suggest that the function decreases with distance at the higher frequencies but that in the in the most important range, i.e. up to 10Hz or so there is not much difference or a clear pattern so we take, for the Monte Carlo study, R = 40 Km.

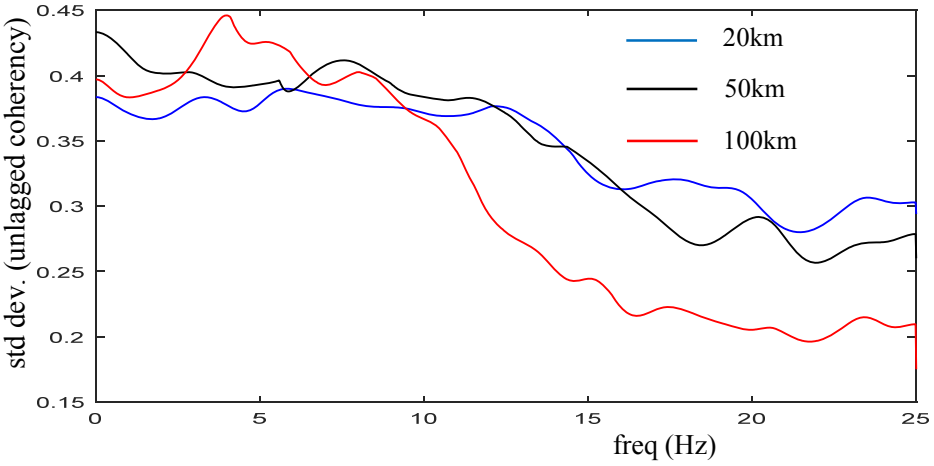

Fig.5. Standard deviation of the unlagged coherency vs frequency, M = 7.5, Strike-Slip, V_{S30}=500 m/sec.

Magnitude

Results illustrating the effect of magnitude are depicted in Fig.6. As can be seen, the curves are not ordered by magnitude in any particular pattern and for the lower frequencies the difference between the results is particularly small. In the Monte Carlo study we operate with M = 7.0.

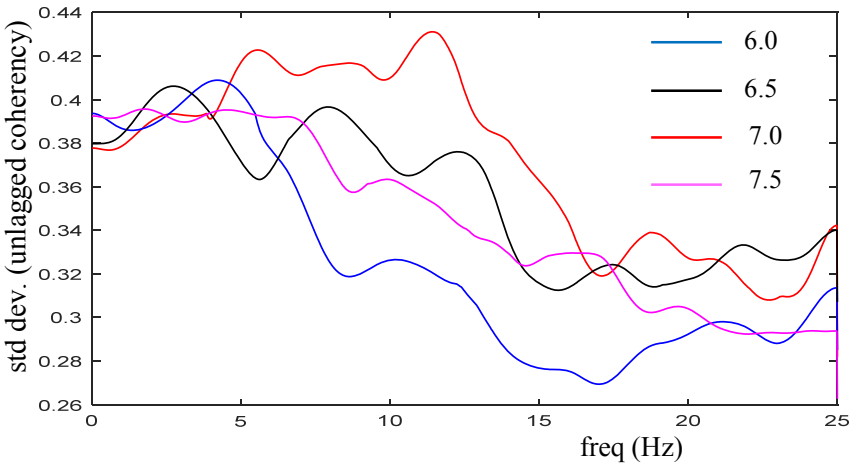

Fig.6. Standard deviation of the unlagged coherency vs frequency, R = 40 Km, Strike-Slip, V_{S30}=500 m/sec.

Shear Wave Velocity

Results plotted in Fig.7 for three values of the shear velocity, which correspond to very soft soil, dense soils and rock, show that the unlagged coherency is larger in the two stiffer soils than in the very soft one, although the difference between the dense soil and the rock situation is not systematic or significant. In the Monte Carlo study we operate with V_{S30} = 750 m/sec

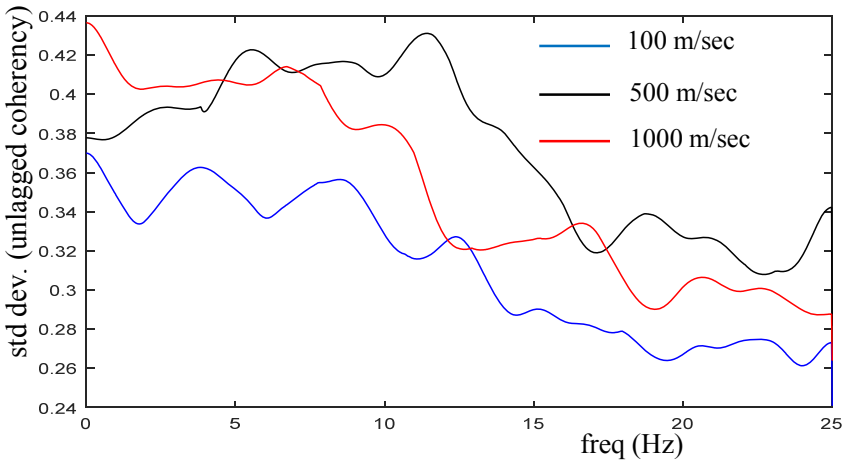

Fig.7. Standard deviation of the unlagged coherency vs frequency, R = 40 Km, Strike-Slip, M = 7.

Probability Density Estimation

On light of the results of the previous examinations we estimate the density of the unlagged coherency based on 500 simulations using the parameters {F=0, M = 7, R = 40 km, V_{S30} = 750m/sec) and plot the results in the same format used previously in Fig.8. As can be seen, the variation of the standard deviation with frequency is small.

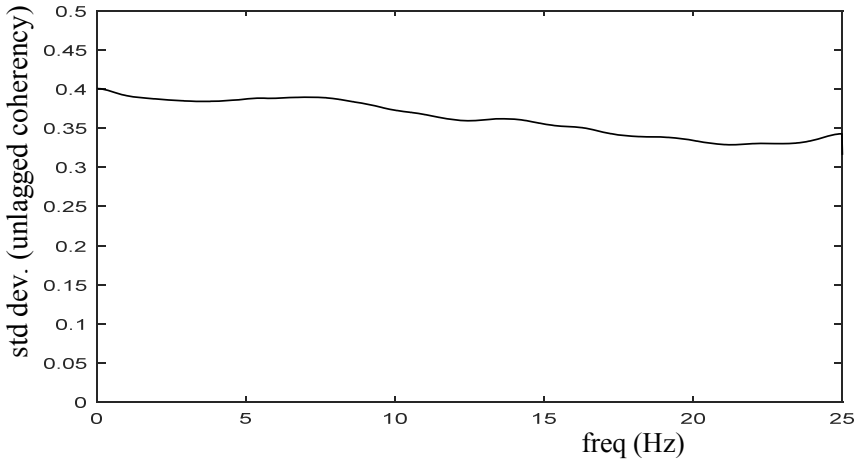

Fig.8. Standard deviation of the unlagged coherency vs frequency based on 500 simulated bi-directional records obtained for the parameters described in the text.

The normalized histograms of the unlagged coherency at three different frequencies are depicted in Fig.9 and a plot of the values at three different probability of exceedance for the full frequency range considered is depicted in Fig.10.

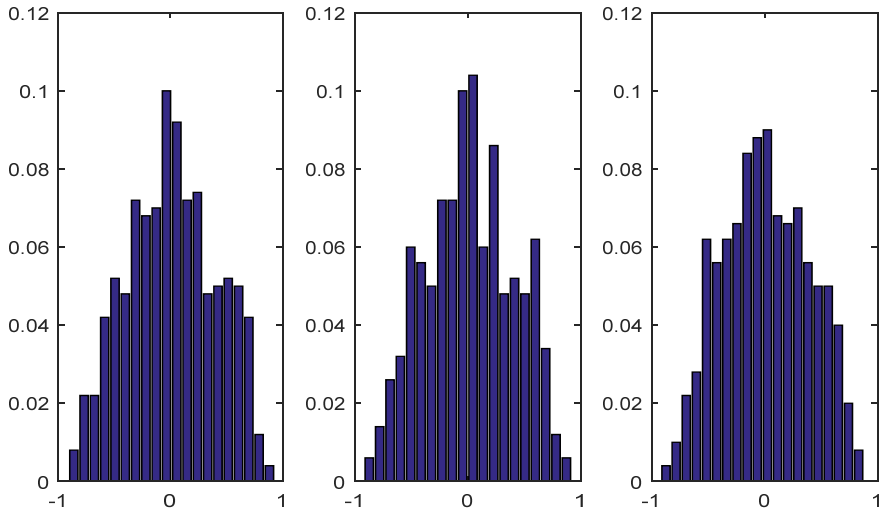

Fig.9. Unlagged coherency vs frequency based on 500 simulated bi-directional records obtained for the parameters described in the text.

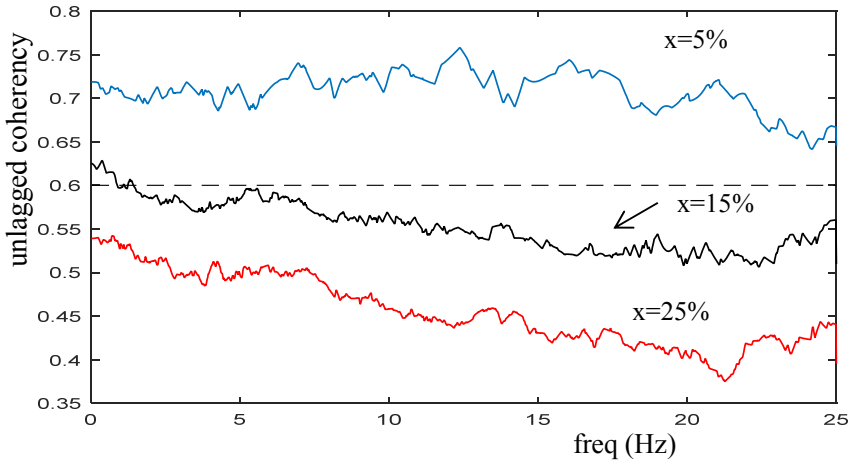

Fig.10. Unlagged coherency vs frequency at 3 different probability of exceedance.

We postulate a shifted scaled symmetric beta function for the *pdf* of the unlagged coherency. Since we have three constraints from the *cdf* in Fig.10 and there is only one free parameter (as $\alpha = \beta$) we select the distribution parameter in a least square sense. Given that the changes in the values in Fig.10 are small for small frequencies and that simplicity is of the essence we opt for a frequency independent *pdf*. Taking the unlagged coherence critical values at {0.72, 0.60 and 0.52} for probabilities of exceedance of 5, 15 and 25% respectively one finds that $\alpha = \beta = 2.55$ provides a good fit, with the theoretical values being {0.75, 0.6 and 0.5}. In the treatment that follows we select the unlagged coherency from the distribution at the 15% probability of exceedance and thus take it equal to 0.6. While we could have selected this value without fitting the analytic *pdf* to the data the *pdf* allows easy selection of the unlagged coherency in case a different probability of exceedance is of interest in some future work.

Response Spectrum Estimation of Maximum Response

For structures on a rigid base subjected to bi-directional excitation the expected value of the maximum response can be written as (Der Kiureghian and Neunhofer 1991)

$$E[\max|z(t)|] = \left(\sum_{k=1}^{2} \sum_{\ell=1}^{2} \sum_{i=1}^{n} \sum_{j=1}^{n} b_{ki} b_{\ell j} \rho_{ski,s\ell j} D_k(\omega_i, \xi_i) D_\ell(\omega_j, \xi_j) \right)^{\frac{1}{2}} \tag{17}$$

where $D_k(\omega_p, \xi_p)$ is the relative displacement spectrum for the *k* motion, b_{ki} is the contribution of the i^{th} mode to the quantity being evaluated due to the earthquake in the *k* direction for a unit value of the displacement spectrum and $\rho_{ski,s\ell j}$ is the correlation between the responses of modes *i* and *j* for input directions *k* and ℓ. The result in eq.17 can be written in convenient matrix form as

$$E[\max|z(t)|] = \left(m_t^T \Gamma m_t + m_x^T \Upsilon m_y \right)^{\frac{1}{2}} \tag{18}$$

where $m_t = m_x + m_y$ with $m_x, m_y \in R^{nx1}$ are the vectors that contain the modal contributions for the input in the x-x and y-y directions, Γ is the matrix of correlation coefficients and Υ is the matrix of cross correlations. In the present seismic guidelines the second term in eq.18 is taken as zero and thus the response is taken as

$$E[\max|z(t)|] = \left(m_x^T \Gamma m_x + m_y^T \Gamma m_y \right)^{\frac{1}{2}} \tag{19}$$

which is the SRSS of the correlated responses to one directional input. The estimation of the peak response based on the work presented previously (neglecting reductions in the correlation with eigenvalue gap) is

$$\max|z(t)| = \left(m_t^T \Gamma m_t \mp 1.2\, m_x^T m_y \right)^{\frac{1}{2}} \tag{20}$$

where the expectation symbol has been removed because eq.22 is no longer (strictly) and expectation estimate.

On the 100% +X% Rule

Consider a quantity y(t) whose contribution from excitation in the 1-1 direction is $y_1(t)$ and from the 2-2 direction $y_2(t)$. If the two time histories are uncorrelated in the particular realization considered then

$$[\max(y)]^2 = \max(y_1^2) + \max(y_2^2) \tag{21}$$

We take $\max(y_2^2) = \beta^2 \max(y_1^2)$ and, without loss of generality assume that y_1 is the response with the largest absolute value so $\beta < 1$ and get

$$|y|_{\max} = |y_1|\sqrt{1+\beta^2} \tag{22}$$

In the 100+ X% combinations rule the estimated maximum response is taken as

$$|y|_{\max} = |y_1| + X\beta|y_1| \tag{23}$$

and it thus follows, equating eqs.22 and 23 and taking X = 0.3 than $\beta = 0.659$. In other words, the SRSS rule and the 30% combination coincide if the smaller of the two responses is around 2/3 of the largest. Assume know that the value of the cross-correlation realized in the response is ρ. Following the same analysis as before one concludes that the maximum response is now

$$|y|_{\max} = |y_1|\sqrt{1+\beta^2+2\beta\rho} \tag{24}$$

and equating this with eq.23 gives

$$\sqrt{1+\beta^2+2\beta\rho} = 1 + X\beta \tag{25}$$

or

$$X = \frac{-1+\sqrt{1+\beta^2+2\beta\rho}}{\beta} \tag{26}$$

The value of X from eq.26 plotted vs. ρ for $\beta = 0.659$ is depicted in Fig.11.

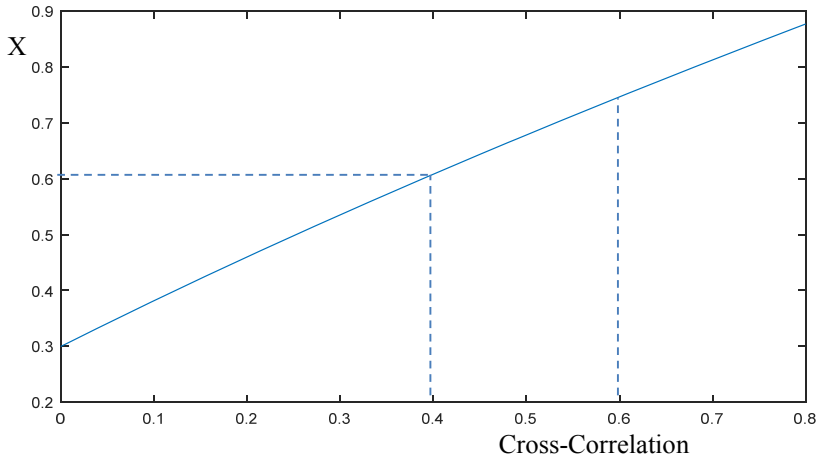

Fig.11. Value of X in the 100+X% rule for which the maximum response is "correctly" estimated vs the cross correlation between bi-direction responses.

If the responses in both directions were governed by modes with identical periods and one accepts the 15% probability of exceedance of the previous section for the cross-correlation one would select to "read" X from Fig.10 using 0.6 for the cross correlation. In most instances, however, the orthogonal responses will be governed by different modes and this selection is perhaps too conservative. Here we (heuristically) select a 50% reduction on the cross-correlation and thus read X at a cross-correlation of 0.4 obtaining the value of 0.6.

Numerical Validation

The previous section suggests a 60% rule. In this section we test this rule using two versions of a 10-story 3-D shear building having the irregular plan distribution shown in Fig.12. The building versions differ only on the rotational inertia of the floor plan and the amount of modal damping; in the case with the higher damping there are some modestly closed periods. The structure is excited with 100 simulated biaxial records and attention is focused on the maximum shear in the inclined wall element at the second floor. The following results are obtained for the two structures:

1) Exact maxima for each of the 100 bi-directional records.
2) Exact maxima for the y-y components of each of the records (single input response)
3) Response spectral solutions for each of the directions of analysis.

For the response spectrum solutions we use the exact spectral ordinates for each motion to ensure that all discrepancy with exact responses derives only from the modal combination. Inspection of numerical results shows that the differences between the CQC and SRSS prediction in the one-directional analyses are trivial.

Since a 60% rule is necessarily more conservative than the 30% one a comparison based on the degree of conservatism is not meaningful. A reasonable gauge, however, is a comparison between the most severe under-predictions when using any of the rules and those that occur in a one directional analysis. A reasonable way to inspect the results is to look at the mean of the largest "n" underestimated responses and compare them with the unidirectional result. The results are depicted in Figs.13 and 14 and show, as expected, that the 30% rule is un-conservative. The suggested 60% rule is slightly conservative in the 2% damped building and less so in the 5% damping case.

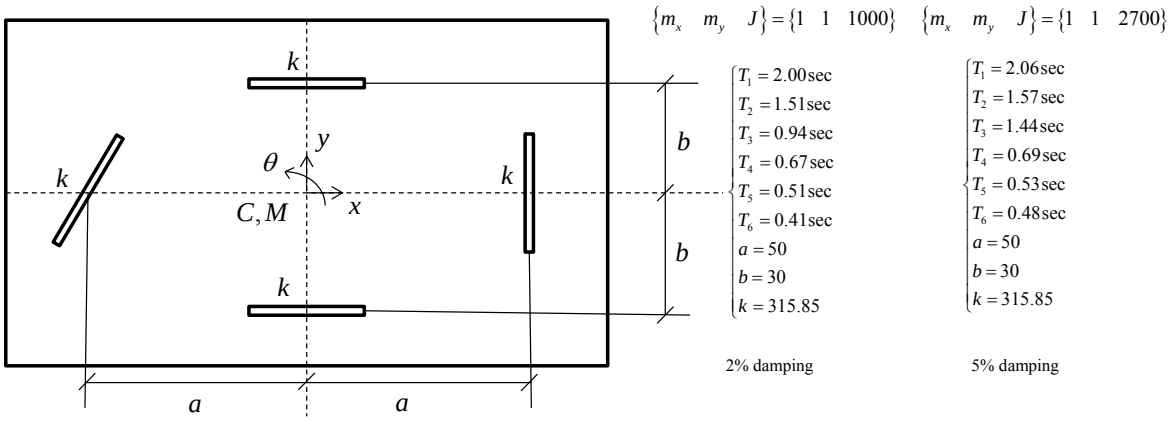

Fig.12. Plan view and periods of the 10 story shear buildings used in the validation study, damping is 2% in all the modes.

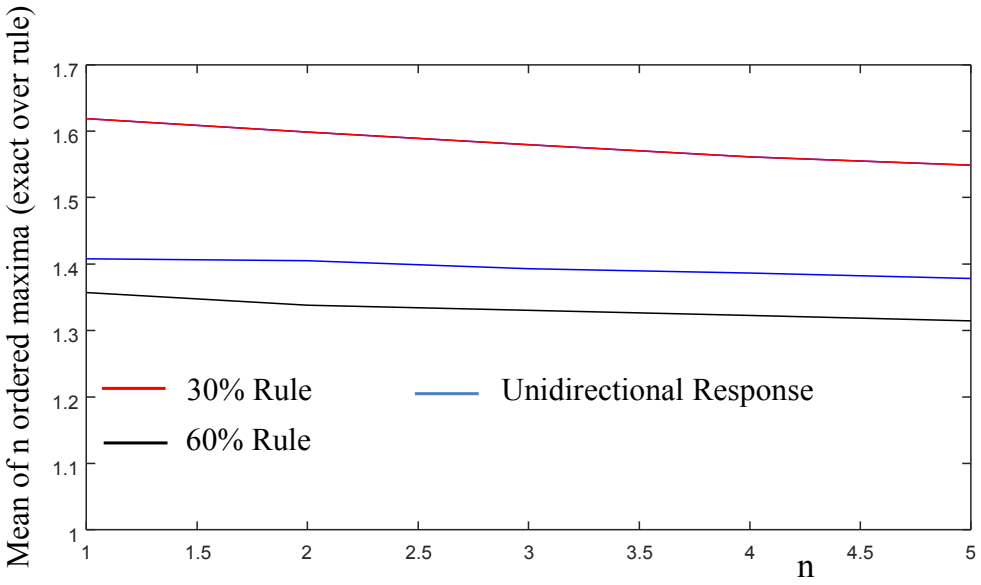

Fig.13. Mean of ordered maxima of the ratio of exact to estimated response based on 100 simulations for building of Fig.12with 2% damping.

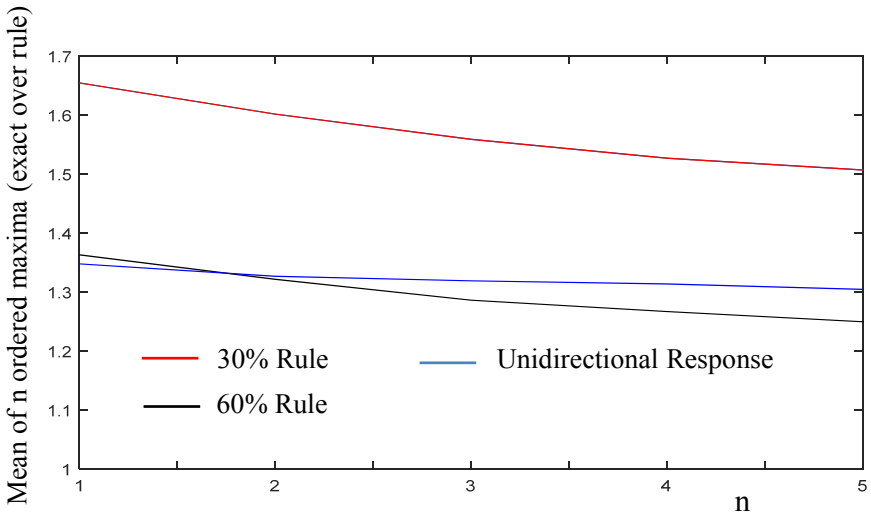

Fig.14. Mean of ordered maxima of the ratio of exact to estimated response based on 100 simulations for building of Fig.12 with 5% damping.

Concluding Comments

Response estimation is presently carried out at the level of expectation. Implicit in this approach is the assumption that variance related under-predictions are adequately accommodated by the design. Since the overwhelming majority of the accumulated numerical experience comes from studies with uni-directional excitation a question that arises is whether the larger variance in elements that are strongly affected by multiple components merits adjustments. On the premise that it is desirable to have the same level of protection against the largest possible underestimations in force demand one can state that the SRSS and the 30% combination rules are unconservative. On this matter the paper shows that similar performance is realized if the cross-correlation coefficient for zero eigenvalue gaps is taken as 0.60 and that, in the case of provisions based on the 100+X% rule, if X is taken around 60.

Acknowledgment

The research reported in this paper was carried out with support from the California Strong Motion Instrumentation Program (CSMIP) through standard agreement 1016-956. This support is gratefully acknowledged.

References

Arias, A. (1970), "A measure of earthquake intensity in seismic design for nuclear power plants: R. J. Hansen, ed., MIT Press, p. 438-483.

Der Kiureghian A., (1979), On the response of structures to stationary excitation, *Report No. UCB/EERC-79/32.*

Der Kiureghian A. and Neuenhofer A. (1991), A response spectrum method for multiple-support seismic excitations, *Report No. UCB/EERC-91/08.*

Gali M. (2015), Combination of effects from orthogonal inputs in seismic design, *Thesis di Laurea Magistrale, Polytecnico di Torino*.

Goodman, L.E., Roenblueth E., and Newmark N.M., (1953), "Aseismic design of firmly founded elastic structures", *Proceedings, Separate No. 349, ASCE, 79, 27 pages. Also Transaction, ASCE, 120, 782-802.*

Heredia-Zavoni, E. and Machicao-Barrionuevo, R. (2004), "Response to orthogonal components of ground motion and assessment of percentage combination rules." *Earthquake Engineering and Structural Dynamics, 33(2): 271-284.*

Kubo, T. and Penzien, J. (1979), "Analysis of three-dimensional strong ground motions along principal axes, San Fernando earthquake." *Earthquake Engineering and Structural Dynamics, 7(3): 265-278.*

Menun, C. and Der Kiureghian, A. (1998a), "A Replacement for the 30%, 40% and SRSS Rules for Multicomponent Seismic Analysis", *Earthquake Spectra, 14(1): 153-156*.

Menun, C. and Der Kiureghian, A. (1998b), "Response to J. J. Hernandez and O. A. Lopez 'Discussion of "A Replacement for the 30%, 40% and SRSS Rules for Multicomponent Seismic Analysis"." *Earthquake Spectra, 14(4): 717-718.*

Menun, C. and Der Kiureghian, A. (2000), "Envelopes for Seismic Response Vectors. I: Theory." *Journal of Structural Engineering, 126(4): 467-473.*

Penzien, J. and Watanabe, M. (1974), "Characteristics of three dimensional earthquake ground motions." *Earthquake Engineering and Structural Dynamics, 3(4): 365-373.*

Rezaeian, S. and Der Kiureghian, A. (2010), "Simulation of synthetic ground motions for specified earthquake and site characteristics", *Earthquake Engineering and Structural Dynamics. 39:1155-1180.*

Rezaeian, S. and Der Kiureghian, A. (2012), "Simulation of Orthogonal horizontal ground motion components for Specified earthquake and site characteristics", *Earthquake Engineering and Structural Dynamics, 41(2): 335-353.*

Rosenblueth E. (1951), A Basis for Aseismic Design, *Doctoral Thesis, University of Illinois, Urbana, Champaign*.

Rosenblueth E. and Elorduy J. (1969). "Response of linear systems to certain transient disturbances", *Proceedings, Fourth World Conference on Earthquake Engineering, Santiago, Chile, I, A-1, 185-196.*

Rosenblueth E. and Contreras H. (1977), "Approximate design for multicomponent earthquakes*", Journal of the Engineering Mechanics Division, ASCE, 103, 881-893*

Serva A and Servas V. (2002), "Spatial variation of seismic ground motions", *Applied Mechanics Review, Vol.55, No.3.*

Smeby, W. and Der Kiureghian, A. (1985), "Modal Combination Rules for Multicomponent Earthquake Excitation." *Earthquake Engineering and Structural Dynamics, 13: 1-12.*

Yeh C. H. and Wen Y. K. (1990), "Modeling of Non-stationary ground motion and Analysis of Inelastic Structural Response*." Structural Safety, 8(1-4): 281-298.*

RAPID POST-EARTHQUAKE SAFETY EVALUATION OF BRIDGES

Roy A. Imbsen[1], P.E., D.Engr.
Shahriar Vahdani[2], P.E., Ph.D.
Jinquan Zhong[1], P.E., Ph.D.

[1]SC Solutions, Inc. Sunnyvale, CA
[2]Applied Geodynamics, Inc., El Cerrito, CA

Abstract

A new procedure for rapid post-earthquake safety evaluation of bridges is being developed, using existing strong motion records, PGA data immediately available following an earthquake, and fragility databases, to assist responsible parties in making timely, informed decisions regarding post-earthquake bridge closures. The New Carquinez Bridge was selected to demonstrate the procedure. This paper provides a procedure overview and its application to safety evaluation of a bridge following an earthquake event, and the development to date of this process, including earthquake scenario selection and generation of ground motions for nonlinear time history analyses of the bridge to establish component fragility data.

Introduction

This study, entitled *Rapid Post-Earthquake Safety Evaluation of the New Carquinez Bridge Using Fragility Curves and Recorded Strong-Motion Data* is part of the Data Interpretation Project of the California Strong Motion Instrumentation Program (CSMIP) in the Department of Conservation (DOC) California Geological Survey. The purpose of this project is to accelerate the application of the strong-motion data in reducing risk due to the strong earthquake shaking which occurs in California.

Figure 1. Aerial View of the New Carquinez Bridge.

The application of the procedure undertaken in this study is to provide for the selected New Carquinez Bridge, as shown in Figure 1, the ability to assess the damage immediately following an earthquake using the ground motion parameters of the earthquake event and fragility curves developed for the bridge so that a decision can be made on the continued use or closure of the bridge.

Overview of the Safety Evaluation Procedure

SC Solutions was tasked to develop a system to improve the current Caltrans rapid post-earthquake decision making process for critical bridges. Immediately after any earthquake, Caltrans has to make decisions about the post-earthquake conditions of bridges. The decision making process will be based on the earthquake intensity, location of a bridge, instrument data, the understanding of the performance of the bridge in the subject earthquake, and other factors related to risk and consequences. Most of the critical bridges that are in high seismic zones are instrumented. These instrument data are monitored in real time and can be used for this decision making process. The foundation or free field ground motions near the bridge and some of the structural performance can be obtained immediately after an earthquake. However, this limited instrument data doesn't provide adequate information about the conditions of all critical components of bridges immediately after an event. Therefore, additional understanding of the bridge performance and fragility functions should be developed for each of these critical bridges to assist the post-earthquake decision making process.

To develop fragility functions, first a set of pre-earthquake scenario events must be selected based on the location of the bridge and the active faults in the vicinity of the bridge site. For this task SC Solution proposed to use the New Carquinez Bridge for the case study. After selecting a set of scenario earthquakes for the New Carquinez Bridge, the existing SC Solutions bridge model could be used to simulate the effects of these ground motions to understand the performance of each critical component in the bridge. After conducting these pre-earthquake seismic analyses, a relationship can be developed between the earthquake intensity parameter (e.g. PGA and spectral acceleration) and the primary response parameter of a critical component. As one example, the primary response parameter can be a drift for a critical tower. Based on the primary response parameter value a damage index (or damage potential) can be developed for each critical component. This damage potential can be related to the seismic intensity parameter as a fragility function for each critical component.

Pre-Event Data Processing

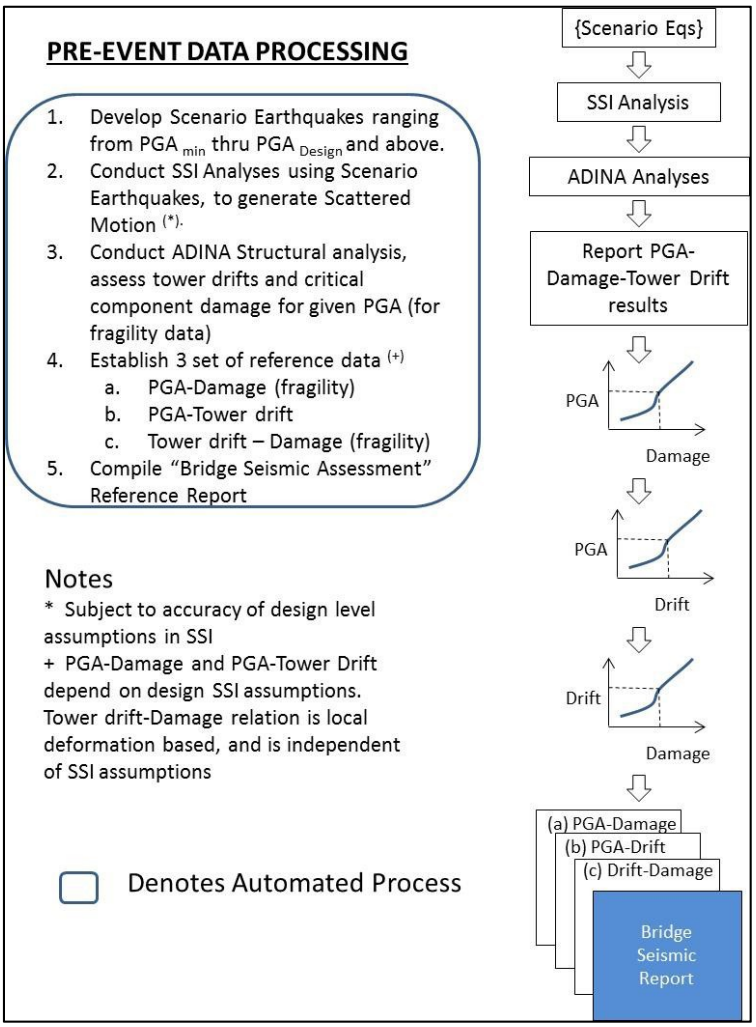

Figure 2. Pre-Event Data Processing.

As shown in Figure 2, prior to an event, several automated procedures will be completed and compiled in a "Bridge Seismic Assessment" report, as a reference document for Caltrans decision making, after an event. The steps include the following:

1. A series of scenario ground motions will be generated based on different magnitude earthquakes on regional faults. These motions will range from low fault activity and spectral acceleration, through Design Spectra, and spectral acceleration values both less than and greater than design levels prescribed for the site.

2. Using the available site specific ground motion, generation tools and design spectra, the SSI analytical model customized for the Carquinez site will be used to bring the scenario earthquakes to the site and to generate scattered motions.

3. The existing Finite Element model of the New Carquinez Bridge, developed by SC Solutions, will be used in the demand analyses under the scenario ground motions. Damage status of critical components of the bridge will be related to spectral acceleration (i.e. fragility data). For each critical component, a primary response parameter will be identified. For example for critical tower member and connections, "Tower Drift" will be the governing primary response parameter. The proposed approach and scope-of-work is based on the use of Tower 3 Drift as the primary response parameter to reflect the damage state of Critical Tower Components, as an example of the process. This methodology can be applied to different primary response parameters to reflect damage status of other critical components. For example foundation movements can reflect pile damage; superstructure movement can reflect damage to critical superstructure components and expansion joints; or cable movements which can reflect condition of cable anchorage.

4. Governing Tower drifts as the primary response parameters will also be documented vs. spectral acceleration, and finally series of relations between Tower Drift and Damage state of the critical tower components will be generated.

5. Based on the analyses, the following response parameters will be related to the scenario earthquake intensity, fault, and distance to site:

   a. Spectral acceleration versus Damage index of critical components (Fragility),
   b. Spectral acceleration versus Tower Drift,
   c. Tower Drift versus Damage index of critical components,

Description of the New Carquinez Bridge and Local Seismic Design Hazard

Description of the New Carquinez Bridge

The New Carquinez Bridge spans the Carquinez Strait with a 2,388 ft. main span bounded by a south span (towards Oakland) of 482 ft. and a north span (towards Sacramento) of 594 ft. as shown in Figure 3. The principal components of this suspension bridge include reinforced concrete towers supported on large-diameter concrete pile foundations, parallel-wire cables, gravity anchorages, and a closed orthotropic steel box deck system. The main concrete towers are approximately 400 ft. tall, and are tied together with a strut below the deck and an upper strut between the cable saddles as shown in the Typical Section view included in Figure 3. The lower strut supports the deck vertically using two rocker links and transversely through a shear key.

The bridge site, located approximately twenty miles northeast of San Francisco, is located in an active seismic zone. Seismic hazard assessments have shown that the site could be subject to strong ground motions originating on the San Andreas Fault, the Hayward Fault, Concord-Green Valley, Napa Valley, and the Franklin Fault. However, studies have shown that the Hayward fault, Concord-Green Valley fault system, and the Napa Valley seismic zones are the dominant sources of seismic hazard for the bridge's frequency range.

The seismic design of the New Carquinez Bridge considers both the Safety Evaluation Earthquake (SEE) and the lower level Functional Evaluation Earthquake (FEE). Caltrans performance requirements for these events are higher than the minimum level required for all transportation structures but below that required for an Important Bridge. As much as possible, the Important Bridge criteria are to be met for the Safety Evaluation Earthquake (SEE) corresponding to a maximum credible event which has a mean return period in the range of about 1,000 to 2,000 years. In this earthquake, the bridge can be subject to primarily "minor" damage with some "repairable" damage to piles, pile caps and anchorage blocks and still remain open.

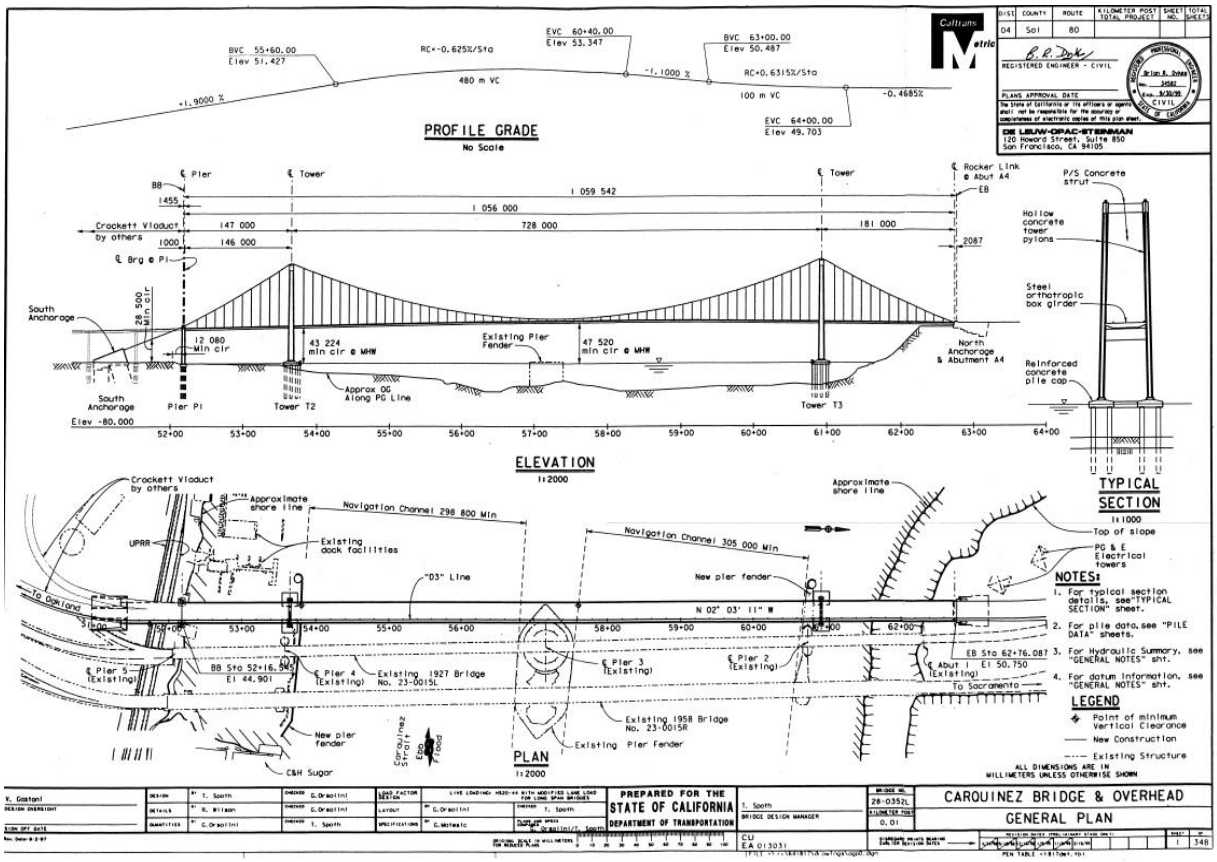

Figure 3. General Plan of the New Carquinez Bridge.

New Carquinez Bridge Local Seismic Design Hazard

For the New Carquinez Bridge, the resulting design response spectra for the Franklin, Hayward, and San Andreas events the values of peak design rock accelerations are taken from the original bridge design report (DLOS, 1999, Third Carquinez Strait Bridge, Seismic Report), and are as follows:

Source/MCE/Distance	Peak Rock Acceleration (g's) Horizontal PGA	Vertical PGA
San Andreas, M_w 8, R=41 km	0.26	0.19
Hayward, M_w 7¼, R=13 km	0.55	0.47
Franklin, M_w 6½, R=1 km	1.00	0.96

Determination of Dynamic Characteristics for the Conditional Mean Spectra (CMS).

Using the results from the dynamic response analysis conducted on the New Carquinez Bridge by SC Solutions for the design, the dynamic characteristics were readily available to determine the periods, mode shapes, and participation factors that were the major contributors to the dynamic response of Tower 3 in the longitudinal direction for Tower 3. Although there are other modes with larger participation factors in the longitudinal direction, their contribution to the longitudinal participation is very small. As shown in Table 1, Modes 11, 12, 13 and 19 show the largest longitudinal mass participation. Therefore it can be concluded that the modes having periods ranging from 2.18 to 2.64 seconds were the primary contributors to the longitudinal response of Tower 3. A target period of 2.4 seconds, within the range, was selected as the target period for the Conditional Mean Spectra (CMS). Conditional Mean Spectra at the period of the tower were developed using the Baker (2011) and Jayaram and Baker (2008) procedure as described below. We judge that the CMS would provide more realistic ground motions than the deterministic 84th percentile ground motions from the ground motion prediction equations (GMPEs) as described in more detail below. Shown in Figure 4 are three views of the displaced shape for Mode 11. Figure 5 shows an enlarged isometric view of Mode 11.

Table 1 Dynamic Response-Modes, Periods and Participation

	Period	mass			accumulated mass		
Mode #	(sec)	MASS(X)	MASS(Y)	MASS(Z)	MASS(X)	MASS(Y)	MASS(Z)
2	6.66	1%	11%	0%	1%	11%	0%
5	4.15	0%	4%	2%	1%	15%	2%
11	2.65	10%	9%	1%	11%	24%	4%
12	2.64	9%	0%	1%	21%	24%	5%
13	2.54	6%	0%	0%	27%	24%	5%
19	2.18	8%	9%	0%	35%	34%	5%
21	2.12	0%	8%	0%	35%	42%	5%
67	0.76	13%	24%	3%	48%	66%	8%
88	0.62	17%	1%	1%	65%	67%	9%

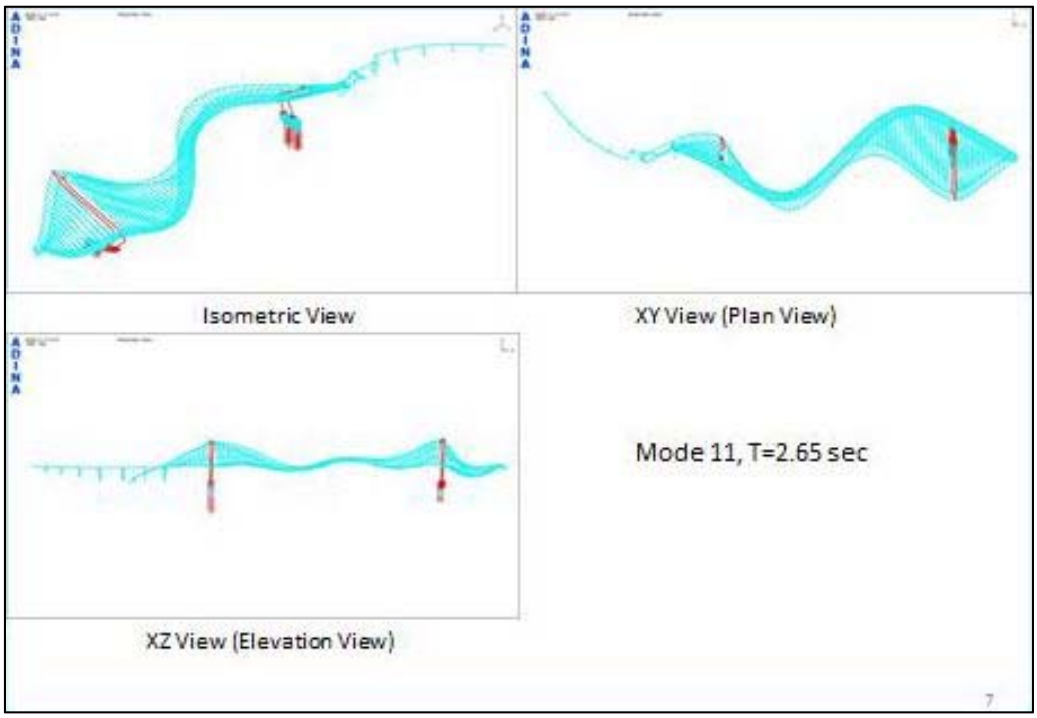

Figure 4. Various Views Showing the Displaced Shape for Mode 11.

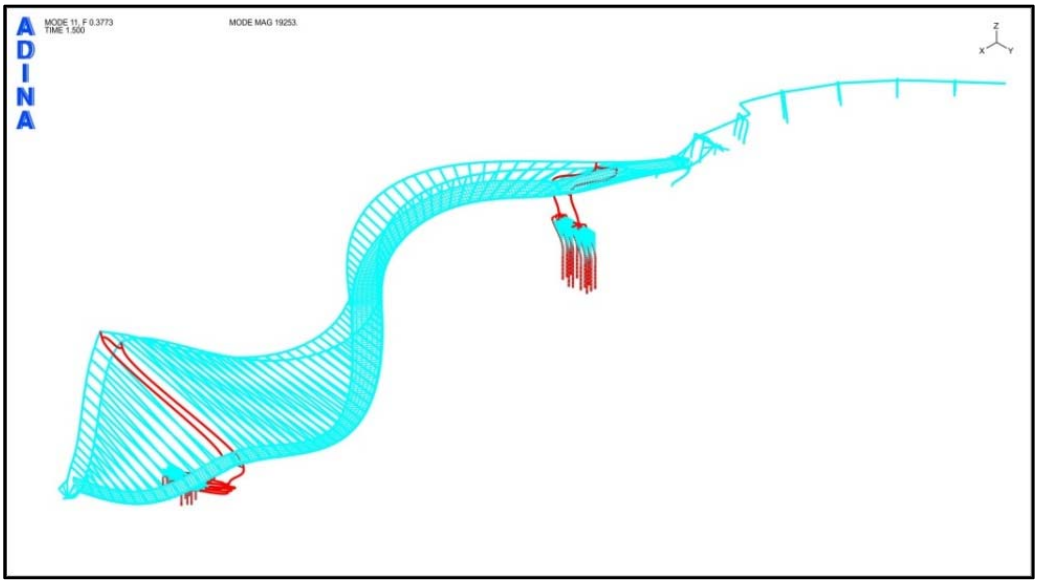

Figure 5. Enlarged Isometric View of Mode 11.

Development of the Scenario Earthquakes

The development of 26 sets of ground motions (each set with two horizontal components and one vertical component) used for time history analysis of the New Carquinez Bridge follows standard practices in determining moment magnitude (Mw) and site-to-source distance (R) of earthquake scenarios and site conditions, computing horizontal and vertical design spectra, selecting seed motions, and spectrally matching selected seed motions. This section presents the details of the procedures used in the ground motion development for 16 different scenario earthquakes (SCS, 2015), i.e., the first 26 scenario earthquakes listed in Table 2 below. Among these 26 scenario earthquakes, 15 of them are designated to have velocity pulses in order to consider directivity effects from near-fault motions. The percentage of scenario earthquakes with velocity pulses is about 60%, consistent with the fraction of ground motions with velocity pulses used for nonlinear time-history analysis in current practice. Figure 6 below shows the significant earthquakes which have happened between 1970 and 2003 and the faults around the bridge site.

Table 2. Selected Scenario Earthquakes for the Pre-Earthquake Analysis

Scenario	Mw	R (km)	Probability Level	Directivity	Pulse Period Tp (Sec.)	Set of Time Histories	Causative Fault
1-3	7.3	13	84th percentile CMS@2.4 sec	Yes	+/- 4.7	3	Hayward+ Rodgers Creek
4	7.3	13	84th percentile CMS@2.4 sec	No	-	1	Hayward+ Rodgers Creek
5	7.3	13	50th percentile	No	-	1	Hayward+ Rodgers Creek
6-8	6.8	13	84th percentile CMS@2.4 sec	Yes	+/- 3.7	3	Hayward/ Green Valley
9	6.8	13	84th CMS@2.4 sec	No	-	1	Hayward/ Green Valley
10	6.8	13	50th percentile	No	-	1	Hayward/ Green Valley
11	6.8	28	84th percentile CMS@2.4 sec	No	-	1	Calaveras
12-14	6.3	13	84th percentile CMS@2.4 sec	Yes	+/- 2.9	3	Hayward
15	6.3	13	84th percentile CMS@2.4 sec	No	-	1	Hayward
16	6.3	13	50th percentile	No	-	1	Hayward
17	6.3	20	50th percentile	No	-	1	Hayward/ Green Valley
18-20	5.8	13	84th percentile CMS@2.4 sec	Yes	+/-2.2	3	Hayward
21-23	6.5	1	0.5(50th+84th)	No	+/-2.3	3	Franklin
24	7.9	42	84th percentile CMS@2.4 sec	No	-	1	San Andreas
25	7.9	42	50th percentile	No	-	1	San Andreas
26	6.5	12	50th percentile	No	-	1	Caltrans Min.
27	6.0	20	-	-	-	1	2014 Napa Event

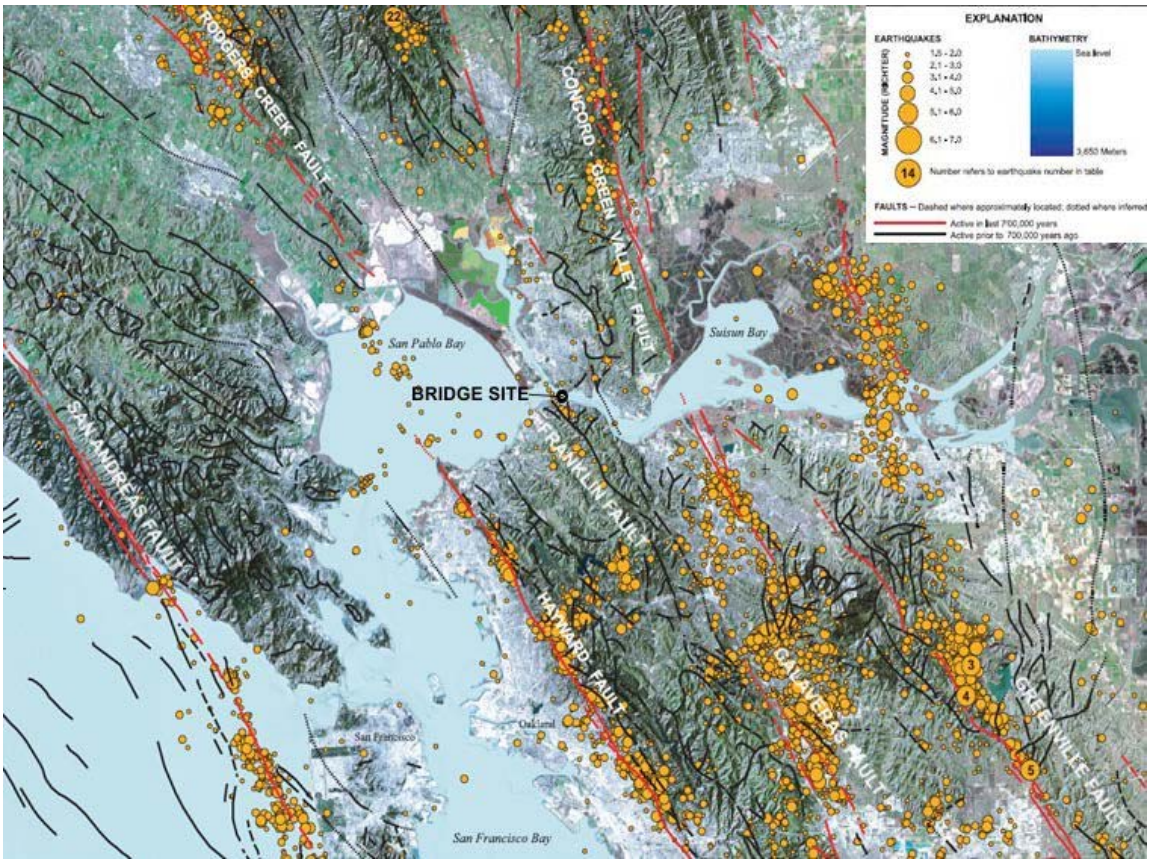

Figure 6. Earthquakes Occurring Between 1970 & 2003 and Faults around the New Carquinez Bridge (after Sleeter et al., 2004)

Horizontal and Vertical Design Spectra

Based on the 26 scenario earthquakes listed in Table 2, horizontal and vertical design spectra were developed at the control point (EMI, 2014) at CGS Array #2 (located to the west of the south anchorage of the bridge), as shown in Figure 7, with a Vs30 value estimated at 305 m/s per EMI (2014) and the original bridge design report (DLOS, 1999). The geometric mean (geomean) of the horizontal design spectra was computed by using four equally-weighted ground motion prediction equations (GMPEs), i.e., ASK14 (Abrahamson et al., 2014), BSSA14 (Boore et al., 2014), CB14 (Campbell and Bozorgnia, 2014), and CY14 (Chiou and Young, 2014), from the NGA-West2 database (Ancheta et al., 2014).

For Scenarios 1-3, 6-8, 12-14, and 18-20, directivity effects (Somerville et al., 1997, Abrahamson, 2000) were incorporated into the developed geomean of the design spectra to develop the fault average (FA) design spectrum, which was further resolved into fault normal (FN) and fault parallel (FP) design spectra. To arrive at a more realistic design spectrum, a conditional mean spectra (Baker, 2011) for FN and FP design spectra were developed, for each

of these scenarios at 2.4 seconds, the period most significantly contributing to the longitudinal response of Tower 3 of the New Carquinez Bridge.

For Scenarios 21-23 (the original design event), the average of the 50th and 84th percentiles of geomean spectra computed from NGA-West2 GMPEs was used as the FA design spectrum to avoid undue conservatism due to the high uncertainty regarding the existence, location, and activity of the Franklin fault. The FA spectrum was further resolved into FN and FP design spectra using the factors determined from DLOS (1999). To determine the FN design spectrum, the ratios between FN and FP design spectra presented in DLOS (1999) were calculated and applied to the FA design spectrum. The FP design spectrum was taken to be the same as the FA design spectrum.

The geomean spectra (at the 50th percentile) were used as the horizontal design spectra for Scenarios 10, 16, 17, 25, and 26. CMS was developed for Scenarios 4, 9, 11, 15, and 24 based on the geomean of horizontal spectra (at the 84th percentile) at 2.4 seconds.

The developed horizontal design spectra, including geomean, CMS, FN and FP design spectra, for all 26 scenarios are presented in Figure 8. From this figure it can be seen that the FN and FP design spectra for Scenarios 1-3 are larger than the original design event at 2.4 seconds while the horizontal spectra for other scenarios are lower than the original design event at 2.4 seconds. Once all horizontal design spectra are determined, the V/H ratios developed by Gülerce and Abrahamson (2011) were then multiplied with horizontal (geomean, CMS, or FA design spectrum as appropriate) design spectra for vertical spectra. The computed vertical design spectra for all 26 scenarios are presented in Figure 9. Vertical design spectra for all 26 scenarios

Figure 7. Plan View of CGS Array#2 at the South End of the New Carquinez Bridge Located at Latitude and Longitude of (38.0545, -122.2264)

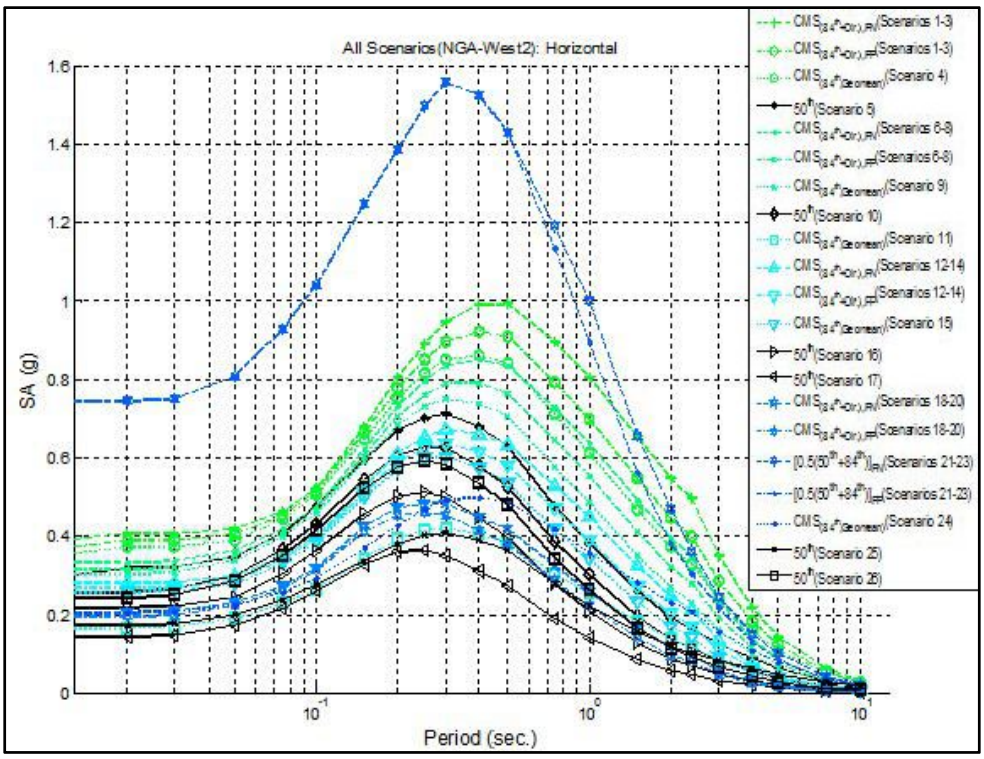

Figure 8. Horizontal design spectra for all 26 scenarios.

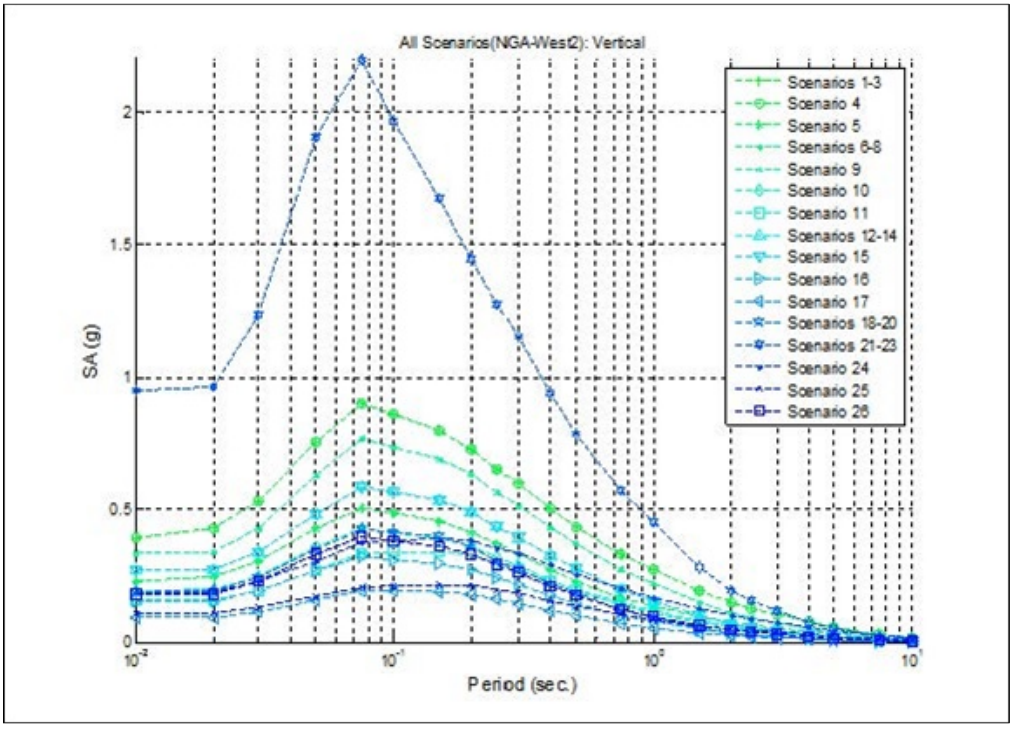

Figure 9. Vertical design spectra for all 26 scenarios.

Selection of Seed Motions

The NGA-West2 database provides 19,880 sets of recorded motions with three-component time histories available in digital formats. In these available recorded motions, the magnitudes vary from 2.9 to 7.9, the site-to-source distances vary from 0.05 to 1,156.9 km, Vs30 values vary from 89 m/s to 2,100 m/s, and periods of velocity pulse (Tp) vary from 0.322 seconds to 13.120 seconds. In particular, there are 142 sets of recorded motions with velocity pulse in the NGA-West2 database.

The six factors discussed below (listed in priority order) were considered in selecting 26 sets of seed motions (each with two horizontal components and one vertical component) suitable for further spectral matching:

1. Tp of the horizontal component of seed motion is similar to the target Tp computed to be consistent with magnitude and site-to-source distance (Shahi and Baker, 2011). The target Tp values considered in seed motion selection are listed in Table 3 below:

Table 3. Period of velocity pulses for 15 scenarios with directivity effects

Scenarios	Mw	R (km)	Tp (sec.)
1-3	7.3	13.0	4.7
6-8	6.8	13.0	3.7
12-14	6.3	13.0	2.9
18-20	5.8	13.0	2.2
21-23	6.5	1.0	2.3

2. Moment magnitude of seed motion is close to the magnitude of scenarios listed in Table 2;
3. Site-to-source distance of seed motion is close to the magnitude of scenarios listed in Table 2;
4. Seed motion recorded at site condition with Vs30 values is close to the target 305 m/s;
5. The spectral shape of each component of a seed motion is similar to the target design spectrum (horizontal or vertical as appropriate); and
6. Waveforms of each component of a seed motion are similar to the target, with distinguishable arrivals of P- and S-waves.

Table 4 below lists the metadata for the seed motions selected from the NGA-West2 database for further spectral matching in terms of RSN number in the NGA-West2 database, earthquake event, year, record station, Mw, R, Vs30, and Tp values. Note that the source-to-site distances for 12 of the selected seed motions (for Scenarios 1-3, 6-8, 12-14, and 18-20) are all smaller than 13km. The selected seed motions represent the balance among all six factors considered with the highest priority given to Tp values close (+/– 1 second) to the values listed in Table 3, as opposed to one single factor of source-to-site distance.

Table 4. Metadata for 26 Sets of Seed Motions Selected from the NGA-West2 Database

Scenario	RSNno	Earthquake Event	Year	Record Station	Mw	R (km)	Vs30 (m/s)	Tp (sec.)
1-3	1176	Kocaeli Turkey	1999	Yarimca	7.51	1.38	297.00	4.95
	292	Irpinia Italy-01	1980	Sturno (STN)	6.90	6.78	382.00	3.28
	1244	Chi-Chi Taiwan	1999	CHY101	7.62	9.94	258.89	5.31
4	864	Landers	1992	Joshua Tree	7.28	11.03	379.32	-
5	5831	El Mayor-Cucapah Mexico	2010	EJIDO SALTILLO	7.20	14.80	242.05	
6-8	1045	Northridge-01	1994	Newhall - W Pico Canyon Rd.	6.69	2.11	285.93	2.98
	1114	Kobe Japan	1995	Port Island (0 m)	6.90	3.31	198.00	2.83
	161	Imperial Valley-06	1979	Brawley Airport	6.53	8.54	208.71	4.42
9	4847	Chuetsu-oki Japan	2007	Joetsu Kakizakiku Kakizaki	6.80	9.43	383.43	-
10	6961	Darfield New Zealand	2010	RKAC	7.00	13.37	295.74	-
11	6923	Darfield New Zealand	2010	Kaiapoi North School	7.00	30.53	255.00	-
12-14	292	Irpinia Italy-01	1980	Sturno (STN)	6.90	6.78	382.00	3.28
	8123	Christchurch New Zealand	2011	Christchurch Resthaven	6.20	5.11	141.00	1.55
	1045	Northridge-01	1994	Newhall - W Pico Canyon Rd.	6.69	2.11	285.93	2.98
15	313	Corinth Greece	1981	Corinth	6.60	10.27	361.40	-
16	8099	Christchurch New Zealand	2011	Kaiapoi North School	6.20	17.86	255.00	-
17	4078	Parkfield-02 CA	2004	Coalinga - Fire Station 39	6.00	22.45	333.61	-
18-20	569	San Salvador	1986	National Geografical Inst	5.80	3.71	455.93	1.13
	147	Coyote Lake	1979	Gilroy Array #2	5.74	8.47	270.84	1.46
	149	Coyote Lake	1979	Gilroy Array #4	5.74	4.79	221.78	1.35
21-23	1120	Kobe Japan	1995	Takatori	6.90	1.46	256.00	2.49
	159	Imperial Valley-06	1979	Agrarias	6.53	0.00	242.05	2.28
	1054	Northridge-01	1994	Pardee - SCE	6.69	5.54	325.67	2.05
24	1236	Chi-Chi Taiwan	1999	CHY088	7.62	37.48	318.52	-
25	2111	Denali Alaska	2002	R109 (temp)	7.90	42.99	341.56	-
26	313	Corinth Greece	1981	Corinth	6.60	10.27	361.40	-

Spectral Matching of Selected Seed Motions

The selected seed motions in Table 4 were spectrally matched to a 5%-damped target spectra for the frequency range of interest, i.e., between 0.2 Hz and 2.0 Hz. Although we focused on this frequency range during spectral matching, additional attempts were taken to match frequencies beyond this range, usually between 0.2 Hz and 100 Hz, without significantly altering the waveform character of the seed motions.

Before spectral matching, a linear scaling factor was applied to each seed motion component such that each seed motion component had the same spectral ordinate as that of the target spectrum at 100 Hz. The scaled seed motion component was then spectrally matched to the 5%-damped target design spectrum using RSPMatch09 (Atik and Abrahamson, 2009).

To limit the number of frequencies used to compute the response spectrum, the requirements of ASCE 4-98 and Section 2.4(b) of ASCE43-05 on the number of and the spacing of frequencies were followed:

1. The frequencies shall be calculated such that each frequency is within 10% of the previous frequency (or alternatively use Table 2.3-2 of ACSE 4-98); and
2. Spectral accelerations shall be computed for at least 100 points per frequency decade and uniformly distributed on a $\log_{10}$ scale between 0.1 to 50 Hz.

To meet both requirements, 315 frequencies were populated over the frequency range of 0.1 Hz to 100 Hz for spectral matching. The tolerance between the 5%-damped response spectrum of each SMM component and the target design spectrum was set at +/-5% of the target spectrum.

Rotation of Horizontal Components into Longitudinal and Transverse Bridge Directions

After the spectral matching, the FN and FP components need to be rotated into the longitudinal and transverse directions of the New Carquinez Bridge for fragility analysis. The angles used to rotate the FN and FP components into the longitudinal and transverse directions of the bridge are measured from the projected fault line to the longitudinal axis of the bridge. The rotation angles from each fault line to the longitudinal axis of the bridge are listed in Table 5 below. For all other scenarios, the H1 and H2 components can be applied directly into to the longitudinal and transverse axes of the New Carquinez Bridge.

Table 5. Angles Measured from Projected Fault Line to the Longitudinal Axis of the Bridge

Scenarios	Fault Name	θ (deg., measured clock wise from fault line to the longitudinal axis)
1-3	Hayward/Rodgers Creek	20.3
6-8	Hayward/Green Valley	2.3
12-14	Hayward	20.3
18-20	Hayward	20.3
21-23	Franklin	18.0

Future Development Tasks: Time History Analyses & Fragility Database

Time History Analysis

The SC Solutions Finite Element (FE) models of the New Carquinez Bridge, as shown in Figure 10, has been verified and correlated with both physical testing and with models developed by others. Shown in Figure 10 is the ADINA model for both a simple model and a more complex finite element model. The bridge is fully instrumented with sensors placed on the bridge as shown in Figure 11 and Figure 12. At this stage in the project several families of scenario ground motions have been generated as described above. These motions are being applied to the bridge to establish critical component fragilities and corresponding tower drift data, to be included in the "Bridge Seismic Assessment" report. This process of using the available ADINA FE model for all earthquake scenarios, and to extract fragility and drift information will be developed and automated so that it can be repeated efficiently to accommodate any adjustments to design or earthquake intensities for future projects or post-earthquake investigations.

Fragility Database

A Fragility Database will be generated using the results from the time history analyses of the developed time history ground motions. The FE model is used to assess the response of critical bridge components with their appropriate CMS as described above, and relate their response to the event strength (PGA). In addition, for each event, tower response parameters that include drift, displacements, bending moments and shear forces, concrete and steel strains, and curvatures will also be processed and reported to correlate with the observed damage states and response parameters obtained in the research conducted by Vosooghi and Saiidi (2010). In their work they obtained data from 32 bridge column models, most of which were tested on a shake table, to develop fragility curves for the seismic response of reinforced concrete bridge columns. Photographs of the physical damage imparted to the test columns were taken during the testing to correlate with the analytical models and the measured concrete and steel strains in the test columns.

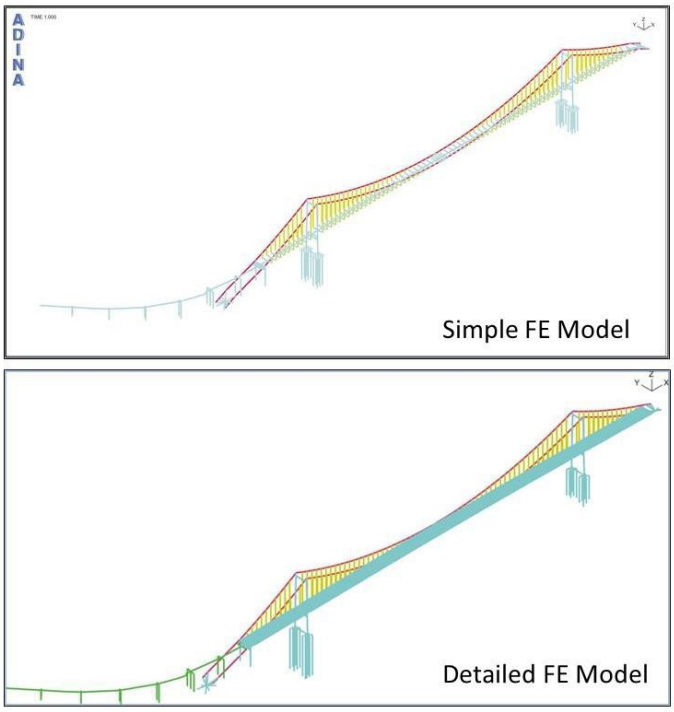

Figure 10. SC Solutions' Finite Element Models for the New Carquinez Bridge.

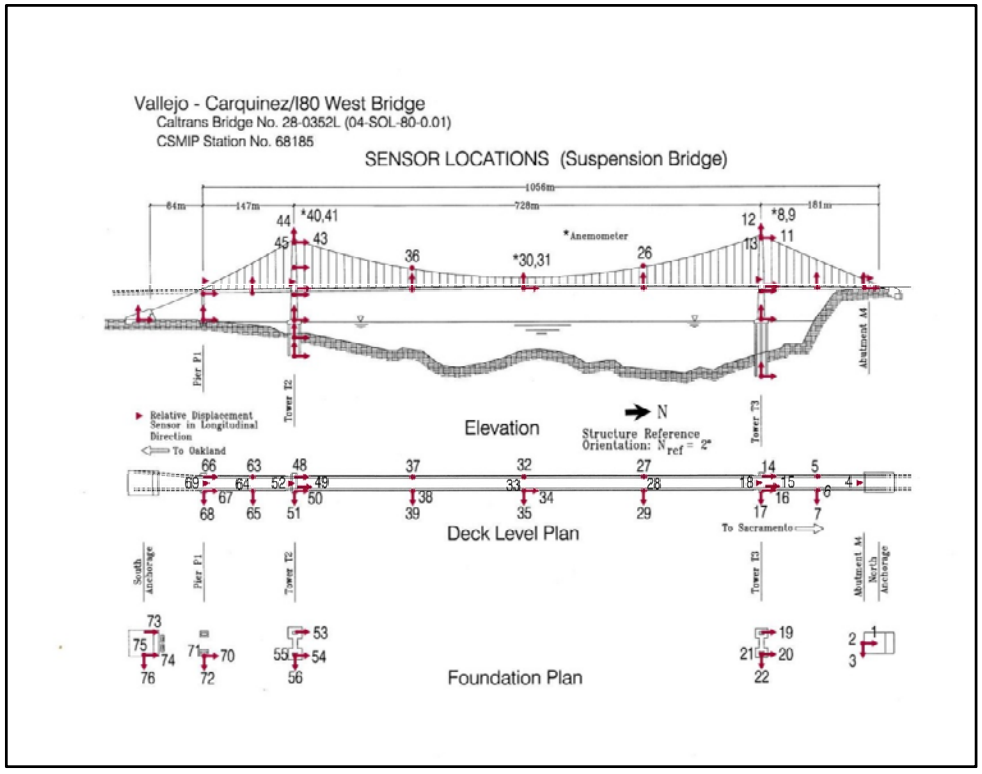

Figure 11. Foundation Plan with Sensor Locations

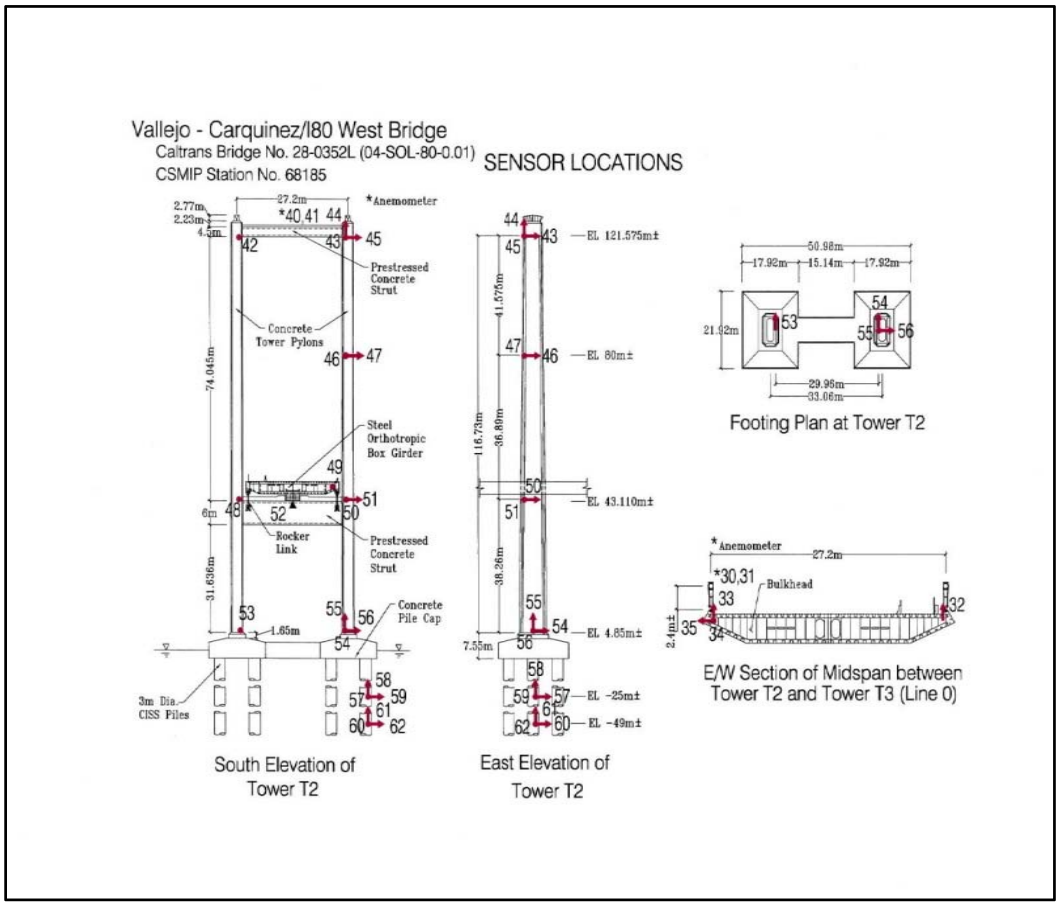

Figure 12. Substructure Components Showing Locations for the Development of Fragility Functions

Based on this work Vosooghi and Saiidi (2012) proposed five distinct apparent damage states (DSs) for reinforced concrete columns subjected to earthquakes, as follows:

- DS-1: Flexural cracks;
- DS-2: Minor spalling and possible shear cracks;
- DS-3: Extensive cracks and spalling;
- DS-4: Visible lateral and/or longitudinal cracks and/or visible reinforcing bars;
- DS-5: Compressive failure of the concrete core edge (i.e., imminent failure).

It is envisioned that both the analytical and recorded test data along with the photographed damage will be key in developing the fragility data that can be related to operability of the bridge and aid in the decision to keep the bridge open for public and/or emergency vehicles, or to close the bridge to all traffic.

Nonlinear quasi-static (push-over) Analysis

Push-over analysis will be conducted on Tower 3 using the ADINA model for the as-built plans and materials using the response spectrum for the design hazard to determine actual capacity of the tower and to determine if the intensity of the applied ground motion is below or above the design earthquake.

References

Abrahamson, N.A. (2000) "Effects of rupture directivity on probabilistic seismic hazard analysis", Proceedings of the Sixth International Conference on Seismic Zonation, Earthquake Engineering Research Inst., Oakland, California.

Abrahamson, N.A., W. J. Silva, and R. Kamai, (2014) "Summary of the ASK14 Ground Motion Relation for Active Crustal Regions." Earthquake Spectra: August 2014, Vol. 30, No. 3, pp. 1025-1055.

ADINA Toll Bridges Project, sponsored by California Department of Transportation, Caltrans, 2014.

ADINA R&D, Theory and Modeling Guide, Vol. I. Watertown, MA: ADINA Solids & Structures, 2009.

American Society of Civil Engineers (1998). "Seismic Analysis of Safety-Related Nuclear Structures and Commentary." Reston, VA: ASCE, 19998. 978-0-7844-0433-1.

American Society of Civil Engineers (2005). "Seismic Design Criteria for Structures, Systems, and Components in Nuclear Facilities." American Society of Civil Engineers, 2005. ASCE/SEI 43-05.

Ancheta, T.D., Robert B. Darragh, Jonathan P. Stewart, Emel Seyhan, Walter J. Silva, Brian S.-J. Chiou, Katie E. Wooddell, Robert W. Graves, Albert R. Kottke, David M. Boore, Tadahiro Kishida, and Jennifer L. Donahue (2014) "NGA-West2 Database." Earthquake Spectra: August 2014, Vol. 30, No. 3, pp. 989-1005.

Atik, L.A. and Abrahamson, N. (2009) "An Improved Method for Nonstationary Spectral Matching." Earthquake Spectra, Vol. 26, No. 3, pp 601-617.

Baker, J.W. (2011). "Conditional Mean Spectrum: Tool for ground motion selection," Journal of Structural Engineering, Vol. 137 No.3, pp 322-331.

Boore, D. M., J. P., Stewart, E. Seyhan, and G.G., Atkinson. (2014) "NGA-West2 Equations for Predicting PGA, PGV, and 5% Damped PSA for Shallow Crustal Earthquake." Earthquake Spectra: August 2014, Vol. 30, No. 3, pp. 1057-1085.

Caltrans (2010), Data DVD provided by Steve Mitchell of Caltrans to Hassan Sedarat of SC Solutions on December 13, 2010.

Caltrans, Construction Marked up Drawings of Alfred Zampa Memorial Bridge.

Caltrans Contract 59A007, "3rd Carquinez Strait Bridge Seismic Report"

Caltrans Contract No. 59A007, "Third Carquinez Strait Bridge Structural Design Criteria"

Campbell, K.W. and Bozorgnia, Y., (2014) "NGA-West2 Ground Motion Model for the Average Horizontal Components of PGA, PGV, and 5% Damped Linear Acceleration Response Spectra." Earthquake Spectra 30:3, 1087-1115.

Chiou, B.S.J. and Young, R. R., (2014) "Update of the Chiou and Youngs NGA Model for the Average Horizontal Component of Peak Ground Motion and Response Spectra." Earthquake Spectra: August 2014, Vol. 30, No. 3, pp. 1117-1153.

De Leuw–OPAC–Steinman (DLOS) (1999) "Third Carquinez Strait Bridge, Seismic Report, 100% submittal", San Francisco, CA, February 1999

EMI (2014) "Kinematic Soil Pile Interaction for New Carquinez Bridge." Technical Memorandum, March 24, 2014, Earth Mechanics, Inc., Fountain Valley, CA

Gülerce, Z. and Abrahamson, N.A. (2011) "Site-Specific Design Spectra for Vertical Ground Motion." Earthquake Spectra: November 2011, Vol. 27, No. 4, pp. 1023-1047.

Hassan Sedarat, Iman Talebinejad, Abbas Emami-Naeini, David Falck, Gwendolyn van der Linden, Farid Nobari, Alex Krimotat, Jerome Lynch (2014), "Real-Time Estimation of the Structural Response using Limited Measured Data", SPIE Smart Structures and Materials + Nondestructive Evaluation and Health Monitoring, Nondestructive Characterization for Composite Materials, Aerospace Engineering, Civil Infrastructure, and Homeland Security 2014, Proceeding of SPIE Vol. 9063, 906311 © 2014 SPIE.

Hassan Sedarat, Alexander Kozak, Joyce Lee, Alex Krimotat, Vince Jacob, and Steve Mitchell (2013), "Efficient Techniques in Finite Element Analysis and Seismic Evaluation of Suspension Bridges", , 7NSC, Seventh National Seismic Conference on Bridges & Highways, Oakland, CA, May 20-22, 2013.

Hassan Sedarat, SC-Cable, Suspension Bridge Construction Sequence Application, SC Solutions, Inc., Sunnyvale, CA.

Jayaram, N., and Baker, J. W., (2008) "Statistical Tests of the Joint Distribution of Spectral Acceleration Values" Bulletin of the Seismological Society of America, Vol. 98, No. 5, pp. 2231-2243,

Kurata, M., Kim, J., Lynch, J.P., van der Linden, G., Sedarat, H., Thometz, E., Hipley, P. and Sheng, L.H., "Inter- net-Enabled Wireless Structural Monitoring Systems: Development and Permanent Deployment at the New Carquinez Suspension Bridge", ASCE Journal of Structural Engineering

OPAC Calculation Book Volume 4 – Seismic Analysis Calculation.

SCS (2015) "Rapid Post-Earthquake Safety Evaluation of the New Carquinez Bridge Using Fragility Curves and Strong-Motion Data: Seismic Hazard Memorandum." March 18, 2015, SC Solutions, Inc., Sunnyvale CA

Shahi, S.K. and Baker, J. W. (2011) "An Empirically Calibrated Framework for Including the Effects of Near-Fault Directivity in Probabilistic Seismic Hazard Analysis." Bulletin of the Seismological Society of America, Vol. 101, No. 2, pp. 742–755

Sleeter, B.B., Calzia, J.P., Walter, S. R., Wong, F.L., and Saucedo G. J., (2004), "Earthquakes and faults in the San Francisco Bay Area (1970-2003)" http://pubs.usgs.gov/sim/2004/2848/, Last access, 085/27/2015;

Vosooghi, Ashkan and Saiidi, M. Saiid (2010), "Seismic Damage States and Response Parameters for Bridge Columns" ACI Special Publication Series SP-271, Structural Concrete in Performance –Based Seismic Design of Bridges, 271 CD, 2010

Vosooghi, Ashkan and Saiidi, M. Saiid (2012), Experimental Fragility Curves for Seismic Response of Reinforces Concrete Bridge Columns" ACI Structural Journal, November/December, 2012 pp 825-834

IDENTIFICATION AND VALIDATION OF NATURAL PERIODS AND MODAL DAMPING RATIOS FOR STEEL AND REINFORCED CONCRETE BUILDINGS IN CALIFORNIA

Angie Harris, Yijun Xiang, Farzad Naeim, and Farzin Zareian

Department of Civil & Environmental Engineering
University of California, Irvine

Abstract

Sixty-four buildings, with a total of 693 distinct seismic event and building direction records, are selected from the CSMIP database to identify modal quantities (i.e., natural periods and equivalent viscous damping ratios). The selected buildings include steel and reinforced concrete moment resisting frames (i.e., SMRF, and RCMRF), and reinforced concrete walls (RCW). Variation of modal quantities to structural system types, building height, amplitude of excitation, and system identification technique is studied. Results, tentatively, show median values for modal damping ratio are %2.7, %3.1, and %3.6 for RCW, RCMRF, and SMRF structures, with COVs in the order of 50%.

Introduction

Except for seismic design methods that are explicitly based on equivalent linearization, such as the Capacity Spectrum Method contained in ATC-40 (Applied Technology Council, 1996) or the Direct Displacement-Based Seismic Design (Priestly, Calvi and Kowalski, 2006), the use of equivalent damping in seismic design has been at best ambiguous and not well defined. This is a major issue for seismic design of new buildings, and retrofit of existing structures alike, because no matter what design method is implemented, an estimate of equivalent modal viscous damping is necessary for the structural design process. In the prescriptive (code-based) structural design approach the reduction in design forces attributable to expected nonlinear behavior of the structure, and the structural system's expected or assumed ductility, is primarily considered using the Response Modification Coefficient (i.e. R). In modern performance-based design (PBD), which relies on explicit nonlinear analyses of structures, the energy dissipated in the structure due to nonlinear hysteretic behavior of structural components is explicitly modeled.

In the modern PBD context the term structural damping refers not to the energy dissipated in the structure due to its nonlinear response, but, refers to sources of energy dissipation that are not explicitly considered in the structural model. There is an extensive body of research currently available on characterization and modeling of structural damping. A detailed literature review is presented in publications such as Spence & Kareem (2013) and ATC (2010). The research summarized here is in contrast with previous efforts in that it aims to use the vast data available from the network of CSMIP instrumented buildings to identify meaningful, and practical, structural period and damping coefficients to improve both the seismic

design provisions of the building codes and the practice of performance-based design and retrofit of structures. The main focus here is on three types of lateral load resisting systems: (1) Reinforced Concrete Walls (RCW), (2) Reinforced Concrete Moment Resisting Frames (RCMRF), and (3) Steel Moment Resisting Frames (SMRF). The results presented herein are preliminary and work is in progress to finalize the main objectives of this research.

Proper modeling of the structural damping must consider the effect of variables that are fundamental to energy dissipation in structures. These factors include, but are not limited to, the building height, building construction materials, cladding and other nonstructural components, characteristics of the structure-soil-foundation interface, and excitation amplitude (Jeary, 1986; 1997). For all practical purposes structural damping is currently modeled using equivalent linear viscous damping (ASCE, 2010; ATC, 2010; ASCE, 2007). This approach is considered largely due to its modeling convenience where damping is often expressed as a percentage of the critical damping (i.e., damping ratio) in one or more vibration modes– Rayleigh Damping, Caughey Damping–(Chopra, 2001). The effect of damping is accounted for at a global scale and through modal properties. It is general practice to use a damping ratio between 2% and 5% for the first mode of vibration; damping ratios for other modes are a matter of judgment. There have been efforts to provide guidelines for proper assignment of damping ratio by relating this parameter to building type (ASCE, 2007). For example, using a damping ratio as high as 10% for wood-frame construction are allowed based on ASCE (2007); however, the same standard restricts damping in most structures to 5% or less.

In the contemporary practice, equivalent viscous damping forces are assumed to be proportional to velocities and not dependent on the amplitude of excitation. However, experimental data shows that damping is primarily a function of displacement rather than velocity. In addition, the use of a linear viscous damping model in many cases produces inaccurate estimates of displacements and internal forces in members (Bernal, 1994; Charney, 2006; Hall, 2005; Zareian & Medina, 2010). These inaccurate estimates of internal forces are related to responses in which static equilibrium is not satisfied. Despite these implications, the benefits of using a simple, applied, and practical equivalent viscous damping for modeling energy dissipation in structural systems seems to outweigh its shortcomings.

Data Collection and Description

CSMIP database of instrumented buildings contains structural records from more than166 events (including main shocks and aftershocks) ranging in date from 1979 to 2015. Due to the recent move to digital recording, the data is skewed towards more recent earthquakes resulting in a sharp increase in the number of records obtained from more recent events. For the research study presented herein, a subset of the CSMIP database with the following constraints are utilized:

1. Only buildings whose lateral load resisting system contains Reinforced Concrete Walls (RCW), Reinforced Concrete Moment Resisting Frames (RCMRF), and Steel Moment Resisting Frames (SMRF) are considered.
2. Data sets corresponding to cases where noticeable structural damage was observed were eliminated. This includes notable building-record sets for the Van Nuys 7-story Hotel (CSMIP ID: 24386), Sherman Oaks 13-story Commercial Bldg. (CSMIP ID: 24322), El

Centro - Imperial County Services Building (CSMIP ID: 1260), and Los Angeles 19-story Office Bldg. (CSMIP ID: 24643).

3. The building-record sets corresponding to systems that utilized energy dissipating devices such as dampers and seismic isolation systems were eliminated.

Our selection process has resulted in a dataset that includes 64 buildings with a total of 693 distinct seismic event and building direction records. The list of the CSMIP instrumented buildings used in this study is presented in Appendix A (Table A.1). Among the 64 buildings used in this study, there are 30 RCW, 11 RCMRF, and 23 SMRF buildings with 370, 121, and 202 distinct seismic event and building direction records. Figure 1 provides further information on the statistics of the dataset used in this study; it illustrates the number of distinct seismic event and building direction records for each lateral load resisting system and building height category.

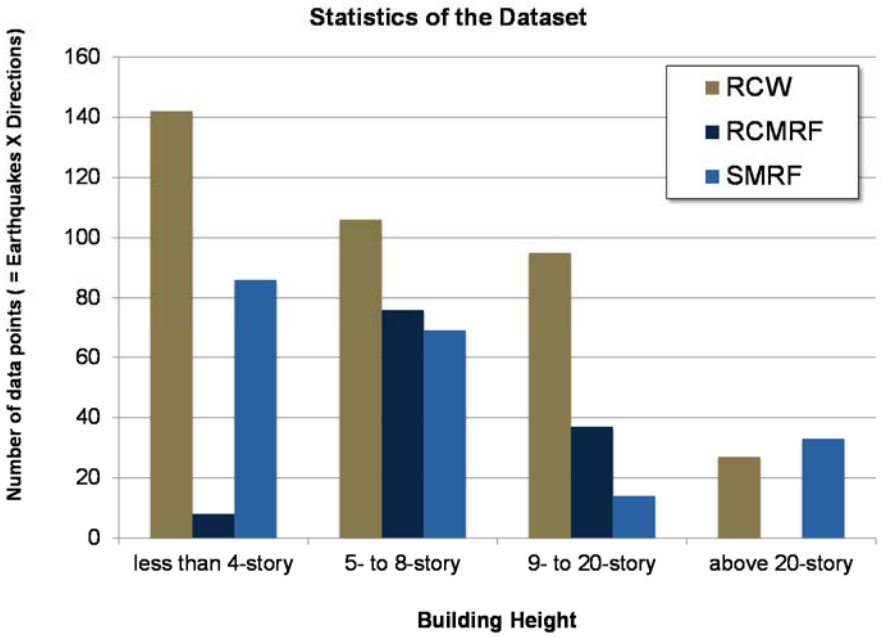

Figure 1. Statistics of the dataset used in this study

System Identification

Three system identification methods are used for assessing natural periods and structural damping of the dataset. These system identification methods include: (1) ERA-OKID method, (2) SRIM method, and (3) EFDD method. ERA-OKID and SRIM methods are input-output methods whereas EFDD is an output only method. A brief description of each methods is provided in the following.

ERA-OKID Method

ERA-OKID is an input-output time-domain system identification method which consists of two steps: (1) Eigensystem Realization Algorithm (ERA) to identify modal parameters, and (2) Observer/Kalman Identification (OKID) to increase the efficiency of the identification process. The ERA methodology is based on the discrete state-space model of the system

represented with two equations: $\mathbf{x}_{k+1} = \mathbf{\Phi x}_k - \mathbf{\Gamma u}_k$, and $\mathbf{y}_{k+1} = \mathbf{C x}_k - \mathbf{D u}_k$, where **Φ**, **Γ**, **C** and **D** are Markov parameters of the system that embody natural period and modal damping information, **x** and **y** are the state and output vectors, and *k* denotes time steps. A Hankel matrix is formed by packaging the output data **y** at every time step from *k* to *k*+2*s*-2 where integers *k* and *s* represent the beginning time step, and the number of following steps used for identification, respectively. Since $\mathbf{y}_k$ is generated by Markov parameters **Φ**, **Γ**, **C** and **D,** the Hankel matrix is expressed by Markov parameters as well. By the factorization of the Hankel matrix using singular value decomposition, a minimum realization of Markov parameters is derived from which modal parameters are estimated. The OKID approach aims to increase the stability of the system identification by eliminating the redundant part of the Hankel matrix from information obtained from input excitation. Detail description of the ERA-OKID system identification methods can be found in Luş *et al.* (1999).

SRIM Method

System Realization using Information Matrix (SRIM) is an algorithm based on the concept of data correlation. In this method, a state-space vector equation in the form of $\mathbf{y}_p(k) = \mathbf{O}_p\mathbf{x}(k) + \mathbf{T}_p\mathbf{u}_p(k)$ is developed where $\mathbf{y}_p(k)$ and $\mathbf{u}_p(k)$ are stacked output and input data from time step *k* to *k*+*p*-1 respectively, and the observability matrix $\mathbf{O}_p$ and the Toeplitz matrix $\mathbf{T}_p$ are stacked system matrices that embody **Φ**, **Γ**, **C** and **D** by the order from 1 to *p*-1. The integer *p* is chosen such that $p \geq n/m+1$, where *n* is the order of the system and *m* is the number of outputs. $\mathbf{O}_p$ and $\mathbf{T}_p$ are estimated from the auto-correlation and cross-correlation matrices of input and output data from which **Φ**, **Γ**, **C** and **D** and ultimately modal properties of the system are estimated. Detail description of the SRIM system identification methods can be found in Juang (1997).

EFFD Method

Enhanced Frequency Domain Decomposition (EFDD) is an output-only frequency domain system identification method (Ghahari *et al.* 2014). In this system identification method, response signals are decomposed into contributions from each mode by modal coordinates: $\mathbf{y}(t) = \phi\mathbf{q}(t)$. Preliminary mode shapes are estimated from the singular vectors of the correlation matrix of output signals in the frequency domain. These preliminary mode shapes are utilized to select meaningful regions of the correlation matrix of output signals in the frequency domain via a Modal Assurance Criterion. The select regions of the output correlation matrix in the frequency domain is transformed into the time domain from which modal properties can be estimated using logarithmic decrement technique.

Identified Natural Periods & Modal damping ratios for buildings

This section focuses on assessing the variation of modal properties with structural system types, construction materials, building height, amplitude of excitation. Only the data obtained from the SRIM system identification method is used—a short sensitivity study on variation of modal properties to system identification method is described. A separate investigation, using the system identification toolbox developed by Chang *et al.* (2012) called *SMIT*, was used to demonstrate that the SRIM system identification method provides a more stable and reasonable result compared to other system identification methods. *SMIT* was used to implement the SRIM method to identify modal properties of the buildings described in Table A.1.

A subset of the identified modal properties that this research group deemed reliable was selected for further analysis and discussion presented in this paper. The information that was temporarily discarded include 7 data-points for the Oakland - 24-story Residential Bldg. (CSMIP ID: 58483), and one data-point for the Hemet - 4-story Hospital (CSMIP ID: 12267).

Modal Properties and building Height

In general, the identified first mode period, T_1, and equivalent viscous damping ratio, ξ_1, follow the trend observed in previous research (Goel and Chopra, 1997, 1998; Satake et al., 2003; Bernal *et al*., 2012). Figure 2 shows the variation of T_1 and ξ_1 to building height. It is evident from the figure that estimation of both modal values is associated with high level of variability. Nevertheless, some of the trends identified by other researchers can be observed in the present data.

Figure 2a, 2c, and 2e shows that T_1 increases with building height for SMRF, RCMRF, and RCW structures. This increase saturates for taller buildings as illustrated in Figure 2a for SMRF buildings. The data was discriminated against amplitude of vibration, represented by PGA, and no specific trend was observed. ξ_1 in SMRF structures tends to decrease with increase in building height. This trend was observed by other researchers such as Jeary (1986), Satake *et al.* (2003), and Bernal *et al.* (2003). However, the same trend is not evident for RCMRF and RCW buildings. This is mostly due to high level of scatter in the estimated data especially information from low amplitude excitation (i.e. PGA < 0.01g).

Modal Properties and Ground Motion Intensity Measure

T_1 is slightly correlated with the recorded PGA at the location of the building; similar trend was observed in previous research by Satake et al. (2003) and Bernal *et al.* (2012). To show the sensitivity of T_1 to PGA, the data obtained from system identification is presented in a format that can be utilized for validation of ASCE 7-10 (2010) equation for estimation of building's period. According to ASCE 7-10, building period, denoted as T_a, is estimated as: $T_a = C_t {h_n}^x$ where C_t and x are coefficients specific to the building's lateral load resisting system, and h_n is the height of the building. ASCE 7-10 suggests that (C_t, x) is equal to $(0.028, 0.8)$ for RCMRF, $(0.016, 0.9)$ for SMRF, and $(0.02, 0.75)$ for RCW. Figures 3a, 3c, and 3e show the variation of coefficient C_t estimated from the data identified for this study (i.e. $C_t = T_1/H^x$) in which H is the height of the building from the CSMIP database, and x is equal to the value suggested by ASCE 7-10 for each lateral load resisting system. Despite large variability in estimated values of C_t, one can postulate that the code values, depicted with dash lines in Figures 3a, 3c, and 3e, mimic the central tendency of the data.

Sensitivity of ξ_1 to PGA is less than what one may expect. Figures 3b, 3d, and 3f show the variation of ξ_1 with PGA for SMRF, RCMRF, and RCW buildings. The expectation is that higher levels of excitation would lead to further energy dissipation, hence, larger value for ξ_1. One can postulate, however, that higher levels of excitation will result in reduction of the contribution of nonstructural elements in the energy dissipation effort, which are mostly coulomb-based, and increase the contribution of structural elements. The authors are currently studying this phenomenon. At this time, results show median values for modal damping ratio are %2.7, %3.1, and %3.6 for RCW, RCMRF, and SMRF structures, respectively, with COVs in the order of 50%.

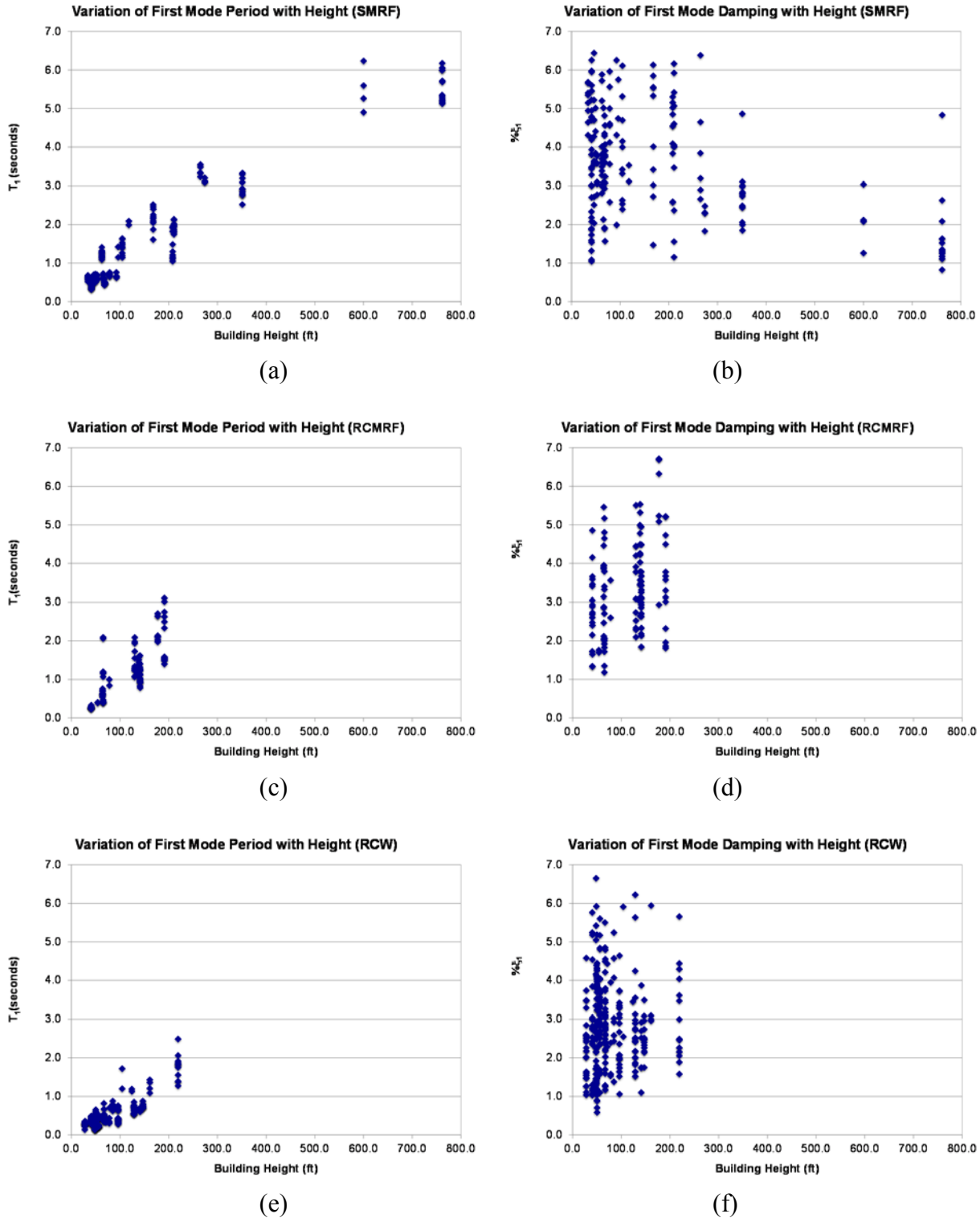

Figure 2. Variation of first mode period and damping ratio to building height: a,b) SMRF; c,d) RCMRF; and e,f) RCW (Identification method: SRIM)

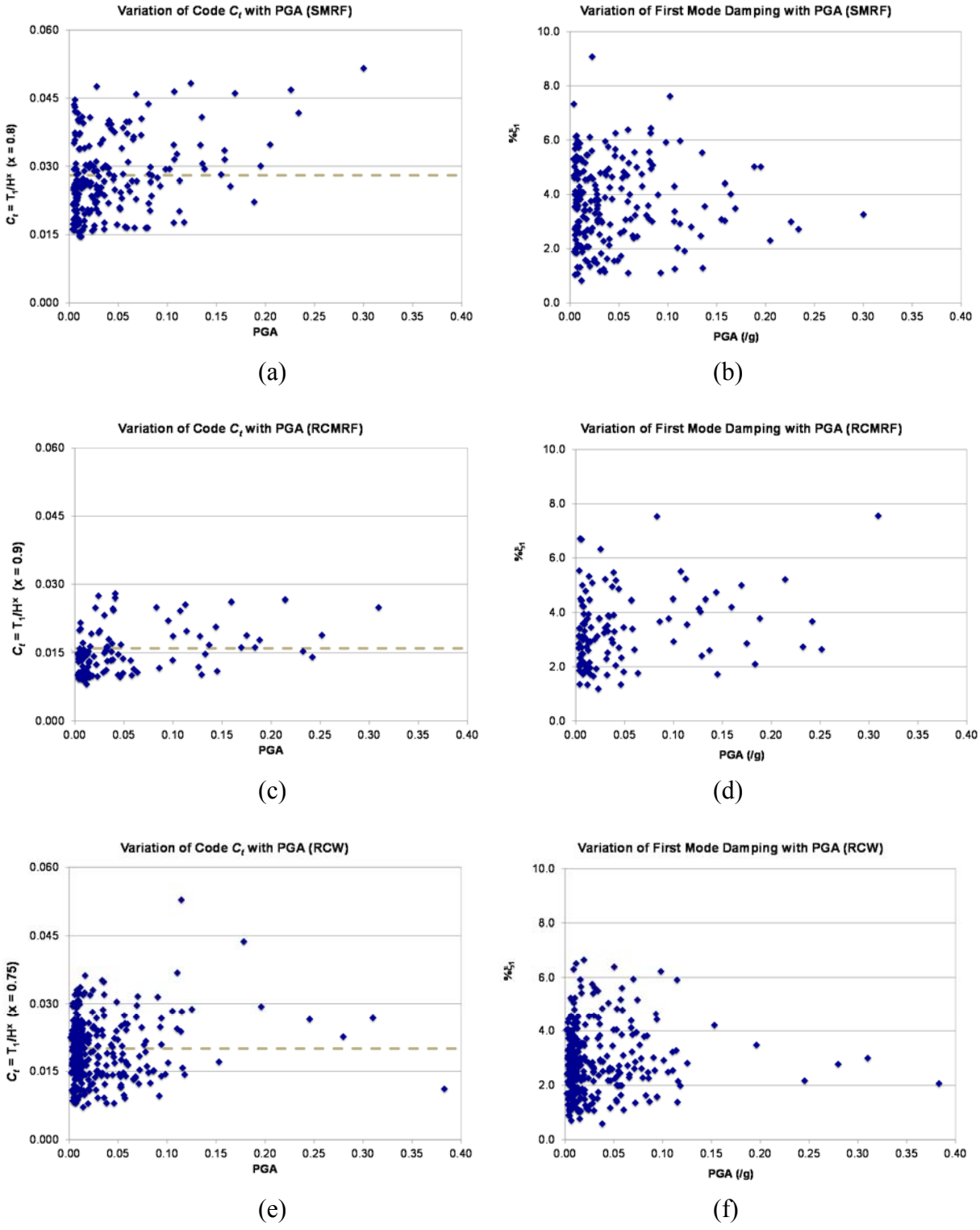

Figure 3. Variation of first mode period and damping ratio to PGA: a,b) SMRF; c,d) RCMRF; and e,f) RCW

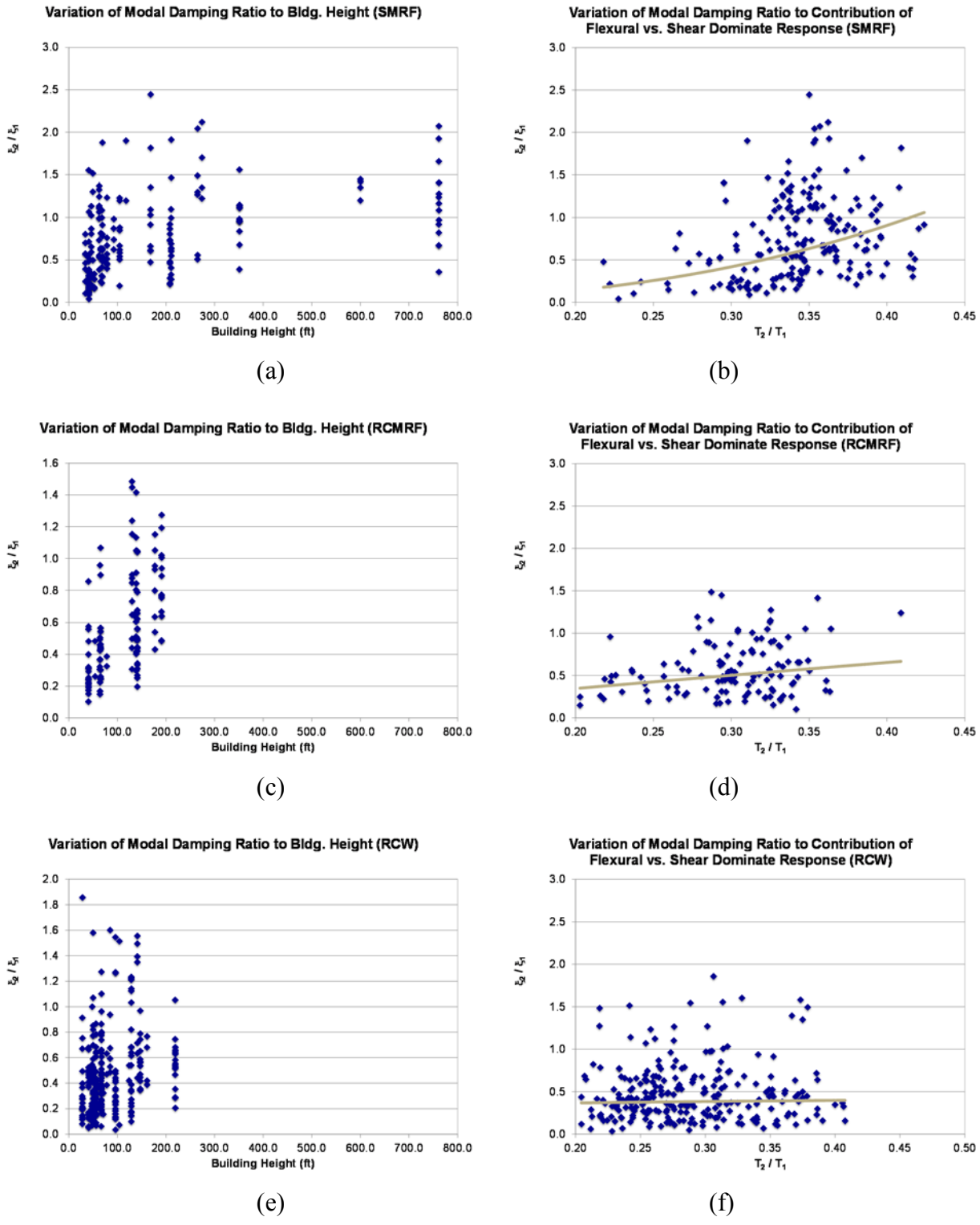

Figure 4. Sensitivity of first to second mode damping ratio to building height and ratio of first to second mode period: a,b) SMRF; c,d) RCMRF; and e,f) RCW (Identification method: SRIM)

Equivalent Viscous Damping at Higher Modes

Contrary to the suggestion by Satake et al. (2003), the results obtained in this research indicate that in average, the damping ratio of higher modes is smaller than the damping ratio of the first mode. Figures 4a, 4c, and 4e show the variation of ξ_2/ξ_1 with building height. The median of ξ_2/ξ_1 is 0.2, 0.3, and 0.4 for RCW, RCMRF, and SMRF structures, respectively. Bernal *et al.* (2010) suggests that ξ_n/ξ_1 is a function of the lateral load resisting systems behavior; it is expected that buildings with dominant flexural response (e.g. shear wall buildings, tall frame buildings) have different a trend in ξ_n/ξ_1 compared with buildings with dominant shear response (e.g. short frame buildings). In this study, relative contribution of flexural and shear response is measured with T_2/T_1 ratio; small values of T_2/T_1 (e.g. $T_2/T_1 < 0.3$) represents high levels of contribution from flexural mode to the building response, and otherwise. Figures 4b, 4d, and 4f show the variation of ξ_2/ξ_1 with T_2/T_1. It is evident from these plots that there is a positive correlation between ξ_2/ξ_1 with T_2/T_1. Large T_2/T_1 represents dominance of the shear mode of response to the total response and leads to further engagement of mechanisms that result in energy dissipation in higher modes.

Sensitivity of Identified Modal Properties to System Identification Method

Variability in estimated modal properties for a given building and ground motion is large and deserves further investigation. Figure 5a shows the statistics of the ratio of T_1 obtained from other system identification methods (i.e., ERA-OKID, and EFDD) to T_1 obtained from SRIM method for RCW structures. Figure 5b shows similar statistics for ξ_1. It is evident from these plots that estimation of T_1 is stable and relatively independent from the identification method. However, estimation of ξ_1 is highly variable and dependent on the system identification method.

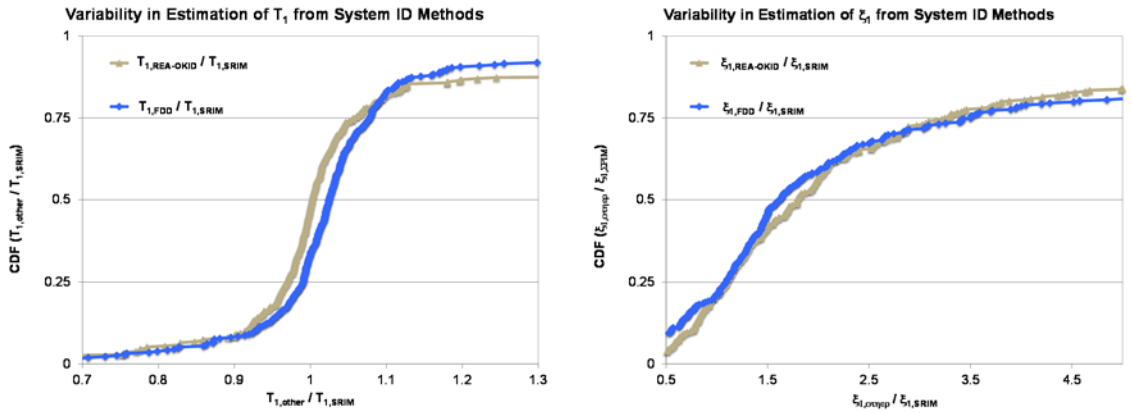

(a) (b)

Figure 5. Sensitivity of first to second modal properties to system identification technique: a)first mode period, b)first modal damping ratio

Future Work

The results presented herein are preliminary and work is in progress to finalize the main objectives of this research. The authors plan to further investigate the sources of variability in estimation of modal damping, and utilize new methods for system identification. Within this setting, Spence and Kareem (2013) have proposed a new method for identification of structural damping where it assumes that the total energy dissipated in a building has viscous and frictional nature. Results of their study shows that including the amplitude dependent energy dissipation term in calculation of structural damping coefficient increases the accuracy of such estimates and is in line with the physics of the building response.

The authors plan to compare the natural periods and structural damping ratios obtained for a subset of buildings obtained herein with the results obtained from previous CSMIP sponsored study (Naeim et al, 2005; 2006). In a previous CSMIP sponsored study (Naeim *et al*., 2004), a set of 75 buildings were carefully selected to highlight CSMIP instrumented buildings and value of seismic instrumentation in a database system and a visualization software titled CSMIP-3DV. A subset of 40 CSMIP-3DV buildings were utilized in a subsequent CSMIP sponsored study for development of damage detection techniques (Naeim *et al.*, 2005; 2006) and development of modal identification techniques using genetic algorithms (Alimoradi *et al.*, 2006; Alimoradi & Naeim, 2006).

Ultimately, the authors envision developing simplified/practical equations for estimation of natural periods and structural damping coefficient based on building information

Acknowledgements

The research reported in this paper was carried out with support from the California Strong Motion Instrumentation Program (CSMIP) through standard agreement 1014-962. This support is gratefully acknowledged. The authors would like to acknowledge the many valuable suggestions made by Dr. Reza Baghaei and lending his expertise in engineering system identification.

References

Alimoradi, A., Miranda, E., Taghavi, S., and Naeim, F. (2006), Evolutionary modal identification utilizing coupled shear-flexural response - implication for multistory buildings. Part I : Theory, *The Structural Design of Tall and Special Buildings*, **15**(1):, 51-65.

Alimoradi, A. and Naeim, F. (2006), Evolutionary modal identification utilizing coupled shear-flexural response - implication for multistory buildings. Part II: Application, *The Structural Design of Tall and Special Buildings*, **15**(1): 67-103.

ASCE-American Society of Civil Engineers (2010). *Minimum Design Loads for Buildings and Other Structures* (ASCE/SEI 7–10). American Society of Civil Engineers: Reston, VA.

ASCE-American Society of Civil Engineers (2007). *Seismic rehabilitation of existing buildings*. ASCE/SEI 41-06, Reston, VA.

ATC-Applied Technology Council (1996). *Seismic Evaluation and Retrofit of Concrete Buildings, Volume 1*. Appl. Technology Council: Redwood City, CA

ATC-Applied Technology Council (2010). *Modeling and acceptance criteria for seismic design and analysis of tall buildings*. PEER/ATC-72-1. Appl. Technology Council: Redwood City, CA

Bernal, D. (1994). Viscous damping in inelastic structural response. *ASCE Journal of Structural Engineering*, **120**(4): 1240-1254.

Bernal, D., Mozaffari Kojidi, S., Kwan, K., Döhler, M. (2012). Damping identification in buildings from earthquake records. *SMIP12 Seminar on Utilization of Strong-Motion Data, p. 39 - 56*.

Chang, M., Leonard, R.L., Pakzad, S.N. (2012). Structural Modal Identification Toolsuite (SMIT). Lehigh University.

Charney, F.A. (2006). Unintended consequence of modeling damping in structures: Rayleigh damping. *Procedures of 17th Analysis and Computation Specialty Conference*.

Chopra, A.K (2001). *Dynamics of structures*. Second Edition. Prentice Hall.

Hall, J.F. (2005). Problems encountered from the use (or misuse) of Raleigh damping. *Earthquake Engineering and Structural Dynamics*, **35**(5): 525-545.

Ghahari, S.F., Abazarsa, F., Ghannad, M.A., Celebi, M., Taciroglu, E. (2014). Blind modal identification of structures from spatially sparse seismic response signals. *Earthquake Engineering and Structural Dynamics*, **21**(6): 649-674.

Goel, R., Chopra, A.K. (1997). "Period formulas for moment-resisting frame buildings". *Journal of Structural Engineering*; **123**(11): 1454 – 1461.

Goel, R., Chopra, A.K. (1998). "Period formulas for concrete shear wall frame buildings". *Journal of Structural Engineering*; **124**(4): 426 – 433.

Jeary, A.P. (1986). "Damping in tall buildings – a mechanism and a predictor". Earthquake Engineering and Structural Dynamics; 14: 733 – 750.

Jeary, A. P. (1997). Damping in structures. *Journal of Wind Engineering and Industrial Aerodynamics*, 72: 345 – 55.

Juang, J. (1997). Identification of linear structural systems using earthquake induced vibration data. *Journal of Guidance, Control, and Dynamics*, **20**(3): 492-500.

Ljung, L. (1999) *System Identification: Theory for the User*, Upper Saddle River, NJ, Prentice-Hal PTR.

Luş, H., Betti, R., Longman, R. W. (1999). Identification of linear structural systems using earthquake induced vibration data. *Earthquake Engineering and Structural Dynamics*, 28:1449-1467.

Naeim, F., Lee, H., Bhatia, H., Hagie, S. and Skliros, K (2004). CSMIP Instrumented Building Response Analysis and 3-D Visualization System (CSMIP-3DV). *SMIP04 Seminar on Utilization of Strong-Motion Data*, p. 83 - 102.

Naeim, F., Hagie, S. and Alimoradi, A. (2005). Automated Post-Earthquake Damage Assessment and Safety Evaluation of Instrumented Buildings. *SMIP05 Seminar on Utilization of Strong-Motion Data*, p. 71 - 88.

Naeim, F., Lee, H., Hagie, S., Bhatia, H., Alimoradi, A., and Miranda, E. (2006).Three-dimensional analysis, real-time visualization, and automated post-earthquake damage assessment of buildings, *The Structural Design of Tall and Special Buildings*, **15**(1): 105-138.

Priestley, M.J.N., Calvi, M.J., Kowalsky, M.J. (2006). *Displacement-Based Seismic Design of Structures*. IUSS Press.

Spence, S., Kareem, A. (2014). Tall Buildings and Damping: A Concept-Based Data-Driven Model. *J. Struct. Eng.*, **140**(5): 04014005.

Zareian, F., Medina, R. (2010). A practical method for proper modeling of structural damping in inelastic plane structural systems. *Computers and Structures*; **88**(1-2): 45-53

Appendix A

Table A.1. Set of buildings used in this study

Index	Building Station	Primary VLLR	Building Height (ft)	Number of Stories	Number of Eqs X Dir
1	58224	RCW	28.0	2	24
2	58334	RCW	49.0	3	18
3	58348	RCW	40.6	3	20
4	58503	RCW	47.5	3	12
5	12267	RCW	48.0	4	10
6	12284	RCW	50.0	4	20
7	58488	RCW	50.0	4	10
8	68387	RCW	50.0	4	2
9	68489	RCW	50.0	4	2
10	89770	RCW	50.0	4	24
11	13620	RCW	67.0	5	2
12	14311	RCW	67.0	5	2
13	23285	RCW	67.0	5	28
14	23287	RCW	56.0	6	36
15	24514	RCW	96.0	6	10
16	24655	RCW	67.0	6	12
17	58394	RCW	84.8	6	2
18	58462	RCW	84.8	6	8
19	13329	RCW	0.0	8	6
20	47459	RCW	141.0	10	4
21	57355	RCW	141.0	10	7
22	57356	RCW	96.0	10	14
23	58364	RCW	128.5	10	22
24	13589	RCW	146.9	11	14
25	58337	RCW	0.0	11	14
26	24680	RCW	114.9	12	4
27	25339	RCW	114.9	12	12
28	58479	RCW	241.0	18	4
29	58480	RCW	219.0	24	4
30	58483	RCW	219.0	24	23
31	57355	RCMRF	64.0	4	6
32	24454	RCMRF	64.0	4	2
33	23511	RCMRF	138.5	5	20
34	24579	RCMRF	65.2	7	14
35	24463	RCMRF	65.2	7	16
36	24322	RCMRF	65.2	7	14
37	24571	RCMRF	65.2	7	12
38	24464	RCMRF	130.0	9	8
39	58490	RCMRF	141.0	10	2
40	12493	RCMRF	191.0	13	12
41	24386	RCMRF	191.0	13	15
42	13312	SMRF	41.0	2	10
43	24288	SMRF	41.0	2	16
44	24609	SMRF	41.0	2	8
45	58532	SMRF	41.0	2	4
46	23516	SMRF	46.2	3	18
47	24104	SMRF	34.0	3	16
48	14533	SMRF	46.2	3	6
49	14323	SMRF	46.2	3	2
50	58261	SMRF	52.5	4	6
51	24198	SMRF	78.5	5	8
52	24629	SMRF	78.5	5	14
53	23515	SMRF	69.0	5	2
54	58506	SMRF	62.5	6	12
55	24370	SMRF	92.5	6	13
56	24566	SMRF	62.5	6	10
57	57562	SMRF	62.5	6	4
58	68669	SMRF	104.5	7	6
59	58755	SMRF	208.0	13	4
60	23634	SMRF	208.0	13	10
61	57357	SMRF	351.2	32	12
62	23481	SMRF	600.0	47	10
63	12299	SMRF	761.5	57	7
64	24569	SMRF	761.5	57	4

IDENTIFICATION OF SOIL-FOUNDATION IMPEDANCE FUNCTION FROM SEISMIC RESPONSE SIGNALS OF INSTRUMENTED BUILDINGS

S. Farid Ghahari, Fariba Abazarsa, and Ertugrul Taciroglu

Department of Civil and Environmental Engineering
University of California, Los Angeles, CA

Abstract

Substructure method is generally used in engineering practice to take Soil-Structure Interaction (SSI) effects into account in seismic design. In this method, soil is modeled using discrete spring elements—Impedance Functions (IF)—that are attached to the superstructure; and the Foundation Input Motions (FIMs) are applied at the remote ends of these springs. While the application of the substructure method is simple and it is computational costs is low, the determination of FIMs and the IFs are generally quite challenging. In the present study, we present a new approach to identify IFs and FIMs from response signals recorded during earthquakes. To do so, we use a flexible-based Timoshenko beam model is to represent the structure and its soil-foundation system and updated the parameters of this model such that its responses match real-life data. The impedance functions of a large set of instrumented buildings are identified using this novel method and compared against various analytical solutions. Additionally, a computer program named CSMIP-CIT is developed that automatically extracts data for selected buildings in the CSMIP database and applies the method developed in this study.

Introduction

Soil- Structure Interaction (SSI) has been a research subject for more than 40 years (Jennings & Kuroiwa, 1968; Richat, 1975; Wolf, 1976). SFSI effects can be classified into two distinct effects: *kinematic* and *inertial* (Wolf & Deeks, 2004). Foundation's stiffness and distinct geometry alter earthquake excitations experienced by the system, dubbed the Foundation Input Motions (FIMs), which are different from the Free-Field Motions (FFM)s that would have been recorded in the absence of the foundation. Inertial interaction effects are due to the mass of the foundation-superstructure system, which imparts inertial forces onto the surrounding soil and causes the foundation to experience a response different from the FIM. Due to the inertial effects, the vibrating structure operates as a wave source and alters the wave field around the foundation system. Consequently, motions should be recorded adequately away from the structure to be qualified as FFM (Abrahamson *et al.*, 1991).

The *direct* and the *substructure* methods are two approaches used for taking SSI effects into account in seismic response analyses. In the direct method, a Finite Element (FE) model of the complete soil-structure system is created wherein the soil medium is represented as a semi-infinite domain (Pak & Guzina, 1999; Rizos & Wang, 2002). Due to its labor-intensive finite element model development and computational cost, the direct method is typically avoided in engineering practice. In the substructure method, the SSI problem is decomposed into three

distinct parts that are combined to formulate the complete solution (Stewart *et al.*, 1998). These three parts are (*i*) estimation of FIMs, (*ii*) determination of the frequency-dependent soil-foundation Impedance Functions (IFs), and (*iii*) dynamic analysis of the super-structure supported on a compliant base represented by the IFs and subjected to the FIMs (Wolf & Deeks, 2004).

Accurate estimation of FIMs and IFs control the accuracy of the substructure method. However, available formulations for estimation/determination of FIMs and IFs are primarily limited to analytical and numerical studies (Gazetas, 1983; Iguchi & Luco, 1981; Çelebi *et al.*, 2006) and experimental data (Tileylioglu *et al.*, 2010), which only represent simple cases—e.g., surface circular foundation on homogenous half space. Motivated by this, we seek here a robust and broadly applicable method to identify IFs and FIMs from earthquake-induced response signals recorded on instrumented buildings, because such data actually represents full-scale experimental data with actual environmental conditions. Recently, we have devised two distinct approaches for this purpose, dubbed *Tier A*, which involves the identification of a frequency-dependent IF from several modes of a multi-degree-of-freedom structure (tall building), and *Tier B*, which involves investigating the frequency-dependency using a large number of buildings, but concentrating on the fundamental mode.

In Tier A, the superstructure is modeled with relatively high detail using the Finite Element (FE) method. This is because SSI effects at higher modes are typically minor (Jennings & Bielak, 1973), and extrating that information requires a detailed representation of the super-structure. Then, the soil-foundation stiffnesses are identified such that the response of the FE model supported on soil-foundation springs match the measurements. We validated the Tier A approach through earthquake data recorded on the Millikan Library (Ghahari *et al.*, 2015a), and were able to identify soil-foundation dynamic stiffness values at several modes. Due to computational expense of Tier A, we devised the second approach—Tier B—in which the superstructure is represented by using a continuous Timoshenko beam model, which has a small number of model parameters (Taciroglu *et al.*, 2015; Taciroglu and Ghahari, 2015). Such a simplified model generally precludes the investigation of the frequency-dependency of the foundation system of a given building, but it can be easily applied to a large set of buildings. Therefore, with the Tier B approach, it was possible to investigate different classes of foundation systems' frequency-dependency by using several buildings with various fundamental frequencies, rather than by using several modes of a single building. In the present study, we introduce a new version of Tier B, which is currently implement it into a Matlab toolbox named CSMIP-CIT. In what follows, the formualtion details of the new Tier B approach are presented first. This is followed by various representative results obtained through the application of CSMIP-CIT to a large set of buildings.

Identification Methods

Dynamic Response of Timoshenko Beam Using Modal Superposition

Let's assume a Timoshenko beam on a sway-rocking foundation. Partial differential equations governing a Timoshenko beam (Timoshenko, 1921) are given by (Huang, 1961)

$$\mathbf{M}\ddot{\boldsymbol{v}}(x,t) + \mathbf{K}\,\boldsymbol{v}(x,t) = \boldsymbol{f}(x,t)\,, \tag{1}$$

with

$$\mathbf{K} = \begin{bmatrix} GA_s \frac{d^2}{dx^2} & -GA_s \frac{d}{dx} \\ GA_s \frac{d}{dx} & EI \frac{d^2}{dx^2} - GA_s \end{bmatrix}, \quad \mathbf{M} = \begin{bmatrix} -\rho A & 0 \\ 0 & -\rho I \end{bmatrix} \tag{2}$$

$$\boldsymbol{v}(x,t) = \begin{bmatrix} y(\mathrm{x},t) \\ \alpha(x,t) \end{bmatrix} \tag{3}$$

$$\boldsymbol{f}(x,t) = \begin{bmatrix} P(x,t) \\ M(x,t) \end{bmatrix} \tag{4}$$

where a double dot indicates a second time-derivative. E, G, ρ, and A are the Young's and shear moduli, mass density, and section area, respectively. To consider the non-uniform distribution of shear stress on section, $A_s = \kappa A$ is used as the effective shear cross-sectional area, where κ can be assumed as 0.85 for rectangular sections (Cowper, 1966). The terms $y(x,t)$ and $\alpha(x,t)$ denote, respectively, the lateral displacement and bending-induced rotation of section with respect to the input excitations. $P(x,t)$ and $M(x,t)$ represent the distributed forces and moments, acting on the beam. For a flexible-base beam under horizontal earthquake base excitations $P(x,t) = \rho A \ddot{u}_g(t)$ and $M(x,t) = 0$ (we assume rocking ground motion is negligible). Using modal superposition (Clough & Penzien, 1975), the beam's response can be described as

$$\boldsymbol{v}(x,t) \approx \sum_{j=1}^{n} \boldsymbol{\varphi}_j(x)\, q_j(t) \tag{5}$$

with

$$\boldsymbol{\varphi}_j(x) = \begin{bmatrix} W_j(x) \\ \Theta_j(x) \end{bmatrix} \tag{6}$$

in which $W_j(x)$ and $\Theta_j(x)$ are two functions describing the j-th normal mode shapes for lateral displacement and rotation deformations, respectively. Function $q_j(t)$ denotes j-th modal coordinate, which is the relative displacement of a Single Degree Of Freedom (SDOF) system under $P(x,t)$ multiplied by the contribution factor. Eq. (5) is expressed as an approximation, because only n modes are used whereas the actual system has an infinite number of modes.

In what follows, the calculation of the aforementioned mode shapes (and natural frequencies) is briefly reviewed. Under free vibration conditions, both the lateral displacement and the bending-induced rotation are separable as $y(x,t) = W(x)T(t)$ and $\alpha(x,t) = \Theta(x)T(t)$. So, Eq. (1) can be presented in the frequency domain as (Han *et al.*, 1999)

$$\mathbf{K} \begin{bmatrix} W(x) \\ \Theta(x) \end{bmatrix} = \omega^2 \mathbf{M} \begin{bmatrix} W(x) \\ \Theta(x) \end{bmatrix} \tag{7}$$

By solving Eq. (7), the normal mode shapes for $\omega_j < \sqrt{GA_s/\rho I}$ are[1]

$$W_j(x) = c_1^j \sin(p^j \tilde{x}) + c_2^j \cos(p^j \tilde{x}) + c_3^j \sinh(q^j \tilde{x}) + c_4^j \cosh(q^j \tilde{x}) \tag{8}$$

$$\Theta_j(x) = d_1^j \sin(p^j \tilde{x}) + d_2^j \cos(p^j \tilde{x}) + d_3^j \sinh(q^j \tilde{x}) + d_4^j \cosh(q^j \tilde{x}) \tag{9}$$

[1]For brevity, we only present formulation for frequencies below the critical frequency. For frequencies above the critical frequency similar formulation with a few modifications are obtained.

with $\tilde{x} = x/L$, $p^j = \left|\text{Imag}(m_1^j)\right|$, and $q^j = m_3^j$. m_1^j and m_3^j are wave numbers corresponding to each mode and are calculated from following relationship

$$m_{1,3}^j = \sqrt{\frac{-\left(b_j^2 s^2 + b_j^2 R^2\right) \mp \sqrt{\left(b_j^2 s^2 + b_j^2 R^2\right)^2 - 4\left(b_j^4 s^2 R^2 - b_j^2\right)}}{2}} \tag{10}$$

with dimensionless parameters as

$$s^2 = \frac{EI}{GA_s L^2}, \quad b_j^2 = \frac{\rho A {\omega_j}^2 L^4}{EI}, \quad R^2 = \frac{I}{AL^2} \tag{11}$$

Unknown coefficients c_i^j and d_i^j are related parameters as

$$\begin{aligned} d_1^j = \lambda_1^j c_2^j = \tfrac{1}{L}\left(\tfrac{b_j^2 s^2}{p^j} - p^j\right) c_2^j, \quad d_2^j = \lambda_2^j c_1^j = \tfrac{1}{L}\left(-\tfrac{b_j^2 s^2}{p^j} + p^j\right) c_1^j, \\ d_3^j = \lambda_3^j c_4^j = \tfrac{1}{L}\left(\tfrac{b_j^2 s^2}{q^j} + q^j\right) c_4^j, \quad d_4^j = \lambda_4^j c_3^j = \tfrac{1}{L}\left(\tfrac{b_j^2 s^2}{q^j} + q^j\right) c_3^j \end{aligned} \tag{12}$$

To find c_i^j, we must apply the boundary conditions on the free vibration response. For the problem at hand, the shear force and bending moment at the base must be equal to the force and moment produced by the sway and rocking springs, respectively. Also, the shear force and bending moment at top of the beam must be zero. By applying these four boundary conditions, we have the following system of homogenous linear equations

$$\begin{bmatrix} (L\lambda_2^j - p^j) & k_T & (L\lambda_4^j - q^j) & k_T \\ -k_R \lambda_2^j & p^j \lambda_1^j & -k_R \lambda_4^j & q^j \lambda_3^j \\ (L\lambda_2^j - p^j)\, cos(p^j) & (L\lambda_1^j + p^j)\, sin(p^j) & (L\lambda_4^j - q^j)\, cosh(q^j) & (L\lambda_3^j - q^j)\, sinh(q^j) \\ -p^j \lambda_2^j\, sin(p^j) & p^j \lambda_1^j\, cos(p^j) & q^j \lambda_4^j\, sinh(q^j) & q^j \lambda_3^j\, cosh(q^j) \end{bmatrix} \begin{bmatrix} c_1^j \\ c_2^j \\ c_3^j \\ c_4^j \end{bmatrix} = \mathbf{0} \tag{13}$$

where the additional dimensionless parameters are given by

$$k_T = \tfrac{K_T}{GA_s/L}, \quad k_R = \tfrac{K_R}{EI/L} \tag{14}$$

To avoid trivial solutions in Eq. (13), the determinant of the matrix must be zero. Equation obtained by this constrain is dubbed the *frequency equation*, through which the natural frequencies ω_j are found. For each natural frequency, the unknown coefficients c_i^j can be obtained by solving Eq. (13) after assigning one of the c_i^j an arbitrary constant value (for example, $c_4^j = 1$).

To calculate the modal coordinates, modal orthogonally with respect to matrix **M** (Han *et al.*, 1999) is used. Hence, $q_j(t)$ can be identified from the equation below, deduced from Eq. (1)

$$\ddot{q}_j(t) + {\omega_j}^2\, q_j(t) = \frac{L_j^*}{m_j^*} \ddot{u}_g(t) \tag{15}$$

where and L_j^* and m_j^* are respectively the generalized influence factor and mass, defined as

$$L_j^* = \rho A \int_0^L W_j(x)\, dx\,, \quad m_j^* = \int_0^L \boldsymbol{\varphi}_j(x)^T\, \mathbf{M}\, \boldsymbol{\varphi}_j(x) \tag{16}$$

Up to now, we assumed that the system has normal mode shapes—i.e., the mode shapes and undamped natural frequencies are independent from damping effects (classical damping). To consider damping, while retaining the normal mode assumption, we add a term $2\,\omega_j\,\xi_j\,\dot{q}_j(t)$ to Eq. (15) to make it similar to the response of a damped SDOF system (Chopra, 2001). This damping term is equivalent to adding a $\mathbf{C}\,\dot{\boldsymbol{v}}(x,t)$ term to the matrix form of Eq. (1), in which $\mathbf{C}$ is a matrix such that

$$\int_0^L \boldsymbol{\varphi}_j(x)^T\,\mathbf{C}\,\boldsymbol{\varphi}_k(x) = 2\,m_j^*\omega_j\,\xi_j\delta_{jk} \tag{17}$$

where δ_{jk} is Kronecker delta. It is expedient to note here that we are not interested in knowing the actual form of matrix $\mathbf{C}$, because only the modal damping is important. We just assumed this form to make the formulation as simple as possible and to have real-valued mode shapes.

Identification Method

According to the previous section, the absolute acceleration of the building under horizontal base acceleration, which is recorded in real life, can be written as

$$\ddot{y}^t(x,t) = \sum_{j=1}^{n} W_j(x)\; + \ddot{u}_g(t) \tag{18}$$

where $\ddot{q}_j(t)$ is relative acceleration of a SDOF system under $L_j^*\ddot{u}_g(t)/m_j^*$. For the proposed identification method, we assume that the absolute acceleration of a flexible-base building is available in three levels—namely, the foundation level $\ddot{y}^t(0,t)$, mid-height level $\ddot{y}^t(x_m,t)$, and roof level $\ddot{y}^t(L,t)$. According to Eqs. (15) and (18) each of these response signals can be expressed in the frequency domain as

$$\ddot{y}^t(x,\omega) = \left[\sum_{j=1}^{n} W_j(x)\;\frac{L_j^*}{m_j^*}H_j(\omega) + 1\right]\ddot{u}_g(\omega) \tag{19}$$

with

$$H_j(\omega) = \frac{-\omega^2}{{\omega_j}^2 - \omega^2 + 2i\xi_j\omega_j\omega} \tag{20}$$

Accordingly, the response at the mid-height and the roof levels can be predicted by the response of the foundation level by eliminating the input excitation as in

$$\ddot{y}^t(x,\omega) = \frac{\left[\sum_{j=1}^{n} W_j(x)\;\frac{L_j^*}{m_j^*}H_j(\omega) + 1\right]}{\left[\sum_{j=1}^{n} W_j(0)\;\frac{L_j^*}{m_j^*}H_j(\omega) + 1\right]}\ddot{y}^t(0,\omega) \tag{21}$$

Therefore, by defining and solving a proper minimization problem, the unknown parameters of the system can be identified. This approach has been successfully used by Lignos and Miranda (2014) to identify the input motion of fixed-base structures who linked shear and flexural beams to represent their parametric model. We define the following optimization problem here

$$\min_{\bar{b},s,k_T,k_R,\xi_1,\ldots,\xi_n} \left\|\ddot{y}^t(x_m,t) - \ddot{\tilde{y}}^t(x_m,t)\right\| + \left\|\ddot{y}^t(L,t) - \ddot{\tilde{y}}^t(L,t)\right\| \tag{22}$$

where $\ddot{\tilde{y}}^t(x_m, t)$ and $\ddot{\tilde{y}}^t(L, t)$ denote the response signals at mid-height and roof levels predicted by Eq. (21) and transformed to the time domain through Inverse Fourier Transform. We replace the dimensionless parameter b with $\bar{b}$ to make it mode-independent. This optimization problem is not convex and may have several local minima. We, therefore devise constraints to decrease the possibility of being trapped in a local minimum. As the first flexible-base natural frequency can be easily detected from the Fourier spectrum of the roof response using Peak Picking, we add this information as a constraint to the optimization problem. Moreover, we start the optimization procedure with many random starting points.

Once the unknown parameters are identified by solving the optimization problem, the, unknown input motion, $\ddot{u}_g(\omega)$, can be back calculated through Eq. (19) using any of the available measured response signals. Additionally, the foundation rocking response can be estimated by converting the foundation translational response, as in

$$\ddot{\alpha}(x, \omega) = \frac{\left[\sum_{j=1}^{n} \Theta_j(0) \frac{L_j^*}{m_j^*} H_j(\omega)\right]}{\left[\sum_{j=1}^{n} W_j(0) \frac{L_j^*}{m_j^*} H_j(\omega) + 1\right]} \ddot{y}^t(0, \omega) \tag{23}$$

By carrying out the optimization procedure mentioned above, the modal damping ratios of flexible-base system are identified.

To identify the pseudo-flexible and fixed base damping ratios, we can easily define optimization problems similar to Eq. (22). For the pseudo-flexible model, we can predict the response of mid-height and roof levels by analyzing a pseudo-flexible base Timoshenko beam subjected to horizontal foundation response, using Eqs. (19) and (20). In this case, all modal properties—i.e., ω_j, ξ_j, m_j^*, L_j^*, and $W_j(x)$—must be calculated for a pseudo-flexible Timoshenko beam, while $\ddot{u}_g(\omega)$ must be $\ddot{y}^t(0, \omega)$. The modal properties of the pseudo-flexible base Timoshenko beam model can be easily obtained through the same approach as that used for the flexible base model, by using appropriate boundary conditions. That is, the mode shapes have the same form as Eqs. (8) and (9), but the unknown coefficients must be calculated by employing proper boundary conditions—to wit, by having zero base displacement, by equating the base moment to moment-induced in the rocking spring, and by having zero shear force and bending moment at the top. Based on these boundary conditions, Eq. (13) can be converted to

$$\begin{bmatrix} 0 & 1 & 0 & 1 \\ -k_R\lambda_2^j & p^j\lambda_1^j & -k_R\lambda_4^j & q^j\lambda_3^j \\ (L\lambda_2^j - p^j)\cos(p^j) & (L\lambda_1^j + p^j)\sin(p^j) & (L\lambda_4^j - q^j)\cosh(q^j) & (L\lambda_3^j - q^j)\sinh(q^j) \\ -p^j\lambda_2^j \sin(p^j) & p^j\lambda_1^j \cos(p^j) & q^j\lambda_4^j \sinh(q^j) & q^j\lambda_3^j \cosh(q^j) \end{bmatrix} \begin{bmatrix} c_1^j \\ c_2^j \\ c_3^j \\ c_4^j \end{bmatrix} = \mathbf{0} \tag{24}$$

All other modal properties (ω_j, m_j^*, and L_j^*) are calculated identically to the flexible base model, but by using these new frequency equations and mode shapes. The damping ratio is then identified by solving a minimization problem such that the predicted mid-height and roof level responses match the recorded responses.

To identify the fixed-base damping ratio, we use the same approach again—that is, we can predict the response at mid-height and roof levels by analyzing a fixed-base Timoshenko

beam subjected to horizontal and rocking foundation responses and by minimizing the difference between predicted and recorded signals. Note that foundation-rocking response is already predicted through Eq. (23). To predict the response of a fixed-base Timoshenko beam model under base horizontal and rocking excitations, earthquake-induced distributed inertia force $P(x,t)$ introduced in Eq. (1) is equal to $\rho A\ddot{u}_g(t) + \rho Ax\ddot{\theta}_g(t)$, while $M(x,t) = \rho I\ddot{\theta}_g(t)$ (where $\ddot{u}_g(t)$ and $\ddot{\theta}_g(t)$ are the horizontal and rocking foundation accelerations in our case). So, Eq. (19) is rewritten as

$$\ddot{y}^t(x,\omega) = \left[\sum_{j=1}^{n} W_j(x)\ \frac{L_j^*}{m_j^*} H_j(\omega) + 1\right]\ddot{u}_g(\omega) + \left[\sum_{j=1}^{n} W_j(x)\ \frac{\bar{L}_j^*}{m_j^*} H_j(\omega) + x\right]\ddot{\theta}_g(\omega) \tag{25}$$

where L_j^* and m_j^* are calculated using Eq. (16) and $H_j(\omega)$ is calculated using Eq. (20), in which fixed-base mode shapes and natural frequencies must be used. $\bar{L}_j^*$ is the generalized influence factor for rocking excitation and must be calculated as follows

$$\bar{L}_j^* = \rho\, I \int_0^L \Theta_j(x)\, dx + \rho\, A \int_0^L x\, W_j(x)\, dx \tag{26}$$

using the fixed-base mode shapes. To calculate the fixed-base mode shapes (and natural frequencies), proper boundary conditions (zero displacement and rotation at bottom, and zero shear and moment at top) will yield to the following frequency equations

$$\begin{bmatrix} 0 & 1 & 0 & 1 \\ \lambda_2^j & 0 & \lambda_4^j & 0 \\ (L\lambda_2^j - p^j)\cos(p^j) & (L\lambda_1^j + p^j)\sin(p^j) & (L\lambda_4^j - q^j)\cosh(q^j) & (L\lambda_3^j - q^j)\sinh(q^j) \\ -p^j\lambda_2^j \sin(p^j) & p^j\lambda_1^j \cos(p^j) & q^j\lambda_4^j \sinh(q^j) & q^j\lambda_3^j \cosh(q^j) \end{bmatrix} \begin{bmatrix} c_1^j \\ c_2^j \\ c_3^j \\ c_4^j \end{bmatrix} = \mathbf{0} \tag{27}$$

Based on the identification method presented above (i.e., the Tier B approach), we developed a Matlab (2013) toolbox named CSMIP-CIT (Ghahari *et al.*, 2015b). In addition to the identification capabilities, this software offers a user-friendly graphical tools for classification of *all* buildings instrumented through the California Strong Motion Instrumentation Program (CSMIP) that are available in the Center for Engineering Strong Motion Database (CESMD)[2]. CSMIP-CIT (Figure 1) is able to connect to the data center through Internet and download the data, and to apply the proposed identification approach.

[2] www.strongmotioncenter.org

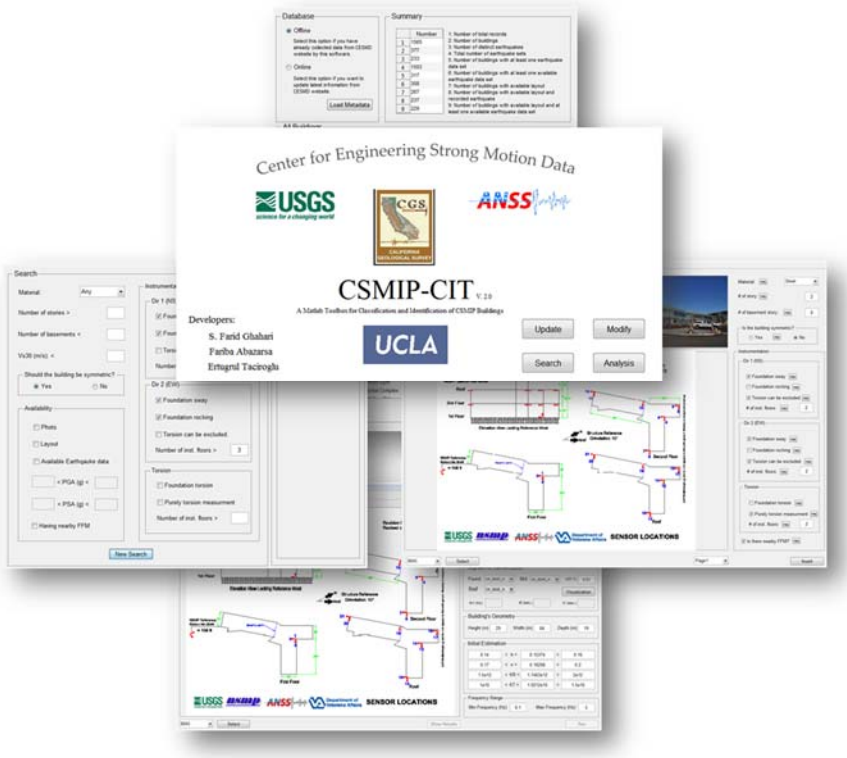

Figure 1. Graphical user interface of the CSMIP-CIT software (Ghahari *et al.*, 2015b).

A Validation Example

To validate the identification approach presented above, we use real-life earthquake data recorded on the Millikan Library. The Millikan Library—named after Robert Andrew Millikan, who is a 1923 Nobel-laureate experimental physicist—is a reinforced concrete building with a basement level and 9 stories above the ground. It is located on the campus of California Institute of Technology (Caltech) in Pasadena, California, and was constructed during 1966 to 1967. It is one of the world's most densely instrumented buildings, and due to its structural and soil conditions, it has been the subject of numerous studies on soil-structure interaction (see, for example, Jennings & Kuroiwa, 1968; Luco, *et al.*, 1988; Bradford, *et al.*, 2004; Snieder & Safak, 2006; Todorovska, 2009; Cheng & Heaton, 2013). We have recently analyzed the response signals of the Millikan Library recorded during the 2002 Yorba Linda earthquake using a new blind modal identification method (Ghahari *et al.*, 2015a). Significant soil-structure interaction effects in the North-South (NS) direction have been already detected by many researchers (e.g., Todorovska, 2009). So, we use the signals and the identified modal properties of this particular direction here, for comparisons.

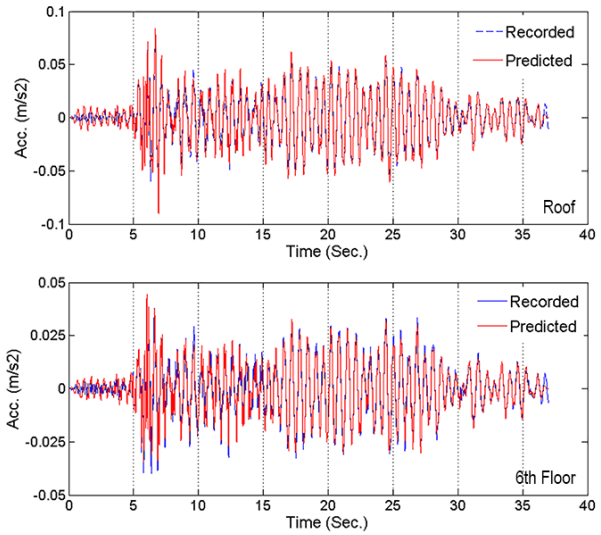

Figure 2. Comparison between response signals recorded and predicted.

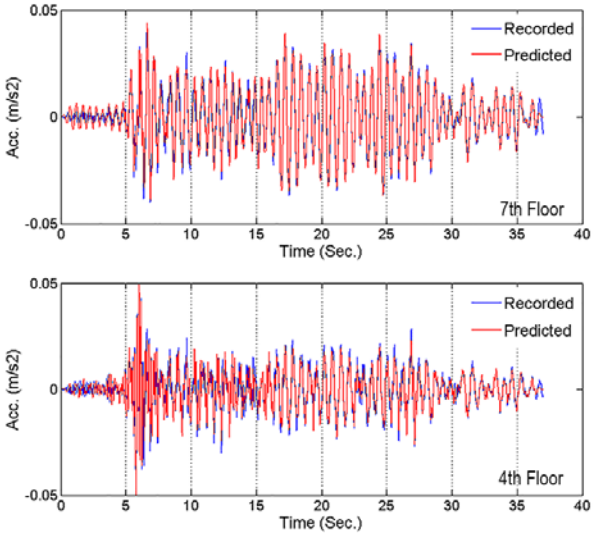

Figure 3. Comparison between response signals recorded and blindly predicted.

By using only the acceleration signals recorded on the foundation (sway), 6th floor, and the roof, the unknown parameters of flexible-base Timoshenko beam model are identified first. Figure 2 displays the recorded and predicted acceleration signals. There is a very good agreement, but it is not surprising, because both signals are used in the objective function of the minimization procedure. Figure 3 shows results of a blind prediction of the responses at two other floors. As seen, the same level of agreement is observed for these two floors. Multiplying the identified mass normalized sway and rocking stiffness parameters with the estimated mass of the Millikan Library (Ghahari *et al.*, 2015a), the soil-foundation sway and rocking stiffnesses are obtained as 1.89×10^{10}N/m and 2.32×10^{12}N, respectively. Using the identified stiffnesses from the Tier A approach (Ghahari *et al.*, 2015a) as reference values, the newly identified stiffnesses have 17% and 13% relative errors, respectively. As CSMIP-CIT identifies a frequency-independent soil-foundation impedance function, it is expected to exhibit larger errors/variability in comparison with Tier A, with which the soil-foundation stiffnesses were identified for each mode separately. Also, the larger error of sway stiffnesses is due to the fact that foundation sway relative to the soil is negligible for this particular building.

Finally, the natural frequencies of identified model with two different base-fixity conditions (i.e., flexible and fixed) are shown in Table 1 and compared with identified and FE model values. As seen, the two first flexible-base modes are almost identical to the identified and Tier A values. The source of difference in third mode's natural frequency of the flexible-base model is described in Taciroglu *et al.* (2015). Results in Table 1 also indicate that the first fixed-base natural frequency of both Tier A and the identified Timoshenko beam model are identical to the identified value.

The damping ratios of the Millikan Library have not been identified in any prior studies from earthquake data. Through application of CSMIP-CIT, these values for three base-fixity conditions are identified here. As there is negligible foundation sway, the first mode's damping ratios of both flexible- and fixed-base models are 1.62%, while for the fixed-base model, it is

2.34%. Indeed, foundation rocking could not compensate the reduction in the overall damping ratio, which is caused by a decrease in the natural frequency of the system that occurs due to the soil-foundation-system's hysteretic and radiation damping.

Table 1. Natural frequencies identified using different methods.

	Flexible-base System			Fixed Base System		
Mode No.	Identified	FE Model	CSMIP-CIT	Identified	FE Model	CSMIP-CIT
1	1.68	1.68	1.68	2.05	2.07	2.04
2	6.64	6.64	6.71	---	7.51	7.14
3	12.48	12.53	13.87	---	13.96	14.63

Application to CSMIP Data

Data Classification

In this section, results obtained through the application of CSMIP-CIT to building data available in the CESMD database are presented. Table 2 displays a summary of available building data in the aforementioned database. This classification is carried out by the *classification* capabilities of the developed software. As seen in Table 2, from among 381 instrumented buildings, only 234 can be studied at the present time due to the availability of both instrumentation layouts and earthquake data.

Table 2. Available building data in CESMD (Last update: 10/02/2015)

Item Description	Number
Number of total records	1604
Number of buildings	381
Number of earthquakes	240
Number of earthquae sets	1541
Number of buildings with at least one earthquake	320
Number of buildings with at least one available earthquake	312
Number of buildings with available layout	269
Number of buildings with available layout and at least one recorded earthquake	241
Number of buildings with available layout and at least one available earthquake	234

Material distribution of 381 buildings is shown in Figure 4(a). As seen, metadata of 35% (135) of the buildings are not available (there are 23 buildings that have instrumentation layouts, but it is not possible to determine their material type through CESMD). A similar plot for buildings with instrumentation layout and available earthquake data is given in Figure 4(b). As seen, more than 74% of such buildings have steel or concrete lateral resisting systems, and feature no seismic isolation devices. We concentrate on these buildings in the current study, of which there are 174.

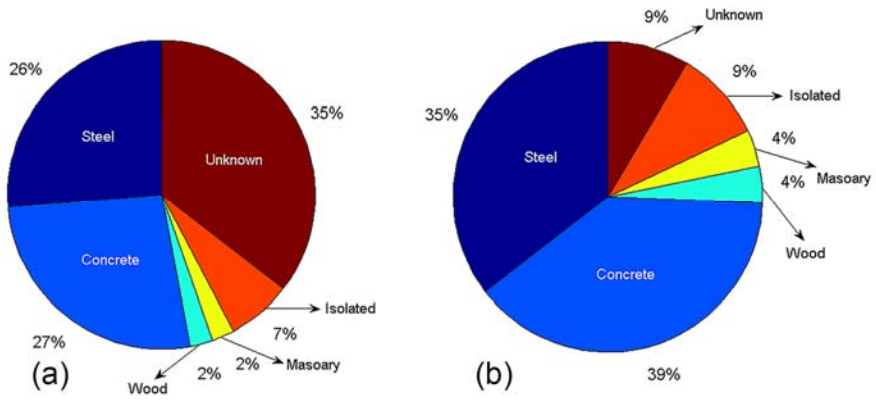

Figure 4. Material distribution of (a) all 381 instrumented buildings, and (b) 234 buildings with available earthquake data and instrumentation layout.

Theoretically, soil-foundation flexibilities can be identified by investigating the difference between the so-called flexible-based and fixed-base system's properties (Stewart *et al.*, 1999a, b). To identify both the fixed- and flexible-base properties, the FFM, foundation sway, foundation rocking, and building responses must be measured (Stewart, 1996). However, the number of CSMIP buildings with necessary instrumentation for this purpose is very limited. As shown in Figure 5 under Case 1, among the 174 selected buildings, the total number of steel and concrete buildings that have instrumentation layouts, available earthquake records, nearby Free-Field Motion (FFM) stations, foundation sway and rocking instrumentations, and at least one instrumented floor is less than 10 (out of the selected 174 buildings)! Note that it is actually possible to find FFM stations close to some of other buildings, but the aforementioned classification is based on FFM stations shown on the instrumentation layouts available in CESMD. If we can relax this requirement, then the number of specimen buildings increases to 25 (denoted as Case 2). Such a number is still very small and cannot be used to extract aggregate results from which broad conclusions can be drawn.

Another critical limitation is the availability of the foundation rocking measurement. By relaxing this condition as well, the number of buildings increases from 25 to around 170 (denoted as Case 3). Having only one sensor on the structure may not capture contribution of different modes. Therefore, it is more favorable to have additional sensors. As the figure shows, by adding one more sensor as an additional requirement (denoted as Case 4), the number of buildings available for study decreases[3], but not significantly (~152). Based on this, we designed CSMIP-CIT for Case 4 —i.e., we analyzed 152 instrumented buildings.

From the 152 candidates e, we gave priority to buildings that have (1) symmetric plans, and uniform mass and stiffness distributions along their height; (2) *several* recorded earthquakes; and (3) known soil shear wave velocity values. These properties helped us to be able to use the Timoshenko beam theory, to make sure that the identified results were consistent, and to combine dynamic foundation stiffness values identified from different buildings in a consistent manner. According to these criteria, 66 buildings with a total of 279 earthquake data sets were

[3] Requiring one additional sensor beyond that would reduce this number to 105.

analyzed. These buildings were classified according to their lateral resisting systems into three groups as shown in Figure 6.

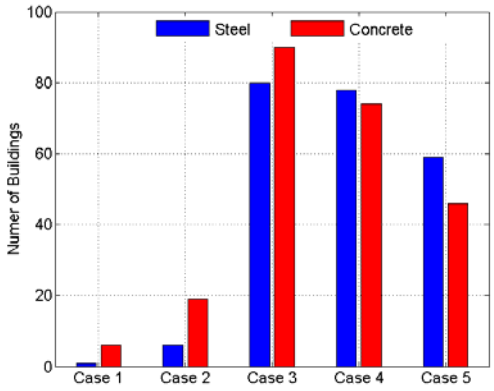

Figure 5. Number of instrumented buildings for various instrumentation scenarios.

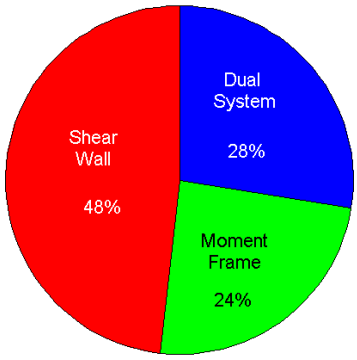

Figure 6. Distribution of chosen buildings according to their lateral system type.

Superstructure Parameters

The algorithm designed for CSMIP-CIT is able to identify the super-structure parameters, the soil-foundation system's sway and rocking stiffnesses, as well as natural frequencies and modal damping ratios of the entire system for flexible-, pseudo-flexible, and fixed-base conditions. Figure 7 shows the shear wave velocity of the buildings, $\sqrt{G/\rho} = L/(\sqrt{k}s\bar{b})$. As seen and expected, buildings with shear wall and moment frame systems have the highest and lowest values of wave velocity, respectively. Note that the structural nonlinearity is implicitly included in this figure, because results from various earthquakes with various levels of excitations have been used.

Building damping ratio is one of the challenging parameters to estimate in earthquake engineering, as it is not directly computable and many factors contribute to it. As such, identification of damping values from vibration data is the only viable path to quantification. As summarized by Bernal *et al.* (2013), several researchers suggested simplified formulae for first mode damping ratios using different parameters and calibrated these by using damping ratios estimated/identified from vibration data. Building height, material type, and vibration intensity were utilized as the primary physical parameters. There has been no discussion about the amplitude-dependency of the damping ratios. Bernal *et al.* (2013) also stated that there is no direct correlation between the damping ratio and the natural frequency. Indeed, taller buildings (having lower natural frequency) have higher aspect ratios, so the damping provided by the soil would be less, and consequently the overall damping ratio would be less. Based on this conjecture, they suggested an empirical formula for the first mode damping ratio using the building height and the material type (Bernal *et al.*, 2015). Their conjecture may indeed be true; nevertheless, Bernal *et al.* (2013) have only identified the pseudo-flexible damping ratio, because they have used the foundation sway as input in their input-output identification study. Therefore, foundation rocking may alter the overall damping ratio due to hysteretic and radiation damping

that the soil-foundation interface nominally exhibits (the same statement is true for the natural frequency). In our approach, it is possible to exclude the soil-foundation system's effects and to identify the natural frequency and damping ratio of the superstructure itself.

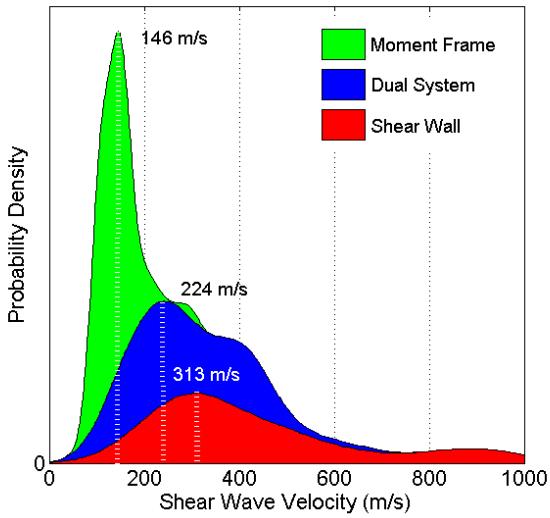

Figure 7. Probability distribution of shear wave velocity in fixed-base buildings.

Figure 8 displays the identified fixed-base natural frequencies and damping ratios of all 279 cases. Histograms of the identified values are also shown alongside. According to this figure, we can state:

1. Fixed-base natural frequencies of shear-wall buildings have higher variances (note that amplitude-dependency is included) in comparison to moment-frame systems. This is expected because natural frequencies of shear-wall buildings are more sensitive to cracking than moment frame systems.
2. Contrary to the natural frequency, damping ratio behaves in the reverse manner. That is, the variation of damping ratios in moment-frame systems is higher, probably because of the direct relationship between friction in connections and the level of vibrations.
3. There is a direct relationship between the damping ratio and the natural frequency. In stiffer systems, more elements are interacting with each other, and thus the damping level should be higher. Also, the slope of variation for moment-frame structures is greater than that for shear wall systems.

We do not present any regression results here, because it is out of scope of the present study. However, by excluding the amplitude-dependency from the identified results, it appears possible to reach a more realistic empirical formula for damping prediction of buildings.

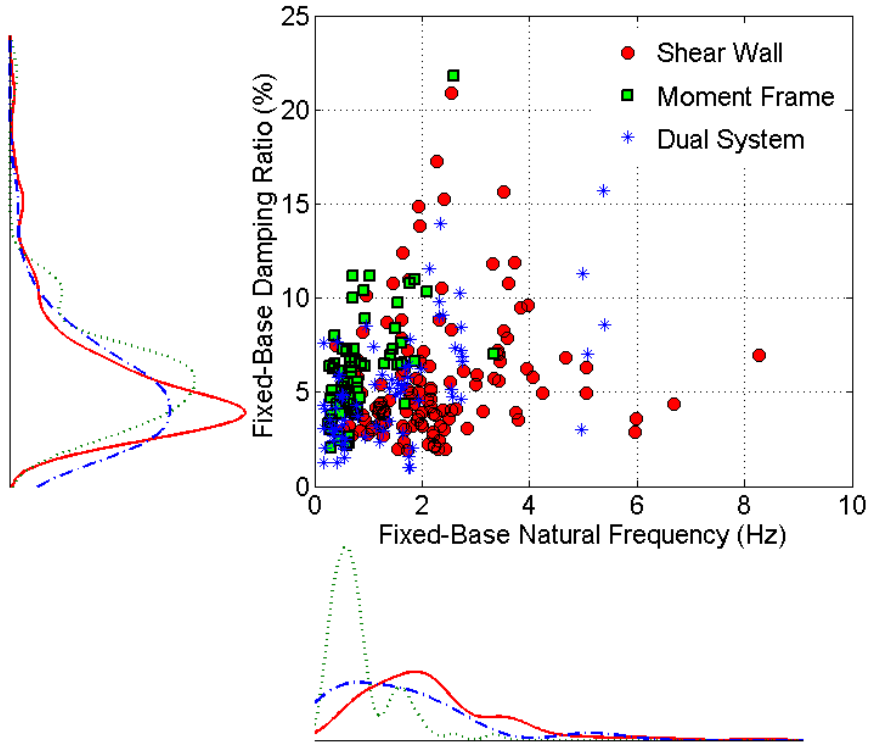

Figure 8. Variation of the fixed-base damping ratio versus fixed-base natural frequency.

Soil-Foundation Parameters: Frequency-Dependency

Here, the identified flexible-base modal properties are compared with available models. Period elongation and foundation damping are two parameters that are used in design codes for considering soil-structure interaction effects (e.g., ASCE-7, 2010). Figure 9(a) displays the period elongation—which is the ratio of the identified flexible-base to the fixed-base natural periods ($T_{Flexible}/T_{Fixed}$)—versus a dimensionless measure of the structure-to-soil stiffness—i.e., $h/(V_s T_{Fixed})$ where h is effective height, V_s is effective soil's shear wave velocity, and T_{Fixed} is fixed-base fundamental natural period. For comparison, the theoretical results derived by Veletsos and Nair (1975) for rigid surface circular foundation with 10% soil material damping and for three structural aspect ratios are shown. Circles shown in this figure denote results for a subgroup of the 66 buildings for which the identified flexible- and fixed-base natural periods are different (i.e., they exhibit inertial SSI effects). To calculate the aspect ratio of each building, their rectangular foundations (footprint of the building) are approximated by their equivalent circular foundation (Wolf and Deeks, 2004) and 70% of the height of the building is used as the effective height. For buildings that have already been studied by Stewart and Stewart (1997), the same earthquake data are used, so that the effective V_s values can be directly taken from their study. In cases where effective V_s was not available, earthquakes with minimum Peak Ground Acceleration (PGA) and V_s reported by Seyhan *et al.* (2014) were used. In the absence of small PGA earthquakes, V_s was reduced according to Table 4-1 of National Institute of Standards and Technology (NIST).

As seen in Figure 9(a), considering all available uncertainties (embedment, shear wave velocity, nonlinearity, etc.), the theoretical model by Veletsos and Nair (1975) produces good predictions. A similar graph for foundation damping is shown in Figure 9(b). Foundation damping is identified as the difference between flexible-base damping ratio and fixed-base damping ratio reduced by a factor of $(T_{Flexible}/T_{Fixed})^3$. This graph indicates that the theoretical model overestimates the foundation damping for most cases. Finally, foundation damping is presented versus period elongation in Figure 9(c). Similar graph is currently used in ASCE-07 (2010). Again current formula overestimates foundation damping for a specific period elongation.

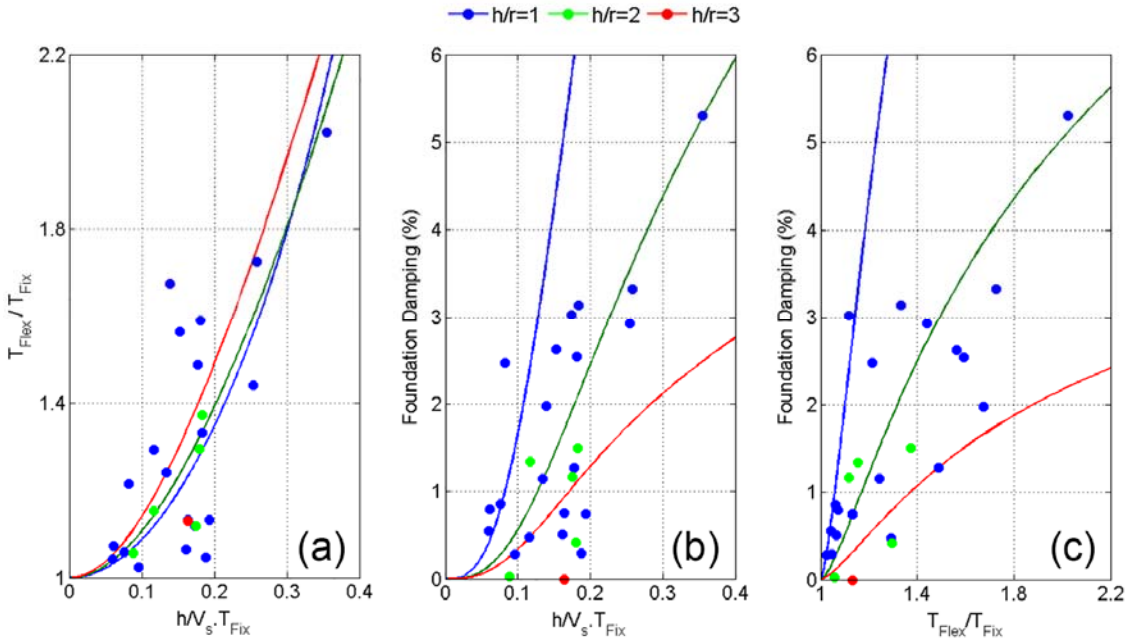

Figure 9. Comparison between identified (symbols) period elongation and foundation damping values with those predicted using the model by Veletsos and Nair (1975) (solid lines).

By selecting those buildings for which the identified fixed-base and pseudo-flexible-base natural frequencies are different, it is possible to investigate the frequency-dependency of the soil-foundation rocking stiffness. To do so, the identified stiffnesses are multiplied by an estimation of the buildings' masses and are normalized by the theoretically calculated static stiffnesses (Wolf and Deeks, 2004). Frequency-dependent impedance functions are typically presented versus the dimensionless parameter $a_0 = \omega r/V_s$. For each building, a_0 is calculated at its fundamental flexible-base natural frequency. The equivalent radius of the foundation (r) and soil's shear wave velocity ($\underline{V_S}$) were discussed earlier. The extracted frequency-dependent rocking stiffnesses are shown in Figure 10 as single points. For comparison, a theoretical curve proposed by Veletsos and Verbic (1973) is also shown. The identified values are denoted using four different symbols. There were two buildings for which the results are not close to the theoretical values, and these are suspected to have flexible foundation systems (Stewart and Stewart, 1997). For another three buildings, we could not find strain-compatible shear wave velocity values. Finally, there were two buildings that were also are far from theoretical values

due to unspecified reasons. The remaining buildings in the dataset (a majority) were interestingly in very good agreement with formula proposed by Veletsos and Verbic (1973), while noting that a Poisson's ratio of 0.45 and 10% material damping was used to generate the theoretical curve.

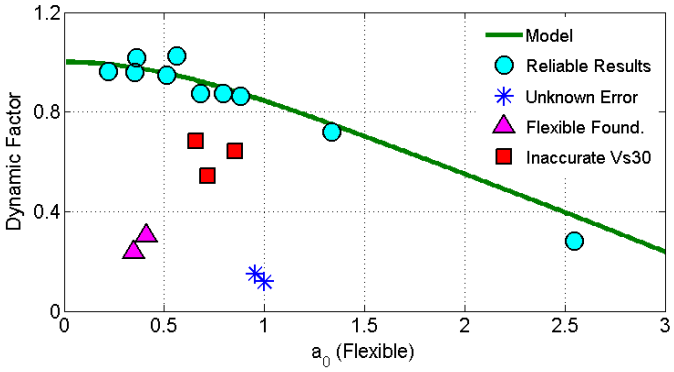

Figure 10. Identified soil-foundation rocking stiffness' frequency-dependency versus what predicted by Veletsos and Verbic (1973).

As a final result, we investigated kinematic interaction effects. Kinematic interaction has been rarely studied by solving inverse problems using real-life data. A study by Kim and Stewart (2003) is one of these rare studies; however, they extracted the Transfer Functions between the nearby FFM and the recorded foundation motions, which are not equal to FIM. By contrast, we used the true FIM here, which we could extract using identification approach proposed in this paper. As an example, Figure 11 displays the Transfer Function calculated between the FIM recovered for the 2011 Berkeley Earthquake from the transverse direction of Station 58503, and its nearby FFM station 58505. Per the recommendation by Kim and Stewart (2003), the Transfer Function is shown only for frequencies at which coherence (Pandit, 1991) is greater than 0.8. The theoretical Transfer Function for a rigid rectangular foundation with the same dimensions and shear wave velocity under vertical incoherent SH waves with incoherency factor of $\gamma = 0.5$ (Veletsos *et al.*, 1997) is also shown. As seen, while the extracted Transfer Function is jagged, its mean value follows the theoretical prediction fairly well.

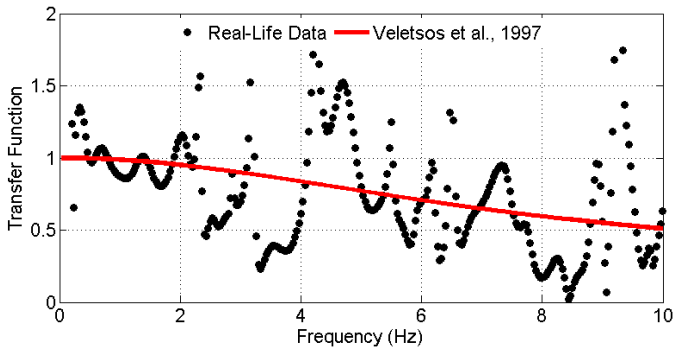

Figure 11. Comparison between the identified kinematic transfer function with that predicted through the model by Veletsos *et al.* (1997) using vertical incoherent shear wave formulation.

Soil-Foundation Parameters: Amplitude-Dependency

In the previous section, we attempted to avoid the inherent amplitude-dependency of impedance functions by using only low-intensity earthquake data or by *correcting* the soil shear wave velocities. However, soil nonlinearity is ever-present and must be well studied. As an example, the time-history and time-frequency distribution of foundation rocking and roof acceleration of CSMIP station #57356 recorded during the 1989 Loma Prieta Earthquake are shown in Figure 12. As this figure shows, there are significant temporal variations. As the large amplitude excitations arrived, the natural frequency reduced to its minimum and it gradually recovered at the end of the event. Therefore, depending on which time segment of signals are used in CSMIP-CIT, different values of impedance functions will be identified.

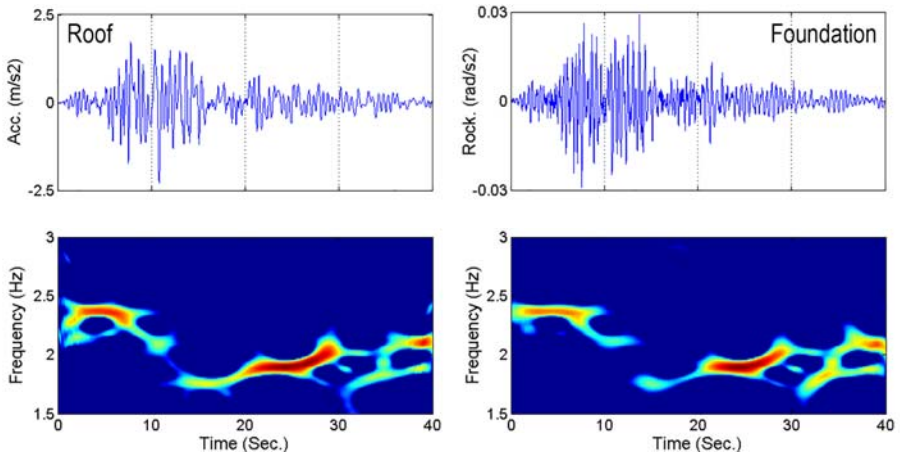

Figure 12. Time variation of the first natural frequency of CSMIP57356 during the 1989 Loma Prieta Earthquake[4].

We carried out identification for CSMIP 57356 using several earthquake data sets. For the Loma Prieta earthquake, which was a severe event at this station, we carried out identification in four successive time segments. The idenitified rocking stiffnesses (mass normalized values) versus Peak Foundation Accelerations are shown in Figure 13. As seen, there is a clear amplitude-dependency. That is, the rocking stiffness decreases when the level of vibration increases. This figure also shows that the soil stiffness does not quickly recover. In other words, the identified rocking stiffnesses at the third and the final time windows for the Loma Prieta earthquake (1989) are lower than those expected for the given earthquake intensity.

[4] Colors do not reflect the actual signal energy at each time instant, because the signal has been scaled with its instantaneous amplitude to show its instantaneous frequencies more clearly.

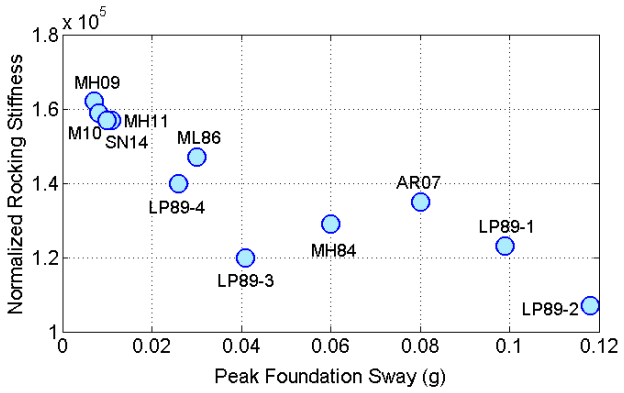

Figure 13. Amplitude dependency of the soil-foundation rocking stiffness observed at station CSMIP57356.

As a final observation, we try to see the compatibility between the amplitude-dependency of the results with those predicted by a formula usually used in practice. For this purpose, we first have to translate the peak foundation (~ground) acceleration to shear strain. To do so, we use following relationship between maximum shear strain and amplitude of a vertically propagating sinusoidal shear wave (Beresnev and Wen, 1996),

$$|\gamma_{max}| = \frac{A}{2\pi f V_s} \tag{28}$$

where A is the acceleration amplitude, f is the wave frequency, and V_s is the soil shear wave velocity. We use amplitude of the Fourier Transform of foundation response at first mode's flexible-base natural frequency (f) as an approximation of A. For the shear wave velocity, we use the small strain value proposed by Stewart and Stewart (1997). Figure 14 presents the same data points of Figure 13 but in different axes. The horizontal axis is now shear strain, which is calculated through Eq. (28), and the vertical axes is rocking stiffness scaled by the maximum value obtained among all data points —*viz.*, during the 2009 Morgan Hill Earthquake. For comparison, we have shown the shear reduction curve suggested by Ishibashi and Zhang (1993). The best-fit curve was obtained when we adjusted the plasticity index to 0 (i.e., sandy soil). As seen, there is very good agreement between the theoretical formula and the identified values.

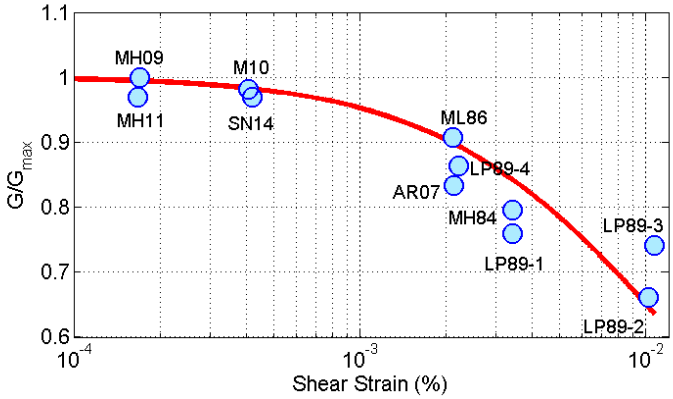

Figure 14. Soil's shear modulus reduction identified in station CSMIP57356.

Conclusions

We proposed an efficient method through which the soil-foundation systems impedance functions and foundation input motions can be identified using earthquake-induced response signals of an instrumented buildings recorded on three levels: foundation, mid-height, and roof. In this method, the building is represented with a simple Timoshenko beam model and the soil-foundation system's impedance function is estimated through an optimization problem without the need to have the foundation input motions (FIM). After identifying the flexible-base beam, the FIM is back-calculated. To facilitate broader use of this method and to simplify its application to CSMIP data, we developed a software tool, dubbed CSMIP-CIT. We used this toolbox and analyzed more than 60 buildings, which, in total, have more than 250 earthquake data sets. The results obtained so far validated some of the theoretical approximations, and also indicated that SSI effects have various intrinsic features that the soil-foundation systems of real-life structures *do* exhibit under seismic shaking, such as frequency- and amplitude-dependency. Kinematic interaction effects as well as superstructure damping values were quantified from the datasets used thus far. Broader findings will be possible once the method proposed herein is applied to more datasets.

Acknowledgments

The work presented in this manuscript was funded, in part, by the California Geological Survey (Contract No. 1014-963) and by the California Department of Transportation (Grant No. 65A0450). Any opinions, findings, conclusions or recommendations expressed in this material are those of the authors and do not necessarily reflect the views of the sponsoring agencies.

References

Abrahamson, N.A., Schneider, J.F. & Stepp, J.C. 1991. Empirical spatial coherency functions for applications to soil-structure interaction analyses." *Earthquake Spectra,* 7(1), 1-27.

American Society of Civil Engineers, ASCE, 2010. Minimum Design Loads for Buildings and Other Structures, Report ASCE/SEI 7-10, Reston, VA.

Aristizabal-Ochoa, J., 2004. Timoshenko beam-column with generalized end conditions and nonclassical modes of vibration of shear beams. *Journal of Eng. Mech.,* 130(10), 1151-1159.

Beresnev, I.A., & Wen, K. L., 1996. Nonlinear soil response—a reality?. *Bulletin of the Seismological Society of America*, 86(6), 1964-1978.

Bernal, D., Kojidi, S.M., Kwan, K., & Döhler, M., 2013. Damping Identification in Buildings from Earthquake Records. In SMIP12 Seminar Proceedings, 39-56.

Bernal, D., Döhler, M., Kojidi, S. M., Kwan, K., & Liu, Y. 2015. First mode damping ratios for buildings. *Earthquake Spectra*, 31(1), 367-381.

Bradford, S., Clinton, J., Favela, T. & Heaton, T., 2004. *Results of Millikan library forced vibration testing*: Earthquake Engineering Research Laboratory.

Çelebi, M., Firat, S. & Çankaya, I., 2006. The evaluation of impedance functions in the analysis of foundations vibrations using boundary element method. *Applied Mathematics and Computation,* 173(1), 636-667.

Cheng, M. & Heaton, T., 2013. Simulating building motions using the ratios of its natural frequencies and a Timoshenko beam model.. *Earthquake Spectra.*

Chopra, A., 2001. Dynamics of structures: theory and applications to earthquake engineering. 2nd ed. s.l.:Prentice-Hall.

Clough, R. & Penzien, J., 1975. *Dynamics of Structures*, McGraw-Hill.

Cowper, G., 1966. The shear coefficient in Timoshenko's beam theory. *ASME Journal of Applied Mechanics,* 33(2), 335-340.

Gazetas, G., 1983. Analysis of machine foundation vibrations: state of the art. *International Journal of Soil Dynamics and Earthquake Engineering,* 2(1), 2-42.

Ghahari, S., Abazarsa, F., Ghannad, M. & Taciroglu, E., 2013. Response-only modal identification of structures using strong motion data. *Earthquake Engineering and Structural Dynamics,* 42(8), 1221-1242.

Ghahari, S., Abazarsa, F., Ghannad, M.A., Celebi, M. & Taciroglu, E., 2014. Blind modal identification of structures from spatially sparse seismic response signals. *Structural Control and Health Monitoring,* 21, 649-674.

Ghahari, S., Abazarsa, F., Avci, O., Celebi, M. & Taciroglu, E., 2015a. Blind identification of the Millikan Library from earthquake data considering soil structure interaction. *Structural Control and Health Monitoring* (in press).

Ghahari, S., Abazarsa, F. & Taciroglu, E., 2015b. *CSMIP-CIT.* V2.

Han, S., Benaroya, H. & Wei, T., 1999. Dynamics of transversely vibrating beams using four engineering theories.. Journal of Sound and Vibration, 225(5), 935-988.

IBC, 2012. *International Building Code,* Washington D.C: International Code Council.

Iguchi, M. & Luco, E., 1981. Dynamic response of flexible rectangular foundations on an elastic half-space. *Earthquake Engineering & Structural Dynamics,* 9(3), 239-249.

Ishibashi, I., & Zhang, X., 1993. Unified dynamic shear moduli and damping patios of sand and clay. *Soils and Foundations*, 33(1), 182-191.

Jennings, P. & Bielak, J., 1973. Dynamics of building-soil interaction.. *Bulletin of the Seismological Society of America,* 63(1), 9-48.

Jennings, P. & Kuroiwa, J., 1968. Vibration and soil-structure interaction tests of a nine-story reinforced concrete building. *Bulletin of the Seism. Society of America,* 58(3), 891-916.

Kim, S., & Stewart, J.P., 2003. Kinematic Soil-Structure Interaction from Strong Motion Recordings. *Journal of Geotechnical and Geoenvironmental Engineering*, 129(4), 323-335.

Lignos, D. & Miranda, E., 2014. Estimation of base motion in instrumented steel buildings using output-only system identification. *Earthquake Engineering and Structural Dynamics*, 43(4), pp. 547-563.

Luco, J., Trifunac, M. & Wong, H., 1988. Isolation of soil-structure interaction effects by full-scale forced vibration tests. *Earthquake Engineering and Structural Dynamics,* 16(1), 1-21.

MATLAB, 2013. The language of technical computing., s.l.: Mathworks.

National Institute of Standards and Technology, NIST (2012). Soil-Structure Interaction for Building Structures, Report NIST/GCR 12-917-21, presented by NEHRP Consultants Joint Venture, J.P. Stewart (project director), September.

Pais, A. & Kausel, E., 1988. pproximate formulas for dynamic stiffnesses of rigid foundations.. *Soil Dynamics and Earthquake Engineering,* 7(4), 213-227.

Pak, R. & Guzina, B., 1999. Seismic soil-structure interaction analysis by direct boundary element methods. *International Journal of Solids and Structures,* 36(31), 4743-4766.

Pandit, S.M., 1991. Modal and Spectrum Analysis: Data Dependent Systems in State Space. Wiley-Interscience.

Richart, F., 1975. Some effects of dynamic soil properties on soil-structure interaction. *Journal of the Geotechnical Engineering Division (ASCE),* 101(2), 1193-1240.

Rizos, D. & Wang, Z., 2002. Coupled BEM–FEM solutions for direct time domain soil–structure interaction analysis. *Engineering Analysis with Boundary Elements,* 26(10), 877-888.

Seyhan, E., Stewart, J.P., Ancheta, T.D., Darragh, R.B., & Graves, R.W., 2014. NGA-West2 site database. *Earthquake Spectra*, 30(3), 1007-1024.

Snieder, R. & Safak, E., 2006. Extracting the building response using seismic interferometry: Theory and application to the Millikan Library in Pasadena, California. *Bulletin of the Seismological Society of America,* 96(2), 586-598.

Stewart, J.P. 1996. An empirical assessment of soil-structure interaction effects on the seismic response of structures. Doctoral dissertation, University of California, Berkeley.

Stewart, J.P., & Stewart, A.F., 1997. Analysis of soil-structure interaction effects on building response from earthquake strong motion recordings at 58 sites. *Earthquake Engineering Research Center*, 97(1).

Stewart, J., Seed, R. & Fenves, G., 1998. *Empirical evaluation of inertial soil-structure interaction effects*: Pacific Earthquake Engineering Research Center (PEER).

Stewart, J.P., Fenves, G.L., & Seed, R.B., 1999a. Seismic soil-structure interaction in buildings. I: Analytical methods. *Journal of Geotechnical and Geoenv. Eng.*, 125(1), 26-37.

Stewart, J.P., Seed, R.B., & Fenves, G.L., 1999b. Seismic soil-structure interaction in buildings. II: Empirical findings. *Journal of Geotechnical and Geoenv. Eng.*, 125(1), 38-48.

Taciroglu, E., Ghahari, S. & Abazarsa, F., 2015. Efficient model updating of a multi-story frame and its foundation stiffmess from earthquake records using a Timoshenko beam model. *Soil Dynamics and Earthquake Engineering* (under review).

Taciroglu, E. & Ghahari, S., 2015. Identification of Soil-Foundation Dynamic Stiffness from Seismic Response Signals. *ACI Special Publication*.

Tileylioglu, S., Stewart, J. & Nigbor, R., 2010. Dynamic stiffness and damping of a shallow foundation from forced vibration of a field test structure. *Journal of Geotechnical and Geoenvironmental Engineering,* 137(4), 344-353.

Timoshenko, S., 1921. On the correction for shear of the differential equation for transverse vibrations of prismatic bars. *The London, Edinburgh, and Dublin Philosophical Magazine and Journal of Science,* 41(245), 744-746.

Todorovska, M., 2009. Soil-structure system identification of Millikan Library North–South response during four earthquakes (1970–2002): what caused the observed wandering of the system frequencies?. *Bulletin of the Seismological Society of America,* 99(2A), pp. 626-635.

Veletsos, A. & Verbic, B., 1973. Vibration of viscoelastic foundations. *Earthquake Engineering & Structural Dynamics,* 2(1), 87-102.

Veletsos, A.S., & Nair, V.V., 1975. Seismic interaction of structures on hysteretic foundations. *Journal of the Structural Division*, 101(1), 109-129.

Veletsos, A.S., Prasad, A.M., & Wu, W.H., 1997. Transfer functions for rigid rectangular foundations. *Earthquake engineering & structural dynamics*, 26(1), 5-17.

Wolf, J., 1976. Soil-structure interaction with separation of base mat from soil (lifting-off). *Nuclear Engineering and Design,* 38(2), 357-384.

Wolf, J. & Deeks, A., 2004. Foundation Vibration analysis: A Strength of Materials Approach. Butterworth-Heinemann.